Sparse canopy parameterizations for meteorological models

B.J.J.M. van den Hurk

- **Promotor**
  Dr. J. Wieringa, hoogleraar in de meteorologie

- **Co-promotor**
  Dr. H.A.R. de Bruin, universitair hoofddocent meteorologie

Sparse canopy parameterizations for meteorological models

B.J.J.M. van den Hurk

Proefschrift
ter verkrijging van de graad van doctor
in de landbouw- en milieuwetenschappen
op gezag van de rector magnificus
dr C.M. Karssen
in het openbaar te verdedigen op
maandag 22 januari 1996
des namiddags te vier uur
in de Aula van de
Landbouwuniversiteit Wageningen

■ **CIP-gegevens Koninklijke Bibliotheek, Den Haag**

Hurk, B.J.J.M. van den

Sparse canopy parameterizations for meteorological models/ B.J.J.M. van den Hurk. - [S.l. : s.n.]. - Ill
Thesis Landbouwuniversiteit Wageningen. - With ref. - With summary in Dutch.
ISBN 90-5485-491-X
Subject headings: SVAT-schemes / sparse canopies / landsurface-PBL interactions.

NWO

■ **Coverpage**
Christien van den Hurk-Alferink
What's UNDER *the surface?*

■ **Financial support**
This study was carried out at the Department of Meteorology of the Wageningen Agricultural University. Financial support was provided by the European Committee under contract number EPOC CT90 - 0030, and by the Netherlands Organisation for Scientific Research (NWO) under contract number 762-365-030.

Abstract

Meteorological models for numerical weather prediction or climate simulation require a description of land surface exchange processes. The degree of complexity of these land-surface parameterization schemes — or SVAT's — that is necessary for accurate model predictions, is yet unclear. Also, the calibration of these SVAT's for relatively complex terrain, such as sparse canopies, is not completely resolved. This thesis pays attention to the sensitivity of the atmospheric boundary layer to the parameterization of surface exchange processes for a sparse canopy surface.

During two experimental campaigns carried out in a sparsely vegetated vineyard surface in La Mancha, Spain, detailed measurements were collected, including the flux densities of sensible, soil and latent heat, radiative fluxes, aerodynamic properties, and soil and vegetation characteristics. These measurements were used for calibration and validation of various SVAT-models and their components.

In a theoretical analysis the traditional treatment of aerodynamic transport of heat and moisture between a sparse canopy surface and the atmosphere was considered, and compared by an alternative formulation based on Lagrangian diffusion theory. An analysis of field observations was carried out to quantify the spatial and temporal variability of the surface albedo of a sparsely vegetated surface. Furthermore, a model for the stomatal conductance, based on the calculation of leaf photosynthesis and its relations with stomatal water vapour transport, was tested and scaled-up to the canopy level.

Various existing SVAT's, designed for sparse canopies, were described and compared to field measurements in a zero-dimensional mode, that is, with forcings measured at reference height close above the surface. These models were all based on different physical treatment of soil heat flux, aerodynamic exchange and canopy resistance. None of the included models gave an optimum description of the observed fluxes, but a model could be constructed that combined the best parts of each of these SVAT's.

In an additional model study, this new description has been coupled to a one-dimensional planetary boundary-layer (PBL) model. Parts of the SVAT were replaced by other components, and the impact on simulated PBL-dynamics has been evaluated. Large effects are found when (a) the reference two-layer model was replaced with a single layer ('big leaf') model, (b) soil heat flux was simulated with a resistance scheme rather than a diffusion or force-restore scheme, and (c) the aerodynamic resistance between the reference level and the bare soil was chosen too low. Since vegetation cover was small, smaller effects resulted from an alteration of the canopy resistance formulation. Also, it was found that the simulated entrainment of heat at the top of the boundary layer is low compared to entrainment ratios cited in literature.

Keywords: sparse canopy, surface fluxes, surface-PBL interaction, land-surface processes.

Dit boek draag ik op aan mijn vader
en mijn moeder

Voorwoord

Het eeuwige dilemma tussen 'het perfecte levenswerk' en 'het is maar een proefschrift' is op het werk dat in dit boek beschreven staat zeker van toepassing. Het onderwerp: modellering van land-oppervlak processen in meteorologische weer- en klimaatmodellen. Het materiaal waar uit te putten is: een erg groot aantal bestaande land-oppervlakmodellen, met ieder een eigen gedachtengang, behoefte aan invoergegevens, en mate van beschikbare documentatie en validaties. De opdracht: een vooral 'eerlijke' vergelijking tussen een aantal van die modellen uit te voeren met behulp van een zelf verzamelde dataset. Het lijkt een overzichtelijke opgave, maar de waarheid is anders.

Nog helemaal niet van plan om te promoveren kreeg ik na mijn vervangende diensttijd aan de vakgroep Meteorologie een aanstelling als EFEDA-projectmedewerker (wordt in dit boekje verder uitgelegd). Een jaar daarvoor begon **Anno van Dijken** in het kader van een promotie-baan moedig aan het uitvissen van de benodigde mate van detail in land-oppervlakmodellen voor meteorologische toepassingen, en wisselde deze onderzoeksopdracht in voor een baan bij MeteoConsult. Hij liet een portie denk- en programmeerwerk achter waar ik dankbaar gebruik heb kunnen maken. Want, van **Henk de Bruin** kreeg ik het verzoek het promotie-onderzoek af te ronden. Na wat aarzelen, en wat passen en meten met betrekking tot een kleine bijstelling van de oorspronkelijke onderzoeksvraag – zodat ik het werk wat ik voor EFEDA had gedaan grotendeels kon gebruiken voor het proefschrift – heb ik deze baan aanvaard. Aan deze Henk de Bruin dank ik niet alleen een slordige zes jaar betaald werk, maar bovendien een enorme bijdrage in de vorm van morele steun, kritische en vaak zeer praktisch georienteerde vragen, contact met een flink aantal vakmensen binnen en buiten de EFEDA-gemeenschap, een gezonde dosis twijfels en een even grote dosis zelfvertrouwen, een muziek-compagnon op diverse feestjes, een gewillig oor voor boze en vreugdevolle momenten, en zo kan ik nog wel even doorgaan. Hij is verder een drijvende kracht achter gigantisch veel werk op de vakgroep, en mijn dank voor al deze bemoeienis is groot, bijzonder groot.

Ik weet eerlijk gezegd niet of ik collega-promovendi zoals met name **Anne Verhoef, Cor Jacobs, Berenice Michels, Rushdi El-Kilani, Aafke Atzema, Joost Nieveen, Job Verkaik** en **Theo Jetten** nou moet bedanken, of dat ik gewoon maar blij moet zijn met hun aanwezigheid en onze wederzijdse contacten. Nou ja, Anne is natuurlijk een maat uit duizenden geweest. Samen zweten in Spanje tijdens de EFEDA-campagne, de talloze gesprekken en small-talks over alles in onze werkkamer en daar buiten, en ook het sterke gevoel van solidariteit die gepaard ging met de gezamenlijke eindsprint voor een proefschrift in het laatste jaar. Als dankjewel het goede woord hiervoor is, nou, dan dankjewel. Aan Cor ben ik een vergelijkbare dosis solidariteit verschuldigd, maar omdat hij nou eenmaal anderhalf jaar voor liep op ons functioneerde hij ook als veelgebruikte vraagbaak en brainstorm-tank. Ook dankjewel. Kamer- en EFEDA-genoot Berenice, de talloze bieren bij José van Alhambra (ook in Spanje) zijn memorabel, en daardoor blijvend. En we hebben samen een mooie poster gemaakt voor de vakgroep.

Collega-vakgroepsmensen zijn al net zo bedankbaar. **Jon Wieringa**, die tijdens mijn promotie-tijd als hoogleraar aantrad, en mij als een soort erfenis op zijn bord kreeg: bedankt voor de geleverde ondersteuning. Over ondersteuning gesproken: **Bert Heusinkveld**, het 'veulen' van EFEDA, een ware aanwinst voor de vakgroep: heel erg

dankjewel. Minstens zoveel dank verdienen **Kees van den Dries**, de computer-beheerder, **Ad van den Berg** en **Rolf Krikke**, programmeer-nymphen en kroegtijgers, **Anton Janson**, de levensgenieter van de werkplaats, en zijn Siamese tweeling **Teun Jansen** – de conversaties op 13m hoogte boven een Spaanse wijngaard zijn onvergetelijk. **Frits Antonysen** en **Johan Birnie** die een nieuwe ervaring aan hun levens toevoegden door het EFEDA-gebeuren, medezaalvoetballer **Willy Hillen**, en natuurlijk **Dick Welgraven**, met zijn eeuwig optimisme en bereidheid tot medewerking. Een gigantische ondersteuning kreeg ik ook van secretaresse **Gerrie van den Brink** en haar collega's (**Annelies, Jolanda**), voor de vele even-tussendoor-vraagjes-en-formuliertjes. Voor hen allen gold dat zij hun baan op een voor mij erg plezierige manier invulden. Heel veel bedankt daarvoor.

Van de stafmedewerkers **Adrie Jacobs, Leo Kroon** en **Michaël Saraber** ontving ik naast een prettige hoeveelheid collegialiteit ook vaak repliek op mijn (semi-)wetenschappelijke beschouwingen. En Adries bijdrage aan het EFEDA-werk valt niet op de achterkant van een bierviltje te vermelden, en een extra dankjewel is hier op zijn plaats. Dit geldt overigens evenzeer voor de verschillende studenten die meer of minder tijd aan EFEDA hebben besteed en nog niet zijn genoemd: Arnold Moene, Erik Beek, Laurens Ganzeveld, Ad Jeuken, Harold ten Dam, en Diedert Spijkerboer.

This work is fun! It is funny to share lots of beers in Tomelloso with **Henrik Søgaard** and his colleagues, and to share the enthousiasm about well-working material with **Jan Elbers, Han Dolman** and other members of the Winand Staring Centre. It has also been a pleasure to have worked with the people from the French Meteorological Service CNRM, in particular with **Pierre Bessemoulin** and **Joel Noilhan**. Joel probably helped me a lot to convince me that the EFEDA-work should be converted into a PhD-thesis. And now he helps me even more by playing the role of criticizer in my promotion committee. I am grateful to that, as I am grateful to **Bert Holtslag, Hans Vugts** and **Reinder Feddes**. The EFEDA-community consists of many more people with whom I have experienced a pleasant collaboration, and taking the risk for forgetting people for granted, I would like to thank the people from the Amsterdam Free University, **Yadvinder Malhi, Ford Cropley** and others from the Reading University, the Wageningen colleagues **Rene Kim, Wim Bastiaanssen, Peter Droogers, Han Stricker** and a lot more, **Martina Berger** and others from the Free University of Berlin, **Kevin Sene, Howard Oliver, Colin Lloyd, Eleanor Blyth** and colleagues from the Institute of Hydrology in Wallingford, and **Antonio Brasa** and others from the University of Albacete.

Apart from this long list of colleague scientists, I am particularly greatful to the inspiration I have pleasantly received from a few great (micro)meterologists: **Keith McNaughton** from HortResearch, Palmerston-North, New Zealand, who has spent an awfully large amount of time and patience in explaining how Lagrangian theory should be interpreted, how to write that down in a scientific paper, how moths can be used as meteorological sensor, how Christmas looks in summer, and, last but not least, how people are dressed for weddings in New Zealand. His participation to my wedding in April 1994 was a party on its own, and he once more proved himself to be a very pleasant and easy-to-go-along-with person. In an earlier stage, **Dennis Baldocchi** brought me irreversably on the path of scientific research, by sharing his great enthousiasm while I visited Oak Ridge. **John Monteith**, who has effectively "invented" many ideas micro-meteorologists work with nowadays, sincerely inspired me at a few occasions, in particular during the evaporation workshop in Copenhagen. And finally, the many conversations with **Anton Beljaars** about now-adays SVAT's (see this booklet) turned out to be productive enough for writing a joint scientific paper. And of course, I thank him a lot for showing his confidence in me by offering a job at KNMI.

Mijn hart gaat naar veel dingen. Natuurlijk naar mijn vrouw **Christien**, die me met zoveel dingen heeft geholpen. Maar ook naar 'mijn' theatergroep **De Stichting Lens**, waar ik een hele berg van de inspiratie die nog over was naast mijn werken aan SVAT's kwijt kon. Een groep bestaat uit mensen, en de mensen van Lens worden erg bedankt.

Contents

Abstract 5

Voorwoord 6

1. Introduction 11
1.1 Atmosphere - land surface interaction 11
1.2 Land surfaces and land-surface models 14
1.3 A sensitivity analysis using a coupled SVAT-PBL model 15
1.4 Organization of the thesis 18

2. Data collection and processing 20
2.1 The EFEDA-experiments 20
2.1.1 Context and goal 20
2.1.2 EFEDA-I 21
2.1.3 EFEDA-II 22
2.1.4 Correspondence of goals 23
2.2 Measurements taken by WAUMET during EFEDA-I (1991) 23
2.2.1 Site description 23
2.2.2 General set-up of WAUMET 24
2.2.3 Determination of available radiative energy 28
2.2.4 Determination of scalar and momentum flux densities 30
2.2.5 Determination of soil heat flux density 38
2.2.6 Determination of vegetation parameters 40
2.2.7 Various determinations 46
2.3 Measurements taken by WAUMET during EFEDA-II (1994) 47
2.3.1 General setup 47
2.3.2 Site description 49
2.3.3 Determination of available energy and surface temperature 50
2.3.4 Determination of scalar and momentum flux densities 51
2.3.5 Soil measurements 52
2.3.6 Determination of vegetation parameters 53
2.4 Derived quantities 57
2.4.1 Aerodynamic roughness and displacement height 57
2.4.2 Roughness length for heat 59
2.4.3 Energy balance terms 61
2.4.4 Soil thermal properties 65

3. Aerodynamic transfer, albedo, and crop conductance for a sparse canopy surface 68
3.1 Introduction 68
3.2 Aerodynamic transfer 69
3.2.1 Concepts based on diffusion theory 69
3.2.2 Implementation of near-field dispersion in a simple two-layer surface resistance model 70
3.2.3 A 'Lagrangian' revision of the resistors in the two-layer model for calculating the energy budget of a plant canopy 80

3.3 The albedo of a sparse vineyard canopy during the growing season 87
3.3.1 Processes determining the albedo of a sparse vineyard canopy 88
3.3.2 Albedo measurements taken in a sparse vineyard canopy 92
3.3.3 Conclusions 97
3.4 A photosynthesis model for the crop conductance applied to a sparse vineyard canopy 98
3.4.1 Theory 99
3.4.2 Site description and measurements 101
3.4.3 Results 102
3.4.4 Discussion and conclusions 103
3.5 Conclusions 106

4. Selected surface layer and boundary layer models 108
4.1 Surface layer models for sparse canopies 108
4.1.1 The modified big-leaf model 109
4.1.2 The ECMWF surface scheme 111
4.1.3 Impact of some simplifying assumptions in the new ECMWF-surface scheme 116
4.1.4 The two-layer model of Deardorff 129
4.1.5 The two-layer models of Shuttleworth & Wallace and Choudhury & Monteith 136
4.2 Treatment of the planetary boundary layer 142
4.2.1 A numerical diffusion scheme for the planetary boundary layer 142
4.2.2 Slab model for the convective PBL 144
4.3 Limitations to the coupled 1-dimensional atmospheric model 146

5. An intercomparison of three soil/vegetation models for a sparse vineyard canopy 148
5.1 Description of data, model settings and used forcings 150
5.1.1 Collected data 150
5.1.2 Forcings and specific model settings 151
5.2 Simulations with the SVAT-schemes 155
5.2.1 Soil heat flux density 156
5.2.2 Sensible heat exchange and surface temperature 158
5.2.3 Evaporation and soil water budget 160
5.3 Discussion and conclusions 162

6. Sensitivity of the planetary boundary layer to surface description 165
6.1 Model specification 167
6.1.1 The reference model 167
6.1.2 Model variations 168
6.2 Set-up of the sensitivity analysis 172
6.2.1 Basic strategy 172
6.2.2 Specification of considered SL- and PBL-parameters 174
6.2.3 Radiative forcings and initial profiles 175
6.3 Results of the sensitivity analysis for daytime conditions 177
6.3.1 The surface representation group 178
6.3.2 The soil heat and water vapour flux group 182
6.3.3 The aerodynamic exchange group 186
6.3.4 The canopy resistance group 188
6.3.5 PBL-sensitivity and an analytical approach 191

6.4 Results of the sensitivity analysis for nighttime conditions 194
6.4.1 The surface representation group 194
6.4.2 The soil heat and water vapour flux group 195
6.4.3 The aerodynamic exchange group 196
6.4.4 The canopy resistance group 197
6.5 Simulations using EFEDA-observations 197
6.5.1 Selection of the simulation period 198
6.5.2 Initialization and forcing 199
6.5.3 Control run 200
6.5.4 Results of the sensitivity analysis 202
6.6 Discussion and conclusions 207
6.6.1 Differences of model parts 208
6.6.2 Practical considerations for SVAT's 212
6.6.3 Guidance for future research 213

Appendix I: List of symbols and acronymns 215

Appendix II: Instrumental aspects and data processing 220
1 Low-pass filtering (detrending) 220
2 Eddy-correlation corrections 221
3 Surface temperature and radiometer corrections 232
4 Soil heat flux density corrections 235

Appendix III: The bulk leaf boundary-layer resistance 236

Appendix IV: The photynthesis model at the leaf scale and calculation of ambient conditions 238

Appendix V: Numerical aspects of the SVAT-models 241

Appendix VI: Values of the surface layer and boundary layer parameters, calculated with the reference SVAT coupled to the PBL-model 245

Samenvatting 247

Summary 254

Literature 261

Curriculum 271

1

The gap between politicians and climate researchers is difficult to bridge, as long as politicians don't understand politics, and climate researchers don't understand climate

Introduction

The population living on the Earth's surface is very familiar with processes as heating of the air after sunrise, wilting of crop leaves after a long period without rain, or the development of cumulus clouds by the end of a summer day. These processes are all simple results of a complex set of interactions between the surface and the air just overlying the ground. When the soil receives radiation, it returns this energy partially back into the atmosphere by heating it, or by using this energy for evaporation, humidifying the air. Heating the air above the ground enhances turbulence intensity, which can cause intense mixing with higher air layers. In its turn, this affects the state of the air near the surface. Rising of moist air can also result in the formation of clouds, which will modify the amount of radiation penetrating to lower levels, or can eventually cause rain (McIntosh and Thom, 1983). The land surface and the overlying atmosphere clearly interact.

This thesis reports on a study of this interaction. It pays attention to the transport of water vapour, sensible heat and momentum between the surface and the atmosphere. It focusses on a surface that is only partially covered with vegetation. The framework is provided by measurements, theoretical analysis, and modeling efforts. In this chapter we will discuss the atmosphere-land surface interaction in more detail, and an outline and the main purposes of the research will be given.

1.1 Atmosphere - land surface interaction

Generally, the land surface-atmosphere interaction influences the dynamics of the entire atmosphere, both on the shortterm regional and the longterm global scale. The transfer of momentum and sensible and latent heat between the surface and the atmosphere primarily modifies the local surface and air adjacent to it, but atmospheric motions act as a major redistributor of energy at a global scale (Schmugge and André, 1991).

By conducting experiments with atmospheric General Circulation Models, GCM's, it

has been shown that the large end of the range of spatial and temporal scales, the global climate, is sensitive to the land-surface exchange processes (Garratt, 1993). Early GCM studies revealed a climate sensitivity to surface evaporation and initial soil moisture content, albedo, or surface roughness (see reviews by Mintz, 1984, and Rowntree and Sangster, 1986). For instance, Shukla and Mintz (1982) noticed a large reduction of continental precipitation over most continents when a potentially evaporating surface was changed into a surface without any evaporating at all using a GCM. Charney *et al.* (1977) found that an increase of the albedo of the Sahelian region would lead to a reduction of both the regional evaporation and precipitation in the area. Treatment of the transfer of water from deeper soil layers into the atmosphere via transpiration plays a significant role in the long term predictions of cloud development, precipitation, evaporation and soil moisture content (Milly and Dunne, 1994). GCM studies were also applied to investigate the impact of large scale changes in vegetation cover. Particularly, a series of simulations was dedicated to the effects of tropical deforestation (Henderson-Sellers and Gornitz, 1984; Dickinson and Henderson-Sellers, 1988).

Also, at somewhat smaller timescales a sensitivity of atmospheric behaviour to land surface description is evident. Beljaars *et al.* (1995) found a considerable difference in predicted USA rainfall after changing the land surface parameterization scheme in the ECMWF Numerical Weather Prediction (NWP) model. Moene *et al.* (1995) used the meso-scale High Resolution Limited Area Model (HIRLAM) covering Western-Europe, and found very different rainfall predictions for different soil moisture initializations.

At smaller time and spatial scales, the interaction with the Planetary Boundary Layer (PBL) is important. The PBL is defined as the layer which is directly affected by the state of the underlying surface. It senses the diurnal variations of the surface properties (such as the surface temperature or evaporation) and adapts to a change of surface roughness. The condition and growth of the PBL depends on the partition of available energy at the surface. Using a numerical PBL-model with a simple energy balance scheme as lower boundary condition, Troen and Mahrt (1986) found a non-linear reduction of the PBL height when the surface evaporation was increased.

The turbulent mixing of air in the PBL partly determines the state of the atmosphere at screen height, just above the surface. Since the driving force of heat and water vapour exchange at the surface is the gradient of the particular constituent between the surface and a reference level just above, feedback processes between the surface and the boundary layer contribute to the properties of the lowest layers of the atmosphere (De Bruin, 1987). This mechanism is denoted as *PBL-feedback*.

PBL-feedback can result in either an increase or a decrease of the effect of changing surface properties on the energy balance of the surface. Jacobs and de Bruin (1992) demonstrated that including PBL-dynamics implies a negative feedback on evaporation when the crop resistance is modified: a reduction of the resistance causes at first instance an increase of the evaporation, which results in a decrease of the humidity deficit at reference height when boundary layer mixing is considered. Alternatively, positive feedback on evaporation occurs when the net radiation is changed, for instance due to a changing albedo. Both sensible and latent heat will be reduced when total radiant energy is reduced. Accounting for boundary layer mixing, also a reduction of the reference temperature will be

simulated, which reduces the humidity deficit and thus the evaporation. Rowntree (1991) pointed at a positive feedback mechanism that occurs when the surface resistance increases due to a removal of vegetation. A progressive reduction of the vegetation may be the result of a drying atmosphere and a decrease of precipitation.

A second mechanism of feedback is the response of stomata to ambient conditions. In coupled models in which the stomatal conductance for water vapour is reduced as the ambient humidity deficit increases, a positive feedback on surface evaporation is simulated. A reduction of evaporation will result in a drier and warmer boundary layer, which will more rapidly entrain into the free atmosphere owing to the larger amount of sensible heat supplied from below. This entrainment will further reduce the air humidity close to the surface, to which vegetation often responds by a further reduction of the stomatal aperture (Jacobs, 1994). These feedback mechanisms obviously have a pronounced effect on the interaction between the surface and the atmosphere, and thus on the atmospheric response to surface characteristics.

The implications of the feedback mechanisms for the exchange between the surface and the atmosphere on a regional scale have been made clear by use of simple concepts to describe PBL-dynamics and surface fluxes. For instance, De Bruin (1983) coupled a simple slab model for the convective PBL (Driedonks, 1981) to the Penman-Monteith combination equation providing surface fluxes. He showed that the the ratio of the surface evaporation to the so-called equilibrium evaporation (Priestley and Taylor, 1972) depends on the surface resistance for water vapour transfer, entrainment of heat from above the PBL, and aerodynamic surface characteristics. Monteith (1995a) explored the accomodation between transpiration from vegetation and the convective boundary layer by use of a similar model for the PBL and a linear response of stomatal conductance to ambient humidity. McNaughton and Jarvis (1983) introduced the concept of a 'coupling factor' Ω, to indicate the degree of interaction between a (vegetated) surface and the atmosphere. A strong interaction is present when the aerodynamic exchange occurs very efficient, or when the surface resistance is large.

Only for a constant surface forcing, both in time and space, the PBL will eventually be completely adapted to the underlying surface. Adaptation to spatially heterogeneous surfaces depends on the scale of the surface inhomogeneities. Hypothetically, fluxes from small scale heterogeneities are blended at the scale of the boundary layer, but the PBL will adjust to the local surface when the scale of the heterogeneities is large enough (De Bruin, 1987; Shuttleworth, 1988). Raupach (1991) pointed out that a PBL is rarely fully adapted to the underlying surface, due to the relatively short time scale of the change of the lower boundary conditions associated with the diurnal variation. This scale consideration provides a second justification for considering surface-atmosphere interaction by using coupled surface-PBL models to simulate surface boundary conditions for large scale modelling purposes (Brutsaert, 1986).

These conceptual studies reveal the significance of land-atmosphere interactions, but their results are not directly applicable as surface forcing in GCM's or NWP models. For these applications a large range of parameterization schemes have been developed in the last two decades. In the next section we will pay attention to these schemes.

1.2 Land surfaces and land-surface models

The experiments listed above clearly demonstrate the need for a realistic land surface parameterization scheme in meteorological models. The surface energy balance equation is widely used to provide the lower boundary condition for atmospheric modelling purposes:

$$Q_* = H + \lambda E + G \tag{1.1}$$

Here, Q_* is the net radiation absorbed by the surface, H and λE are the sensible and latent heat released to the atmosphere, respectively, and G is the heat stored in the ground and surface elements, such as vegetation. A list of all symbols and acronymns can be found in Appendix I. In eq. 1.1 the radiation term is defined positive downwards, while the remaining terms are defined positive when directed away from the surface. Small amounts of energy used for photosynthesis or other chemical processes are ignored and excluded from this equation. Eq. 1.1 states that the total amount of radiative energy that is absorbed by the Earth's surface is used to heat the air, to heat the soil, or to evaporate liquid water that is a source of latent heat that can be used to heat higher atmospheric layers, when condensation of evaporated water vapour occurs.

The amount of radiative energy absorbed by the surface, or its partitioning over the terms on the right hand side of eq. 1.1, is importantly determined by the type of surface. For polar regions covered with fresh snow a large part of the incoming shortwave radiation will be reflected, leaving relatively little energy that can be used to melt ice (incorporated in G) or heat the air aloft. A bare dry soil will show a quick increase of its temperature when Q_* is positive due to the absence of available water that can be evaporated. The low thermal conductivity of a bare dry soil will result in a relatively small heat loss to G, and the surface will thus release most of its energy as sensible heat (Oke, 1978). When vegetation is present, it allows a significant energy release as latent heat, due to its capacity to transport water from deeper soil layers via the root system. However, the water transport capacity of most vegetation types is limited, and a vegetated surface will also act as a source of sensible heat.

Many micrometeorological studies have been dedicated to the description of the energy balance for vegetated surfaces. A very well known concept is the so-called 'big leaf' model (Monteith, 1965), that regulates the partitioning of available energy ($Q_* - G$) over sensible and latent heat by means of a series of transport resistances, which are governed by both aerodynamic and plant physiological characteristics. Using such scheme a surface must be characterized by parameters describing its aerodynamic roughness (Thom, 1975), radiative properties (Goudriaan, 1977) and physiological resistance for evaporation (Kelliher *et al.*, 1995).

Parameterizations using the simple big-leaf concept are often based on detailed modelling and measurement studies of the microclimate within a canopy. Even for horizontally homogeneous vegetation covers a significant vertical variation of radiation, temperature or moisture exists within a vegetation stand. Multi-layer models describing these gradients (see e.g. Waggoner and Reifsnyder, 1968) require often too much input data and computation time to be useful in GCM's. Single layer models are more useful for this purpose, as made clear in a – suggestively entitled – paper by Raupach and Finnigan (1988).

The simple 'big leaf' concept appears to lack realism in cases where the vegetation

structure becomes more complex, for example, if the surface is only partially covered with plants. In this case, a major part of the available radiative energy reaches the bare soil and contributes to additional processes as heating of the underlying ground or of the air close to it. This heating leads to interaction between the heat fluxes from the canopy and bare soil components, in particular in cases where the canopy resistance is a function of ambient temperature or air humidity. Furthermore, canopy evaporation is generally smaller than that of fully vegetated surfaces as a result of the reduced leaf area. These surface types are denoted as *sparse canopies*. Agricultural crops early in the growing season, natural vegetation in dune landscape, tundra or savannah, or permanent orchards or vineyards in semi-arid areas are general and widespread examples of sparse canopies.

Black *et al.* (1970) were probably the first to present a surface model computing the evaporation from a surface that was only partially covered with vegetation. A few years later, Deardorff (1978) presented a so-called two-component land surface scheme. In this approach, the energy balance of a surface is split into a canopy and a bare soil component. Deardorff's model was the first Soil-Vegetation-Atmosphere-Transfer (SVAT) model that could be applied in large scale meteorological models. Since then several SVAT's were developed which either regarded the Earth's surface as a single layer with various surface components (Noilhan and Planton, 1989), or proposed major improvements to Deardorff's model (Dickinson *et al.*, 1986), or applied the Penman-Monteith combination equation to a similar two-component scheme (Shuttleworth and Wallace, 1985). Apart from these papers, numerous surface schemes were proposed that adapted one of these models for specific conditions or modified the complexity of these schemes to either the simpler or more complicated end (e.g. Sellers *et al.*, 1986; Warrilow *et al.*, 1986; Choudhury and Monteith, 1988; Shuttleworth and Gurney, 1990; Xue *et al.*, 1991; Koster and Suarez, 1992; Dickinson *et al.*, 1993; Dolman, 1993; Braud *et al.*, 1995; Viterbo and Beljaars, 1995; Bosilovich and Sun, 1995).

This abundant number of surface schemes provokes the call for intercomparison experiments. Various studies have been dedicated to comparing several of these surface schemes at various temporal and spatial scales. For instance, Dolman and Wallace (1991), Inclán and Forkel (1995) and Huntingford *et al.* (1995) compared various SVAT's with ranging complexity in a zero-dimensional mode, that is, by simulating fluxes using atmospheric forcings measured close above the surface. At the global scale, Sato *et al.* (1989) and Sud *et al.* (1990) compared the impact of replacing a very simple bucket hydrological model (Manabe, 1969) by the sophisticated Simple Biosphere (SIB) model (Sellers *et al.*, 1986). The aforementioned review of Mintz (1984) compares the sensitivity analysis of Shukla and Mintz (1982) to a similar experiment conducted by Suarez and Arakawa (cited by Mintz, 1984) (and found considerable differences in continental rainfall for some areas). Recently, the Project for Intercomparison of Land surface Parameterization Schemes (PILPS; Henderson-Sellers *et al.*, 1993; 1995) has been started, designed for a systematic intercomparison of about thirty surface schemes that are operational in current GCM's or NWP models. PILPS foresees in an extensive model documentation, sensitivity tests, and intercomparison experiments ranging from zero-dimensional model runs, using both synthetic and really measured forcings, to runs using fully coupled 3-dimensional global scale meteorological models.

1.3 A sensitivity analysis using a coupled SVAT-PBL model

Comparison experiments have shown that considerable differences exist between surface fluxes simulated by different SVAT's. GCM and NWP simulations are shown to be particularly sensitive to the parameterization of moisture transfer from deeper soil layers to the atmosphere (Henderson-Sellers *et al.*, 1995), and the treatment of this transfer is executed rather differently by the various models.

An important question – one that is also one of the research topics in this thesis – that arises is what level of complexity a land surface scheme must contain (Garratt, 1992, 1993). The large scale GCM or NWP sensitivity simulations contain so many degrees of freedom that the results are often difficult to interpret, and can only be expressed in very general terms. On the other hand, the stand-alone verifications of the various surface models using *in situ* observations allow a more transparent evaluation of aspects that play a key role in the exchange processes between the land surface and the atmosphere (and should be parameterized well in meteorological models). A disadvantage of these zero-dimensional intercomparison experiments is that atmospheric feedback processes cannot be taken into account, and their results seem to depend strongly on the test conditions and input data chosen. Furthermore, the number of processes that is simulated – even in relatively simple surface schemes as Deardorff (1978) – is still large enough to inhibit a straightforward interpretation of results.

In order to answer the question about the required level of model complexity, the drawbacks of both the large global scale and small zero-dimensional comparison studies should be avoided optimally. The strategy that is adopted in the current study is to consider surface-atmosphere interaction using a coupled one-dimensional SVAT-PBL model. The single dimension of the analysis allows a focus on the surface exchange processes, and disregards large scale atmospheric effects as horizontal advection, cloud formation, radiation penetration through the air mass, precipitation and other synoptic events. By considering the transport of momentum, latent and sensible heat in a vertical column with a height exceeding the typical PBL-height, surface-atmosphere feedback processes are allowed to modify the surface fluxes.

Within this one-dimensional framework a range of surface models of varying complexity will be coupled to a model for the PBL, and its response evaluated by performing simulations over a specified surface. Parameterizations are compared that currently are used in large scale meteorological models. This strategy differs in two ways from the PBL-sensitivity experiments conducted by for instance Troen and Mahrt (1986) or Jacobs and de Bruin (1992), who altered the lower boundary condition of a coupled surface-PBL model by changing some of the surface parameters (albedo, crop resistance or fraction of potential evaporation, aerodynamic roughness length):

(1) the interactions between surface and atmosphere are investigated for a specified surface, rather than studying the effect of changing the land surface itself

(2) different existing parameterization schemes for land surfaces will be coupled to a selected PBL-model, rather than that the sensitivity of one selected SVAT to the values of the model parameters or input data is considered.

A further attempt to focus on the physical exchange processes is carrried out by disentangling the various parameterizations of the surface models. The various processes that play a role in a land-surface parameterization scheme show many mutual interactions. For instance, suppose that a certain SVAT that is used to calculate the energy balance of a sparsely vegetated surface under conditions of strong radiation, describes an erroneously small transport of water within the soil. Under the specified conditions, the bare soil surface will soon dry out, which shows up as a strong increase of the soil surface temperature, which affects net radiation and reduces the aerodynamic resistance owing to a stability correction, which perhaps enhances the evaporation from the canopy component, which will lead to an increase of the atmospheric humidity, *etcetera*. A sensitivity study will only be able to compare various soil water transport modules if these are implemented in an identical reference framework that describes the aerodynamic resistance, net radiation, canopy fluxes *etcetera*.

In this study, we coupled a reference SVAT to a PBL-model, and four – more or less isolated – parts of this SVAT are replaced with parameterizations taken from other land surface schemes. The SVAT components that are distinguished and the reason for their selection are:

(1) the representation of an incomplete vegetation cover. A crucial issue in the complexity of land surface schemes is the importance of discerning between bare soil and vegetation, in terms of surface temperature, radiation absorption and latent and sensible heat exchange
(2) the type of soil model used. Various degrees of complexity are in use with respect to the number of soil layers and the parameterization of heat and moisture fluxes within the soil
(3) the aerodynamic exchange between the surface and the atmosphere. Apart from selection of appropriate aerodynamic surface characteristics, a range of parameterizations can be applied to account for the turbulent exchange efficiency
(4) the canopy resistance for evaporation. Not only the value of a minimum canopy resistance can be specified according to the type of present vegetation, also the complexity of crop resistance models varies widely.

Most of the parameterizations of these components are taken from models that have been published in literature. We feel that the range of existing SVAT's is large enough, and the development of new schemes should be based on an evaluation of existing material. The results of the strategy of replacing model components will partly depend on the choice of the reference model and the simulated surface. The coupling between various surface processes will be different for different ways of representing surface processes or types of surfaces.

As discussed before, the representation of sparsely vegetated areas induces stronger demands on land-surface parameterization than closed canopies. The applicability of the big-leaf model for dense vegetation covers has been demonstrated successfully, if the surface resistance for evaporation can be well defined. A larger discrepancy between various models is expected for sparse canopies, and these therefore serve as a better test environment for our purpose. Sparse canopies form a common surface type in semi-arid

areas, where the limited amount of available water constrains the biomass growth. A second reason for focusing on sparse canopy surfaces is that, at the time when this project was started, relatively little was known about the energy balance of a sparse canopy surface. Since then, considerable work on this issue has been published, and these studies have been useful here.

For the current study, a well-defined sparse canopy surface is selected to serve as test case. This surface is a sparsely vegetated vineyard in a Mediterranean climate zone in La Mancha, Spain, which was one of the investigated sites during the regional scale EFEDA experiment (Bolle *et al.*, 1993). EFEDA focussed on the surface energy balance of various types of vegetation covers in the Mediterranean summer season, during which the evaporative fraction of the surface available energy decreased considerably for many vegetation types. This change of the surface energy balance enabled the verification of measurement and modelling techniques in a large evaporation range in semi-arid conditions. Relevant for the current study are data for calibrating the surface models, providing initial and temporal forcings, as well as verification material. In the framework of this thesis these data were collected during two measurement campaigns conducted in the summer growing seasons in 1991 and 1994.

The central aims of this thesis are:

(1) to provide insight in the physical processes governing the transport of momentum and sensible and latent heat between a sparsely vegetated (Mediterranean) vineyard canopy and the overlying atmosphere

(2) to compare existing land surface parameterization schemes for this particular dataset with respect to the simulation of these fluxes

(3) to evaluate the sensitivity of the Planetary Boundary Layer to modifications of the land surface parameterization scheme.

1.4 Organization of the thesis

This thesis pays attention to various aspects of (Mediterranean) sparse canopies, land surface and PBL schemes and their intercomparisons. In chapter 2 the case study area is described. A setup of the EFEDA project is discussed, and the site layout and measurements collected in the Spanish vineyard area are presented. Special care was dedicated to existing theory concerning corrections to measured quantities, in particular eddy-correlation. An outline of the correction algorithms applied is included in one of the appendices to this thesis.

Chapter 3 contains a survey of some processes governing the exchange between a sparsely vegetated surface and the overlying atmosphere. It discusses the implementation of sophisticated Lagrangian theory in the traditional aerodynamic exchange resistances, and the shortwave reflectance (or albedo) of the case study area, illustrated by measurements. Also discussed is the crop resistance for evaporation, where attention is focussed on the application of a photosynthesis model for describing crop resistance (Jacobs, 1994).

Chapter 4 presents an overview of the land surface schemes and PBL model that are selected for this analysis. The included surface models are selected in order to cover a certain range of complexity with respect to aerodynamic transfer, soil heat and moisture

transport, and surface representation. Selected are a form of the 'big leaf' model (Monteith 1965), and the earlier mentioned models of Deardorff (1978), Choudhury and Monteith (1988), and Viterbo and Beljaars (1995). The selected range could arbitrarily have been extended, but encompasses the desired range of possible parameterizations. Both single- and dual source models are included, as are differences in treatment of soil heat flow, aerodynamic exchange and canopy resistance. Also, special attention is paid to a small modification of the model of Viterbo and Beljaars (1995), which results in a clear improvement of flux predictions under some conditions. For the range of canopy resistance models the schemes of Choudhury and Monteith (1988) and Viterbo and Beljaars (1995) were chosen. Also included here is an operational version of the photosynthesis-resistance model of Jacobs (1994). A description of the latter canopy resistance model is included in chapter 3. The boundary layer model that was selected is originally developed by Troen and Mahrt (1986), modified by a convective closure scheme proposed by Holtslag and Moeng (1991). This is the same model as was used for the work carried out by Jacobs and de Bruin (1992) and Jacobs (1994).

In chapter 5 three land surface models that describe surface fluxes by explicitly discerning between vegetation and bare soil (Deardorff, 1978; Choudhury and Monteith, 1988; Viterbo and Beljaars, 1995) are compared by means of a five day simulation of EFEDA measurements collected during the 1991 campaign. This comparison is zero-dimensional, which implies that forcings measured at screen height were used as boundary conditions. The intercomparison focusses on the aerodynamic transfer and sensible heat flux, the soil heat flux, and the canopy evaporation and soil moisture budget.

Based on this comparison the SVAT components are selected that provide an optimum description of the observations. From these different components a reference model is constructed, for use in the coupled sensitivity runs reported in chapter 6. The coupled SVAT-PBL model is run for two artificial sets of initial and temporal boundary conditions separately. Components of the reference SVAT are replaced as outlined above, and the response of the boundary layer to this exchange is discussed. The PBL-response is evaluated in terms of surface and entrainment fluxes, mixed layer height, -temperature and -specific humidity. After this set of artificial simulations, measured initial and temporal boundary conditions are applied to the coupled SVAT-PBL model, in order to evaluate its skill to reproduce the actually measured meteorological conditions. This time the PBL-response is evaluated relative to a model run using measured surface fluxes as lower boundary conditions. The conclusion section of chapter 6 discusses the results, and presents suggestions regarding the sensitivity of the PBL to the parameterization of the land surface fluxes over a sparsely vegetated Mediterranean vineyard canopy.

2

To measure is to know
(for what unknowns to correct for)

Data collection and processing

This chapter addresses the collection and processing of the data, used for this study. The data presented in this chapter were collected in the context of the so-called EFEDA-project, of which purpose and context will be explained first. Also the correspondence between the EFEDA-purpose and that of this study is discussed. Then, the contribution of the Wageningen Department of Meteorology to two EFEDA-measurement campaigns is presented, including a description of the measurement sites. The data collection strategy is discussed, where methods for determination of scalar and momentum flux densities, available radiative energy, soil heat flux density, and vegetation parameters are adressed separately. Finally, some quantities derived from the described measurements are presented: aerodynamic roughness, roughness length for heat, soil thermal properties and energy balance components.

2.1 The EFEDA-experiments

2.1.1 Context and goal

Since long mankind has influenced its environment. In Europe, land surfaces have been transformed by human agricultural activities, as well as by the development of cities, modern industries and traffic. These effects have gained special interest in the context of climate changes induced by the greenhouse effect, as predicted by GCM's. Particularly at the regional scale, model predictions of effects of change in global climate show large differences. These are partially caused by inadequate parameterizations of the interaction between the land surface and the atmosphere (Garratt, 1993).

In this context the Commission of the European Communities have developed the European project on Climatic and Hydrological Interactions between the Vegetation, the Atmosphere and the Land Surface (ECHIVAL), as an important component of the European Programme on Climate and Natural Hazards (EPOCH). The first major activity of the

programme was the ECHIVAL Field Experiment in a Desertification-threatened Area (EFEDA). The main goal of EFEDA was to "get a better understanding of the processes, including the impact of mankind, that may lead to land degradation and desertification" (Bolle *et al.*, 1993). More specifically, studies were carried out addressing the interaction between the vegetation, the soil below and the atmosphere above at regional scales, compatible with the grid scale of GCM's. Better parameterizations of these interactions are to be included in these large scale models, in order to improve their predictive power. Earlier GCM-results showed that the Mediterranean area is one of the most vulnerable European regions in case of a progressing greenhouse effect. Therefore, and for reasons of orographical simplicity, EFEDA-activities were concentrated in the relatively flat area of Castilla-La Mancha in Spain, in the dry period of the growing season. Observations of the hydrological cycle, atmospheric processes, vegetation development and soil properties were collected in a wide range of spatial (from cm to 100 km) and temporal (from 0.1 s to 3 months) scales. Furthermore, evaluation of data supports modelling activities, ranging from one-dimensional SVAT models to three-dimensional mesoscale models.

The EFEDA-programme was split into two parts. The first part (EFEDA-I) consisted of an intensive measurement campaign in the area of Castilla-La Mancha in June 1991, and a first step towards linking the surface measurements to regional scale processes using satellite images, airplane measurements and modelling activities. The project period was limited to 2½ years. EFEDA-II was funded for 2½ more years mainly to execute additional data processing and modelling. Furthermore, a few smaller experiments were carried out in order to survey particular instrumental differences and repeat some of the measurements carried out during EFEDA-I. The latter part of EFEDA-II took place in June-July 1994.

2.1.2 EFEDA-I

The spatial configuration of the ground-truth data collected during EFEDA consisted of three 'supersites', at mutual distances of about 70 km: Tomelloso, Belmonte and Barrax (Figure 2.1). Each of these supersites was considered representative for larger areas with similar landuse. Tomelloso (39°10'N, 3°1'W, 670 m) represented unirrigated vineyards, Belmonte (39°34'N, 2°27'W, 800 m) hilly natural and unirrigated agricultural vegetation, and Barrax (39°3'N, 2°6'W, 700 m) both irrigated and unirrigated farm land, respectively. At each of these supersites atmospheric, soil and vegetation data were collected at a number of sites simultaneously. Airplane measurements played a key role in linking surface measurements to the regional scale. Four airplanes were available, of which two carried flux measurement equipment, and two carried remote sensing instruments.

About 30 scientific groups contributed to EFEDA-I. In the Tomelloso area continuous measurements of the energy balance components, vegetation characteristics and soil properties were collected at 9 sites by 7 groups, at typical mutual distances of 3-5 km. The Department of Meteorology of the Wageningen Agricultural University (WAUMET) coordinated and participated the collection of atmospheric and vegetation data in the Tomelloso supersite. A further description of the collection strategy is given below.

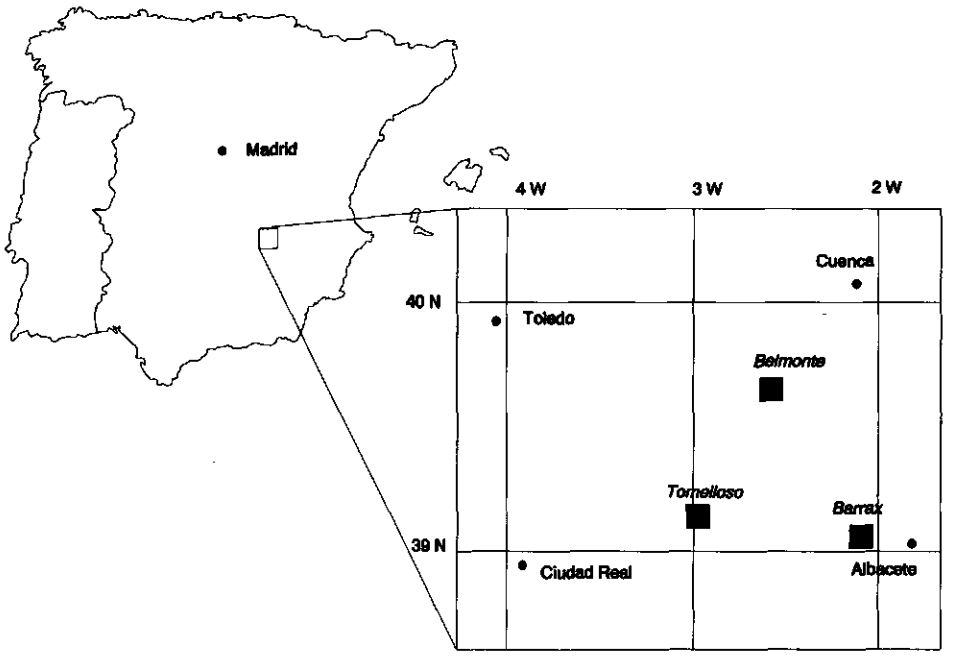

Figure 2.1: Geographic location of the EFEDA-area

2.1.3 EFEDA-II

EFEDA-II allowed some follow-up activities with respect to data processing, archiving and measuring. Important gaps in the dataset of EFEDA-I were the availability of soil moisture data in the entire rooting zone in the Tomelloso vineyard area, and a poor coverage of the airborne flux measurements, especially the three-dimensional distribution of the latent and sensible heat flux densities in the boundary layer. Apart from this, a number of groups felt it necessary to reconfirm some issues noticed during EFEDA-I by additional measurements. In this context a few participating groups decided to carry out a second observation session in the Tomelloso area. Again airplane flux measurements were carried out, together with a limited number (3) of ground stations. Also, WAUMET participated by contributing to a single ground flux station, in close collaboration with the Wageningen Winand Staring Centre (WSC) and the Copenhagen University (COP). A site close to Tomelloso, which had been under investigation during EFEDA-I as well, was selected. For EFEDA-II, data were collected during two months (June-July) in 1994.

Unfortunately, a planned measurement scheme of horizontal, vertical and temporal variations of the soil moisture content was cancelled just before the experiment was undertaken, due to problems with customs administration. Despite of this major lack of the goal of EFEDA-II, the planned experiment was continued.

Apart from the routine flux measurements, two instrumental intercomparison experiments were carried out in EFEDA-II. A net radiometer intercomparison was conducted for ten days in June 1994 at a bare soil site near Tomelloso, and 10 sets of eddy-correlation equipment were intercompared for ten days in May 1994 in Swifterbant, the Netherlands. WAUMET coordinated the latter experiment.

2.1.4 Correspondence of goals

The goal and setup of the EFEDA-project fit very well in the current thesis. Similar to the EFEDA-goals, the importance and skill of various surface-atmosphere interaction schemes for predictions at larger scales is under study here. Furthermore, EFEDA provides a framework for the collection of data necessary for evaluation of the various surface layer models. As indicated before, these models were to be evaluated under dry sparse-canopy conditions, with limited orographic influence.

A second aspect of the EFEDA-project which was very convenient, was that all participants agreed on mutual use of collected data. By this collaboration structure, data collected by other groups than WAUMET could be used for the present work. This particularly applies to the radiosoundings, collected by the Centre National de Réchèrche Météorologique (CNRM) of Toulouse, and the soil moisture data from the Dept. of Water Resources from the Wageningen University (WAUHBH). An overview of all surface flux data collected during EFEDA-I can be found in Chapter 5 of the Final EFEDA-report (Van den Hurk and De Bruin, 1993).

2.2 Measurements taken by WAUMET during EFEDA-I (1991)

2.2.1 Site description

The site where WAUMET collected data during EFEDA-I was situated in a vineyard near Tomelloso (39°08'30"N, 2°55'48"W, 693 m ASL), Castilla-La Mancha, Spain (see Figure 2.1). The prevailing wind directions were E and W. The surface type was almost homogeneous for a distance exceeding 1 km in both directions. Particularly in eastern directions the terrain slightly sloped, and height differences of about 5 m over a horizontal distance of a few 100 m were present. Approximately 15 km more southward the terrain was hilly.

The vegetation at the site consisted of grape vine plants (Vitis Vinifera, L. cv. Airen), placed in a regular grid of about 2.6 × 2.6 m. The plants had an age of about 50 years, and consisted of low stems (± 30 cm), from which early in the measurement season only a few minor branches emerged. Each branch carried 10-50 leaves, which are light green and hairy on emergence, darker, flat and with an area of ± 70-100 cm^2 in their full-grown stage, and dark green, stiff and irregularly shaped by damage when they are old (see also section 3.4). Due to night frost prior to the experimental period the vegetative development was somewhat delayed. During June 1991, the plants grew considerably, both in height and in diameter, and developed ovaries. The growing stage was not completely ended by the end of the campaign. This canopy type covered approximately 80% of the area within the direct surroundings of the measurement site. Apart from vineyards, arable crops, bare soil and a small fraction of irrigated maize was found.

The soil was classified as a sandy loam soil with a fine texture. A large fraction was covered with stones with an average diameter of ± 3 cm. Due to a high iron oxide content the soil was red. At a depth of approximately 30 cm a zone consisting of hard, compact calcarous material was present. Investigations carried out in 1994 revealed that this layer extended to several meters depth, and not only a few decimeters, as was thought originally. A deep rooting zone enabled the vine plants to obtain water from the compact layer, which

has a large porosity. The upper soil layer was virtually dry during most of the period, and hardly any low vegetation developed.

Once every 3-4 weeks the vineyard was cultivated, to remove bits of weed and to loosen the upper layer. Moreover, during the growing season shoots who did not bear ovaries were removed manually. The harvest of the vine grapes occurred mid October. This type of land use could be considered typical for an extensive area of at least 100 km^2 in the direct surroundings.

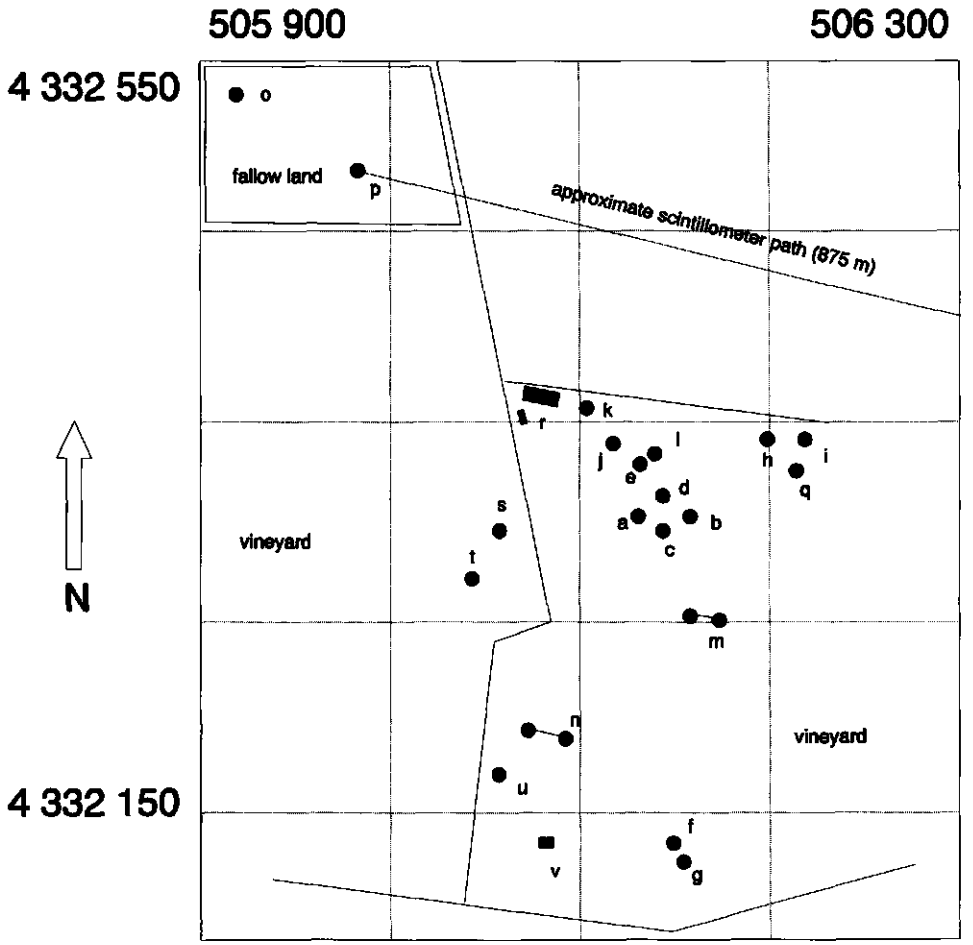

Figure 2.2: site layout and UTC-coordinates during EFEDA-I. Grid lines indicate a distance of 100 m. Labels are explained in Table 2.1

2.2.2 General set-up of WAUMET

The main task of WAUMET was to collect data of scalar and momentum flux densities between the vegetated surface and the atmosphere. In the period 2 - 29 June 1991 seven triangular masts (with diameter 0.20 m) were installed. Furthermore, soil measurements were carried out, together with the operation of a scintillation device, a SODAR device (both

operated by the Royal Netherlands Meteorological Organisation, KNMI as subcontractor) and radiometric surface thermometers moved horizontally along two cables at some height above the surface (operated by sub-contractor Free University of Amsterdam, VU). Synoptic observations were carried out hourly, whereas various relevant vegetation parameters were collected throughout the entire month. An extensive project description is given by Michels and Moene (1991). Here only a summary is given.

All automatic sensors were logged on a home-made datalogger controlled by a PDP-11 minicomputer situated in a van at the site. Raw data were stored on magnetic tape, copied to optical disk and processed afterwards. Eventually a tape had to be changed every 7-8 hours. From 7 June onwards, software adaptations allowed tapes to run for 17 hours. Power for the measurement and processing system was supplied by a 220V generator, located next to the van. The sampling frequency was 1 Hz for most sensors. The fast response sensors were sampled mostly at 10 Hz. At some days the sampling frequency for these sensors was increased to 100 Hz, since the generator was suspected to introduce a significant 50 Hz noise on these signals. Under these conditions, tapes lasted for only 2½ hrs. Changing a tape took normally about 10 minutes, during which no data could be collected.

Early in the period only daytime data were available. Thunderstorms frequently caused instrumental damage, even without any direct strike. Sensors were disconnected from the datalogger when thunderstorms were nearby. Later in the period these storms showed up less frequently, enabling more overnight measurements. Maintenance activities were another source of gaps in the data sequence.

A second goal of WAUMET was to test a stand-alone flux station, which was being developed for use in the Hydrological Atmospheric Pilot Experiment HAPEX-Sahel experiment in Niger, 1992 (Goutorbe *et al.*, 1994). Two Campbell 21X dataloggers were used rather than the PDP-device in the measuring van. The station included a one-dimensional sonic anemometer (Kaijo Denki DAT110) with a home-made thermocouple and Lyman-α fast response humidity sensor, and standard wind-profile, Bowen-ratio and radiation devices. The energy was provided by solar panels. This station was operated from 9 June 1991 onwards. Data of this station were not used for the present study, and an extensive description is not given.

Table 2.1 gives an overview of all sensors being in operation during EFEDA-I, grouped according to the mast in which they were mounted. Figure 2.2 gives a site layout. In addition, Bolle *et al.* (1993) present a photograph of the measurement site, taken in the second measurement week. The following sections describe the sensors used and the sampling strategy operated during EFEDA-I. A presentation of correction procedures applied to raw data is given in Appendix II.

All data collected during this EFEDA-I campaign by WAUMET are stored in a database (Krikke, 1994a). Surface flux measurements from all participants of EFEDA-I are collected in a database prepared by colleagues from CNRM, and were disseminated on CD-ROM (Anonymous, 1994).

Table 2.1: Instruments in operation during EFEDA-I; the indicated distance refers to the mast, the angle to the orientation with respect to the North

mast	sensor	type	height/depth (m)	distance (m)	angle (°)
a. profile mast	5 psychrometers East-side	home-made (PT100)	0.71, 1.42, 2.93, 4.93, 9.93	0.85	70
	5 psychrometers West-side	home-made (PT100)	0.69, 1.50, 2.98, 5.04, 9.98	0.90	285
	wind vane	home-made	10.20	0	-
b. σ_T mast	5 thermocouples	home-made (CuCo)	0.67, 1.47, 2.95, 4.94, 9.87	1.35	155
	5 cup anemometers	home-made	0.70, 1.48, 2.94, 4.93, 9.86	0.90	95
	wind vane	home-made	10.20	0	-
c. sonic mast	sonic anemometer	Kaijo Denki DAT310	4.35	0	0-360 [1]
	Lyman-α	home-made	4.42	0	0-360 [1]
	thermocouple	home-made (CuCo)	4.40	0	0-360 [1]
	net radiometer (above plant)	Middleton	1.07	1.10	240
d. 13 m mast	sonic anemometer	Kaijo Denki DAT310	12.50	0	0-360 [1]
	Lyman-α	home-made	12.50	0	0-360 [1]
	thermocouple	home-made (CuCo)	12.50	0	0-360 [1]
e. radiation mast	net radiometer (above soil)	Middleton	1.03	1.15	170
	incoming shortwave pyrheliometer	Kipp CM5	1.30	1.65	245
	reflected shortwave (plant)	Kipp CM5	1.07	1.65	245
	reflected shortwave (bare soil)	Kipp CM5	1.05	0.78	120
	infrared thermometer	Heimann KT14	4.20	0.30	195 [2]
f. VU mast	6 CO_2-sampling tubes		0.5, 1, 2, 4, 12, 21 [4]	[3]	[3]
	8 cup anemometers East-side	VU-made	0.5, 1, 2, 4, 8, 12, 16, 21	[3]	[3]
	7 cup anemometers West-side	VU-made	1, 2, 4, 8, 12, 16, 21	[3]	[3]
	incoming shortwave pyrheliometer	Kipp CM5	6	[3]	[3]
	reflected shortwave (high)	Kipp CM5	6	[3]	[3]
	net radiometer	Middleton	6	[3]	[3]
	wind vane	home-made	21	0	-
g. VU eddy mast	sonic anemometer	Kaijo Denki DAT310	4	0	[3]
	Lyman-α	VU-made	4	0	[3]
	thermocouple	home-made (CuCo)	4	0	[3]

mast	sensor	type	height/depth (m)	distance (m)	angle (°)
h. stand-alone mast	wind vane	home-made	6.00	0	-
	1-dim. sonic anemometer	Kaijo Denki DAT110	4.13	0.90	140-220 [1]
	Lyman-α	home-made	4.14	0.90	140-220 [1]
	thermocouple	home-made (CuCo)	4.04	0.90	140-220 [1]
	thermocouple	home-made (CuCo)	2.05	1.35	295
	4 cup anemometers	home-made	0.90, 1.50, 2.96, 4.94	0.90	350
	net radiometer	Middleton	1.30	1.03	170
	incoming shortwave pyrheliometer	Kipp CM5	1.30	0.85	205
	2 psychrometers	home-made (PT100)	0.75, 2.00	0.75	120
i. Heimann mast	infrared thermometer (plant)	Heimann KT15	0.97	0	190 [5]
	infrared thermometer (soil)	Heimann KT15	0.91	0	190 [5]
j. Diffuse mast	diffuse shortwave pyrheliometer	Kipp CM5	2.00	0	-
k. Stephenson screen	Assman psychrometer, min. and max. thermometer	Assman	2.00	-	-
	incoming longwave pyrgeometer	Eppley PIR	2.00 [6]	-	-
l. soil plot	5 soil thermometers (under plant)	home-made (PT100)	-0.03, -0.05, -0.10, -0.25, -0.50	-	-
	5 soil thermometers (under bare soil)	home-made (PT100)	-0.03, -0.05, -0.10, -0.25, -0.50	-	-
	3 soil heat flux plates (under plant)	TPD Delft	-0.05, -0.05, -0.15	-	-
	3 soil heat flux plates (under soil)	TPD Delft	-0.05, -0.05, -0.15	-	-
	4 λ_T-needles (under plant)	home-made	-0.03, -0.05, -0.10, -0.20	-	-
	4 λ_T-needles (under bare soil)	home-made	-0.03, -0.12, -0.22, -0.35	-	-
m. cable high	moving infrared thermometer	[3]	6.00	-	-
n. cable low	moving infrared thermometer	[3]	3.00	-	-
o. SODAR	SODAR		-	-	-
p. Scintillometer	Scintillometer (over distance of 875 m)	KNMI	4 [7]	-	-
q. soil plot (stand- alone)	soil thermometer (under plant)	home-made (PT100)	-0.03	-	-
	soil thermometer (under bare soil)	home-made (PT100)	-0.03	-	-

mast	sensor	type	height/depth (m)	distance (m)	angle (°)
	soil heat flux plate (under plant)	TPD Delft	-0.05	-	-
	soil heat flux plate (under soil)	TPD Delft	-0.05	-	-
r. measuring van and power generator					
s. WSC-tower					
t. WSC-albedo sensor					
u. WSC-albedo sensor					
v. TDR-plot					

1 sonics were adjusted to the wind direction regularly
2 the infrared thermometer had an inclination of -45° with the horizontal
3 complete information about exact configuration is not available
4 the upper sampling tube was used to measure the absolute concentration, the rest were measured differentially against this level
5 the infrared thermometers had an inclination of -57° with the horizontal
6 placed on top of the Stevenson screen
7 The height of the scintillometer is not exactly defined, as the underlying surface is not entirely flat

2.2.3 Determination of available radiative energy

■ Shortwave radiation

Three terms of shortwave radiation (0.3 - 3 μm) were measured during EFEDA-I: incoming total, incoming diffuse and reflected total. For all these components Kipp CM5 pyrheliometers were used, consisting of a thermopile, shielded by a double dome filtering light outside this range. Incoming total shortwave radiation ($K^{\downarrow}$) was measured at three places (see Table 2.1): in the radiation mast, in the VU mast, and in the stand-alone mast. The former two values were averaged to yield the best estimate of the incoming shortwave radiation.

The diffuse radiometer was supplied with a solar shadow ring, which had to be adjusted once every few days as the declination between the Earth's rotation axis and the orbit plane changed. Early in the period the ring was not put in its proper position. Comparison with data collected at a neighbouring site by WSC enabled selection of time slots in which erroneous measurements were taken. Values in these time slots were rejected.

The reflected shortwave radiation, $K^{\uparrow}$, was measured at three places as well: over a parcel of bare soil, over a plant, and at 6 m height in the VU mast. The exact position of a downward looking sensor is of great influence for the amount of received reflected shortwave radiation. Apart from differences in reflection coefficient between the plants and the bare soil, local differences in soil humidity, iron content and plant density dictate a large variability in the observed albedo, a (section 3.3).

■ Longwave radiation

From 18 June onwards an Eppley PIR longwave pyrgeometer was installed on top of the Stephenson screen (see Table 2.1). By an internal body temperature measurement, the instrument automatically corrects for the amount of longwave radiation being emitted by itself. Only this corrected total incoming longwave radiation, $L^{\downarrow}$, was registered.

Furthermore, the radiometric surface temperature was measured at a number of locations. A fixed Heimann KT14 was mounted at 4 m height on top of the radiation mast, looking downward at an angle of 45°. The sensor was mounted in a white PVC housing preventing it from heating errors, and supplied with a narrow view angle lens (4°). The instrument determines the radiometric surface temperature by measuring the longwave radiation in a band, where the emissivity of the emitting surface is high and the contribution of atmospheric radiation is low. Generally, surface temperature is measured in the range between 8 and 14 μm. Two newer Heimann KT15 with a 16° view angle objective were installed near the stand-alone mast: one above a parcel of bare soil, and one above an individual vine plant. The temperature measurements from these sensors were also used for the present thesis. These three sensors were calibrated in Wageningen before the experiment. Calibration was carried out by measuring the sensor signal given by a blackened cylinder (with longwave emissivity $\varepsilon = 1$) in a water bath with known temperature.

Also, at two locations a 8-14 μm radiometric surface temperature sensor was moved along a cable of ± 30 m long, at 6 m height and at 3 m height (Van de Griend *et al.*, 1989). Both transects lead over a number of vine plants, separated by stretches of bare soil. A transect was run every 10 minutes, but the sensor crossed the distance in approximately 200 s. Every 2 s a measurement was taken, which corresponds to a spatial resolution of approximately 30 cm. A Campbell 21X datalogger triggered the start of each transect and registered the measured temperatures. The strategy to obtain the average surface temperature is outlined in Appendix II.

- **Net radiation**

During EFEDA-I net radiation was measured with four Funk radiometers manufactured by Middleton (CSIRO). The heart of the sensor is a copper-constantan thermopile between two blackened rectangular plates. On either side a thin (0.05 mm) poly-ethylene hemisphere, transparent in both the longwave (3 - 3000 μm) and shortwave (0.3 - 3 μm) range must be inflated by dry nitrogen gas, to avoid wind speed dependence of the sensor. The instrument gives the total net radiation rather than separate upward and downward components. Results from two net radiometers are used in this study, one situated 1 m over a parcel of bare soil, and one at 1 m overhead the surface with a vine plant underneath. The net radiometer at 6 m height in the VU-mast was not considered to give representative readings due to mast shading, whereas the one used in the stand-alone station was regularly used for net radiometer intercomparisons (see below).

An independent assessment of the net radiation is obtained by considering the surface radiation balance, expressed as

$$Q_* = (1 - a)\,K^{\downarrow} + L^{\downarrow} - \varepsilon_s \sigma \overline{T}_{sur}^{4} \qquad (2.1)$$

in which $\overline{T}_{sur}$ is an 'effective' surface temperature, defined as a area weighted average of the plant and bare soil temperature (Blyth and Dolman, 1995). Incoming and reflected shortwave radiation was measured directly, as well as the incoming longwave radiation from 18 June onwards. The upward longwave radiation can be obtained from the

radiometric surface temperature, provided that the longwave emissivity of the emitting plant and soil surfaces is known. However, to compare a radiation balance obtained in this way with the measurement from a net radiometer introduces the difficulty in determining the contribution of the several different surface elements to the radiation budget at that particular position. Both albedo and radiometric surface temperature vary widely from space to space, and particularly differences between plants and bare soil are large. The net radiation measured at one height does agree with eq. 2.1 only when the surface emissivity and the effective surface temperature are well defined, and when the radiative flux is constant with height. The agreement is expected to be better early in the season, when the plants still have a limited size. For Q_* as obtained using eq. 2.1, $\overline{T}_{sur}$ was derived from the high cable (Appendix II), and a was taken constant, as discussed in section 3.3.

Apart from the decision of where to place the sensor, a major difficulty with net radiation measurement is the accuracy of the instrument itself. Halldin and Lindroth (1992) investigated 6 types of net radiometers, including a Funk-type. Differences of up to 10% between different types of radiometers are not exceptional. This was confirmed by a brief intercomparison experiment carried out at a bare soil site near Tomelloso, at a number of days, and with a number of device configurations (Malhi and Van den Hurk, 1992). Sensors of identical makes gave quite satisfactory correspondence, but instruments of the Funk or REBS-type gave approximately 10% lower values than devices which separately measure the upward and downward radiative flux density, as for instance the actively ventilated Schülze-Däke. Particularly calibration of the longwave response is rather difficult. Furthermore, the cosine response of the sensor is not perfect, underestimating the received radiation at large zenith angles. Excess heating of the thermopile can result in a convective heat loss, which is larger in the top dome than in the bottom dome due to the influence of convection on air stability within the domes. For these reasons the accuracy of the Funk-type instruments applied during EFEDA-I is believed to be no better than 10%, rather than the 5% calibration accuracy specified by the manufacturer.

2.2.4 Determination of scalar and momentum flux densities

One of the key issues of the EFEDA projects is the assessment of the partition of available energy over latent, sensible and soil heat, and the role vegetation plays in this partition. The flux density of momentum is an important parameter for evaluation of the aerodynamic exchange of scalars, such as CO_2, heat or water vapour. Therefore, much emphasis is put on the measurement of the momentum, sensible and latent heat flux density.

The flux densities of scalars and momentum can be obtained using several methods. All the methods employed here have the following assumption in common:

- ideally no distortion of the flow is caused by the measurement device
- the measured fluxes, being representative for the *upwind* terrain, can be related to the *locally* measured available energy. This implies that the upwind terrain must be homogeneous at a large enough fetch to ensure that the measured fluxes can be considered to originate from that type of terrain only.

During EFEDA-I four types of measurements were employed for most quantities: eddy-correlation, variance and scintillation methods, profile and Bowen-ratio methods.

■ The eddy-correlation measurements

The instantaneous vertical transport of a scalar with concentration ρ_x is given by the product of ρ_x and the vertical wind speed w. A flux density averaged over a certain time interval, F_x, is obtained by averaging $w\,\rho_x$:

$$F_x = \overline{w\rho_x} = \overline{w}\,\overline{\rho_x} + \overline{w'\rho_x'} \qquad (2.2)$$

where the right-hand side of eq. 2.2 is obtained by Reynolds averaging. In eq. 2.2 overbars denote time averages, whereas primes denote deviations. The turbulent flux density is defined as the transport perpendicular to the mean wind. In that case $\overline{w} = 0$, and F_x is given by $\overline{w'\rho_x'}$. The flux density of sensible heat H is given by $-\rho c_p \overline{w'\theta'}$, where θ is the potential temperature, ρ is the dry air density, and c_p the specific heat of dry air. A latent heat flux density λE is equal to $-\rho\lambda\overline{w'q'}$, with q the specific humidity and λ the latent heat of vaporization. The momentum flux density τ is $\rho\overline{u'w'}$ with u the horizontal wind speed, while a flux density of scalar c (for instance, a specific concentration of CO_2), F_c is $-\rho\overline{w'c'}$ (in the following both the terms 'flux' and 'flux density' will be used simultaneously to denote the transport of a constituent through a horizontal plane of unit area per unit time).

The eddy-correlation method requires measurements of w and x at a high enough rate to include all the fluctuations contributing to the turbulent flux density. This highest frequency is determined by the small-scale transition from turbulent eddy exchange to exchange determined by the molecular diffusivity of air. The low frequency end of the turbulent velocity range depends on the long term variations of the concentration and wind speed, usually forced by diurnal variation or instationarity caused by large scale weather systems. The turbulent transport takes place in the frequency range between these two limits, in the so-called inertial subrange (Tennekes and Lumley, 1972). In the surface layer this range is generally located between 10 and 0.001 Hz. Atmospheric stability and height affect this frequency range, giving relatively more important contributions from smaller time scales as height decreases or stability increases. Sensors that meet the frequency criteria of the method are needed.

For wind speed, sonic anemometry is widely used. The wind speed in any direction is measured by observing the difference of travel time of a sound pulse travelling over a fixed distance in both directions parallel to the wind. The distance must be short enough to be able to measure at a high enough frequency rate, but large enough to ensure time measurement accuracy and to avoid flow distortion. The Kaijo Denki DAT310 uses an averaging path of 20 cm, and measures the wind speed in three directions: u and v are situated in the horizontal plane, and w is the vertical component. The transducers for the vertical wind component are outside the measuring volume for the two orthogonal horizontal directions. The DAT110 measures the vertical component only.

Temperature fluctuations can be measured accurately with thin fast response thermocouples. A thermocouple uses the temperature dependence of a potential difference over a junction of two different materials, usually copper and constantan. The junction must be fine enough to ensure a high response rate and reduce radiation heating of the wires. It also needs to be strong enough to withstand most environmental features (wind, rain, dust). The thermocouples used here are described by Van Asselt *et al.* (1991).

Sonic anemometry (Schotanus *et al.*, 1983) provides an alternative for fast response temperature measurement. The sound propagation speed V_c depends on absolute air temperature T and specific humidity q according to

$$V_c^2 = 403\,T\,(1 + 0.51q) \tag{2.3}$$

The value of V_c can be measured by adding the transit times of the sound pulse travelling in both directions between the transducers at a known distance. A sonic temperature T_{son} is defined as

$$T_{son} = \frac{V_c^2}{403} \tag{2.4}$$

Due to the dependence of V_c on q, T_{son} (= $T(1 + 0.51q)$) resembles but is not exactly equal to the virtual temperature T_v, given by $T/\{1 - (1 - 0.622)e/p\} \approx T(1 + 0.61q)$, in which e and p are the vapour and air pressure, respectively.

Fast response humidity fluctuations are usually measured using an optical method. Water vapour absorbs light in certain wave frequency bands. The choice of the frequency band should avoid the possibility that light is absorbed by other gasses, specifically oxygen and ozone. The bands commonly used are Lyman-α at 121.56 nm and Krypton at 123.58 nm in the ultra-violet, and some bands in the near-infrared (Buck, 1976; Tillman, 1991). Measuring the intensity I of a monochromatic light beam passing through an open path of length d_s enables the determination of the amount of absorbing gas ρ_v in the volume, using Beer's law:

$$I = I_0 \exp\left(-d_s \rho_v k_v / \rho_{v0}\right) \tag{2.5}$$

Here, I_0 is the beam intensity when $\rho_v = 0$, k_v is the absorption coefficient at standard pressure, and ρ_{v0} the (fictitious) water vapour concentration at standard pressure (1013 mb, $T = 0$°C). A slight inconveniency is the fact that the response of I to ρ_v is logarithmic rather than linear. However, when the fluctuations I' are small relative to the average $\overline{I}$, a linearization of the response can be carried out, since then $\ln(1 + I'/\overline{I}) \approx I'/\overline{I}$, and $\rho_v' \approx -1/k_v\, d_s\, I'/\overline{I}$.

During EFEDA-I eddy-correlation measurements were carried out at 4 stations. Table 2.2 gives an overview of the configuration of each. At the stand-alone station (system 3) a one-dimensional Kaijo Denki DAT110, including a home-made thermocouple and Lyman-α device were operated. Three 3-dimensional Kaijo Denki DAT310 devices were operational, also completed with home-made thermocouples and Lyman-α humidity sensors. Figure 2.3 gives an overview of the orientation of the different configurations. The Lyman-α's in the lower masts (systems 1, 3 and 4) gave poor results throughout the entire measurement period. Results from these sensors are left unconsidered. The two devices of systems 1 and 2 were rotated towards the mean wind regularly, to reduce flow distortion to a minimum. The device of system 4 was left in a fixed orientation, but its data are not included in the current study.

Table 2.2: Configuration of the 4 eddy-correlation systems as used during EFEDA-I

Parameter	system 1	system 2	system 3	system 4
Name of mast (Table 2.1)	eddy mast	13m mast	stand-alone	VU-eddy mast
sonic dimensions	3	3	1	3
height (m)	4.35	12.50	4.10	4.00
frequency (Hz) [1]	10/100	10/100	10	10/100
low-pass filtering of w-signal from 19 June onwards	yes	yes	no	yes

[1] sampling frequency is 100 Hz at days 19, 21, 22, 23, 25 and 26. At other days it was 10 Hz

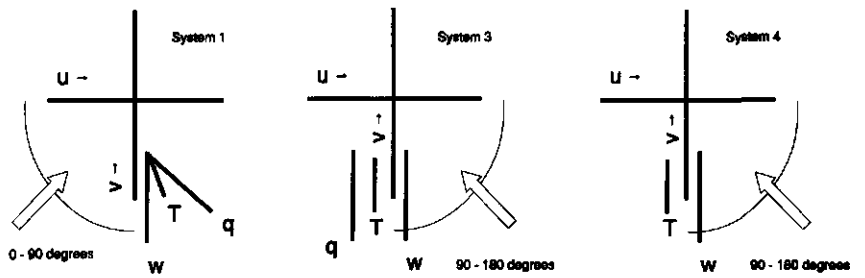

Figure 2.3: configuration of 3-dimensional sonic systems. The arrows indicate the preferred wind angle

In order to reduce the effects of the 50 Hz noise invoked by the generator, all fast response signals should be low-pass filtered at a frequency well below the noise. Due to a limited availability of filters only the signals of the vertical wind speed of systems 1, 2 and 4 were low-pass filtered at 10 Hz, using 4rd order Chebychev filters from 19 June onwards. Before this date no filtering was applied.

All Lyman-α's were calibrated in a controlled humidity chamber at KNMI prior to the experiment. The path length of the Lyman-α of system 2 was regularly changed between 1 and 2.5 cm to optimize signal resolution. The thermocouples were calibrated at WAUMET using a water bath of known temperature. The factory calibration was used for the sonic anemometers, although an offset was detected when placing them in a closed box in Wageningen after the experiment. This offset was subtracted from the measurements during postprocessing.

Corrections regarding rotation of the wind field, frequency response of the measuring system, contribution of buoyancy to vertical velocity and light absorbtion by other gases are discussed in Appendix II.

■ The variance method

In a horizontally homogeneous atmospheric surface layer, Monin-Obukhov similarity theory predicts a universal relationship between the variance of temperature,

humidity and wind speed on one hand, and a dimensionless stability parameter $(z - d)/L_v$ on the other (Panofsky and Dutton, 1984):

$$\frac{\sigma_x}{x_*} = \begin{cases} +/- c_{x1}\left(1 - c_{x2}\dfrac{(z-d)}{L_v}\right)^{+/-1/3} & L_v < 0 \\ c_{sx} & L_v > 0 \end{cases} \qquad (2.6)$$

where x represents horizontal or vertical wind speed (u and w, respectively), temperature (θ) or specific humidity (q). $x_* = u_*$ for both u and w, where u_* is the friction velocity. θ_* and q_* are given by $-\overline{w'\theta'}/u_*$ and $-\overline{w'q'}/u_*$, respectively. In eq. 2.6, c_{x1}, c_{x2} and c_{sx} are universal constants, and the plus sign refers to $x = u$ or w, and the minus sign to $x = \theta$ or q. z represents height, d the zero plane displacement, and the Monin-Obukhov length L_v is specified as

$$L_v = -\frac{\overline{T}_v}{\kappa g}\frac{u_*^3}{\overline{w'\theta'}(1 + 0.61\,\overline{w'q'})} \qquad (2.7)$$

where κ is the Karman constant (taken to be 0.4), and g the gravity acceleration.

From eq. 2.6 the sensible heat flux is given by

$$H = \rho c_p\left[\left(\frac{\sigma_\theta}{c_{T1}}\right)^3\left(\frac{\kappa g(z-d)}{T}\right)\left(\frac{1 - c_{T2}(z-d)/L_v}{-(z-d)/L_v}\right)\right]^{1/2} \qquad (2.8)$$

Assuming that the transport mechanism for heat and water vapour is similar in the surface layer, it can be shown (De Bruin *et al.*, 1993) that λE is given by

$$\lambda E = \lambda\rho\left(\frac{\sigma_q}{c_{T1}^{3/2}}\right)\left[\sigma_\theta\left(\frac{\kappa g(z-d)}{T}\right)\left(\frac{1 - c_{T2}(z-d)/L_v}{-(z-d)/L_v}\right)\right]^{1/2} \qquad (2.9)$$

Temperature-, humidity- and wind-variance measurements were collected during EFEDA-I. Temperature variance was measured with the fast response thermocouples and sonic thermometers already listed above. Moreover, identical fast response thermocouples were mounted at 5 levels between 0.75 and 10.00 m in the so-called σ_T mast (see Table 2.1 and Figure 2.2). For calculations of H and λE differences between σ_T (which were actually measured) and σ_θ were ignored. Humidity variance was measured using the Lyman-α devices described above, and the same applies to the sonic wind parameters. σ_u was also measured with 2 × 5 cup anemometers (see Table 2.1). For $x = u$ there is evidence that eq. 2.6 is not obeyed under unstable conditions due to boundary layer interaction (Panofsky *et al.*, 1977). The dependency of σ_u/u_* on both boundary layer depth z_i and z/L_v was elaborated by Van den Hurk and De Bruin (1995), using the data implied here.

As for σ_θ, Monin-Obukhov similarity theory predicts that also the temperature structure parameter C_T^2 can be defined as a unique function of $(z - d)/L_v$. C_T^2 is defined by

$$C_T^2 = \frac{\langle T(r_1)^2 - T(r_2)^2 \rangle}{r_{12}^{2/3}} \qquad (2.10)$$

where r is a space coordinate, r_{12} the distance between r_1 and r_2, and the angular brackets denote a spatial average. Details can be found in Hill *et al.* (1992). For unstable conditions this relationship reads (Wyngaard *et al.*, 1971)

$$\frac{C_T^2 (z-d)^{2/3}}{\theta_*^2} = c_{TT1}\left(1 - c_{TT2}\frac{(z-d)}{L_v}\right)^{-2/3} \qquad (2.11)$$

The sensible heat flux density H can be obtained from eq. 2.11 when the friction velocity and the universal coefficients c_{TT1} and c_{TT2} are known. De Bruin *et al.* (1993) applied eq. 2.11 using $c_{TT1} = 4.9$ and $c_{TT2} = 9$.

C_T^2 can be measured using scintillometry. Temperature fluctuations cause fluctuations of the refractive index of air. Measuring the fluctuation of the light intensity of a beam transmitted over a horizontal path with known length, this refractive index can be determined. In general, both temperature and humidity fluctuations will cause fluctuations of the refractive index. For operations in the visible or near-infra red range and at large Bowen ratios this humidity contribution can be neglected. The light intensity fluctuations are then directly proportional to C_T^2 (Kohsiek, 1982).

The setup of EFEDA-I consisted of a scintillometer provided by the Dutch KNMI as described by Monna *et al.* (1994). A Campbell 21X datalogger was used to store half hour averages of the refractometer index. The receiver was at a distance of 875 m from the light source (0.94 μm) and at approximately 3.28 m above the local surface. The terrain between the transmitter and the receiver was not exactly flat. The effective height $(z - d)$ in eq. 2.11 is the local height over the entire light path weighted by the sensitivity function of the optical configuration. This function is a bell-shaped function that tapers off to zero at both ends of the optical path. The local terrain height could only be estimated from maps and photographs. For $(z - d)$ a value of 4 ± 0.5 m was found, and this uncertainty adds an uncertainty of 12% to the calculated flux density. A comparison of values of H obtained from this device and from the eddy correlation method is given by De Bruin *et al.* (1995) (see also section 2.4.3).

- **Profile measurements**

The turbulent transport of heat, momentum, water vapour or any other scalar between the surface and the atmosphere aloft is often described using a turbulent diffusivity K, having the same meaning as a molecular diffusivity for laminar flow:

$$H = -\rho c_p K_h \frac{\partial \overline{\theta}}{\partial z} \qquad \tau = \rho K_m \frac{\partial \overline{u}}{\partial z}$$
$$\lambda E = -\lambda \rho K_e \frac{\partial \overline{q}}{\partial z} \qquad F_c = -\rho K_c \frac{\partial \overline{c}}{\partial z} \tag{2.12}$$

In eq. 2.12 c is defined as the specific CO_2-concentration, equivalent to q. In the surface layer the values of the turbulent diffusivity depend on local height, friction velocity and stability. For K, Dyer and Hicks (1970) proposed

$$K_m = \kappa u_* z \left(1 - 16 \frac{z}{L_v}\right)^{1/2}$$
$$K_h = K_e = K_c = \kappa u_* z \left(1 - 16 \frac{z}{L_v}\right)^{1/4} \tag{2.13}$$

for unstable conditions, and

$$K_m = K_h = K_e = K_c = \kappa u_* z \left(1 + 5 \frac{z}{L_v}\right)^{-1} \tag{2.14}$$

for stable conditions. Paulson (1970) derived expressions for the stability corrections in eqs. 2.13 and 2.14 in integrated form.

During EFEDA-I the turbulent flux densities of momentum, sensible and latent heat and CO_2 were determined using eq. 2.12 and measured profiles of u, θ and q and CO_2.

Five wind profiles were measured (see Table 2.1): in the stand-alone mast at four levels, in the σ_T-mast at 5, in the profile mast at 5, and in the high VU-mast at 7 and 8 levels, respectively. Measurements from the VU-mast were discarded due to poor calibration reliability of the cup anemometers. The sensors of the stand-alone mast were also left out of the present analysis. The two remaining profiles were measured using home-made cups mounted on 0.90 m long booms at approximate levels 0.75, 1.5, 3, 5 and 10 m and pointing to approximately East (σ_T-mast) and West (profile mast). A selection of either of these two profiles was made using a wind vane placed on top of the profile mast (East profile selected when the wind direction < 180°). The cup anemometers were calibrated in a wind tunnel in Wageningen before installation in Spain.

The sensors appeared to be very sensitive to electrical charge fields induced by lightning events. The long cable bridging the distance between the masts and the measuring van enabled generation of large voltage differences between the electric poles of the sensors, thereby destroying the electronic circuits. Even without any direct lightning strikes in any of the masts, most cup anemometers were frequently out of order, particularly early in the measurement period.

Three temperature and humidity profiles were measured using home-made psychrometers: one in the stand-alone mast at 2 levels, and two times in the profile mast at 5 levels (see Table 2.1). Again, the stand-alone mast data are left out of consideration. The psychrometers in the profile mast were mounted on booms of about 0.8 m length on both

East and West side of the mast at each level. The psychrometer consisted of a dry bulb and wet bulb temperature sensor (PT100) mounted in a ventilated housing with all-side radiation shielding. Also the thermometers themselves were encased by a single metal radiation shield, open at the bottom side. Air speed within the housing exceeded 6 m/s. Destilled water was pumped actively to the wicks around the wet bulb sensor, and water surplus dripped off. Dry bulb temperatures T were corrected for dry-adiabatic rise by adding 0.01 °C per m above surface. This is a simplified correction obtained from the definition of potential temperature θ, given by $T\,(p_0/p)^{R/c_p}$, with p_0 = 100000 Pa and R the molar gas constant. The temperature profile was obtained by averaging the two dry-bulb temperatures at each level. Vapour pressure e was obtained from the dry bulb T and wet bulb T_w from each psychrometer using

$$e = e_s(T_w) - \frac{c_p p}{\varepsilon \lambda}(T - T_w) \qquad \textbf{(2.15)}$$

$e_s(T)$ is the saturated water vapour pressure at temperature T (computed using $610.7 \times 10^{7.5T/(237.3+T)}$, T in °C), $\varepsilon = m_v/m_a = 0.622$ with m_v and m_a the molar weights of water and dry air, respectively, and air pressure $p \approx 94000$ Pa was derived from the synoptic observations (see below).

The psychrometers suffered from quick pollution of the wet wicks, in spite of changing the wicks about twice a week. Moreover, the water supply was often insufficient to guarantee the wicks to remain constantly wet. A third source of severe error was heating of the instrument bottom caused by upward longwave and shortwave radiation. Since all these errors would obviously lead to an overestimation of T_w, the humidity profile was obtained by selecting the humidity measured with the psychrometer giving the lowest value of T_w at each level. However, this procedure could not ensure that the measured profiles were reliable. Later designs of the psychrometer (as applied during e.g. EFEDA-II) have eliminated most errors.

u_*, H and E were calculated simultaneously using the least squares technique of Robinson (1962) and Covey (1963). This procedure minimizes the difference between the real profiles of u_* and T and a hypothetical one according to eq. 2.12, assuming a constant flux throughout the entire profile. An iteration is necessary in order to include stability effects on these profiles. The contribution of the water vapour flux to L_v was ignored here. Once u_* and H are found, E can be computed from the resulting value of u_* and L_v, again minimizing the difference between the real and a hypothetical profile of q. For computations of u_*, H and E the lowest level (0.75 m) was excluded in every case, since this level was too close to the individual plants to expect the flux density to be constant.

The CO_2 profile measurements were carried out by the members of the Free University of Amsterdam (VU). Unfortunately, severe calibration difficulties of the CO_2 gas analyzers were caused by the high air temperatures, and the profile data could not be used to calculate CO_2-fluxes. It was also decided to refrain from a detailed description of these measurements.

- **Bowen-ratio method**

The Bowen-ratio method is a profile method which uses the assumption that the

transport mechanism for heat is equal to the transport mechanism for humidity, thus $K_h = K_e$. Using this assumption the Bowen-ratio $H/\lambda E$ can be measured according to

$$\beta \equiv \frac{H}{\lambda E} = \frac{c_p}{\lambda} \frac{\Delta\overline{\theta}}{\Delta\overline{q}} \tag{2.16}$$

Together with eq. 1.1 the individual terms H and λE can be computed when the total available energy $Q_* - G$ is known.

During EFEDA-I the psychrometer measurements were also used to obtain values of H and λE using this technique. A regression of a scatter plot of T vs. q yielded the best estimate for $\Delta T/\Delta q$ (Sinclair *et al.*, 1975), and again measurements at the lowest level were not included.

2.2.5 Determination of soil heat flux density

The soil heat flux density G is an important component of the energy balance for a sparse canopy site. Simultaneously, the horizontal distribution of soil heat flux may show considerable differences, caused by surface temperature differences, shading by plants, presence of stones, or variability of soil texture and moisture content. G depends on various soil physical properties and the temperature forcing at the surface. Verhoef *et al.* (1995) discuss various methods to measure soil conductivity, soil heat capacity and soil heat flux density, as applied during EFEDA-I. Here two methods used to measure the soil heat flux density are briefly reported: the flux plate method and the heat capacity method.

The flux plate method uses flux plates consisting of a thermopile embedded in a heat conducting material with a similar thermal conductivity as the ambient medium. The thermopile results in a potential difference if the temperature at either side is different and a heat flow is present. A calibration procedure transfers the voltage difference to an actual heat transport. Major corrections to the heat fluxes determined using this method are presented in Appendix II.

The heat capacity or caloric method measures the change of the heat content of a soil profile between two subsequent time slots. The heat content $\mathbb{C}$ at time t of a soil profile is given by

$$\mathbb{C}(t) = \int_{-\infty}^{0} \rho' C_h(z)\, T_s(z, t)\, dz \tag{2.17}$$

where $\rho' C_h(z)$ is the volumetric heat capacity of the soil at depth z, and $T_s(z, t)$ the soil temperature at time t at the same level. The soil heat flux density at the surface is then given by

$$G(0, t) = \frac{\mathbb{C}(t + \Delta t) - \mathbb{C}(t - \Delta t)}{2\,\Delta t} \tag{2.18}$$

A continuous record of temperature data at a sufficient number of levels between the surface and a depth where the soil heat flux density can be assumed negligible are necessary. The temperature at the surface is important, since the major temperature changes

occur near the heat source. During EFEDA-I the soil heat flux density under a parcel of bare soil was computed using the (corrected) radiometric surface temperature measurements (Appendix II). For the heat flux density under a plant the surface temperature was approximated using a harmonic analysis of the soil temperature at 3 cm depth (van Wijk, 1963). The thermal diffusivity necessary for this method was obtained from measurements of the soil temperature at various depths using the amplitude method (Horton *et al.*, 1983; see Verhoef *et al.*, 1995). For this method the amplitude A_T of the diurnal temperature cycle with radial frequency φ_T must be detected at two levels. The thermal diffusivity k of the soil layer between these two levels is then estimated as

$$k_{z_1-z_2} = \frac{\varphi_T}{2}\left[\frac{z_2 - z_1}{\ln(A_{T,1}/A_{T,2})}\right]^2 \qquad (2.19)$$

k was computed daily for the layers 0-3 cm, 3-5 cm, 5-10 cm, 10-25 cm and 25-50 cm, using the temperature profile of the bare soil parcel completed with the radiometric surface temperature, provided that the fundamental temperature cycle was measured completely. k was assumed not to vary horizontally, thus at any depth being equal for the bare soil and the soil under a plant. The temperature profiles were smoothed using a higher order spline function evaluated at 40 equidistant levels between $z = 0$ and $z = 50$ cm depth (Press *et al.*, 1986).

The volumetric soil heat capacity $\rho' C_h$ appearing in eq. 2.17 is a function of the bulk density of the soil, ρ', and the specific heat C of the various constituents in the soil. ρ' is given by

$$\rho' = \rho_s x_s + \rho_w x_w + \rho_a x_a + \rho_o x_o \qquad (2.20)$$

where x_i is the relative fraction of constituent i, and the subscript w refers to water, s to soil mineral, a to air and o to organic matter. $x_s + x_w + x_a + x_o = 1$, per definition. $\rho' C_h$ is equal to

$$\rho' C_h = \sum x_i \rho_i C_i \qquad (2.21)$$

For practical use $\rho_a C_a \approx 0$, and organic compounds are neglected. $\rho_s C_s \approx 2$ MJ/m^{3}K, and $\rho_w C_w \approx 4.2$ MJ/m^{3}K.

During EFEDA-I six soil heat flux plates (TPD Delft) were in use: two at -5 cm under bare soil, two at -5 cm under a plant, one at -15 cm under bare soil and one at -15 cm under a plant. Furthermore, two temperature profiles of 5 PT100 sensors between -3 and -50 cm were installed, one of them under a parcel of bare soil and one underneath a plant (see Table 2.1). Soil porosity ($1 - x_s$) and soil moisture content (x_w) were measured by members of the Dept. of Water Resources of the Wageningen University (Droogers *et al.*, 1993). Soil porosity was measured once during the campaign, and water content about once every 5 days, both averaged over five 10 cm intervals between 0 and -50 cm. For this, Time Domain Reflectometry (TDR) was used. The contribution of organic material was neglected. Detailed soil moisture measurements were also carried out by colleagues of the Winand Staring

Centre, but these data are not used for the present thesis.

An important soil physical property is the thermal conductivity $\lambda_T = k\,\rho' C_h$. During EFEDA-I it was determined directly, using home-made socalled λ_T-needles (Shiozawa and Campbell, 1990). This instrument measures the rate of change of soil temperature nearby a heating probe. The rate of temperature change and the distance between the heating element and the temperature sensor depend on the heat conductivity of the soil surrounding the probe. Eight needles were installed at various depths in the soil, again under plants and under soil (see Table 2.1). The measurements were carried out manually using a Campbell 21X datalogger, who also regulated the heat supply to the probe. The measurements were carried out approximately twice every campaign day.

The average soil heat flux density was obtained as a weighted average of the heat flux density under bare soil and under a plant for each of the two methods. The fraction of vegetated surface (σ_f, section 2.2.6) was used as the weighting factor. Numerical simulations showed that the influence of horizontal heat flow (induced by horizontal variations of the surface temperature) on the heat flux measurements is limited.

2.2.6 Determination of vegetation parameters

The present vegetation is characterized by its physical dimensions (height, width of canopy elements, leaf density), its relative evaporating surface (Leaf Area Index *LAI*) or areal occupation (fraction of plant cover, σ_f), a canopy resistance for evaporation (r_s^c), and some other features. Since the vegetation showed a significant growth during the measuring period, most measurements have been carried out more than once. Table 2.3 lists the dates at which the several determinations were carried out. All vegetation data presented here were sampled on the right hand side of the terrain depicted in Figure 2.2. Vegetation surrounding masts *s* and *t* in this figure was slightly less developed than in the surroundings of the other masts due to a more severe frost damage which had occurred late in April 1991. A detailed description of the determination of the vegetation parameters during EFEDA-I is given by Michels and Moene (1991).

Table 2.3: Dates at which plant parameters were determined, and total number of sampled plants during EFEDA-I. Date numbers are days in June 1991

parameter	dates	number of plants
crop height ('traditional')	16, 20, 25	-
crop height (individual plants)	5, 9, 11, 14, 17, 20, 23, 28	10
drip area	16, 20, 25	5 (16, 20), 10 (25)
Leaf Area Index	5, 9, 11, 14, 17, 20, 23, 28	10
stem height	16 - 20	10
stomatal resistance	15, 17, 19, 21, 22, 23, 25, 27, 28	2 per sample

- **Canopy height and plant dimensions**

The vine plants were sitated in a regular grid, ± 2.60 m apart. The resulting plant density D_p was 0.15 plants/m^2, valid for the entire field. The crop height h was measured in two ways. By the first 'traditional' method h is assessed by looking over the canopy, and

determine the average height. For a canopy consisting of widely separated plants the method is rather subjective. Alternatively, the height of each plant from a sample of 10 was measured. The crop height was defined as the 70% percentile value of this sample. A cumulative frequency distribution showed a rather sharp increase of the cumulative frequency at this percentile value (Michels and Moene, 1991). Figure 2.4 shows the resulting values of h. Also shown is the estimated crop height before the measurement campaign. The value at 5 June is suspiciously high. At this date, the sampling strategy was probably not yet well-established, and changed afterwards.

Of these ten plants, also the stem height and stem diameter were measured once (divided over two days).

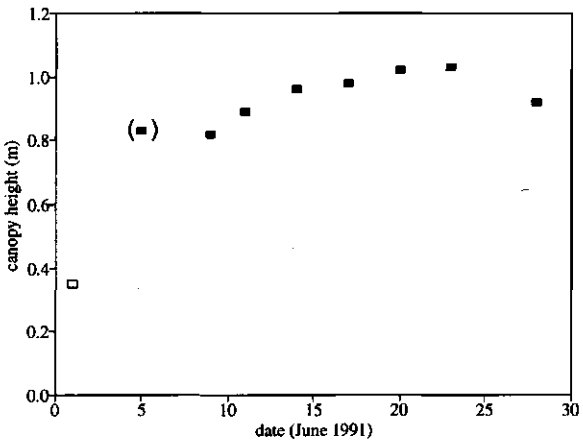

Figure 2.4: ■: Canopy height h measured during EFEDA-I, where h is defined as a 70% percentile value of individual plant height measurements. The measurement taken at 5 June is suspiciously high and marked between brackets; □: the estimated canopy height before June 1991

The drip area A_d is the average surface area occupied by a single plant. It was measured three times by assessing the horizontal diameter of 5 (first and second time) and 10 (third time) plants.

■ **Leaf Area Index and Leaf Area Distribution**

The onesided Leaf Area Index (*LAI*) was obtained by estimating the total leaf area, *LA*, of 10 plants. *LAI*, defined as the average leaf area per unit ground area, is then simply given by

$$LAI = \overline{LA}\, D_p \tag{2.22}$$

An alternative expression for the amount of (onesided) leaf area is the average leaf area per unit plant surface, LAI_*, equal to LAI/σ_f, where σ_f is the fraction of surface covered with vegetation (see below). This parameter is relevant to the description of radiative extinction within the individual plant elements.

The detection of *LAI* was carried out 8 times (see Table 2.3). *LA* is computed as the product of the number of leaves, N, and the average area A_l of a selection of leaves from each plant. N was counted manually, and a separate record was kept for each layer of 20 cm

height. No distinction was made between leaves in separate age classes or light regimes. The average leaf area was also registered per layer, using the so-called vein method (Daughtry, 1990). For this method the length of both the primary and secondary vein of a random sample of leaves is measured, and related to the true area of the leaves using a calibration curve. The calibration is carried out by relating the product of the two vein lengths of a leaf to its area, determined by counting the dots on a graph paper occupied by the leaf. This 'leaf tracing method' was applied to a random selection of 99 leaves once early in the measurement period. The measurement of *LAI* using this strategy took 2 to 4 days per run. The day numbers listed in Table 2.3 refer to the centre of each run. Figure 2.5 shows the resulting values of *LAI*.

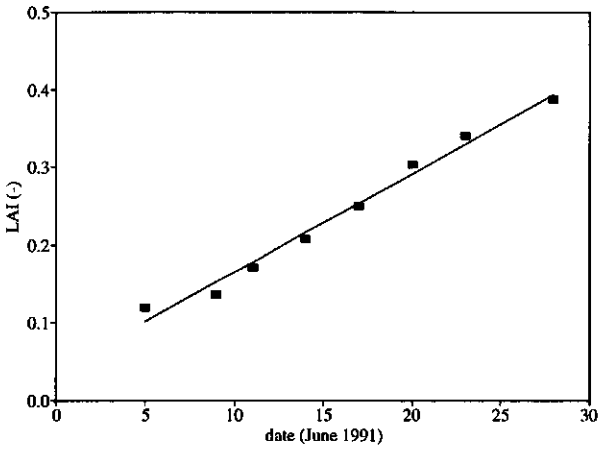

Figure 2.5: ■: Leaf Area Index (per unit ground surface) measured during EFEDA-I. Also shown is the linear regression, given by 0.0382 + 0.0127 *day*, where *day* is the day in June 1991

■ **Fraction of vegetation cover**

The fraction of vegetation cover σ_f is the relative horizontal area occupied by vegetation. When the average drip area A_d is known, it is easily obtained as $A_d D_p$. The parameter plays an important role in the determination of the amount of radiation reaching the surface, the surface albedo and other processes. During EFEDA-I A_d was measured only three times, in a short time range (see Table 2.3). Due to the rapid growth of the vegetation σ_f is expected to vary strongly and alternative ways to assess it are desired. Here σ_f was obtained by a combination of measurements of *LA*, *h* and A_d, and adoption of two assumptions:

- The leaf area density obtained from measurements of A_d is constant throughout the period, since plants are expected to increase volume instead of density as leaf area increases
- The plants can be described using a perfect ellipsoid based on the ground and with equal radius $r_x = \sqrt{A_d / \pi}$ in the two horizontal directions. This assumption is a little different from Hicks (1973), who states that vine plants can accurately be described by cylinders.

From r_x and *h* the average volume *V* of a single plant can be computed using the

description of an ellipsoid:

$$V = \frac{4}{3}\pi\, 0.5\, h\, r_x^2 \tag{2.23}$$

The average leaf area density LAD, defined by LA/V, was found to be 6.3 m^2/m^3. From this σ_f is found from

$$\sigma_f = A_d D_p = \pi\, r_x^2 D_p = \frac{3}{2}\frac{LAI}{h\, LAD} \tag{2.24}$$

Figure 2.6 shows the resulting values of σ_f.

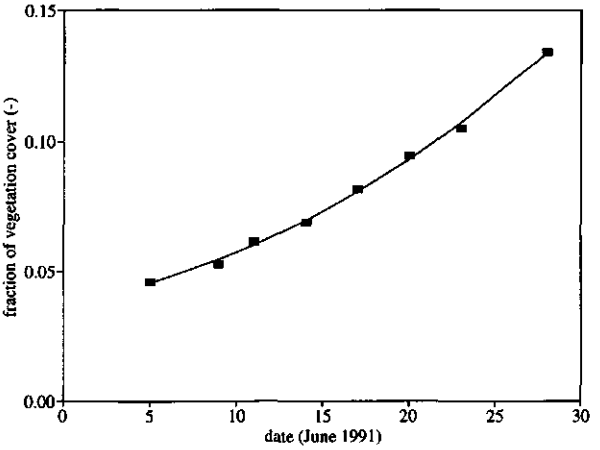

Figure 2.6: ■ Fraction of surface covered with vegetation, σ_f, obtained using eq. 2.24; —— regression of σ_f given by 0.0379 + 0.0011 *day* + 8.26 10^{-5} day^2

■ **Fraction of sunlit leaves**

During EFEDA-I the relative fractions of sunlit or shaded leaves and of the leaves of the several age classes was not measured explicitly. The fraction of sunlit leaves, f_s, was eventually estimated using a numerical model adapted from Norman and Welles (1983). They developed a scheme computing the path length of a beam from a specific direction through an ellipsoidal canopy element with specific dimensions. This scheme was used to compute the average sunlit area of a plant canopy as function of the spatial distribution of plants, their geometrical dimensions, and the direction of the solar beam. The latter parameter is a known function of season and time. f_s is then obtained by

$$f_s = \exp(-k_{bl}\, d_s\, LAD) \tag{2.25}$$

where k_{bl} is the extinction coefficient for black leaves, and d_s the path length of a beam between the leaf and the edge of the canopy element. Leaf area density LAD is assumed constant over the canopy element volume. k_{bl} was parameterized as $0.5/\sin\beta$ (where β is the solar elevation), which applies to a canopy with spherically distributed leaves (Goudriaan, 1977). The average fraction of sunlit leaves is obtained from averaging the values of f_s in a grid box enclosing a single plant element. Taking LAD equal to 5 m^2/m^3, the resulting value

of f_s was very well approached by a fixed value of 0.5 ± 0.1 for all times and days (figure not shown).

- **Stomatal resistance**

Measuring stomatal resistance

The stomatal resistance r_{st} relates the transport rate of gases between a stoma and the air directly surrounding the leaf to the concentration difference of the gas:

$$r_{st} = \rho \frac{c_i - c_s}{F} \tag{2.26}$$

Here, F is the flux density of the gas and c the gas concentration. The subscripts refer to inside the stoma (i) and directly outside (s), respectively (Monteith, 1973). The stomatal resistance is a measure for the pore width of the stomata in an individual plant leaf.

Table 2.4: Sampling details of porometry and photosynthesis measurements during EFEDA-I

parameter	stomatal resistance	photosynthesis
total number of days	9	9
time range per day	sunrise - sunset	sunrise - sunset
measurement frequency	once every two hours	once every two hours
number of plants per measurement	2	1
number of leaves per layer	3 - 6	5 - 10
leaf categories discerned:		
• leaf layer (20 cm each)	6	6
• age	3 (young, normal, old)	3 (young, normal, old)
• light condition	3 (sunlit, intermediate, shaded)	3 (sunlit, intermediate, shaded)
• total	54	54
number of cycles per leaf	3	1
total number of samples	2317	1469

A detailed description of the stomatal resistance measurements during EFEDA-I is given by Jacobs (1994) and can be found in the final EFEDA-I report (Bolle and Streckenbach, 1993). Here only the basic elements are given.

On nine days the stomatal resistance was measured on a random set of plants. A distinction was made between leaves in different layers (20 cm height each), light regime (sunlit and shaded) and age categories (young, normal and old). Leaf age determination was based on the size, thickness, colour, hairiness and regularity of the shape of the leaves. Table 2.4 lists the sampling details.

The stomatal resistance for water vapour transfer was measured using a dynamic diffusion porometer (Delta-T Mk3), which measures the rate of increase of the relative humidity in a cup of approximately 0.3 cm^3 attached to a leaf. The relative humidity rh in the cup will rise due to transpiration through the stomata and the cuticula. The instrument

pumps dry air into the cup until a relative humidity rh_s is reached, where rh_s is a start value approximately equal to the ambient relative humidity. Then, the transit time Δt necessary to increase rh_s by a specified humidity change Δrh is recorded. As soon as $rh > rh_s + \Delta rh$, the drying cycle restarts automatically. Usually Δrh is set to 5%. At each leaf position Δt was recorded three times, after two or three drying cycles in order to achieve a stable value of Δt. A single measurement took 15 - 45 s (depending on g_s), which is considered short enough to avoid adaptation of the leaf to the cup microclimate.

Ideally, $\Delta t/\Delta rh$ depends on $r_{st} = 1/(g_s + g_{cut})$ in a linear way, where g_s is the stomatal conductance and g_{cut} the cuticular conductance of a leaf. The slope and offset of this regression are determined by the cup dimensions and the diffusion coefficient for water vapour. However, temperature differences between the cup and the leaf will affect the water vapour transport speed. Monteith *et al.* (1988) derived expressions to correct for these temperature differences, and these were applied (see also Jacobs, 1994). Furthermore, the limited time response of the humidity sensor and temperature-dependent adsorption of water vapour at the cup walls cause a deviation from the linear relationship between Δt and $1/(g_s + g_{cut})$. These features make a calibration in the field necessary. Calibration was carried out using a plate perforated with six sets of holes of known geometry, whose conductance could be determined from theory. A new calibration was carried out for each measurement, and a linear regression between Δt and $1/(g_s + g_{cut})$, corrected for temperature difference, was used.

Measurements of water vapour conductance on the abaxial side of the leaf (where no stomata are present and thus $g_s = 0$) gave no significant increase of the cup humidity. This leads to the conclusion that the cuticular conductance $g_{cut} \approx 0$, and it can be neglected during further analysis.

Scaling up from leaf to crop

For the surface layer models forming the subject of this research, a crop resistance against evaporation is required, rather than a stomatal resistance on a large number of leaf surfaces. A weighted averaging is applied to obtain the crop resistance from the individual leaf stomatal resistance data. The mean crop resistance r_s^c per unit ground area was obtained following a *LAI*-weighted averaging (Wallace *et al.*, 1990)

$$r_s^c = \left[\int_0^{LAI} \frac{dL'}{r_{st}(L')} \right]^{-1} \tag{2.27}$$

Since r_{st} significantly differed for different age classes and light conditions, the weighting should reflect this as well. From the discrete number of leaf classes r_s^c is given by

$$r_s^c = \frac{1}{LAI} \left[\frac{\sum \frac{f_i}{\overline{r_{st_i}}}}{\sum f_i} \right]^{-1} \tag{2.28}$$

where f_i represents the relative fraction of class i, and $\overline{r_{st_i}}$ is the average value of r_{st} of leaves

in class i. The averaging interval was one hour for all occasions. The discerned classes are the sunlit and shaded leaves (specified by f_s), the leaf age and the vertical position.

During EFEDA-I the value of f_s was assumed equal to a fixed value of ± 0.5 for all times and days. However, the measurements taken during EFEDA-II (see below) showed a significant variation of f_s as function of local time. Therefore the quadratic function shown in Figure 2.9 was taken instead for EFEDA-I data.

The fractions of the various age classes were estimated to be distributed as 20% young leaves, 40% normal and 40% old. Since the average resistance of young leaves is generally much higher than the resistance of the normal and old leaves, a variation of 10% of this figure results in a variation of only 4% of the crop resistance. The small difference between the stomatal resistances of old leaves and normal leaves makes the exact estimation of these fractions of minor importance.

The vertical leaf area distribution was measured directly during EFEDA-I.

■ **Photosynthetic rate**

In the context of EFEDA-I the photosynthetic activity of the plants was also measured. Results from these measurements were used to calibrate a model for g_s based on the computation of the net photosynthetic rate, A_n (Jacobs, 1994; Jacobs *et al.*, 1995; see also section 3.4). A detailed description of these measurements can be found in Jacobs (1994), while here only a basic description is given.

The photosynthetic activity of a leaf can be expressed in terms of the amount of CO_2 being transported to the leaf. The CO_2-concentration c_R of the air at a reference height above the canopy (4 m) was measured using an Infra-Red Gas Analyzer (IRGA). The air was also transported to a transparent cuvette clamped onto a leaf, and the CO_2-concentration c_o of the air returned from the leaf cuvette was also measured. Then the photosynthetic rate A_n can be calculated from the concentration difference (c_R - c_o), the air flow through the chamber and the leaf area in the cuvette (Ball, 1987). A correction for the dilution of CO_2 by the addition of H_2O must be applied.

The sampling strategy resembled the strategy employed during the stomatal resistance measurements (see Table 2.4). Only one instead of two plants was sampled each measurement, but more leaves per sample layer were monitored.

2.2.7 Various determinations

■ **SODAR**

Between 1 June, 13.40 GMT and 29 June, 14.00 GMT a 3-dimensional doppler sodar device was in operation at about 500 m from the WAUMET site (see Figure 2.2). The sodar device was provided by the KNMI (Monna *et al.*, 1994). Profiles of horizontal and vertical wind speed and their standard deviations were detected at a resolution of 25 m between 50 and 500 m height, where the upper level depends on atmospheric conditions. The instrument and datalogger were powered by a 220V generator at sufficient distance to avoid distortion of the measurements caused by the sound of the generator. Data were stored as 20 minute averages. The system clock, however, depended on the generator frequency, and showed a time accuracy of less than 5 min. The SODAR data were not analysed in the context of this study.

■ **Synoptic observations**

During periods that the measuring van was in operation, synoptic observations were carried out approximately every hour, according to the SYNOP-guide of the Dutch weather service (KNMI, 1981) as close as possible. The parameters that were observed were:

- air pressure, measured with a hand held altometer, converted to pressure at sea level using the hydrostatic pressure equation $p(z) = p(0) \exp(-g\, z/R\, \overline{T}_v)$, where $\overline{T}_v$ is the average of the virtual temperature at z = 670 m and a virtual temperature at sea level, equal to T_v - 0.01 z
- air temperature and air humidity with a ventilated Assman psychrometer in the Stephenson screen (see Table 2.1)
- relative humidity with a hygrograph in the Stephenson screen
- maximum and minimum temperature in the Stephenson screen
- total cloud cover, fraction of low, middle and high clouds, and estimated height of lowest cloud base
- codified state of weather.

Observations were noted in the WMO synoptic coding algorithm. Specifically, the observations of air pressure were actually used for several corrections related to thermodynamic properties of the air.

■ **Radiosoundings**

During EFEDA-I the French CNRM carried out a total number of 93 radiosoundings about 1500 m from the measuring site of WAUMET. These soundings were launched on each day between 1 and 30 June 1991 at 11 GMT, and on some days every 2 hours. The balloons were equipped with sensors reading air temperature, air humidity and air pressure. CNRM made these data available to WAUMET.

For each sounding the boundary layer height z_i was estimated as the level of the lowest inversion of potential temperature and specific humidity. Driedonks (1982a) assumes that the error of estimating z_i from a single sounding is approximately 100 m, owing to a considerable horizontal variation of the boundary layer height. Often obvious inversions were observed at several levels below 5 km, as a result of the remaining residual boundary layer from the period before. The estimated PBL-depth varied from 100 m to almost 4000 m. Table 2.5 lists values of z_i observed at times where clear inversions were present. These values were used in the analysis of σ_u-data by Van den Hurk and De Bruin (1995).

2.3 Measurements taken by WAUMET during EFEDA-II (1994)

The second EFEDA-measurement campaign, taking place in June and July 1994, was a joint experiment of the Wageningen Staring Centre (WSC), the Copenhagen University (COP) and WAUMET. All three groups had participated to the EFEDA-I experiment, performing flux measurements in the Tomelloso supersite.

2.3.1 General setup

A single set of equipment was composed from contributions of each group. Roughly

Table 2.5: Times of observations of lowest inversion heights and number of ground observation time slots

Day (June 1991)	time (GMT)	level of lowest inversion (m)	number of ground observations (30 min average)
7	11:30 - 12:30	890	2
9	13:30 - 14:00	2100	1
9	16:00 - 17:00	2520	2
11	11:30 - 12:30	1730	2
11	13:30 - 15:30	2200 - 2230	3
12	9:30 - 10:00	660	1
21	13:00 - 15:00	3100 - 3700	2
22	14:00 - 15:00	3450	2
23	16:00 - 16:30	3200	1
25	9:00 - 10:00	910	2
25	13:30 - 14:30	3850	2
26	8:00 - 8:30	500	1
26	12:00 - 15:00	3400 - 3450	3
27	12:00 - 15:00	2200 - 2450	3
28	8:00 - 10:30	500 - 750	5
28	12:00 - 12:30	1000	1
28	14:00 - 14:30	1500	1
29	9:00 - 9:30	700	1
29	15:00 - 17:00	2200 - 2300	2
total			37

spoken, WSC provided a complete eddy-correlation device, WAUMET the wind-, radiation-, temperature and soil data, and COP a soil respiration-, sapflow- and porometry device. Table 2.6 lists the complete set of equipment. The stations of WAUMET and WSC were assembled and tested during the eddy-correlation intercomparison experiment carried out in Wageningen in May 1994.

Again, a vine site near Tomelloso was selected to install the equipment. Each of the contributing groups operated the station for 3 weeks, and during a few days the take-over by the different teams was organized.

Measurements were taken in the growing season of the vineplants, between 1 June and 30 July 1994. No rainfall occurred during the measurement period. Information from local landowners revealed that there had not been any rain fall for a month preceding the measurement period. Since October 1993, only 50 mm precipitation had fallen in the area.

The eddy-correlation data were measured at a frequency of 10 Hz, and stored on a hard disk of a portable PC in the field. The 'background'-data collected by the equipment of WAUMET were logged on a Campbell 21X datalogger, and only half hour averages were stored. Also sapflow data were collected once every half hour, on a Campbell CR10 datalogger. All devices were powered with solar panels and batteries in the field. During the experiment, almost instantaneous data control was allowed by daily computing mean values and covariances of the eddy-correlation station and major corrections to all data

Table 2.6: Equipment in use during EFEDA-II; the indicated distance refers to the mast, the angle to the orientation with respect to the North

mast	instrument	type	height/depth (m)	distance (m)	angle (°)
eddy-correlation	3-dim. sonic anemometer	Gill/Solent	6.00	-	-
	Krypton hygrometer	Campbell KH20	6.00	0.10	360
	H_2O- and CO_2-gas analyzer	LICOR6262	6.00 [1]	-	-
background station	wind vane	home-made	10.57	-	-
	4 cup anemometers	home-made	2.96, 5.46, 7.48, 10.23	0.90	360
	1 psychrometer	home-made	6.09	0.50	360
	net radiometer	Schülze-Däke	7.91	1.06	180
	incoming shortwave pyrheliometer	Kipp CM5	7.80	0.60	250
	reflected shortwave pyrheliometer	Kipp CM5	7.80	0.60	250
	diffuse shortwave pyrheliometer	Kipp CM5	2.00	-	-
	radiometric surface thermometer	Heimann KT15	7.80	0.50	250 [2]
soil measurement plot	8 soil heat flux plates	CSIRO	4 × 0.01, 4 × 0.05	-	-
	4 soil temperatures	home-made PT100	2 × 0.01, 2 × 0.05	-	-
rain meter	rain gauge		0.30	-	-
sap flow	3 sap flow gauges	Dynagauge	1 whole stem 2 single branches	-	-

[1] The height refers to the sample tube inlet
[2] the Heimann was tilted at an angle of approximately 7°

using a software package developed in collaboration between WSC and WAUMET.

Just like during EFEDA-I, a CO_2 flux density was measured, but this time an eddy correlation method was used rather than the profile method. Also sapflow- and soil respiration measurements were carried out. Results from these are not used for this study, and are described by Friborg (1995).

Unlike EFEDA-I hardly any data collection interruptions occured. The systems proved to be very reliable, and only little maintenance was necessary. Moreover, no threat of thunderstorms was present this time.

2.3.2 Site description

The vinesite of EFEDA-II (39°7'19.94'' N, 2°55'18.55'' W) resembled the EFEDA-I site in most features. Again, a regular grid of plants was situated on a sandy loam soil covered

with stones. The plants were slightly wider separated (2.70 m), and were younger than the plants found at the EFEDA-I site, about 20 years. Compared to that site the terrain was somewhat more unevenly sloped, and the fetch was about 500 m in both East and West conditions. (Inspection of the EFEDA-I site in 1994 revealed that much of the vineyards had disappeared since 1991.) Figure 2.7 gives an overview of the terrain layout.

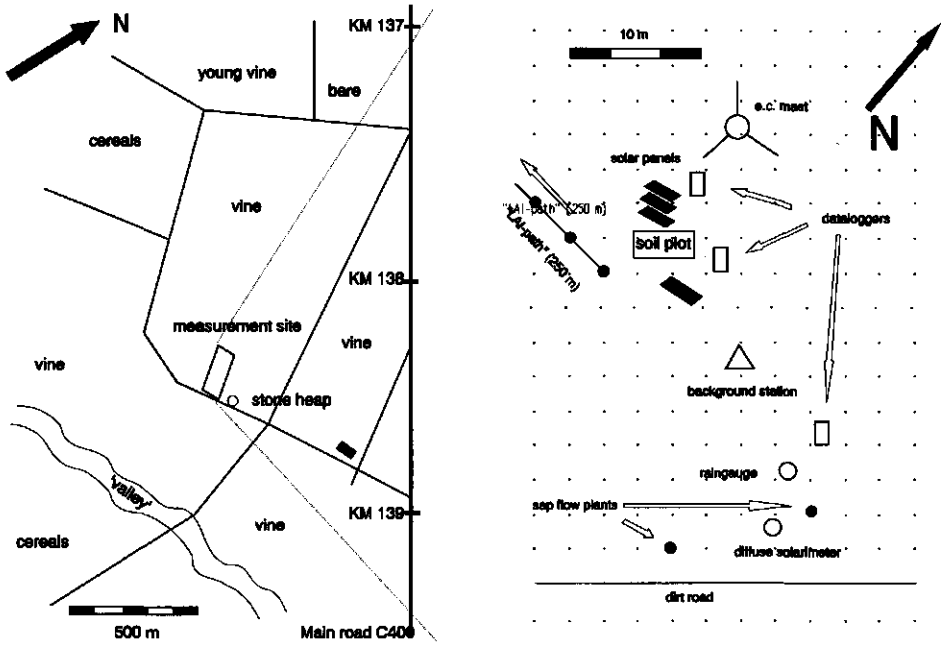

Figure 2.7: Site layout during EFEDA-II; Left: general surroundings of measurement plots, where solid lines indicate (dirt) roads; Right: measurement plot details, where also shown are the locations where the plant parameters were sampled

2.3.3 Determination of available energy and surface temperature

- **Shortwave radiation**

During EFEDA-II the same components of shortwave radiation were measured as the case for EFEDA-I, but each component only once. Both incoming and reflected shortwave were measured with Kipp CM5-sensors at 8 m height above the surface, to obtain an albedo representative for the combined surface and plants system. Calibration of all shortwave radiation sensors was carried out at WAUMET shortly before installation in Spain. However, the new calibration yielded almost identical results as the factory calibration, and the latter set of calibration factors was adopted.

A diffuse radiometer was installed separately on a mast of 2 m (see Table 2.6). A Kipp shadowring was used and installed according to its manual. About once every 5 days the position of the shadowring was adjusted according to the sun's declination.

- **Longwave radiation**

Neither the incoming or outgoing longwave radiation were measured directly during

EFEDA-II. Rather, a two-sided allwave sensor (Schülze-Däke) mounted at 8 m height was used. This sensor measures the allwave radiation (short- and longwave) by two thermopiles, separated by a massive aluminium body. Also the body temperature is measured with a PT100 thermometer. A 0.1 mm thick dome of Lupolen-H eliminates wind speed dependence and is self-supporting. An active wind stream over the outer side of the body housing and domes is caused by a fan, and reduces differences between the temperature of the sensor body and the surrounding air. Each of the two sensors is calibrated for the longwave and shortwave sensitivity separately. The longwave radiation received by either sensor, $L^{\downarrow}$ and $L^{\uparrow}$, can be computed from a separate measurement of the shortwave radiation terms, $K^{\downarrow}$ and $K^{\uparrow}$, and the sensor body temperature T_b:

$$L^{\downarrow,\uparrow} = A^{\downarrow,\uparrow} - K^{\downarrow,\uparrow} + \sigma T_b^4 \qquad (2.29)$$

where $A^{\downarrow}$ and $A^{\uparrow}$ are the measured allwave contributions in downward and upward direction, respectively, and the longwave emissivity of the sensor is assumed to be unity.

Also, the surface temperature was measured using a single Heimann KT15 mounted at approximately 8 m height. The view angle of the instrument was 16°, and the radius of the circle being seen was therefore 4.6 m, large enough to cover bare soil and some plant parts. The areal distribution of plants and soil in this view area is assumed to resemble the true areal coverage.

Apart from the fixed sensor, at several days the surface temperature was observed using a handheld Chinon device. The sensor was placed in several predefined positions over individual plants and stretches of bare soil before reading the temperature. A total number of eight plants was observed this way, where the overhead temperature of all plants was recorded. Moreover, the temperature measured looking to four plants in Northern and Eastern direction was registered, together with the temperature seen looking South and West to the other four. The unshaded bare soil temperature was monitored at eight positions in between the sampling plants. Also, the temperature of soil just Northern and Eastern of four plants was measured, plus the soil just southern and western from the four others. Table 2.7 gives a brief summary of the frequency of the handheld surface temperature measurements.

- **Net radiation**

The net radiation could only be obtained for the level at which the radiation sensors were mounted, that is, 8 m. No distinction between plants and bare soil is made here. Net radiation was calculated as the balance of the (corrected) values of incoming and reflected shortwave and incoming and emitted longwave radiation.

2.3.4 Determination of scalar and momentum flux densities

During EFEDA-II, momentum flux density was measured using both fast-response eddy correlation measurements and the profile method. The results from the profile method are not used here. The scalar flux densities (heat, water vapour and CO_2) were measured using fast-response sensors only.

A three-dimensional Gill/Solent sonic anemometer at 6 m height formed the heart of

Table 2.7: Frequency of handheld surface temperature measurements

quantity	number
Measuring days	173, 179, 182, 184, 194, 202, 204, 205, 208
Measurements per day	appr. every 2 hours (sunrise - sunset)
plants per measurement	8
orientation:	
- overhead plant	8
- N, E, S, W side of plant	4 each
- overhead bare soil	8
- soil N, E, S, W of plant	4 each

the eddy correlation station. Unlike the Kaijo Denki DAT310, u, v and w are measured in the same volume.

No thermocouple was added to the system. A sonic temperature was obtained from the vertical wind signal. WSC obtained experimental evidence for a reliable application of the sonic temperature (corrected for humidity contributions, see Appendix II) for measuring the sensible heat flux density from the earlier HAPEX-Sahel experiment in Niger in 1992. The factory calibrations were used for all signals. The temperature signal, however, was recalibrated using the temperature obtained from the psychrometer at 6 m.

Fast response humidity measurements were carried out with two devices: a Campbell KR20 Krypton hygrometer, and a LICOR6262 closed path gas analyser. The factory calibration of the Krypton appeared to be very stable, both the offset and the gain. An *in situ* correction was applied to the calibration gain using data of the psychrometer at 6 m.

CO_2 concentration fluctuations were measured with the LICOR6262 as well. Air is pumped into a sample cell, and light absorption at two frequencies in the infra-red region is used to detect the concentration of CO_2 and H_2O in the cell. A dry and CO_2-free reference gas is created by a closed second air circuit which is pumped continuously through cristals of magnesium perchlorate (hygroscopic) and soda lime (absorbing CO_2). Calibration of both the offset and the gain of the two signals was carried out once every 10 days in the field using dry nitrogen (zero), a dewpoint generator creating air with a known water vapour concentration, and a bottle with air containing a known CO_2-concentration (227 ppm).

Appendix II lists the eddy-correlation corrections applied.

2.3.5 Soil measurements

- **Soil heat flux density**

During EFEDA-II only the heat flux plate method was used to assess the soil heat flux density. A total number of eight plates (CSIRO) was used, of which four were installed at 1 cm depth and four at 5 cm depth. The plates were placed in pairs above each other in a row between two plants, such that the first two and last two were temporarily shaded by the plants, and the others were under sunlit soil almost all day (see Figure 2.8). Sensor 8 was logged single-ended, due to a limited number of datalogger channels. After the experiment, the measured results of this sensor had to be discarded.

Close to each of four flux plates a PT100 soil thermometer was installed. Two PT100 sensors were buried at 1 and 5 cm under sunlit soil (near plates 3 and 4), and two at similar depths near plates 7 and 8 (see Figure 2.8).

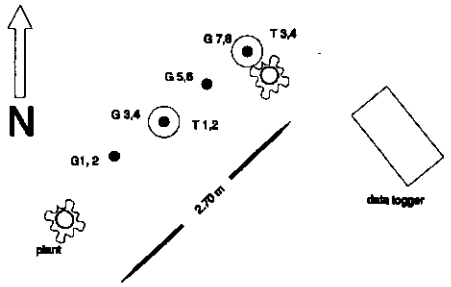

Figure 2.8: Layout of soil measurement plot. *G* = soil heat flux plate, *T* = thermometer

■ **Soil physical parameters**

No further soil physical parameters were collected in the field during the measurement period. It was assumed that soil porosity was identical to the situation during EFEDA-I. The water content in the top soil layer was very low during EFEDA-I (<8%), and this figure was adopted here as well.

The hard lime layer below a depth of 50 cm turned out to extend for a considerable depth, at least 4 m. The material was rather homogeneous and had a high porosity, exceeding 50%. The soil moisture content throughout the layer varied somewhat, but was estimated to be 12 m^3/m^3 everywhere in the layer (Havercamp, personal communication).

2.3.6 Determination of vegetation parameters

■ **Crop height, leaf area**

In principal, during EFEDA-II identical methods were applied to assess crop height and leaf area. The only change compared to EFEDA-I is reflected in the sample selection. 27 plants were now chosen to sample *h* and *LAI*. 25 of these plants were situated in a line approximately East - West, starting at the measurement site (see Figure 2.7). From the start point, every third plant was selected, thereby covering a line of approximately 250 m, which was considered to yield a representative sample. Furthermore, two plants involved with sap flow measurements were also sampled. As was evident from the statistical analysis of the significance of the *LAI*-data measured during EFEDA-I, the period between two *LAI*-measurements must be long enough to detect any change at all (Michels and Moene, 1991). Therefore, the sampling frequency was reduced to once every 10 days. Table 2.8 specifies dates and the number of samples used for the vegetation-measurements.

During EFEDA-II, the crop height *h* was defined as the 80% percentile of the individual plant lengths. The frequency distribution of *h* showed a very gradual increase, and the sharp increase at 70% observed during EFEDA-I was not present.

Jacobs (1994) did not find a significant dependence of stomatal resistance on height, which made a specification of leaf area per vertical layer redundant. On the other hand, *LAI* was specified per age class (young, normal and old). The calibration values to relate the vein product to leaf area (section 2.2.6) were obtained from 100 leaves per age class as well. The calibration was carried out three times, once every three weeks. Figure 2.9 shows the

Table 2.8: Dates at which plant parameters were determined, and total number of sampled plants during EFEDA-II. Date numbers are DOY in 1994

parameter	sampling days	number of samples
crop height	152, 161, 168, 177, 185, 201, 207	27 plants
Leaf Area Index	152, 161, 169, 177, 185, 200, 210[1]	27 plants, 3 age categories: • young • normal • old
calibration *LAI*	152, 173, 210	300 leaves
fraction of vegetation cover	152, 161, 168, 177, 185, 201, 207	27
stem height and diameter	153	27
fraction sunlit leaves	165, 188, 204	15
stomatal resistance	157, 159, 163, 166, 170, 173, 179, 182, 184, 188, 197, 198, 202, 205, 208	6 each day

[1] Measurement days for *LAI* refer to centre of series of days to measure all plants

development of leaf area per age class during the measurement season. A higher order polynomial was fitted through each of the age classes, to be used for the upscaling of porometry measurements to canopy averages (section 3.4).

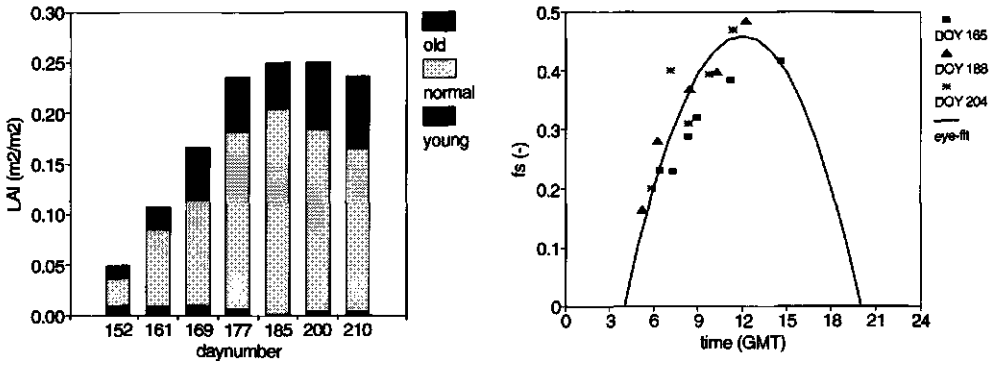

Figure 2.9: Vegetation measurement results from EFEDA-II. Left: leaf area index per age class; Right: Fraction of sunlit leaf area measured at three days. Also shown is the quadratic function given by $f_s = 0.46(1 - [(t - 12)/8]^2)$, where t = time

■ Fraction of sunlit leaves

Since obviously leaf stomatal resistance depends on the light regime of the leaves, the fraction of sunlit leaves, f_s, is an important weighting factor to obtain crop resistance. During EFEDA-I this was not measured explicitly, but was assumed to remain constant during the day (see section 2.2.6). Here, this assumption was investigated by measuring the fraction of sunlit leaves.

The method consisted of counting of the number of leaves being sunlit standing away from a plant, and to relate these countings to the total number of leaves of each plant, as determined during a *LAI*-measurement session. The number of sunlit leaves was counted on 15 plants approximately every two hours before noon, assuming a symmetric response over the day. A distinction was made between three age categories. The method was applied once every 20 days. Figure 2.9 shows the resulting values of f_s. Also shown is an eye-fitted quadratic function of time, which was used for the upscaling of stomatal resistance measurements to the canopy scale.

- **Fraction of vegetation cover**

To determine the fraction of vegetation cover, σ_f, the plant radius of each sampling plant was estimated as the mean of two perpendicular cross section diameters. The cross sections were chosen to lie in the line of sampling plants and perpendicular to that line, over the plant stems. The variation between the plants was very large due to the fact that individual branches contributed to the cross section diameter to a large extent, in spite of their small contribution to the real drip area. Results are shown in Figure 2.10.

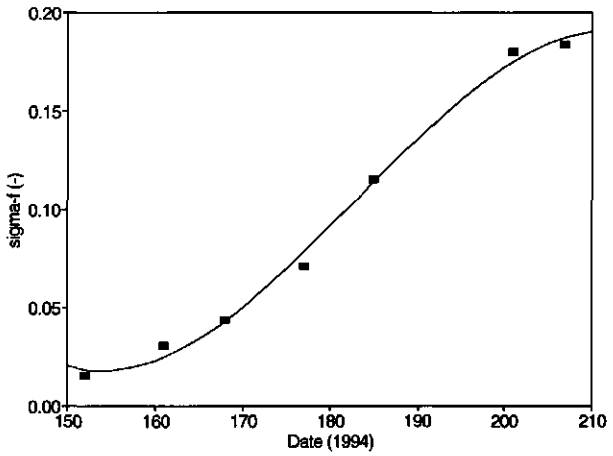

Figure 2.10: σ_f as measured during EFEDA-II. The solid curve represents the best-fit polynomial regression, given by $\sigma_f = 10.33 - 0.18day + 9.9\ 10^{-4}day^2 - 1.81\ 10^{-6}day^3$

- **Stomatal resistance**

Measurements

As during EFEDA-I, the stomatal resistance of the plant leaves was measured with a dynamic diffusion porometer. This time, a newer version (DeltaT, Mk4) was used. The difference with the previous version was a higher degree of automatic data processing. Calibrations were carried out in the field as well, but immediately applied to the data measured after the calibration. A correction for temperature differences between the cup and the leaf (Monteith *et al.*, 1988) was automatically employed.

During most of the 15 sampling days (see Table 2.8) leaf stomatal resistance was measured from sunrise until sunset. A distinction was made between the three different leaf age classes and two classes of radiation regime (shaded and sunlit), yielding a total number of six leaf classes. Until day 173 (22 June) measurements on 18 leaves were equally

distributed over the six leaf classes, but later only four leaves were taken from the young age class (two shaded, two sunlit) and eight from the intermediate age class. Each measurement day, six plants were selected and sampled throughout the entire day: five were selected randomly from the sample line of 25 plants, and one of the plants with a sap flow shoe was always monitored. Measurements were taken nearly continuously during daytime, which yielded approximately 50 leaves per hour (or 750 samples between sunrise and sunset). Also the leaf temperature and the amount of incident Photosynthetic Active Radiation (PAR), as measured with the porometer device, were logged and stored for further analysis.

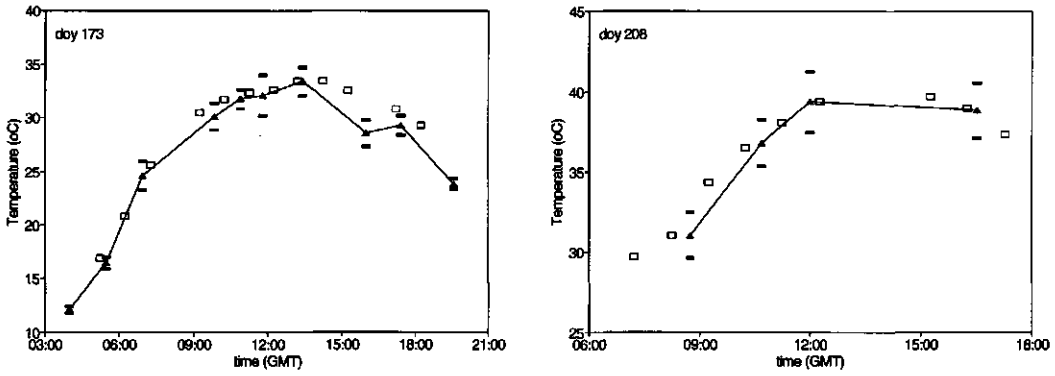

Figure 2.11: Leaf temperature as obtained from (□) the porometer (averaged for both sunlit and shaded leaves) and (—▲—) the manual radiometric surface temperature measurements. Horizontal lines represent one standard deviation from the average of the radiometric temperatures; Left: DOY 173; Right: DOY 208

Upscaling to the canopy scale

During EFEDA-II explicit measurements of f_s and leaf area per age class were available, while the porometry measurements were not divided into different height intervals. The fitted functions of f_s and *LAI* were used to average r_{st} to canopy scale resistances according to eq. 2.28.

Also hourly averages were computed from the leaf temperature measurements and the amount of incident PAR, both for shaded and sunlit leaves separately. The leaf temperature measurements were compared with the plant temperature readings obtained from the manual plant surface temperature measurements (section 2.3.3). Figure 2.11 shows the diurnal course of the average leaf temperatures obtained from the porometer and the manual radiometric recordings for two days in 1994. Porometer readings were averaged over sunlit and shaded leaves. The sunlit leaves were on the average 0.64 °C warmer ($r^2 = 0.994$). Also shown are the standard deviations of the manual measurements. The agreement is satisfactory for the data shown. We conclude that the porometer values are accurate enough to be used for calculations involving the stomatal resistance (section 3.4).

2.4 Derived quantities

2.4.1 Aerodynamic roughness and displacement height

Aerodynamic roughness is an important parameter for the estimation of momentum and scalar flux densities between the surface and the atmosphere. For sparse canopies the aerodynamic properties are a complex function of plant geometry and size, roughness of the bare soil, and distribution of canopy elements with height.

For EFEDA-I the aerodynamic roughness and displacement height have been determined using various methods: the wind profile method, eddy-correlation measurements, and a geometrical method. An additional method using eddy-correlation measurements at various heights (Lloyd *et al.*, 1992), was applied as well, but yielded results that contained a scatter too large to be significant.

■ **Wind profile method**

In the wind profile method, z_{0m} and d are determined as integration coefficients of a theoretical wind profile fitted to observations (Robinson, 1962). This optimalization technique is in fact similar the the method for obtaining sensible heat and momentum flux density from profile measurements (see section 2.2.4). The theoretical wind profile is found by simultaneously solving for the displacement height d, roughness length z_{0m} and friction velocity u_*. Stability corrections to this profile were included using eddy-correlation observations of z/L_v, and the integrated functions of Paulson (1970). Representative values of z_{0m} and d are defined as the median of a sample of results. Since the vegetation grew rapidly, results were grouped per period of approximately 5 days. Only time slots with near-neutral values of z/L_v ($-0.1 < z/L_v < 0$) were included, to minimize the impact of the stability corrections. Measurements carried out by the lowest cup (0.75 m) were discarded.

Figure 2.12 shows the results of z_{0m} and d for the EFEDA-I dataset, obtained by this method. The roughness length is shown to increase significantly as the season proceeded, but the displacement height derived from the profile method remained fairly constant, at a value of about $h/3$ (also shown).

■ **Curve fit method using eddy-correlation measurements**

An alternative computation of the most likely value of both z_{0m} and d is proposed by Jacobs and van Boxel (1988). Measurements of a sonic anemometer at a single height can be used to specify a relationship between z_{0m} and d. For a neutral surface layer these quantities are related according to

$$\frac{z - d}{z_{0m}} = \exp\left(\frac{\kappa u}{u_*}\right) \qquad (2.30)$$

As before, z_{0m} and d are also computed using a least square fitting technique. The resulting values usually show a considerable scatter. The optimum value is found by employing a linear regression through a scatter diagram of z_{0m} and d, and seeking the intersection with the line obtained by the eddy-correlation measurements, eq. 2.30. In fact, this intersection replaces the assumption that the median of the sample determines the optimal values of z_{0m} and d. Resulting values of z_{0m} and d for EFEDA-I are also shown in

Figure 2.12. They correspond well to the results obtained from the profile method.

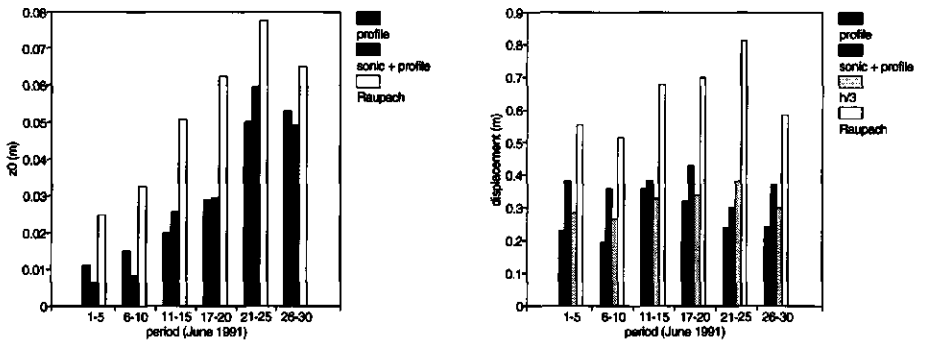

Figure 2.12: Measurements of roughness length (left) and displacement height (right) taken using various methods during EFEDA-I (see text)

- **Geometrical method**

Raupach (1992) developed a general theory about the total drag exerted by a rough surface. The normalized roughness length z_{0m}/h is a function of the roughness density (or frontal area per unit ground area) $\eta = b\,h/D^2$, where b is the characteristic width of the roughness elements, and D the horizontal spacing. z_{0m}/h first increases with η until $\eta \approx 0.3$, and decreases with a further increase of η. This picture was established by the one-dimensional numerical second-order closure computations carried out by Shaw and Pereira (1982). According to Raupach's theory the drag coefficient $C_M(z)$, given by

$$C_M(z) = \left(\frac{u_*}{u(z)}\right)^2 = \left[\frac{1}{\kappa}\ln\left(\frac{z-d}{z_{0m}}\right)\right]^{-2}$$

can be computed from the relationship

$$\gamma_h \equiv \frac{u(h)}{u_*} = (C_S + \eta\, C_R)^{-1/2} \exp(c\,\eta\,\gamma_h/2) \qquad (2.31)$$

where C_S and C_R are the drag coefficients of the unobstructed substrate and an isolated roughness element, respectively, and c is a O(1) coefficient. Eq. 2.31 is an implicit relationship in γ_h, but can be solved fairly easy. The roughness length is then found from

$$\frac{z_{0m}}{h} = \frac{h-d}{h}\exp(\Psi)\exp(-\kappa\,\gamma_h) \qquad (2.32)$$

Ψ is a profile influence function, accounting for the departure of the actual momentum diffusivity profile from the surface layer profile $\kappa\,u_*\,(z - d)$. The displacement height d is defined as the centroid of the drag force profile, affected by both the roughness elements and the underlying substrate. Raupach derived for d the expression

$$\frac{d}{h} = \left(\frac{\beta_R \eta}{1 + \beta_R \eta}\right)\left(1 - c_d \left(\frac{b}{h\eta}\right)^{1/2} \gamma^{-1}\right) \qquad (2.33)$$

where c_d is a constant equal to 0.6, and $\beta_R = C_R / C_S$.

Figure 2.12 shows the results for the EFEDA-I dataset. The width of the canopy elements, b, was derived from the expression for the plant radius (eq. 2.24). Predictions of both z_{0m} and d gives values that are significantly higher than obtained from the profile methods. Verhoef (1995) suggested that the specification of η from the assumed plant shapes and densities might result in values that are too large.

■ **Discussion of roughness parameter results**

The values for z_{0m} found using the profile methods agree very well with the results reported by Sene (1994) for a similar crop, who found $z_{0m} \approx 0.01$ m early in June, and 0.04-0.06 m six weeks later. On the other hand, based on the review by Wieringa (1993) the ratio $z_{0m}/h \approx 0.05$, found here, is rather low. Kawatani and Meroney (1970) noticed that the values of d obtained by the regression method of Robinson (1962) and Covey (1963) show a large variability, and can even become negative. A possible overestimation of d is usually associated with an underestimation of z_{0m}. Wieringa (1993) lists other possible errors in the quantification of the roughness parameters:

- the upwind fetch might have been too short, or the terrain might not have been entirely flat
- the correction for unstable conditions may have been too strong, which gives rise to a too steep wind profile and too low roughness length
- the lowest sensor (± 1.5 m) might have been too close to the canopy top
- cup anemometer overspeeding particularly occurs near the surface where turbulence intensity is strong. This also gives too steep wind profiles.

In spite of these uncertainties, values for z_{0m} and d are interpolated from the results obtained using the profile methods for practical calculations. z_{0m} is given by

$$z_{0m} = \begin{cases} 0.01 + 0.01 \dfrac{day}{15} & day \leq 15 \\ 0.02 + 0.04 \dfrac{day - 15}{15} & day > 15 \end{cases} \qquad (2.34)$$

where *day* is the day in June, 1991. d was kept constant at 0.3 m for further calculations[1].

2.4.2 Roughness length for heat

The aerodynamic resistance for heat transfer between the surface and a reference level, r_a, can be specified according to

[1] De Bruin *et al.* (1995) assumed that d linearly increased from 0.05 m on 15 June to 0.4 m on 30 June, based on preliminary calculations.

$$r_a = \rho c_p \frac{T_{sur} - T_a}{H} \tag{2.35}$$

where T_{sur} is an (effective) surface temperature (defined below eq. 2.1), and T_a the temperature at reference height z_R. From eq. 2.35 a so-called roughness length for heat can be obtained, which can be written as (Blyth and Dolman, 1995):

$$z_{0h} = \frac{z_R - d}{\exp\left(r_a \kappa u_* + \Psi_h\left((z_R - d)/L_v\right)\right)} \tag{2.36}$$

in which Ψ_h is an integrated form of the stability corrections proposed by Dyer and Hicks (1970; eqs. 2.13 and 2.14). The ratio z_{0m}/z_{0h} can be used to define an additional resistance to heat transfer, in series with the aerodynamic resistance for momentum transfer applied in single layer surface models (see section 4.1.1). The quantity $1/\kappa \ln(z_{0m}/z_{0h})$ is often referred to as B^{-1} (Garrat and Hicks, 1973; Kohsiek *et al.*, 1993).

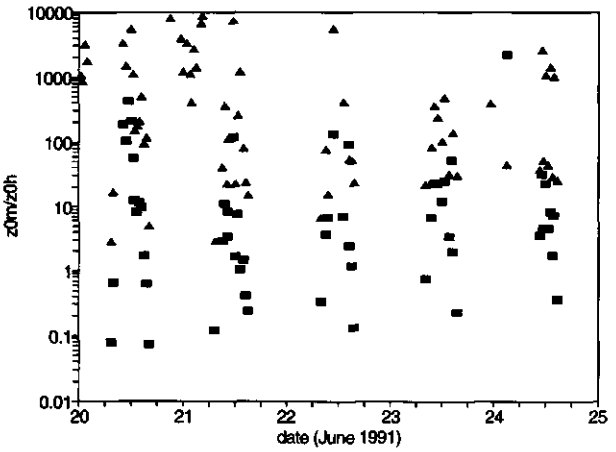

Figure 2.13: Ratio of z_{0m}/z_{0h} as defined using eqs. 2.34 and 2.36. Data shown are derived by using the average (■) and bare soil (▲) temperature from the low cable. Data of H and u_* were obtained from the eddy-correlation device mounted at 4.35 m

Figure 2.13 shows the ratio z_{0m}/z_{0h} for two different effective surface temperatures, measured during EFEDA-I: the bare soil temperature as obtained from the low cable, and an average surface temperature from the same sensor (Appendix II). Around noon, the difference between these temperatures is typically 4 degrees. Apart from a considerable scatter of z_{0m}/z_{0h}, its typical value is somewhat higher than values used in SVAT models presented by Braud *et al.* (1993), Jacobs (1994) or Viterbo and Beljaars (1995). Furthermore, a clear diurnal variation is present. Note that Verhoef (1995) reports a considerably lower value of z_{0h}, by using the single sensor mounted at 4 m height (Table 2.1).

Beljaars and Holtslag (1991) explain that z_{0m}/z_{0h} can vary as a result of a vertical change of the momentum flux to the surface, which is for instance induced by large scale roughness elements affecting high level wind profiles. Blyth and Dolman (1995) point out that additional to this aerodynamic effect, z_{0h} for sparse canopies can vary by an order of magnitude by variations of the distribution of the heat source between the canopy elements

and the underlying soil. More on this issue is discussed in section 5.3, and by Verhoef (1995).

2.4.3 Energy balance terms

During the EFEDA-I campaign many methods were applied to measure the energy balance components. For the model studies reported in later sections a quantitative assessment of the fluxes of heat, moisture and radiation is of importance.

This section presents some results of the measured fluxes, and discusses the selection criteria which were adopted to obtain a dataset for further use. Moene (1992) extensively discussed the methodological differences of various methods, in the context of the comparability of fluxes measured at different sites with different instrumental set-up's and methods.

During EFEDA-II surface energy fluxes were determined with eddy-correlation only, albeit that various sensors were used for the measurement of the latent heat flux (section 2.3.4). In the context of the current work these fluxes were used marginally only for the examination of the canopy resistance models (section 3.4). Therefore no attention will be paid to these measurements here.

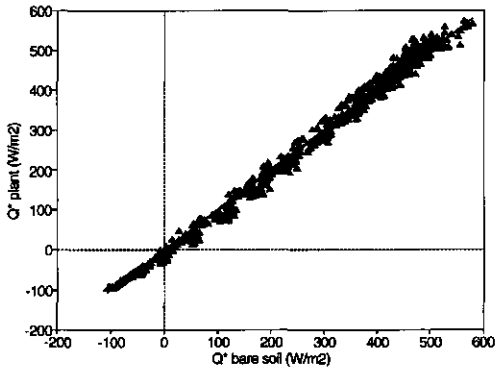

Figure 2.14: Net radiation measured above bare soil and above an individual plant for available half hour averages during EFEDA-I

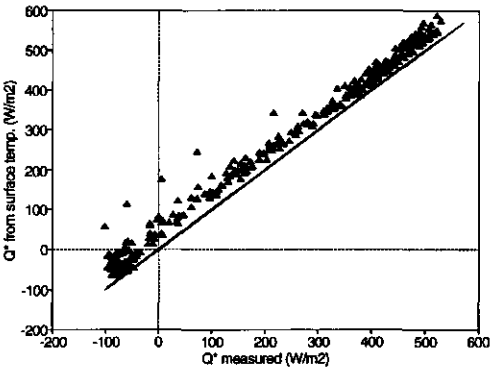

Figure 2.15: Radiation balance from eq. 2.1 plotted against measured net radiation for all available half hour averages during EFEDA-I

- **Net radiation**

In Figure 2.14 the results of the two sensors measuring Q_* are intercompared. Shown are all available half hour averages for 2 - 30 June 1991. The value of $Q_{*,plant}$ exceeds the bare soil net radiation by only 1.4% ($r^2 = 0.996$). This difference is rather small, compared to what is to be expected from differences in the shortwave reflection coefficient of plants (typically 20%) and soil (up to 30%) (Dickinson, 1983). However, the exact position of net radiometers low above the surface is not a trivial issue. Net radiation measured just above the (darker and cooler) plants are affected by the surrounding bare soil as well, and do not give a net radiation equal to a value measured above a homogeneous canopy of the same species. Also the net radiation measured in between plants will not be representative for the bare soil, since the large radiometer view angle enables influence of a surface far from the area just underneath the sensor. These significant mutual effects explain the small differences in the

net radiation values. A 'representative' average net radiation at the field scale was defined as a simple arithmetic average of the two sensor readings.

In Figure 2.15 net radiation obtained from the radiation balance (eq. 2.1) is compared to the arithmetic average of the two sensors. For $\overline{T}_{sur}$ the average surface temperature as measured from the high cable and averaged as outlined in Appendix II is used. The surface albedo, a, was fixed at 0.29 (see section 3.3), and for the surface emissivity a value of 0.98 was taken. The correspondence is good ($r^2 = 0.990$), but an offset of 38 W/m^2 remains. Many factors may be responsible for this difference. First, sensor calibration errors may be significant. Also, the assumption that $a = 0.29$ is uncertain, due to the large variability of the surface colour and wetness. Finally, the net radiometers mounted at some height integrate over a different view angle then the radiation thermometer.

- **Soil heat flux**

The two methods to determine the soil heat flux G during EFEDA-I are compared in Figure 2.16. Both methods are applied by calculating different soil heat fluxes for shaded and sunlit plots, and applying a weighted averaging using σ_f (section 2.2.5). The regression forced through the origin yields a good correspondence ($r^2 = 0.933$). However, the caloric method gives lower values for both nighttime and daytime situations. Without clear evidence for the superiority of either of the methods, we selected the heat fluxes measured by plates to serve as comparison material for future purposes.

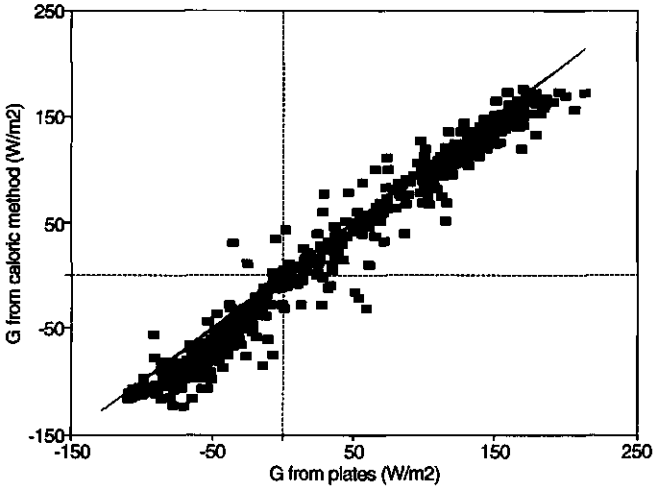

Figure 2.16: Soil heat flux detected using heat flux plates and by means of the caloric method

- **Sensible and latent heat flux**

The sensible heat flux data collected during EFEDA-I can be compared to each other in many ways, due to the many detection methods. De Bruin *et al.* (1995) compared the values obtained using the scintillation method to the eddy-correlation data from the low eddy-mast at $z = 4.35$ m (Table 2.1). They found a fair correspondence, depending on the assumptions made about the terrain height and the strategy to obtain values of the friction velocity. A maximal correspondence was found when u_* was derived from the same eddy-correlation

device and the displacement height was allowed to increase gradually from 5 to 40 cm throughout the measurement period ($r^2 = 0.956$). That result is even slightly better than the correspondence between the two eddy-correlation sensible heat fluxes from the eddy mast and the 13 m mast (H[13 m] = 1.02 H[4.35 m], $r^2 = 0.951$, figure not shown).

Due to instrumental problems, only the eddy-correlation data of the latent heat flux from the sensor in the 13 m mast were reliable. The remaining eddy-correlation data were discarded from the present study.

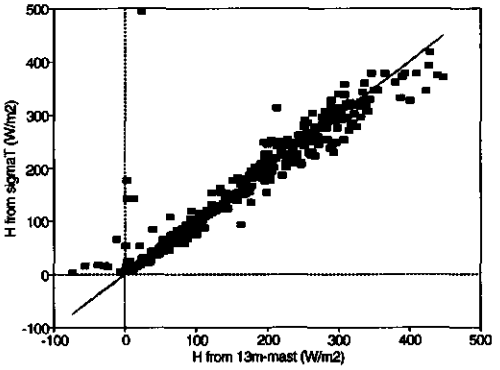

Figure 2.17: Scatterplot of H from the σ_T method and the eddy-correlation measurements, both from the 13m-mast

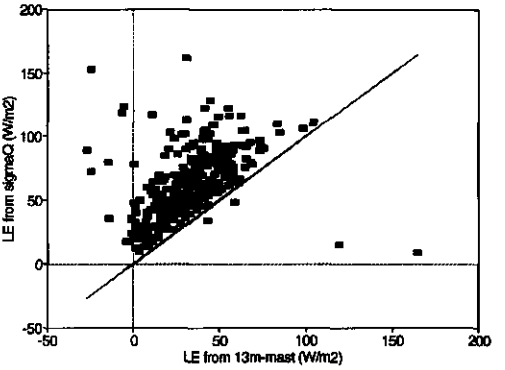

Figure 2.18: *As Figure 2.17, but for the latent heat flux*

A comparison between the eddy-correlation sensible heat flux and H from the σ_T equation from the 13m-mast is shown in Figure 2.17. The coefficients c_{T1} and c_{T2} were specified as 2.9 and 28.4, respectively (De Bruin *et al.*, 1993). The agreement for rather unstable conditions ($H_{eddy} > 50$ W/m^2) is fair, and a linear regression through the origin yields $H_{\sigma T} = 0.975\ H_{eddy}$ ($r^2 = 0.938$). For $H_{eddy} < 0$ the σ_T-method gives undefined results, which is shown clearly in Figure 2.17. A similar plot is given in Figure 2.18 for the latent heat flux measured using the σ_q equation (eq. 2.9), again using the equipment in the 13m mast. The agreement is much worse, and the variance method overestimates the eddy-correlation values significantly. De Bruin *et al.* (1993) present a likewise low correspondence using identical equipment operated during the CRAU experiment. They argue that the method breaks down due to the fact that the correlation coefficient between T and q is significantly lower than 1. Similar to the large impact of eddies scaling with the boundary layer height z_i on the variance of horizontal wind speed (Van den Hurk and De Bruin, 1995), the relative contribution from dry downdrafts to the variance of q near the surface may be rather large. The surface flux is not an appropriate scaling parameter in these cases, and the applicability of Monin-Obukhov similarity breaks down.

A considerable problem was the determination of latent and sensible heat fluxes from the profile or Bowen-ratio method. A fair agreement between eddy-correlation and profile measurements was obtained for the sensible heat flux, but for the latent heat flux the correspondence was poor (Figure 2.19). In both cases the psychrometers at the lowest level were not included. Both fluxes are unadequately reproduced when the Bowen-ratio method is used (Figure 2.20). Again, the lowest measurement level was discarded.

Various combinations of psychrometers (East and West profile, exclusion of extreme readings) were tried, but in no case the humidity profile was adequate enough to derive reliable latent heat fluxes from these.

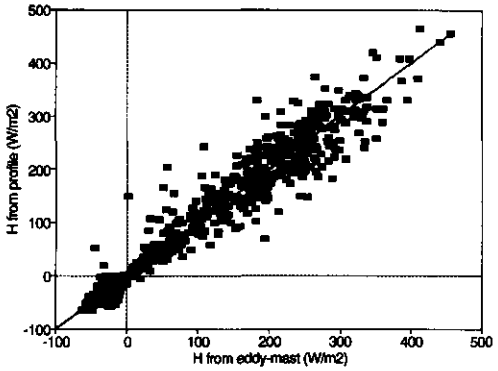

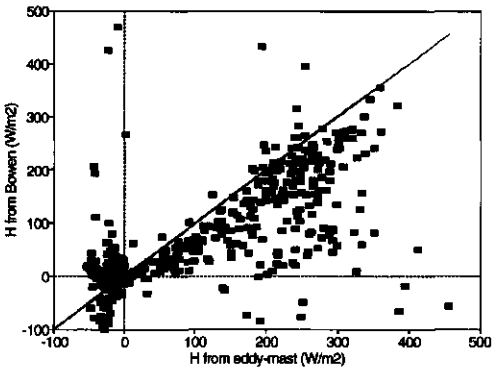

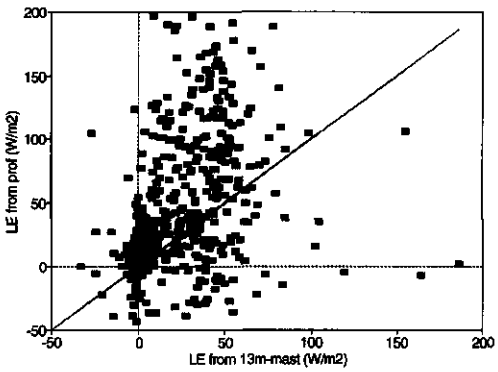

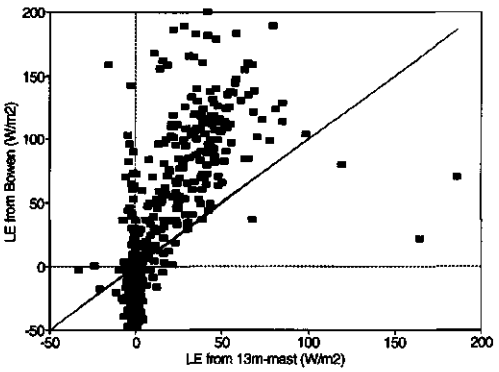

Figure 2.19: Sensible (upper) and latent (lower) heat flux derived from the profile measurements, compared to the eddy-correlation measurements at 4.35 m (H) and at 12.5 m (λE)

Figure 2.20: As Figure 2.19, but fluxes derived from the Bowen-ratio method

- **Energy balance closure**

Based on the presentation of results above the final energy balance that was used for further intercomparison consisted of:

- an average of the net radiometers from the two low sensors
- the soil heat flux derived from the soil heat flux plates and weighted accordig to σ_f
- the sensible heat flux obtained from eddy-correlation measurements in the eddy-mast, at 4.35 m height
- the latent heat flux from eddy-correlation measurements in the 13m mast, at 12.5 m height.

Figure 2.21 shows the energy balance closure, defined as $Q_* - H - \lambda E - G$, from these terms for all days during EFEDA-I. The closure is good during nighttime, although a small

but consistent minimum around sunset persists. This is associated to the soil heat flux correction, which is very large at this time of the day due to a very rapid change of the surface temperature. The derivation of the change of the heat content of the soil above the soil heat flux plates may be wrong due to an error in the estimation of the exact temperature profile near the surface (Appendix II). During daytime generally a surplus of radiative energy occurred, which peaks to approximately 100 W/m^2 at some days. The hourly averaged energy balance closure shows a slightly smaller radiative energy surplus (figure not shown). Especially the low evaporation values recorded during most of the season are suspected to be erroneous. Also shortcomings in the eddy-correlation method may be responsible for this disclosure.

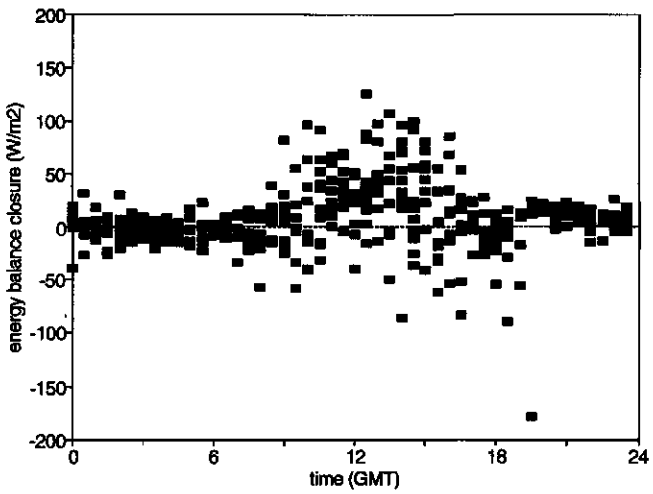

Figure 2.21: energy balance closure for EFEDA-I defined as $Q_* - H - \lambda E - G$, where the energy balance components are defined as indicated in the text

2.4.4 Soil thermal properties

In contrast to atmospheric dispersion, transport of heat in the soil involves hardly any turbulence, and is generally solved using diffusion laws. The model descriptions in chapter 4 include a treatment of thermal diffusion (section 4.1.2), and a generalized description of the surface temperature based on diffusion in a homogeneous soil, the force-restore method (section 4.1.4). These methods make use of the thermal properties of the soil, in particular the thermal conductivity (λ_T), diffusivity (k), and volumetric heat capacity ($\rho' C_h$).

Verhoef *et al.* (1995) describe measurements of these quantities from two campaigns conducted in semi-arid areas: EFEDA-I and HAPEX-Sahel. They discuss the heterogeneity of these thermal soil properties for a semi-arid sparse canopy surface both in space and in time. Apart from mesoscale heterogeneity (induced by variable rainfall or crop appearances) the micro-scale heterogeneity (induced by the partial plant cover) may be important for sparse canopies, owing to shading and variation in soil moisture content.

In their paper, Verhoef *et al.* (1995) describe the courses of k and λ_T for both sunlit and shaded soil from EFEDA-I, and the bulk volumetric heat capacity (a bulk-value could

only be derived since soil moisture measurements and bulk densities were sampled under the assumption of a horizontally homogeneous soil). In the current section a summary of their results is presented.

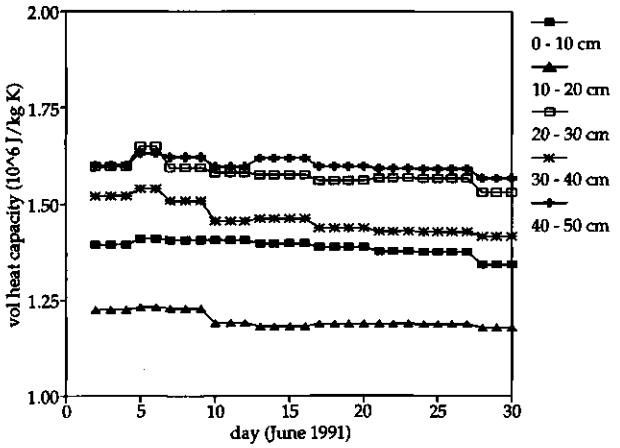

Figure 2.22: Volumetric heat capacity obtained from soil bulk density and soil moisture measurements taken in 5 different layers during EFEDA-I

Figure 2.22 shows the bulk volumetric heat capacity for 5 different soil layers using eq. 2.21. Values of the dry bulk density were found to be 1340 kg/m^3 for the top layer, and 1215 ± 25 kg/m^3 for the remaining layers (Droogers *et al.*, 1993). After the last rainfall (0.5 mm on DOY 155; Sene, 1994) maximum values of around 1.6 MJ m^{-3}K^{-1} were reached in the layers 0.20 - 0.30 and 0.40 - 0.50 m. The minimum value was about 1.1 MJ m^{-3}K^{-1}. $\rho' C_h$ appeared to decrease in all layers as time proceeded, due to a slight reduction of the water content, ω. Values of ω ranged from 0.04 - 0.08 m^3/m^3 for the top layer, and values up to 0.18 m^3/m^3 were recorded in deeper layers.

The soil thermal conductivity, λ_T, was obtained directly from the λ_T-needles and from its definition $\lambda_T = k\, \rho' C_h$. Five methods were applied to derive an estimate of k, of which the results obtained by the amplitude method, as described in section 2.2.5, are presented here. The temperature signal from the sensors installed under individual plants usually showed two maxima, separated by a decreased temperature due to plant shading. This made the use of the amplitude method for obtaining k for shaded soil parts impossible, and we confine ourselves to the estimates for sunlit soil.

Values of soil thermal conductivity λ_T, derived from the solution of soil thermal diffusivity using the amplitude equation (eq. 2.19), exhibit a slight variation as time proceeds (Figure 2.23). In general, λ_T increases with depth. In Figure 2.23 the λ_T values obtained from temperature readings at depths 25 and 50 cm are discarded, due to large uncertainties which are involved with the small signal amplitude at these depths. The high values before 6 June (DOY 157) are a result of the preceding rainfall. The origin of the high datapoint at 24 June (DOY 175) for λ_T(3-5 cm) is not clear.

Measurements of λ_T, carried out at 3 cm depth in both sunlit and shaded soil, resulted in a nearly constant value of ± 0.10 (sunlit) and ± 0.14 (shaded) W/mK, respectively. The values at 10 cm depth showed a larger scatter, but were about 0.1 W/mK

higher. The difference between the sunlit and shaded patches is possibly related to a reduction of evaporation by shading. Yet, these measurements are rather low. Ten Berge (1990) shows that minimum values for dry sandy or loamy sand soils exhibit values varying from 0.15 to 0.30 W/mK. Values smaller than 0.10 can be reached, but only for substances containing a very high organic matter content, which was not the case here. A significant underestimation of up to 0.1 W/mK could be caused by poor contact between the probes and the soil, as a result of the loose character (dry conditions) of the soil and the presence of stones in the upper soil layer (Van Haneghem, 1981). Therefore, the suspiciously low measured values of λ_T were discarded.

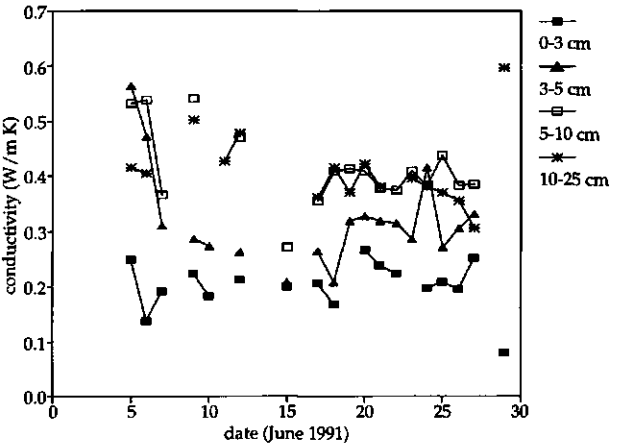

Figure 2.23: Thermal conductivity derived during EFEDA-I from the amplitude equation applied to sunlit soil temperatures at 3 and 5 cm depth, in combination with volumetric heat capacity measurements shown in Figure 2.22

3

Sometimes model equations are presented that make you wonder whether nature knows them as well

Aerodynamic transfer, albedo, and crop conductance for a sparse canopy surface

3.1 Introduction

A sparse canopy can be defined as a surface whose vegetation does not entirely occupy the horizontal space. With regard to surface exchange processes, the transfer of momentum, heat and scalars is governed by both canopy elements and the underlying bare soil. At a relatively small scale, a sparse canopy is very inhomogeneous. Close to the surface the vertical fluxes of heat, momentum or scalars will depend on the proximity of individual canopy elements or obstacles. Horizontal transport between various patches of plants or soil can be significant. A constant flux layer will not be detectable until far enough above the surface, where the fluxes of individual surface patches cannot be discerned anymore.

Atmospheric modellers have paid considerable attention to the fluxes of heat, water vapour and momentum above sparsely vegetated surfaces. Sophisticated surface models have replaced the simple single layer surface description embedded in the 'big leaf' model. In these models the surface is treated as a composite of more than just one source, mostly limited to two (Deardorff, 1978). Various model components (such as aerodynamic transfer between the source and the atmosphere, radiative properties, and others) are treated for each source separately. An extensive description of some of these so-called two-layer or two-component models is given in chapter 4.

In this chapter three aspects which are relevant to the exchange processes for sparse canopy surfaces are considered:

- aerodynamic transfer
- surface albedo, and
- canopy resistance.

With respect to aerodynamic transfer, we have extended the formulations which are applied in existing two-layer models using Lagrangian transport theory for closed canopies.

We have constructed a new set of aerodynamic exchange resistances, and compared these to existing resistance formulations for a range of surface types, including sparse canopies. This theoretical survey is published before by Van den Hurk and McNaughton (1995) and McNaughton and Van den Hurk (1995), and will be described in section 3.2.

Second, the surface albedo is considered. The variability in time and in space at various scales will be presented and discussed in section 3.3.

In section 3.4 the canopy resistance for water vapour exchange will be discussed. Observations taken during EFEDA-II are compared to a canopy resistance model based on photosynthesis modelling (Jacobs, 1994; Jacobs *et al.*, 1995).

The results presented in this chapter will be summarized in section 3.5. They will also be included in the one-dimensional simulation study, presented in chapter 6.

3.2 Aerodynamic transfer

3.2.1 Concepts based on diffusion theory

At the surface interface, the atmosphere is modified by heating or cooling, water vapour release or condensation, and scalar exchange. The motion of air is affected by friction at the surface. The degree of modification of the atmosphere depends on the quantitative fluxes of temperature, water vapour and momentum.

Similar to the process of molecular diffusion, the surface flux of a constituent x can be expressed by a gradient of ρ_x and a turbulent diffusivity K_x, which is a measure of the exchange efficiency:

$$F_x = -K_x \frac{\partial \rho_x}{\partial z} \tag{3.1}$$

Near the surface, turbulence caused by friction and density gradients is the dominant exchange mechanism. The exchange efficiency is therefore parameterized as a function of turbulent fluxes itself.

When over a limited height range the flux doesn't vary significantly with height, eq. 3.1 can be integrated and expressed as a resistance formulation:

$$F_x = \frac{\Delta \rho_x}{r_x} \tag{3.2}$$

where the aerodynamic resistance r_x is equivalent to the integrated value of $1/K_x$ over a fixed height interval, corresponding to the concentration gradient $\Delta\rho_x$. Within an atmospheric 'constant flux layer', which is defined as a layer where the vertical gradient of the flux density of heat, momentum and scalars is insignificant, a resistance formulation is often used to parameterize H, λE or τ. Eqs. 2.13 and 2.14 give expressions for the turbulent diffusivities as function of the atmospheric stability in a homogeneous surface layer.

In order to derive expressions for the aerodynamic resistances between a vegetated surface and the atmosphere, assumptions must be made about the concentration- or windspeed profile in this interval. Calculations of the aerodynamic resistances from an extrapolation of the logarithmic profile to the top of a canopy result in an overestimation of

r_x, owing to extra turbulence generated in wakes behind isolated plant elements (Raupach and Thom, 1981). The Simple Biosphere model of Sellers *et al.* (1986) assumes a logarithmic profile to be valid well above the canopy top, and includes alternative expressions for intermediate levels. Furthermore, for sparse canopies also the aerodynamic exchange between the bare soil surface and the top of the canopy is of importance. Also for this process several resistance parameterizations have been proposed, based on various assumptions about the variation of K_x within the canopy. For instance, Shuttleworth and Wallace (1985) consider an exponential decay of the turbulent diffusivity within the canopy layer, while Jarvis *et al.* (1976) adopt a constant diffusivity within a coniferous forest. Various expressions for resistances within the canopy are included in chapter 4.

In the following sections attention is paid to the physical drawbacks of the concept of an exchange resistance for describing transfer within canopies. Also a simple procedure is proposed to deal with these drawbacks.

3.2.2 Implementation of near-field dispersion in a simple two-layer surface resistance model[1]

Many canopy models have been developed to describe the exchange of sensible and latent heat between plant canopies and the atmosphere. An important function of these models is to predict mean profiles of humidity and temperature of the air in the canopy, because transpiration at each level is controlled by the ambient temperature and humidity at that level. To calculate these profiles the models must employ some assumption about the turbulent transport processes in the canopy. The most common assumption has been that turbulence does transport scalars, such as heat and water vapour, down local concentration gradients by a 'turbulent diffusion' process. That is, these models have been based on *K*-theory (see Waggoner and Reifsnyder, 1968; Shuttleworth and Wallace, 1985; Choudhury and Monteith, 1988).

In recent years *K*-theory has been challenged by observations of fluxes of scalars moving in directions opposed to their local concentration gradients within plant canopies (Denmead and Bradley, 1985). New theories have been developed which explain counter-gradient transport, and these show that the diffusivity approach is unreliable under conditions where the vertical length scale of the turbulence is of the same order as the distance over which the curvature of the concentration profile is significant (Taylor, 1959; Corrsin, 1974; Raupach, 1988). These new theories have been incorporated into canopy models using a 'higher-order-closure' approach (Wilson and Shaw, 1977; Meyers and Paw U, 1987), and a Lagrangian framework (Legg and Raupach, 1982; Wilson *et al.*, 1983; Sawford, 1986; Van den Hurk and Baldocchi, 1990). Unfortunately, such models require detailed information on canopy structure and consume large amounts of computer time, making them unsuitable for larger scale hydrological or global climate models. Simple canopy models are more suited to this application.

Two-layer models designed for sparse canopy surfaces parameterize turbulent transport within and above the canopy in terms of diffusion resistances. Unfortunately, these resistances are still derived from *K*-theory, so the models therefore provide a doubtful

[1] Adapted from Van den Hurk and McNaughton (1995)

framework for calculating scalar exchange within canopies.

Lagrangian models, on the other hand, provide an alternative to *K*-theory, computing concentration and scalar flux density profiles by repeated simulations of a large number of particle trajectories. Recently, Raupach (1989a) introduced an analytical representation of scalar transport inside canopies based on a Lagrangian description of canopy transport processes. Being analytic, it requires much less computation time than the trajectory models.

In Raupach's work the canopy scalar concentration profile is constructed as the sum of two contributions: one obtained using *K*-theory and the other expressing the deviation from diffusive behaviour. Raupach calls these the 'far-field' and 'near-field' components of the canopy concentration profile, respectively. Raupach's theory can replace models based on *K*-theory for calculating the microclimate in a multi-layer canopy model, as confirmed by Dolman and Wallace (1991) and Baldocchi (1992). However, because Raupach's model treats the canopy as a multi-level source, it still requires a layer-by-layer description of the canopy turbulence and source strength as input, so it remains unsuited to large-scale applications.

In this section we develop a strategy to implement Lagrangian theory of scalar transport within a canopy in the practical two-layer resistance model of the canopy energy balance. We use Raupach's theory to develop an analytical correction to the common two-layer model. In the next section we explore the difference between Lagrangian and *K*-theory models with respect to the predicted canopy concentration profile. It is shown that in a two-layer resistance model the calculation of the average concentration in the canopy source layer can be corrected using a 'near-field' resistance added to the usual resistance network. This near-field resistor is parameterized using Raupach's analytical Lagrangian theory. A summary of a strategy to obtain the magnitude of the resistor is given. It will be shown that it depends on the source distribution and turbulence patterns within the canopy, so we do not immediately avoid the requirement for a detailed description of the canopy. Therefore, to see whether individual descriptions of canopies are still necessary, we investigate whether an assumed 'typical' shape for the source and turbulence profiles can adequately represent all canopies in Raupach's model. We do this by testing the sensitivity of the magnitude of the near-field resistor to the shape of these profiles. Details of the Lagrangian theory, and the implications of including the near-field resistor for evaporation predictions using a two-layer model, can be found in the original paper (Van den Hurk and McNaughton, 1995).

■ A Lagrangian extension to a two-layer resistance model

Resistance models are usually based on *K*-theory, with the aerodynamic 'resistors' defined by integration of the 'eddy-diffusivity' over the various sections of the diffusion pathways in the canopy. Integration is possible because the diffusivity has a local value which expresses the ratio of the flux to the gradient at each level in the canopy. That is, the local concentration is influenced by the local flux and turbulence only, not by the fluxes or gradients at other levels in the canopy. However, experimental evidence was provided by Denmead and Bradley (1985) that much of the turbulent scalar transport within a canopy is carried out by eddy structures who have a size comparable to the canopy height. This transport therefore relies on both local gradient diffusion and a larger scale, non-local

contribution. This larger scale contribution is not accounted for by application of first order *K*-theory. Lagrangian models, by contrast, take the non-local scalar transport into account, and show that the concentration gradient at each level depends on the strength of the sources at all other levels. Lagrangian ideas are therefore incompatible with resistance models. There is, however, an exception, which we exploit here.

Consider a model of a canopy that has two distinct source layers, an overstorey and a ground layer. These layers are far enough apart to ensure that the 'non-local' effects which operate within the overstorey do not influence the concentrations at the ground, and *vice versa*. In this case we can therefore describe transfer between the layers, though not within them, purely in terms of diffusion processes. If we extend the definition of 'resistance' to the ratio of concentration difference to flux, without the requirement that this ratio is well defined at all points along the integration path between the layers, then we can describe the transport between these layers in terms of a 'vertical' resistance, and the resistors can play the same formal role as the aerodynamic resistors in, for example, the two-layer model of Shuttleworth and Wallace (1985).

This does not solve all of our problems. The 'vertical' resistances that will give the correct transport between the separate layers, being the ground, overstorey and reference height, will not give the correct concentration *within* the overstorey canopy. In *K*-theory models the strong local concentration gradients near sources cause rapid dispersal of the scalar. In Lagrangian models this is much less marked because scalar movement depends solely on the statistics of the turbulence and not on diffusion over the local concentration gradient. As a result Lagrangian models predict higher concentrations near sources than do *K*-theory models. The origin of the difference between the predicted concentration near the source is the non-local transport of scalar emitted by sources in the entire source range, which is parameterized in Lagrangian models and not in *K*-theory models. Since this concentration rise is not predicted by diffusion theory we call it a 'non-diffusive' contribution to the scalar concentration.

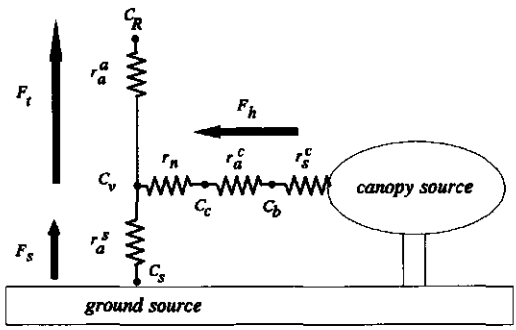

Figure 3.1: Resistance network of a two-layer surface model. The source and corresponding concentration values of only a single scalar source are considered. Flux densities are regulated by appropriate concentration gradients and resistances. Also, the near-field resistance r_n is implemented in the pathway of the canopy source (for further explanation see text; C_b will be introduced in section 3.2.3)

A possible strategy to account for this non-diffusive concentration rise within the overstorey is to add a 'lateral' resistor in the resistance network, which will isolate the canopy from the vertical diffusion components. The arguments for doing this and the

quantification of the magnitude of the resistor are based on the 'Localized Near-Field' theory of Raupach (1989a). We note that the resistance network now departs from the usual forms by having a virtual node where the vertical and lateral resistors join. The new resistance configuration is shown in Figure 3.1.

In Figure 3.1 the total scalar flux from the surface to the atmosphere, F_t, consists of a contribution from the soil or ground vegetation, F_s, and a flux from the canopy layer, F_h. The resistances r_a^c and r_s^c describe transport from the canopy leaves to the air surrounding them, and represent the bulk boundary-layer and bulk stomatal resistance, respectively. Two resistors, r_a^a and r_a^s, describe diffusive transport from the canopy to a reference level above the canopy and from the ground to the canopy. The concentration at the virtual node, C_v, is the concentration resulting from diffusive transport through r_a^a and r_a^s. The extra resistance, labelled r_n, is included to allow a higher concentration, C_c, to build-up because of non-diffusive transport near the source in the overstorey. C_c is an observable concentration value, whereas C_v is observable only when non-diffusive transport is absent.

With this configuration it is possible for the flux through r_a^s to be directed upwards even when the concentration C_c is higher than that at the ground, C_s. That is, this configuration allows observable counter-gradient transport within the lower canopy, even though the fluxes through all the resistors are well-behaved and flow down the concentration gradients. This situation is shown in Figure 3.2. Similarly, a counter-gradient transport above the canopy is allowed according to the scheme in Figure 3.2. Here the reference concentration C_R is smaller than C_c, but a net downward transport is simulated.

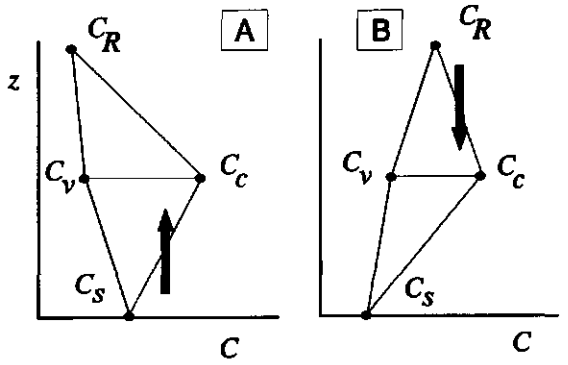

Figure 3.2: Influence of r_n on average concentration represented by the scheme of Figure 3.1. Continuous lines indicate flows according to Figure 3.1, whereas dotted lines represent apparent concentration gradients. The arrows indicate a region of a simulated flux density against the gradient of C. (A) Counter-gradient transport within the canopy; (B) Counter-gradient transport above the canopy

This new model is in a good form to accomplish our purpose since it is no more difficult to implement than existing two-layer resistance models. Just like traditional two-layer models, the vertical concentration profile consists of a reference concentration, a concentration value at the ground surface, and an averaged value of the concentration in the overstorey. The model gives a physically improved value of the average overstorey concentration when the non-local contribution to scalar transport is parameterized by the resistor r_n. The remaining, crucial step is to evaluate the value of r_n. For this we use the 'Localized Near-Field' (LNF) theory of Raupach (1989a). Details of this theory are given by Van den Hurk and McNaughton (1995). The next section gives a brief description of the

strategy to obtain r_n.

- **Parameterization of r_n using Raupach's 'Localized Near-Field' model of scalar transport in a plant canopy**

Raupach's LNF-theory gives an analytical description of a canopy concentration profile, $C(z)$. For reasons outlined by Van den Hurk and McNaughton (1995), Raupach distinguishes two contributions to $C(z)$: the near-field and far-field components. The far-field concentration profile obeys diffusion theory, and can thus be modelled by a multi-layer resistance model like that of Waggoner and Reifsnyder (1968). The origin of the near-field concentration, $C_n(z)$, is non-local: it is determined by the source strength in neighbouring layers. Therefore, $C_n(z)$ can *not* be represented in terms of a resistance model. The values of the resistors would have to depend on the source strength at neighbouring levels.

However, in a larger-scale application we will not require detailed information on the concentration profile within the canopy. Therefore, it will be sufficient to find a successful expression for a *representative average* value of the near-field concentration, $\overline{C}_n$. This average near-field concentration can be related to the scalar flux density originating from the canopy source F_h using a resistance formulation:

$$r_n \equiv \frac{\overline{C}_n}{F_h} \tag{3.3}$$

The *near-field resistance* r_n expresses the average concentration rise in a source layer per unit canopy flux due to near-field effects. To implement r_n in a common resistance model it is required that the scalar transport between the distinguished source layers is diffusive. In other words, the near-field contribution to the scalar concentration in any source layer must originate from that source layer only, and no overlap of near-field contributions from other source layers is allowed. We emphasize that for a two-layer resistance model such a representation is possible only when the whole overstorey is combined into a single layer, and the underlying ground source does not exhibit near-field transport effects. The resistance network then is outlined in Figure 3.1. In multi-layer resistance models the layers must be spaced wide enough to avoid overlap of near-field contributions. Raupach's original methods are appropriate for more complex models.

Two issues must be solved before $\overline{C}_n$ and thus r_n can be found. First, the definition of a 'representative average' $\overline{C}_n$ must be specified before it can be computed from the profile of $C_n(z)$. A weighing function is used for this purpose, and this is discussed hereafter. Second, prediction of the near-field concentration profile requires that we provide a description of the vertical distribution of canopy sources, $S(z)$, and turbulence within the canopy, characterized by the standard deviation of the vertical wind speed, $\sigma_w(z)$, and a Lagrangian time sclae, $T_l(z)$. Usually we will not have a detailed knowledge of these distributions. Therefore, we will investigate whether a standardized description of a typical canopy source distribution and turbulence profile can give a value for the average near-field concentration within the overstorey adequately representing all relevant canopies.

■ **Averaging the near-field concentration**

The average near-field concentration, $\bar{C}_n$, can be calculated in several ways, depending on what is required. Our problem here is to predict the total evaporative flux from the overstorey. This leads us to focus on obtaining the correct average of the saturation deficit D within the overstorey, since the evaporation rate from each leaf is driven by the saturation deficit of the canopy air at that level, D_0. At each level in the canopy the Penman-Monteith equation dictates that the 'effectiveness' of D_0 depends on the leaf area density divided by $(\Delta + \gamma)r_b + \gamma r_{st}$, where Δ is the change of saturated water vapour pressure with changing temperature, γ the psychrometer constant, and r_b and r_{st} represent leaf boundary layer and leaf stomatal resistance, equivalent to the resistors as given in Figure 3.1 (Monteith, 1973; McNaughton and Van den Hurk, 1995). For this reason it is more important that D_0 is accurate at levels with large leaf area density and small resistances. In forming an effective average of D_0 the values at each level should be weighted to reflect this. Unfortunately we cannot assume that profiles of leaf area density, stomatal resistance or leaf boundary-layer resistance are known, so we use the source distribution $S(z)$ itself to represent the weighing function. The source distribution is already needed to obtain $C_n(z)$ (see Van den Hurk and McNaughton, 1995), so this implies no new data requirement. We recall that eventually $S(z)$ is to be replaced by a standardized profile, and the uncertainty with respect to energy balance calculations of this strategy is discussed later.

The average near-field concentration over the depth of the overstorey, $\bar{C}_n$, can now be calculated as the weighted average of the profile of C_n:

$$\bar{C}_n = \frac{\int_0^\infty \phi(z)\, C_n(z)\, dz}{\int_0^\infty \phi(z)\, dz} = \int_0^h \phi(z)\, C_n(z)\, dz \qquad (3.4)$$

Here, $\phi(z)$ is a normalized source distribution function, defined as $S(z)/F_h$. $\phi(z)$ is zero below and above the canopy source range and integrates to unity over the source range height. r_n has dimensions of time/length, so multiplying it by the friction velocity u_* gives a non-dimensional transfer resistance similar in function to the inverse of the drag coefficient often used in momentum calculations. We will identify this quantity, $u_* \bar{C}_n/F_h$ ($\equiv u_* r_n$), by the symbol $\Re_n$ and report the results of all our calculations as values of $\Re_n$. This has the advantage that the reported results are independent of wind speed. To evaluate $\Re_n$ we must know the profiles of σ_w, T_l and ϕ. These profiles will be explored next.

■ **Sensitivity analysis**

(a) The profiles of $\sigma_w(z)$, $T_l(z)$ and $\phi(z)$

The near-field concentration profile $C_n(z)$, and thus its weighted value $\Re_n$ are determined by the profiles of the turbulence parameters, σ_w and T_l. Raupach (1988) argues that the empirical data available justify the formulations

$$\frac{\sigma_w(z)}{u_*} = \begin{cases} c_1 & z/h > 1 \\ c_0 + (c_1 - c_0)\, z/h & z/h \leq 1 \end{cases} \qquad \textbf{(3.5a)}$$

$$\frac{T_l(z)\, u_*}{h} = \max\left[c_2, \frac{\kappa\,(z-d)}{c_1^2\, h}\right] \qquad \textbf{(3.5b)}$$

where h is the canopy height, and d is the displacement height. h and u_* are considered as the governing scaling parameters and assumed known. The coefficients are quantified as $c_0 \approx 0.25$, $c_1 \approx 1.25$ and $c_2 \approx 0.30$. By eqs. 3.5 the eddy-diffusivity $K = \sigma_w^2\, T_l$ approaches the limit $\kappa\, u_*\, (z - d)$ predicted by Monin-Obukhov similarity theory well above the canopy (Raupach, 1988). These relationships are based on both wind tunnel and field observations, but none of them are from very sparse canopies where a significant fraction of the total momentum flux to the canopy is dissipated at the ground. The exact nature of the canopy turbulence is only partially covered by the simplified parameterization of σ_w. The significance of this uncertainty for the average near-field concentration will be examined below by performing calculations with various choices of the parameter c_0, the value of σ_w/u_* at the ground. The Lagrangian time scale T_l inside the canopy is assumed to be uniform with height. There is little reliable information on the variation of this quantity among different canopies so this assumption will not be explored here.

The remaining profile, $\phi(z)$, depends on both physiological and physical properties of the canopy, as explained above. A common procedure to estimate $\phi(z)$ is to assume that it is proportional to the product of net radiation and leaf area density at level z. However, since we cannot assume a detailed knowledge of any of these, our strategy is to explore a range of $\phi(z)$ functions, constructed so as to encompass the source distributions found in a wide range of canopies. To do this we utilize the Beta-distribution and the block-function. These functions are illustrated in Figure 3.3. The Beta-distribution (see eq. 8 in Appendix III) has earlier been used to represent profiles of leaf area density (e.g. Meyers and Paw U, 1986). It resembles the well-known Poisson-distribution but integrates to unity in the range $0 \leq z/h < 1$. Two parameters, p and q, determine the shape of the distribution. When $p > q$, the maximum value occurs where $z/h > 0.5$, so this represents a source which is concentrated in the upper part of the canopy. For dense, horizontally homogeneous vegetation stands, the source profile of water vapour and heat will tend to resemble the absorption profile of net radiation in the canopy. For crops having leaves over the entire canopy depth, like most agricultural crops, the source profile is therefore represented best by a Beta-distribution where $p > q$. Measured profiles of the daytime water vapour flux density in bulrush millet measured by Begg *et al.* (1964) were rather well fitted by a Beta-distribution with $p = 4$ and $q = 2$. Similar profiles in a maize stand described by Brown and Covey (1966) were well reproduced by using $p = 3$ and $q = 2$. Forest stands usually have leaves in a limited height range high in the canopy, and therefore generally show a source profile which is more concentrated near the canopy top. A Beta-distribution with $p = 6$ and

$q = 2$ gave a good simulation of the measured latent heat flux profile in the deciduous forest stand of Denmead and Bradley (1985), whereas a distribution with $p = 4$ and $q = 2$ provided a good fit to the latent heat flux profile measured by Droppo and Hamilton (1973) in a similar stand rather well. Some examples are shown in Figure 3.3a.

The block-function spreads the source uniformly over the upper n% of the canopy, as shown in Figure 3.3b. Corresponding block functions representing sources near the ground surface are not considered, because the definition of the canopy height h becomes questionable when the canopy source does not extend to the top. In all cases $\int_0^h \phi(z)\, dz$ equals 1, as required by our definition of ϕ.

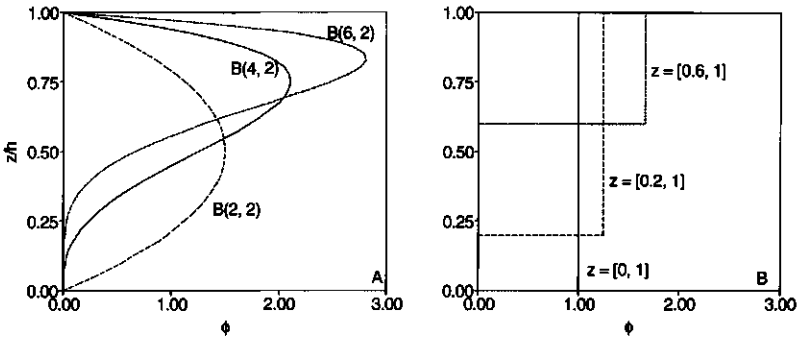

Figure 3.3: Examples of source profiles. (A) Beta distributions with (p, q) parameters as indicated; (B) block function with source concentrated in relative height ranges as indicated

(b) Sensitivity of the average near-field concentration to $\phi(z)$ and $\sigma_w(z)$

Values of $\Re_n$ have been computed using eq. 3.3 with a representative range of source and turbulence profiles. The source profiles, $\phi(z)$, were generated by selecting suitable values of the parameters p and q for the Beta-distribution or source thicknesses for the block function, as described above. The turbulence profiles were generated by selecting a suitable range of values of the parameter c_0 in eq. 3.5a. A value of 0.25 is cited by Raupach (1988) and others as a likely value for most canopies. Here the calculations are extended to 0.25 ± 0.25. $c_0 = 1.25$ is added to include the widest extreme, in which case no gradient of σ_w within the canopy is present. The parameters c_1 and c_2 were set to 1.25 and 0.3, respectively. Results from these calculations are listed in Table 3.1.

The calculated results show that $\Re_n$ is not very sensitive to the selected value of c_0, and hence $\sigma_w(z)$. The sensitivity to the form chosen for the source profile $\phi(z)$ is somewhat larger. The values of $\Re_n$ range from 0.26 to 0.46 for almost all plausible canopy representations, and from 0.32 to 0.40 for the most likely cases. Only where a very thin canopy layer is situated far from the ground (represented by the block function [0.8, 1]) does $\Re_n$ take a higher value.

This conservative behaviour of $\Re_n$ can be explained as follows. A source contributes to the near-field concentration mainly at levels quite near that source. About 80% of the total near-field effect is felt within the distance given by $\sigma_w T_l$, which is less than 37% of the height of the canopy at all levels in the canopy source range, according to eq. 3.5. Therefore, $\bar{C}_n$ will be largest when the source is highly concentrated and smallest when it is widely distributed.

Table 3.1: Values of $\Re_n = r_n u_*$ as function of various profiles of $\phi(z)$ and $\sigma_w(z)$. The profile of σ_w/u_* linearly increases from c_0 at $z = 0$ to $c_1 = 1.25$ at $z/h = 1$. The source profile $\phi(z)$ of type Beta-distribution is changed by adopting various values for the parameters p and q. z_{max} is the level where $\phi(z)$ is maximum (see Figure 3.3a). The source profile represented by the block function is changed by adjusting the lowest boundary of the source range, and keeping the highest boundary fixed at $z/h = 1$ (Figure 3.3b)

Source type: Beta-distribution					
parameters (p, q)	z_{max}/h	c_0=0.0	c_0=0.25	c_0=0.50	c_0=1.25
2, 4	0.25	0.43	0.42	0.41	0.38
2, 2	0.50	0.32	0.31	0.31	0.30
4, 2	0.75	0.36	0.36	0.35	0.33
6, 2	0.83	0.41	0.41	0.40	0.38
Source type: block function					
	range (z/h)				
	0.0 - 1.0	0.26	0.27	0.27	0.26
	0.2 - 1.0	0.31	0.30	0.30	0.28
	0.4 - 1.0	0.37	0.36	0.35	0.33
	0.6 - 1.0	0.46	0.45	0.44	0.42
	0.8 - 1.0	0.63	0.62	0.61	0.59

Thus the narrowest canopy source, described by the block distribution [0.8, 1] gives the largest resistance, and that described by the block distribution [0, 1] gives the lowest value. Along with this effect is the tendency of turbulence to spread the near-field concentration from a source beyond the bounds of the canopy, and so beyond the range of integration. This will tend to reduce $\Re_n$ for larger values of σ_w. We see very little effect of increasing c_0 (which increases σ_w at all levels within the canopy) for well-distributed sources such as the block distribution [0, 1], but a noticeable decrease in $\Re_n$ with increasing σ_w for more concentrated sources.

An average near-field concentration $\Re_n$ can be deduced from Table 3.1, concentrating on the likely values of p and q cited above. This results in a value of 0.36 ± 0.05 for most dense crops. Vegetation stands with a more open structure will distribute the net radiation more equally over the entire canopy depth, and the average near-field concentration will be somewhat lower in these cases.

Van den Hurk and McNaughton (1995) evaluated the effect of including $r_n = 0.36/u_*$ in the two-layer resistance model of Shuttleworth and Wallace (1985). They performed calculations representative for conditions of calm wind and clear sky, for various watering conditions, determined by the choice for the crop resistance and soil evaporation resistance. They concluded that for both dense crops ($LAI = 4$) and sparse crops ($LAI = 1$) including r_n makes very little difference to the energy balance of the canopy and the ground. The largest effect is present when all other resistances in the model (see Figure 3.1) are low.

■ Conclusions

It is possible to represent non-diffusive transport in canopies in a two-layer resistance model, such as that of Shuttleworth and Wallace (1985), by adding a 'near-field' resistor, r_n, in series with the bulk boundary-layer resistance in the upper layer of the model. Addition of this resistor has an improved prediction of the scalar concentration in the canopy source layer as a diagnostic, and allows the model to mimic the counter-gradient transport of scalars that is sometimes observed within real canopies. The procedure of adding a near-field resistor into the upper layer can only be applied when the near-field contributions from the separate source layers do not overlap.

The value of the normalized near-field resistor can be calculated using the analytical Lagrangian model of canopy transport developed by Raupach (1989a). The calculated values of $\Re_n = r_n u_*$ range from 0.26 to 0.63, with the likely value for most canopies described by 0.36 ± 0.05. The higher values in this range are for canopies where the leaf area is concentrated in a narrow range, while the lower values are for canopies with well-distributed leaf areas. The values of r_n are rather insensitive to how the turbulence (expressed in terms of σ_w) is described within the canopy, and moderately sensitive to the shape of the source profile.

Addition of this near-field resistance into the Shuttleworth and Wallace model has only a small effect on the predicted evaporation rate from both the canopy and the underlying soil, under calm wind and clear sky conditions. This is because r_n is less than one tenth the magnitude of either of the aerodynamic resistances included in the Shuttleworth and Wallace model. The overall minor influence on the surface evaporation justifies the crude estimation of r_n given above.

In this study the physiological response of leaves to the ambient water vapour deficit is not taken into account. The canopy resistance is explicitely specified and not made dependent on the canopy water vapour deficit. Since r_n affects the average concentration within the overstorey a possible extra effect via r_s^c might take place. Under conditions of strong canopy evaporation the effect of r_n will be to reduce the canopy water vapour deficit, thereby possibly also reducing r_s^c and counteracting the (slight) reduction of the canopy evaporation. The opposite takes place when sensible heat flux dominates the canopy evaporation. Further examination of a system where these feedback mechanisms are included requires a description of the response of r_s^c to changing canopy water vapour deficit, and is a possible item for future research.

Theoretically, r_n could also be evaluated using other sophisticated theories such as higher-order-closure. The improved prediction of within canopy concentration profiles compared to first-order closure (Meyers and Paw U, 1987) makes this excercise certainly worthwile. An experimental evaluation of r_n will encounter major difficulties in defining effective averages of the relevant resistances (including r_n) and in measuring the canopy source and turbulence profiles.

The small value of r_n is somewhat surprising, given the weight of the objections against using *K*-theory for the description of canopy transport processes. Simultaneously it gives also rise to questioning the need to implement near-field effects in larger scale models. The present study shows that for a correct prediction of energy fluxes from relatively complex surfaces much emphasis must be laid on a correct parameterization of the other

aerodynamic and physiological resistances. A theoretical discussion of r_a^a, r_a^s and r_a^c is presented in the next section.

3.2.3 A 'Lagrangian' revision of the resistors in the two-layer model for calculating the energy budget of a plant canopy[2]

In the previous sections (Van den Hurk and McNaughton, 1995) it was shown that Raupach's 'Linearized Near-Field' theory (Raupach, 1989a) can be used to construct a two-layer resistance model. This new model has the same structure as earlier two-layer models, except that a 'near-field resistor' is placed in series with the boundary-layer resistor. The other resistors of the two-layer model were not discussed. McNaughton and Van den Hurk (1995) completed this revision of the two-layer models by re-evaluating them, again basing calculations on the Lagrangian LNF-model of Raupach (1989a,b). Using Raupach's concepts they replaced the aerodynamic resistors of e.g. Shuttleworth and Wallace (1985) with 'far-field' resistors, and quantified them using Raupach's expression for the 'far-field' diffusivity (Raupach, 1988). The same was done with the boundary-layer resistance of the foliage in the overstorey canopy. The result is a completely-reformulated two-layer resistance model.

In the following sections the derivation of the newly defined far-field resistors is summarized. Calculated values of (normalized) far-field and boundary-layer resistances are compared with those of Shuttleworth and Wallace (1985) and Choudhury and Monteith (1988). McNaughton and Van den Hurk (1995) also compared the resistors from these two-layer models to experimental values found in the literature, expressed in terms of the 'excess' resistance. This experimental comparison is not repeated in this thesis.

- **The Far-Field resistors**

In the previous sections Van den Hurk and McNaughton defined a near-field resistor as the ratio of an effective average near-field concentration, $\overline{C}_n$, to the canopy flux (eq. 3.3). $\overline{C}_n$ is defined as the single value of C_n whose inclusion in the two-layer model would have the same effect on the energy fluxes as inclusion of the true profile, $C_n(z)$, has in the full model. This average concentration was found by integrating Raupach's profile equations and applying a weighing function (eq. 3.4). McNaughton and Van den Hurk (1995), referred to as MH95 hereafter, continued to use effective concentration values to define the remaining resistors in their model.

Because the far-field profile in Raupach's LNF theory is described by *K*-theory, vertical diffusion within and just above a canopy can be represented by a vertical chain of resistors. In a two-layer model only two layers are present, so this chain has only two resistors: an 'upper far-field resistor' and a 'lower far-field resistor', labelled r_a^a and r_a^s in Figure 3.1.

Their methods for evaluating the resistors from the *K*-profile differ from those used by Shuttleworth and Wallace (1985) and Choudhury and Monteith (1988). MH95 based their calculations on complete integrations over the far-field concentration profile, $C_f(z)$, without first reducing the source profile to a single source at a specified level. This avoids any *ad hoc* specification of 'the source level' and allows to discuss the effect that the shape of the source

---

[2] Adapted from McNaughton and Van den Hurk (1995)

profile has on the calculated resistances.

The Upper Far-Field Resistor

Referring to Figure 3.1, the upper far-field resistor, r_a^a, is defined by the equation

$$r_a^a = \frac{C_v - C_R}{F_t} \tag{3.6}$$

where the concentration at the reference level, C_R, and the total scalar flux upwards at the reference level, F_t, are observable quantities. C_v is the effective weighted average of the far-field concentration within the overstorey, given by

$$C_v = \int_0^1 \phi(\varsigma) C_f(\varsigma)\, d\varsigma \tag{3.7}$$

where C_f is the solution of the diffusion equation (see McNaughton and Van den Hurk, 1995), $\varsigma = z/h$, and $\phi(\varsigma)$ is the same weighing function as outlined above. This leads, with eq. 3.6 and a little manipulation, to an expression for the dimensionless upper far-field resistor:

$$u_* r_a^a = \int_0^1 \phi(\varsigma) \left[\int_\varsigma^{\varsigma_R} \left(1 - \frac{F_h}{F_t} \int_{\varsigma'}^1 \phi(\varsigma'')\, d\varsigma'' \right) \frac{hu_*}{K(\varsigma')}\, d\varsigma' \right] d\varsigma \tag{3.8}$$

The expression on the right can be expanded by splitting the innermost integral into integrals from ς to 1 and from 1 to ς_R. Some further manipulation then leads to the dimensionless equation

$$\begin{aligned} u_* r_a^a = {} & \int_1^{\varsigma_R} \frac{hu_*}{K(\varsigma)} d\varsigma + \int_0^1 \phi(\varsigma) \int_\varsigma^1 \frac{hu_*}{K(\varsigma')} d\varsigma' d\varsigma - \\ & - \frac{F_h}{F_t} \int_0^1 \phi(\varsigma) \int_\varsigma^1 \frac{hu_*}{K(\varsigma')} \int_{\varsigma'}^1 \phi(\varsigma'') d\varsigma'' d\varsigma' d\varsigma \end{aligned} \tag{3.9}$$

Eq. 3.9 has three terms on the right. The first, $\Re_I$ (where $\Re$ denotes a dimensionless resistance, equal to $r\, u_*$), represents the part of the far-field resistor above the top of the canopy. The second, $\Re_{II}$, represents the far-field resistance up to canopy top calculated as if the whole canopy source were located at the bottom of the canopy, but with the effectiveness weighing distributed through the canopy. The third term, $(F_h/F_t)\Re_{III}$, is a correction for the true distribution of sources. The ratio F_h/F_t lies in the range 0 – 1. This third term will be different for each canopy so its presence signals the impossibility of constructing a perfect two-layer model with resistors independent of the source distribution.

Table 3.2 lists values of $\Re_I$, $\Re_{II}$ and $\Re_{III}$ for various profile shapes of σ_w (modified by ranging c_0 in eq. 3.5) and ϕ (parameterized as a Beta-function, as before). ς_R is set at 2

Table 3.2: Components of the dimensionless far-field resistor calculated for three values of c_0 and a range of assumed source distributions, $\phi(\zeta)$, described by Beta-probability distributions with the p and q values shown (see also Figure 3.3a). $\Re_I$, $\Re_{II}$ and $\Re_{III}$ are the three integrals in the respective terms on the right of eq. 3.9. $\Re_I$ is computed by using $\zeta_R = 2$ and $d/h = 0.66$. The upper far-field resistor, $\Re_a^a$, is calculated assuming $F_h/F_t = 0.5$, so that $\Re_a^a = \Re_I + \Re_{II} - 0.5\ \Re_{III}$. $\Re_{IV}$ is the dimensionless resistor defined by eq. 3.12 and 3.15, and $\Re_a^s$ is the dimensionless lower far-field resistor, also for $F_h/F_t = 0.5$, so that $\Re_a^s = \Re_{IV} - \Re_{II} + 1\ \Re_{III}$

c_0	p	q	$\Re_I$	$\Re_{II}$	$\Re_{III}$	$\Re_a^a$	$\Re_{IV}$	$\Re_a^s$
0.15	1.25	2	2.1	4.3	1.9	5.5	17.8	15.4
	1	1	2.1	3.4	1.9	4.6	17.8	16.3
	2	2	2.1	2.7	1.2	4.2	17.8	16.4
	3	2	2.1	1.7	0.8	3.4	17.8	16.9
	6	2	2.1	0.8	0.3	2.8	17.8	17.3
0.25	1.25	2	2.1	3.4	1.4	4.9	10.7	8.6
	1	1	2.1	2.7	1.4	4.1	10.7	9.4
	2	2	2.1	2.3	0.9	3.9	10.7	9.3
	3	2	2.1	1.5	0.6	3.3	10.7	9.8
	6	2	2.1	0.7	0.3	2.7	10.7	10.2
0.35	1.25	2	2.1	2.9	1.0	4.5	7.6	5.8
	1	1	2.1	2.3	1.1	3.9	7.6	6.4
	2	2	2.1	2.0	0.8	3.8	7.6	6.4
	3	2	2.1	1.4	0.6	3.3	7.6	6.8
	6	2	2.1	0.7	0.3	2.7	7.6	7.1

(above this level the scalar profile should be well described by the usual Monin-Obukhov similarity forms, so resistance from that level up to any other level can be calculated in the conventional way), and $d/h = 0.66$ is assumed.

The above-canopy part of the far-field resistance, $\Re_I$, is the same for all cases, but the resistances within the canopy are somewhat sensitive to the shape of the σ_w profile, as specified by c_0, and very sensitive to the assumed source distribution. The values of $\Re_{II}$ and $\Re_{III}$ for a source concentrated near the top of the canopy are only about one fifth of those for a source concentrated near the bottom. The values of $\Re_a^a$ can be roughly estimated by rewriting eq. 3.9 as

$$\Re_a^a = \Re_I + \Re_{II} - \frac{F_h}{F_T}\Re_{III} \tag{3.10}$$

and setting F_h/F_t to a mid value of 0.5. These values are also shown. An $\Re_a^a$-value of 3.6 ± 1.0 is appropriate for most canopies. This gives the dimensioned value of the upper far-field resistor as $r_a^a = 3.6/u_*$, where the value of u_* is assumed known.

The Lower Far-Field Resistor

As with the upper far-field resistor, the lower far-field resistor was defined as to

preserve correctly a particular quantity: in this case the concentration at the ground, C_s. Referring to Figure 3.1, the lower far-field resistor, r_a^s, is defined by the equation

$$r_a^s = \frac{C_s - C_v}{F_s} \tag{3.11}$$

where C_s is found by integrating down the concentration gradient, $C_f(z)$, from the reference height right down to the ground. Substituting for C_v using eq. 3.7 leads to the dimensionless equation

$$\Re_a^s = \frac{u_*(C_s - C_R)}{F_s} - \frac{\Re_a^a F_t}{F_s} \tag{3.12}$$

where $(C_s - C_R)$ is found by extrapolating the far-field concentration profile down to the ground at $\varsigma = 0$, so that

$$\frac{u_*(C_s - C_R)}{F_s} = \int_0^{\varsigma_R} \frac{u_* h}{K(\varsigma)} d\varsigma + \frac{F_h}{F_s} \int_0^{\varsigma_R} \frac{u_* h}{K(\varsigma)} \int_0^{\varsigma} \phi(\varsigma') d\varsigma' d\varsigma \tag{3.13}$$

The first integral here may be split into integrals from 0 to 1 and from 1 to ς_R. The integral from 0 to 1 we designate $\Re_{IV}$ while that from 1 to ς_R is already designated $\Re_I$. The second integral term in eq. 3.13 is just $F_h/F_s(\Re_I + \Re_{II})$. With these substitutions eq. 3.13 becomes

$$\frac{u_*(C_s - C_R)}{F_s} = \left(1 + \frac{F_h}{F_s}\right)\Re_I + \frac{F_h}{F_s}\Re_{II} + \Re_{IV} \tag{3.14}$$

Substitution of eq. 3.10 into 3.14 leads to

$$\Re_a^s = \Re_{IV} - \Re_{II} + \frac{F_h}{F_s}\Re_{III} \tag{3.15}$$

Calculated values of $\Re_{IV}$ are shown in Table 3.2, using $F_h/F_s = 1$ as before.

Table 3.2 shows that, for a given value of c_0, $\Re_a^s$ varies less than about 20% over the full range of assumed overstorey source distributions when $F_h/F_s = 1.0$. On the other hand, the table shows that $\Re_a^s$ varies by a factor of 2.5 as c_0 ranges from 0.15 to 0.35. Even this range of c_0 may not express the true uncertainty because the profile equation 3.5 becomes unreliable as the ground is approached. This is just where the diffusivity is smallest and makes the largest contribution to $\Re_a^s$, so the value $\Re_a^s$ is, in fact, highly uncertain. Similar uncertainty exists in other two-layer models for the same reason.

From Table 3.2 we choose $\Re_a^s = 10$ as a representative value, so that $r_a^s = 10/u_*$.

The Boundary-Layer Resistance

MH95 defined the dimensionless boundary layer resistance, $\Re_b$, to be the one that satisfies the relationship

$$\Re_b = \frac{u_*(C_b - C_c)}{F_h} \tag{3.16}$$

Here, C_c is the canopy airstream concentration (Figure 3.1), and $(C_b - C_c)$ is the effective increment of concentration given by an equation similar to eq. 3.4. The concentration difference across the boundary-layer resistances at each level in the canopy is given by

$$C_b(\varsigma) - C_c(\varsigma) = \frac{r_b(\varsigma) S_h \phi(\varsigma)}{LAD(\varsigma)} \tag{3.17}$$

where S_h is the total canopy source strength. This leads to

$$\Re_b = u_* \int_0^1 r_b(\varsigma) \frac{\varphi(\varsigma)\phi(\varsigma)}{LAD(\varsigma)} d\varsigma \approx \frac{u_*}{LAI} \int_0^1 r_b(\varsigma)\phi(\varsigma)\, d\varsigma \tag{3.18}$$

where an effectiveness weighing, $\varphi(\varsigma)$, was eliminated by (crudely) assuming that its profile resembles the profile of $LAD(\varsigma)$.

The leaf boundary-layer resistance, $r_b(\varsigma)$, depends on leaf dimension, l_w, wind speed, $u(\varsigma)$ and other factors such as leaf shape and degree of mutual sheltering of the foliage and the intensity and scale of turbulence. If we model the leaf as a flat plate parallel to the flow, then heat transfer from both sides is given by (Appendix III)

$$r_b = 150 \beta_s \sqrt{\frac{l_w}{u}} \tag{3.19}$$

where the sheltering factor β_s was assumed to be 1. The wind speed, u, was expressed using an exponential decay function with attenuation coefficient α_u (Cionco, 1972, 1978; Pereira and Shaw, 1980). Furthermore, MH95 assumed that, in cases where the canopy is dense enough that very little momentum is transferred to the ground, the ratio $u_h/u_* \approx 3.2$ (Raupach, 1992). This leads to an expression for the dimensionless boundary-layer resistance of the overstorey canopy, written as

$$\Re_b = 84 \frac{\sqrt{l_w u_*}}{LAI} \int_0^1 \exp\left(\frac{\alpha_u}{2}(1 - \varsigma)\right) \phi(\varsigma)\, d\varsigma \tag{3.20}$$

from which $\Re_b LAI/\sqrt{l_w u_*}$ can be evaluated directly using an appropriate range of α_u-values to represent a range of wind profiles, and the Beta function to represent a range of source profiles. The results of the calculations are shown in Table 3.3.

In Table 3.3 the small values of α_u represent sparser canopies, where we might expect good radiation penetration and the flux sources to be spread more evenly or concentrated low in the canopy. Larger values of α_u, on the other hand, represent denser canopies, where flux sources would often be concentrated higher in the canopy (Cionco, 1978; Pereira and Shaw, 1980). The p and q parameter values in Table 3.3 reflect, from left to right, a similar trend towards higher sources. The most representative values from Table 3.3

Table 3.3: Values of $\Re_b LAI/\sqrt{l_w u_*}$, in $s^{1/2}m^{-1}$, calculated using eq. 3.20 for various values of the attenuation coefficient for the canopy wind profile, α_u, and the source distribution function $\phi(\zeta)$ represented by the Beta-function with values of the parameters p and q as shown. The α_u-values 1, 2, 3 and 4 correspond to leaf area indices of about 0.6, 2, 4 and 9, respectively, depending on canopy structure, according to calculations by Pereira and Shaw (1980)

wind profile	$p = 1.25$ $q = 2$	$p = 1$ $q = 1$	$p = 2$ $q = 2$	$p = 3$ $q = 2$	$p = 6$ $q = 2$
$\alpha_u = 1$	115	109	109	103	95
$\alpha_u = 2$	160	144	142	128	109
$\alpha_u = 3$	224	195	188	160	125
$\alpha_u = 4$	319	268	252	203	145

should therefore lie about the diagonal through the table from upper left to lower right. Wind profiles in most crops are described by α_u values between 1.3 and 2.8; higher values of α_u are observed in many forests. A representative value of $\Re_b LAI/\sqrt{l_w u_*}$ from Table 3.3 is about 130 $s^{1/2}m^{-1}$ with most canopies probably within ± 30 $s^{1/2}m^{-1}$ of this figure. Unlike $\Re_a^a$, $\Re_a^s$ and $\Re_n$, which take fixed values, $\Re_b$ depends on the momentum flux to the canopy and on the canopy leaf area index and leaf dimension. Values of $\Re_b$ can vary over two orders of magnitude, depending on the values of these parameters, so some direct information about the canopy is needed. An estimated dimensional value of the bulk boundary-layer resistance, r_a^c, is therefore $\Re_b/u_* \approx 130/LAI\sqrt{l_w/u_*}$.

■ **Comparisons with resistors of other two-layer models**

MH95 compared the values of the resistors in their re-evaluated two-layer canopy model with formulations presented by Shuttleworth and Wallace (1985; SW85) and Choudhury and Monteith (1988, CM88). The CM88 model differs from the original SW85 model in two principal ways: a better treatment of leaf boundary-layer resistances, and modifications which allow a continuous transition from canopies with dense overstoreys to canopies without overstoreys. The model of MH95 was not intended for use with very sparse overstoreys, so the comparison was restricted to canopies with overstoreys that are dense enough that very little momentum reaches the ground.

Table 3.4: Intercomparison of dimensionless resistances; $\Re_n$ is the near-field resistance, $\Re_a^a$ the upper far-field (or aerodynamic) resistance, $\Re_a^s$ the lower far-field (or within canopy aerodynamic) resistance, and $\Re_b$ the leaf boundary-layer resistance

quantity	SW85	CM88	MH95
$\Re_n$	0	0	0.30 - 0.42
$\Re_a^a$	5.5	5.4 - 6.7	2.6 - 4.6
$\Re_a^s$	28	15 - 60	6 - 17
$\Re_b LAI/\sqrt{(l_w u_*)}$	-	75 - 97	100 - 160

Table 3.4 gives a summary of the dimensionless resistors. In each case the reference height is set at $2h$, and stability corrections are ignored.

Both SW85 and CM88 calculate $\mathfrak{R}_a^a$ and $\mathfrak{R}_a^s$ by integrating the inverse of a diffusivity function, equal to $K(\varsigma)/u_*h = \kappa(\varsigma - d/h)$ above the canopy, and $K(1)\exp\{n(\varsigma - 1)\}$ below $\varsigma = 1$. n is an eddy-diffusivity extinction coefficient, set to 2. $\mathfrak{R}_a^a$ is found from an integration from a source level at height $(z_{0m} + d)$ up to the reference height. $\mathfrak{R}_a^s$ is integrated between the source height to a level near the ground, z_0'. The value of z_0' has almost no effect on the calculation. The principal difference between the models is how z_0 and d are calculated. SW85 assumes $z_{0m}/h = 0.13$ and $d/h = 0.63$, which values are typical of agricultural crops. CM88 lets z_{0m} and d depend on the leaf area index of the overstorey. For canopy drag coefficients ranging from 0.05 to 1.5 they calculate values of d/h ranging from 0.43 to 0.82, and values of z_{0m}/h from 0.13 to 0.06 (section 4.1.5).

The ranges for $\mathfrak{R}_a^a$ do not overlap for CM88 and MH95. The range in each derives from variation in the location of the canopy source, but by quite different mechanisms. In CM88, $\mathfrak{R}_a^a$ depends on the height of the momentum source, $(z_{0m} + d)$, which varies in a fixed way with *LAI*. In MH95, it depends on how the source is distributed, which is only partly related to leaf area index. The CM88 model gives values at the lower end of the range in intermediate canopies, with a drag coefficient of 0.2, while the MH95 values tend to be smaller in denser canopies.

Also for $\mathfrak{R}_a^s$ the MH95 model has smaller resistance values, but this time the ranges overlap slightly. The spread of values in MH95 derives mainly from uncertainty in the diffusivity profile, while the spread in the CM88 values derives mainly from changes in source height with changing canopy density. The lack of a common cause for the spread of values predicted by each model is particularly disturbing, since each — for its own distinct reasons — has $\mathfrak{R}_a^s$ varying over a threefold range. Overall, the predicted values range from 6 to 60. This gives some indication of the uncertainty.

The boundary-layer resistance can't be described by simple representative values of $\mathfrak{R}_b$ because it varies widely with leaf area index, leaf dimension and wind speed. The values for each model are best described by formulae (Table 3.4). The SW85 model was designed for a particular crop so its form was not intended to be general. Again the ranges calculated using the CM88 and MH95 models do not overlap, though this time the difference is principally through the choice of the β_s value in eq. 3.19. The range of values from the MH95 scheme would be 67 - 110 if they were calculated using $\beta_s = 2/3$, as in CM88. The remaining difference originates from use of different averaging schemes and different exponents for the canopy wind profile. The ranges of $\mathfrak{R}_b$ do not reflect the full uncertainties. The range of values from CM88 is increased to 64 - 116 by varying the extinction coefficient for the wind profile from 1.5 to 3.5. The ranges of $\mathfrak{R}_b$ are increased substantially in both CM88 and MH95 models if the uncertainty in β_s is included.

- **Discussion**

Also in comparison to the resistances in the MH95 model, the near-field resistor introduced in section 3.2.2 is usually insignificant, and far-field theory is adequate for building two-layer models, provided the far-field *K*-profile is known correctly. Here Raupach's suggested form for the far-field diffusivity profile was used, which is larger than those used by SW85 and CM88, implying that the calculated far-field resistors are smaller. An interesting question is how much difference this makes to calculated energy balances. In

chapter 6 the impact of this difference is investigated using the coupled surface layer-PBL models. Referring to the calculation of surface evaporation, McNaughton and Van den Hurk (1995) state that the differences are important only when the evaporation rate is large compared to available energy, the saturation deficit at reference height is high, and the surface resistance of the canopy or underlying ground low. Also Dolman and Wallace (1991) calculated very similar total evaporation rates from millet growing in Niger, using a complete Lagrangian model, the Shuttleworth and Gurney (1990) two-layer model (nearly similar to CM88), and the Penman-Monteith single-layer model. Saturation deficits and evaporation rates are not notably high in that data set.

Another matter to comment on is the fact that MH95 have broken with the methods introduced by SW85 and followed by CM88 and Shuttleworth and Gurney (1990) in that no overstorey source is located at a fixed height. The idea that there is any necessary connection between the distribution of scalar sources within the canopy and the parameters of the wind profile were rejected. Instead, they integrated the diffusion equation directly for a distributed scalar source, following the kind of methods pioneered by Cowan (1968).

Their results still rely on the quality of the far-field diffusivity profile used (eqs 3.5a and 3.5b). Unfortunately, none of the field data of σ_w/u_* which Raupach (1988) used to construct these profiles extend down to the ground, and the two profiles from wind tunnels that do so have a threefold range near the floor of the tunnel. Therefore profiles of σ_w are poorly known near the ground. The T_l profiles are even more uncertain. The diffusivity profile is therefore unreliable near the ground, and the value of $\Re_a^s$ calculated from it has great uncertainty.

Of particular concern is that we don't know how to describe K-profiles near mixed under-storey of bare soil and grass. This is disturbing because field results show that temperature differences between bare soil and grass can be very large (e.g. Garratt, 1978). Therefore we don't know how to construct a plausible model for transport from an understorey, nor how to describe the excess resistance for sparse canopies. This is a serious matter because excess resistance is needed to calculate heat fluxes from surface temperature measurements made from aircraft or satellites (Bastiaanssen, 1995). The turbulence profiles used here summarize profiles measured in canopies where little momentum reaches the ground. That is, we expect that they apply only to rather dense canopies, for which the profile area density exceeds 0.1 (Raupach, 1992). Fortunately, many 'sparse' canopies are dense enough to satisfy this condition. It is difficult to build a model for very sparse canopies with profile area densities < 0.1 because theory is currently inadequate and there are no suitable experimental data for guidance. The two-layer model developed by Shuttleworth and Gurney (1990) does 'extend' to very sparse canopies, but it does so simply by interpolation between canopies with 'dense' overstorey, as modelled by CM88, and ones where the overstorey vanishes.

3.3 The albedo of a sparse vineyard canopy during the growing season

Studies considering the energy balance of the Earth's surface involve the quantification of the radiative energy supply, referred to as net radiation. This net radiation consists of both longwave and shortwave terms. The latter contribution (0.3 - 3 μm) is to a

large extent determined by the reflecting properties of the surface, usually denoted as the shortwave albedo or reflectance. Both the seasonal variation and the diurnal change of the surface albedo can be of importance for describing the exchange of heat and water vapour between the surface and the atmosphere. The seasonal variation is essential for climatological studies and crop growth simulation models, whereas the diurnal variation is important for short term weather forecasting and simulation of boundary layer development. The shortwave albedo of a sparse canopy during part of its growing season is the subject of the following sections.

Among the surface characteristics playing a major role for the shortwave albedo, an important one is the fraction of plant cover, with a closed canopy or a completely bare soil as the possible limits. The geometry of a closed canopy and the spectral properties of its components can give rise to surface albedo values ranging between 0.10 and 0.25. Surface roughness and content of moisture, organic materials and iron compounds in the upper soil layer are important parameters for the albedo of bare soil, which can vary between 0.05 and 0.40 (Dickinson, 1983). A large part of the global surface is covered with sparse canopy. This surface type is heterogeneous on a scale comparable to the individual vegetation elements, but may well be considered homogeneous on a larger catchment scale. Due to the complicated geometry and contribution both from bare soil and vegetation components, the albedo of a sparsely vegetated surface depends on a large set of effects of the various relevant surface properties.

The processes related to the surface albedo of the sparse vineyard canopy endeavoured during the EFEDA-I campaign (section 2.2.3) is the subject of the following. Albedo measurements were carried out in a period of rapid plant growth; the fraction of vegetation cover increased from 0.05 (primarily bare soil) to 0.15 within a period of 25 days (section 2.2.6). The diurnal and seasonal variation of the measured surface albedo are explained from available theory and models. Also, the horizontal inhomogeneity of the surface albedo on a scale of 200 × 200 m is discussed. For this purpose, remotely sensed data are used.

3.3.1 Processes determining the albedo of a sparse vineyard canopy

- **The surface albedo**

The shortwave hemispherical reflectance of a surface, or (surface) albedo, is defined as the upward reflected part of shortwave (0.3 - 3 μm) radiation reaching a horizontal plane on the surface. An incoming light beam I of wave length λ from any azimuth direction ϕ_0 and zenith angle ζ_0 may partially be reflected upward in directions ϕ and $\mu = \cos \zeta$. The total albedo a is then obtained by considering the amount of reflected radiation from all beams integrated over the hemisphere:

$$a = \int_{\lambda=0.3}^{3} \int_{\mu_0=0}^{1} \int_{\phi_0=0}^{2\pi} \int_{\mu=0}^{1} \int_{\phi=0}^{2\pi} \mu\, r(\phi,\mu,\lambda \mid \phi_0,\mu_0)\, I(\phi_0,\mu_0,\lambda)\, d\phi\, d\mu\, d\phi_0\, d\mu_0\, d\lambda \qquad (3.21)$$

where $r(\phi, \mu, \lambda|\phi_0, \mu_0)$ is the reflection coefficient of $I(\phi_0, \mu_0, \lambda)$ into direction (ϕ, μ).

■ **Shortwave reflectance of bare soil**

Generally, soil reflectance increases as the wavelength increases from 0.3 to 3 μm (Coulson and Reynolds, 1971). The amount of highly absorbing organic and iron compounds in the soil have a pronounced effect on the reflectance in the visible range of the spectrum. Beside this, other factors such as soil moisture content, zenith angle and the structure of the top layer affect the albedo of a soil.

Dickinson (1983) discusses a model to describe the albedo of a flat soil, a_s, constisting of large distinctive particles. The model is based on a "delta-Eddington" approximation and was used by Wiscombe and Warren (1980) to obtain the albedo of snow. Information is needed about the reflectance of individual particles and the average angle of reflection. The results show a clear dependence of soil albedo on zenith angle ζ. Generally more light is reflected when the zenith angle is large, especially for flat dry surfaces. The zenith angle response reduces considerably when the fraction of diffuse radiation, f_d, is significant, and thus depends on cloud cover and atmospheric turbidity. A simpler approach was followed by Menenti *et al.* (1989), who used a semi-empirical relationship to describe the variation of the bare soil albedo a_s with ζ:

$$a_s(\zeta) = a_0\left[g(\Delta_l)\right]^{\sin\zeta} \tag{3.22}$$

In this equation, a_0 is the albedo when the sun stands in zenith, Δ_l is the optical depth of the atmosphere in the direction of the solar beam, and $g(\Delta_l)$ is a surface dependent function, assumed to be a linear function of Δ_l:

$$g(\Delta_l) = g_0 + c_g \Delta_l \tag{3.23}$$

where g_0 and c_g are regression coefficients, to be obtained from field measurements. The optical depth is defined by (Slater, 1980)

$$\Delta_l = -\ln\left(\frac{K^{\downarrow}}{K_e^{\downarrow}}\right) \tag{3.24}$$

where $K^{\downarrow}$ is the downward shortwave radiation at the surface level and the subscript e refers to the extraterrestrial solar radiation. $K^{\downarrow}/K_e^{\downarrow}$ is known as the transmission factor, the relative amount of absorbed and reflected solar radiation by the atmosphere. Eq. 3.22 ensures that $a_s \rightarrow a_0$ for $\zeta \rightarrow 0$. a_0 is surface specific and depends on values of humus and iron content and moisture content in the top soil layer. In this simple approximation, the effect of increase of the fraction of diffuse radiation, f_d, with increasing ζ is implicitly included. The effect of a change of f_d due to cloud formation or changing atmospheric transmission is not parameterized.

The moisture content of the upper soil layer is known to have a pronounced effect on the bare soil albedo (Graser and van Bavel, 1982; Idso *et al.*, 1975). Wet soils reflect shortwave radiation less than dry soils, and this difference can be as large as a factor five. Graser and van Bavel (1982) found that the albedo of three different types of soil changed within a very small range of water potential, but remained constant when soil humidity was

outside this range. They conclude that the original Angström-theory, explaining the reduction of reflectivity by trapping of radiation in the soil water films caused by a total internal reflection, is consistent with the abrupt change of the albedo as soil moisture changes. The soil moisture content of the top layer of the soil often shows a clear diurnal cycle. Water vapour transported upward over temperature gradients and by capillary rise is not removed by evaporation during the night. When the upper soil layer is dry, capillary rise will be limited, but temperature gradients near the soil surface can be extremely large, particularly when no vegetation is present. This effect combined with the process of dewfall often results in a moisture content of the top soil layer which is higher in the morning than at later times. In this case, the observed soil albedo shows an asymmetric response with respect to solar time, being lower in the morning. The difference between morning and afternoon albedo can be larger than 1.5%, as was for instance observed by Menenti *et al.* (1989) above deserts. They applied an empirical correction for the lower albedo in the morning (time $t < 12{:}00$ solar time), using a reduction factor m_d obtained from field measurements. m_d was expressed as linear function of sin ζ with coefficients m_{d0} and c_m:

$$m_d = \begin{cases} m_{d0} - c_m \sin\zeta & t < 12{:}00 \\ 1 & t \geq 12{:}00 \end{cases} \qquad (3.25)$$

Surface elevation differences can result in a variation of the soil moisture at many scales. This effect, and the variability of the contents of iron and organic compounds, can cause a strong horizontal variability of the soil albedo at scales ranging from a few cm to hundreds of meters.

Wetting or roughening the soil decreases both the albedo and the sensitivity to solar elevation. A near normal incident radiation can penetrate deeper into a coarse surface, and becomes trapped by multiple reflections in the soil cavities. The laboratory studies reviewed by Myers and Allen (1968) conclude that an increase of the soil particle diameter or aggregation of particles into clumps reduces the reflectance of the soil, but that these differences are usually overshadowed by the effect of differences in soil moisture and humus content.

- **Shortwave reflectance of plant canopies**

The reflectance properties of plant canopies have been studied by many authors. Dickinson (1983) gives a good review of most of the recognized factors affecting the albedo of plant canopies.

Obviously, the reflectance and transmittance of individual leaves plays an important role. These properties are a function of the wave length of the light. For simple purposes, leaf reflectance ρ_l and transmittance τ_l are quantified as $\rho_l = \tau_l = 0.15$ for visible light (0.3 - 0.7 μm) and 0.4 for near infra-red (0.7 - 3 μm) (Goudriaan, 1977). The leaf angle distribution plays a role in the zenith angle response of canopy reflectance. If all leafs are in a horizontal position, the reflection is independent of ζ. A canopy with e.g. spherically distributed leaves reflects more radiation from lower angles of incidence. Closed canopies with multiple leaf layers also tend to trap part of the reflected radiation, in particular at overhead sun. For low

solar altitude this trapping is much less pronounced, and the canopy reflectance can increase to 3 times its value around noon (Sellers, 1985; Goudriaan, 1977). On the other hand, radiation above spruce forests with widely spaced spire-shaped crowns penetrates deeper at large zenith angles (Dickinson, 1983). Finally, the degree of vegetation cover determines the influence of the underlying soil upon the canopy reflectance.

A model for the albedo of a closed plant canopy plus its underlying ground, a_c, was developed by Goudriaan (1977) and also applied by Jacobs and van Pul (1990). Goudriaan (1977) computed a_c by regarding the decrease of the radiation with canopy depth as an exponential function. For the albedo of a canopy with horizontal leaves, a_{hor}, this resulted in

$$a_{hor} = \frac{a_\infty(1 - a_\infty a_{soil}) - (a_\infty - a_{soil})\exp(-2\,k_r\,LAI)}{1 - a_\infty a_{soil} - a_\infty(a_\infty - a_{soil})\exp(-2\,k_r\,LAI)} \qquad (3.26)$$

a_∞ is the albedo of the canopy when $LAI \rightarrow \infty$, a_{soil} the reflectance of the underlying soil and k_r a semi-empirical extinction coefficient. Under the assumption that the reflectance of an individual leaf, ρ_l, equals its transmissivity τ_l and by definition of a scatter coefficient $\sigma_l = \rho_l + \tau_l$, a_∞ is parameterized by

$$a_\infty = \frac{\sigma_l}{2(1 + k_r) - \sigma_l} \qquad (3.27)$$

and $k_r = (1 - \sigma_l)^{0.5}$. The scatter coefficient for visible light, $\sigma_{l,vis}$, is approximately 0.3, whereas the value of 0.8 is adopted for the near-infra red value, $\sigma_{l,nir}$. Also the reflectance of the underlying soil, a_{soil}, must be specified for these bands separately.

The shortwave reflectance of a canopy with horizontal leaves does not depend on zenith angle, as can be seen from eqs. 3.26 and 3.27. By contrast, for spherically distributed leaf angles the canopy albedo, a_{sph}, depends on ζ. Goudriaan (1977) gives a simple expression for a_{sph}, reading

$$a_{sph}(\zeta) = a_{hor}\frac{2}{1 + 1.6\cos\zeta} \qquad (3.28)$$

The contribution of diffuse radiation to the albedo of a closed canopy can be simulated using a weighted average of 3 direct beams with zenith angles 15°, 45° and 75°. The weighing reflects the ratio of the projected areas of three band circles of a hemisphere centred at these angles (Goudriaan, 1988). This yields

$$a_{sph}(dif) = 0.25\,a_{sph}(15^o) + 0.50\,a_{sph}(45^o) + 0.25\,a_{sph}(75^o) \qquad (3.29)$$

Assuming that the incoming shortwave radiation is roughly equally divided over the visible and near-infra red bands, the albedo of a canopy is obtained by averaging the albedos of the two bands $a_{sph,vis}$ and $a_{sph,nir}$. Accounting for the fraction of diffuse radiation, a_c is finally expressed as

$$a_c = f_d\left(\frac{a_{sph,vis}(dif) + a_{sph,nir}(dif)}{2}\right) + (1 - f_d)\left(\frac{a_{sph,vis}(\zeta) + a_{sph,nir}(\zeta)}{2}\right) \qquad (3.30)$$

The reflectance of a closed canopy is generally lower than the reflectance of bare soil. Trapping of radiation and strong absorption in the visible range cause this difference.

■ **The shortwave reflectance of a sparse canopy**

By definition, a sparse canopy consists of both vegetation and a considerable part of uncovered soil. Thus, the albedo of such a surface will depend on the soil moisture, texture and iron content, on the geometry of the plant elements, the leaf density and leaf angle distribution, on the position of the sun and the fraction of diffuse light. However, a few special effects occur above sparse canopies with widely spaced plants.

First, a solar beam with a low angle of incidence will penetrate horizontally deep into widely spaced canopy elements. However, a significant part will be reflected near the top of the plants, where the angle of the beam to the normal of the canopy surface is large. This effect makes the exact position of an albedo sensor far from trivial. Only far above the canopy top the measured quantity can be regarded representative for the surface. Moreover, the reflectance measured straight above a vine plant will depend more importantly on the reflectance of the surrounding soil when the zenith angle is large. This makes interpretation of albedo measurements of individual plant elements difficult.

Second, the shading of the soil by the plants will cause a reduction of the amount of radiation reflected by the soil, especially in the visible range of the spectrum where the plant elements absorb most radiation. This reduces the soil albedo, particularly at large zenith angles and with dense plant elements, when much radiation is intercepted by the plants. This shading effect will reduce the zenith angle response of the soil albedo.

Third, the large amount of radiation that penetrates into canopy elements at low solar incidence obviously is associated with a reduction of the reflectance. The zenith angle response of the albedo of a sparsely vegetated surface is therefore expected to be much less pronounced than for a closed vegetation stand.

These effects formally imply that the albedo of a sparse canopy surface cannot simply be expressed as a weighted average of the albedos of bare ground and of the vegetation. The effects of vegetation on the albedo of bare soil will have to be incorporated in parameterizations of a_s, and the influence of the presence of bare soil on the vegetation albedo must be expressed in the equations for a_c. Only when these requirements are satisfied, the average surface albedo can be estimated using a weighing over the fraction of surface covered with vegetation, σ_f, according to

$$a = \sigma_f a_c + (1 - \sigma_f) a_s \qquad (3.31)$$

3.3.2 Albedo measurements taken in a sparse vineyard canopy

In this section the theoretical considerations listed above are evaluated using albedo measurements conducted over a sparse vineyard area. Attention is paid to the issue of horizontal variability, seasonal change and diurnal variation of the surface albedo. The site

description and instrumental layout can be found in section 2.2. A brief summary of used instrumentation is given first.

■ **Instrumentation**

All shortwave radiation sensors were located in a single vineyard with distances of 10 to 100 m in between. Measurements were carried out well above the surface, above parcels of bare soil, and above individual plants. Soil moisture measurements were taken every 3 - 5 days using TDR at depths 0 - 50 cm with 10 cm intervals. Table 3.5 lists the set-up of these sensors.

Table 3.5: Acronyms of sensors measuring reflected shortwave radiation and soil moisture (TDR). The mast indication refers to the layout figure in section 2.2 (Figure 2.2; Table 2.1). WSC = Winand Staring Centre, WAUMET = Wageningen Agricultural University, Dept. of Meteorology, WAUHBH = Wageningen Agricultural University, Dept. of Hydrology

acronym	surface type	mast	height/depth (m)	operating team
AH4	overall	*s*	4	WSC
AH6	overall	*f*	6	WAUMET
AB1	bare soil	*e*	1.5	WAUMET
AB2	bare soil	*t*	0.3	WSC
AP1	plant	*e*	1.5	WAUMET
AP2	plant	*u*	0.3 m above plant	WSC
TDR		*v*	0.1, 0.2, 0.3, 0.4, 0.5	WAUHBH

Furthermore, an overpass of the NASA aircraft ER-2 carrying a Thematic Mapper Simulator (TMS NS001) multispectral sensor at 29 June, 10:20 am, yielded reflectance data of the measurement site with a resolution of approximately 18.5 × 18.5 m. Reflected radiation was monitored in 7 different channels, enabling the derivation of a spectral albedo map of the terrain. Calibration of the TMS albedo was carried out using six ground-truth measurements in both the Tomelloso and the Barrax major sites. For details about the procedure to obtain this map we refer to Bastiaanssen *et al.* (1993).

The albedo observed by the ground-truth sensors will be equal to the hemispherical albedo defined by eq. 3.21, when a) these sensors are mounted exactly horizontal, b) its cosine response is perfect, and c) the spectral response is constant within the shortwave spectrum range, and zero outside this range. In practice, none of these conditions will generally be met exactly. The albedo observed by the TMS NS001 platform deviates stronger from the hemispherical albedo due to the very small opening angle of the nadir viewing sensor.

■ **Spatial variability of observed albedo**

The heterogeneity of the albedo at a scale of the measurement site is clearly illustrated by an albedo map constructed from data of the TMS NS001. The relevant reflectance statistics of a square of 21 × 23 pixels with indicated coordinates are given in Table 3.6. The square covers the measurement site of Figure 2.2 completely, and is totally occupied by vineyard, apart from a few dirt roads. The TMS-data show that the albedo of the

site varies between 0.17 and 0.27 with a standard deviation of 0.017. The statistics show that the variability between pixels is significant.

Three factors may explain the large heterogeneity of the effective surface albedo observed with the TMS NS001. First, the horizontal variability observed by the remote sensor may overestimate the variability of the hemispherical albedo (eq. 3.21). Radiation from large reflectance angles are not detected by the platform, but can reduce the horizontal variability considerably by spatial averaging. Second, the sandy loam soil had a red colour caused by the presence of iron compounds. This colour was not uniform over the entire field, as could be seen at the site. The iron content showed a clear variation, causing a variability of the albedo, particularly in the visible range. Third, the field was not entirely flat. Estimated height differences of about 0.5 m were observed on a horizontal scale of about 100 m. This micro-relief might have caused local differences in the water content in the top layer, and consequently differences in the mineralization of organic disposals. Darkness variations as a result of this spatial variation induce a variability of the albedo.

Table 3.6: Statistics of TMS surface albedo map. The pixel resolution was 18.5 m; map size is 21 × 23 pixels

property	value
UTM-coordinates	
Western and Eastern border	505898 - 506305 (426 m)
Southern and Northern border	4332078 - 4332448 (389 m)
albedo values	
minimum	0.173
maximum	0.271
average	0.223
median	0.223
standard deviation	0.017

- **Seasonal variation**

Figure 3.4 shows the course of the average albedo around noon, a_0, as measured by AH6 between 11.30 and 12.30 GMT, for the entire measurement period. The albedo early in the period, applying to a very small vegetation cover, is typically 0.28. This value corresponds with data for dry sandy soils cited by Ten Berge (1990). Feddes (1971) reports a slightly lower albedo (0.24) for one case of dry sandy loam.

Due to the rapid increase of the vegetation cover a clear reduction of the surface albedo was expected. This was for instance observed by Jacobs and van Pul (1990) above a growing maize stand. On the contrary, except for a cloudy day (7 June) a gradual increase of a_0 is observed until day 19, followed by a sudden reduction and gradual changes after this date. Measurements of the soil moisture content in the top 10 cm of the soil showed a very gradual decrease until 21 June (from 0.055 m^3/m^3 on 3 June to about 0.043 m^3/m^3 on 21 June, see Figure 3.5) (Droogers *et al.*, 1993). In spite of the fact that these measurements cannot be considered representative for the moisture content near the surface, a reduction of

the surface soil moisture may be deduced from Figure 3.5, which can possibly explain the increase of a_0 early in the period. Inspection of the albedos around noon measured by sensor AH4 revealed an average difference of about -0.035 compared to AH6. This systematic difference can be ascribed to local differences in the soil composition.

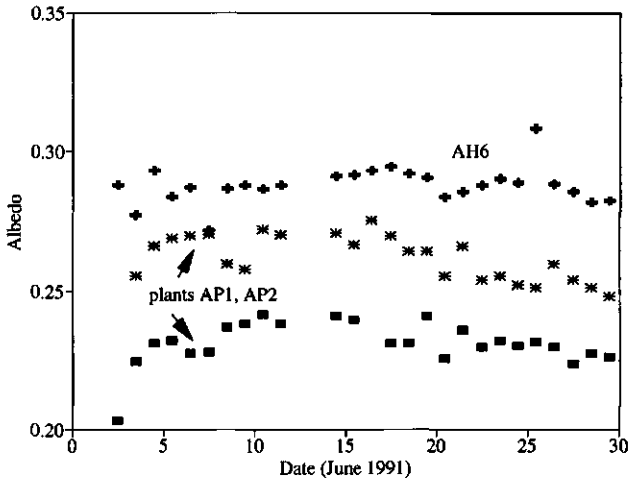

Figure 3.4: +: Average albedo between 11:30 and 12:30 GMT measured at 6 m height above a sparse canopy, and above two individual plants (* and ■)

Figure 3.4 also shows the albedo around noon measured above 2 individual plants. The albedos differ by typically 2.5%. These differences are most likely caused by a different albedo of the underlying soil, which significantly contributes to the measured albedo. The long term variability resembles the observations by sensor AH6. As long as the plants cover only a small part of the underlying soil the measured albedo increases, but a decline is observed from 17 June onwards. This decline is somewhat stronger for the highest albedo. Although the scatter is large and the measurements ended before complete vegetation cover was reached, the data suggest that the two albedos tend to approach each other towards the limit of a full vegetation cover.

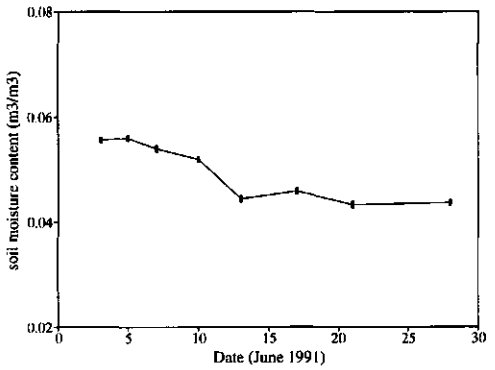

Figure 3.5: Soil moisture content of upper 10 cm, measured using TDR (Droogers *et al.*, 1993)

- **The diurnal variation**

The zenith response of the albedo measured by sensor AH6 after noon changed somewhat as the measuring period proceeded. Figure 3.6 shows the albedo measured by AH6 at days 5, 17 and 28 as function of zenith angle ζ, for afternoon data only. The selection of days represents different stages of the plant growth. The zenith response of the albedo at all days is very small for $\cos(\zeta) > 0.5$. This small response is associated with the rough structure of the soil. Only when the zenith angle is large a clear response is observed.

The response increases as the vegetation covers more of the surface (day 28). This response is shown to be stronger for the albedo measured overhead an individual plant (Figure 3.6). Early in the season (day 5), when a large fraction of the measured upward radiation is reflected by the surrounding soil rather than by the plant, the variation is less pronounced. As the plants becomes denser and the surface albedo approaches the characteristics of a closed canopy, the zenith angle dependence becomes stronger, and observable at smaller zenith angles than for a bare soil.

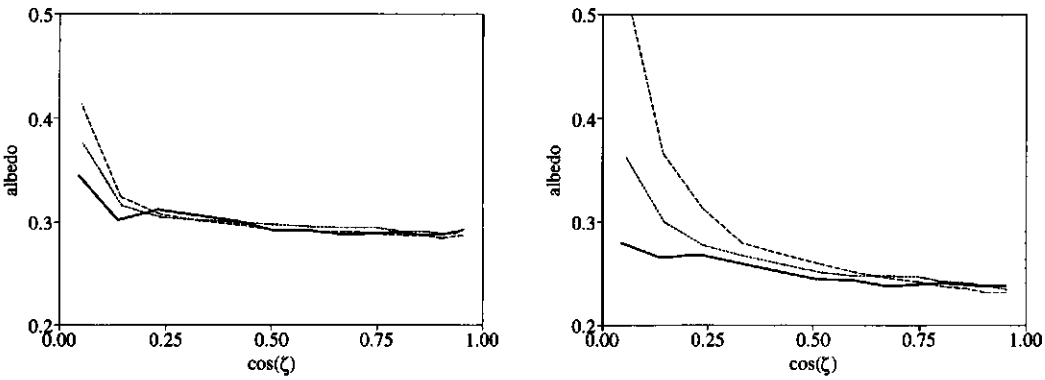

Figure 3.6: The measured albedo after noon; Left: at 6 m height; Right: just overhead an individual plant for three different days in June 1991: —— day 5, ····· day 17, - - - day 28

In Figure 3.7 the diurnal courses of the surface albedo observed at 4 days with sensor AH6 are shown. Day 5 represents fair weather conditions of a virtually bare soil. Days 20 and 21 are chosen as to represent a medium stage in the growing canopy, but with more clouds on 21 June than on 20 June. At day 28 the canopy has almost reached its maximum size.

Also shown in Figure 3.7 are regressions obtained using eqs. 3.22 - 3.31. The albedo for the plant area was computed by inserting the leaf area index per unit plant area, LAI_*, in eq. 3.26. The coefficients entering the equations are obtained from the field measurements and summarized in Table 3.7.

In Figure 3.7 the effect of clouds on the measured surface albedos is clearly present. Clouds increase the fraction of diffuse radiation, which enhances the contribution of beams with small elevation angles. Particularly at day 21, when cloud overpass occurred during most of the day, the scatter around and after noon is larger than at the other days.

As time proceeded from day 5 to day 28, the assymetric response of the observed surface albedo to the zenith angle gradually decreased. Possibly, the reduction of the albedo in the morning is smaller at later times than early in the period, by a progressively declining

moisture content in the top soil layer (Figure 3.5).

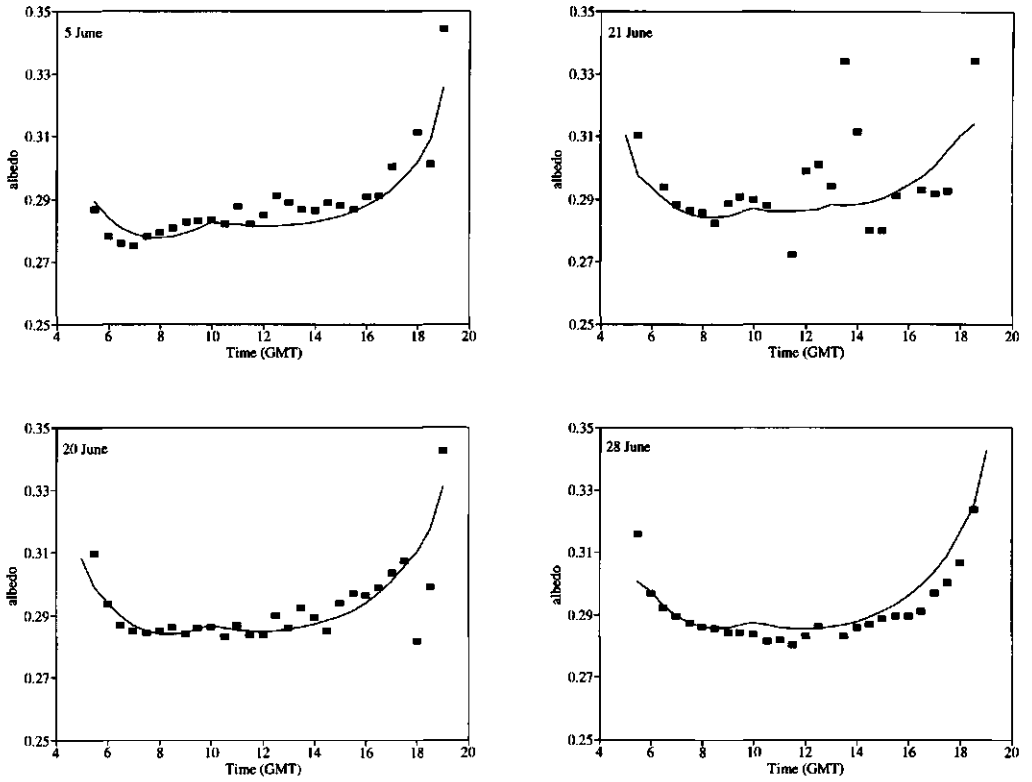

Figure 3.7: ■: Diurnal courses of albedo measurements using sensor AH6 at 4 different days in June 1991; —— regressions of data using eqs. 3.22 - 3.31 and the coefficients listed in Table 3.7

3.3.3 Conclusions

The albedo of the sparse vineyard canopy shows a variation at different scales, both in time and in space. The large scale time variation includes a gradual increase of the albedo around noon caused by drying of the soil, and a slight decrease related to the development of the vegetation. These simultaneous and counteracting effects resulted in a rather conservative value of a_0, for which 0.285 ± 0.005 is a reasonable estimate. The dependence of surface albedo on zenith angle and – possibly – soil moisture fluctuations are causes of a diurnal variation which exceeds the variability of a_0. Most of this variation is observed at large zenith angles, and therefore has a limited impact on the net radiation balance. Also clouds can give rise to sudden albedo changes by a change of the fraction of diffuse radiation. Considerably larger is the spatial variation at the scale of a single field, caused by differences in soil composition and water content. Smaller scale spatial variations originated from different reflectance properties of the plant elements and the open bare soil spaces in between.

Table 3.7: regression coefficients applied to eqs. 3.22 - 3.31

parameter	symbol	equation	value at day			
			5	20	21	28
bare soil albedo around noon	a_0	3.22	0.284	0.292	0.292	0.292
offset of zenith response function	g_0	3.23	0.96	0.96	0.96	0.96
slope of zenith response function	c_g	3.23	0.2	0.2	0.2	0.2
offset of asymmetry function	m_{d0}	3.25	1.06	1.06	1.06	1.06
slope of asymmetry function	c_m	3.25	0.12	0.12	0.12	0.12
leaf area index per unit plant area	LAI_*	3.26	3.0	4.2	4.2	3.9
fraction of vegetation cover	σ_f	3.31	0.05	0.09	0.10	0.13

3.4 A photosynthesis model for the crop conductance applied to a sparse vineyard canopy

To describe the exchange of water vapour between the land surface and the atmosphere many meteorological models use a so-called crop conductance (g_c), or its reciprocal crop resistance (r_s^c), which expresses the efficiency of water transport from the substomatal cavities in canopy leaves to the ambient air. This crop conductance can be considered as a physiological parameter, since it is mainly determined by the behaviour of leaf stomata. Models describing the crop conductance usually include a dependence on various environmental parameters, in particular light intensity, humidity of the ambient air, leaf temperature and soil moisture availability (see for instance Dolman and Stewart, 1987; Stewart, 1988; Noilhan and Planton, 1989). Very often statistical regression of stomatal conductance data on values of environmental parameters is used to obtain a mathematical prognostic model for the crop conductance (Jarvis, 1976; Stewart, 1988). Functions for each parameter are then simply multiplied to yield a prognostic expression for g_c:

$$g_c = g_{s,\max} LAI \cdot f_1(x_1) \cdot f_2(x_2) \cdot \ldots \cdot f_n(x_n) \qquad (3.32)$$

In this expression $g_{s,max}$ is a maximum stomatal conductance, and $f_i(x_i)$ expresses some functional dependence of g_c on environmental factor x_i.

Since water vapour evaporated from substomatal cavities is transported along an identical pathway as the CO_2-transfer associated with photosynthesis, other workers determine the crop conductance by parameterizing a leaf stomatal conductance g_s as function of the photosynthetic rate. Some algorithm to scale up g_s to the conductance at canopy level, g_c, is then adopted. A stomatal conductance for CO_2-transfer, $g_{s,CO2}$, is defined as the ratio of the net CO_2-transport between the ambient air and the leaf stomata, F_{CO2}, and a difference between the CO_2-concentration within the stomatal cavities, C_i, and in the air directly surrounding the leaf, C_s:

$$g_{s,CO_2} \equiv \frac{F_{CO_2}}{C_s - C_i} \tag{3.33}$$

An analogy is assumed between the stomatal conductances for water vapour and for CO_2:

$$g_s = 1.6\, g_{s,CO_2} \tag{3.34}$$

where the factor 1.6 accounts for the difference between the molecular diffusivities of both gases. In practice, the CO_2-transport is governed by the net leaf photosynthetic rate. Following this approach a model for g_s is assessed by using a model for the leaf photosynthesis, A_n, and adopting some assumption for the concentration gradient C_s - C_i (see, e.g., Goudriaan and Van Laar, 1978; Wong *et al.*, 1979; Goudriaan *et al.*, 1985; Jacobs, 1994). This type of model is hereafter referred to as a A_n-g_s model. Since these models consider a physical and physiological mechanism for gas exchange between plants and ambient air, they gain significant generality compared to the statistical models.

Field and laboratory observations reveal that the stomatal conductance shows a dependence on ambient humidity. Although the mechanism of this response is not completely resolved, a reduction of g_s is usually observed as the ambient humidity deficit, D_s, increases (see for instance Turner, 1991; Morison and Gifford, 1983), and this effect can even result in a reduction of the plant evaporation, in spite of an increase of the humidity gradient (Choudhury and Monteith, 1986). In recent studies the dependence of g_s on D_s was incorporated in a A_n-g_s model by a number of parameterizations. Jacobs (1994) proposed to express C_s - C_i as a function of D_s. Alternatively, Kim and Verma (1991a) first calculated g_s without including humidity effects, and adopted an empirical adjustment of the conductance as function of D_s afterwards. This approach resembles the semi-empirical Jarvis-type model (eq. 3.32), and various shapes of these response functions were proposed (Kim and Verma, 1991a; Winkel and Rambal, 1990).

The aim of this section is to evaluate the parameterization of the crop conductance of a sparse Mediterranean vineyard canopy using a photosynthesis approach. The leaf photosynthetic rate was calculated using the photosynthesis model of Goudriaan *et al.* (1985). Three different parameterizations of the response of g_s to air humidity (Jacobs, 1994; Kim and Verma, 1991a; Winkel and Rambal, 1990) are explored using leaf conductance data collected in the context of the EFEDA research program. A simple weighing scheme is used to scale up modelled leaf conductances to the canopy scale, for practical applicability in large scale meteorological models. Leaf conductance data were aggregated to a crop conductance using a similar weighing procedure, and model results are compared to data at the canopy level.

3.4.1 Theory

■ The A_n-g_s model and parameterization of humidity response

In the A_n-g_s model, g_s is calculated by adopting a model for $A_n = F_{CO2}$ in eq. 3.33, and using an explicit parameterization for C_s - C_i. The net photosynthetic rate A_n is a balance between the gross photosynthetic rate and the losses due to photorespiration and dark respiration. Goudriaan *et al.* (1985) developed a model to describe A_n for a leaf as function of

the amount of absorbed PAR by the leaf, its temperature, T_l, and the ambient CO_2-concentration, C_s. A distinction was made between the different metabolisms of C3 and C4 plants. Details of the algorithm for A_n can be found in Appendix IV.

The parameterization of C_s - C_i by Jacobs (1994) is based on a strong correlation often found between the photosynthetic rate and the leaf conductance under a wide range of field circumstances. The strong correlation is related to a conservative ratio between C_i and C_s, as observed by e.g. Goudriaan and Van Laar (1978) and Wong *et al.* (1979). This conservative behaviour is thought to reflect the plant's strategy to optimize the relation between water use and CO_2-assimilation (Cowan, 1982). Some workers found the ratio C_i/C_s to decrease with ambient humidity deficit (Wong *et al.*, 1979; Morison and Gifford, 1983). Regarding eq. 3.33, this implies that apparently A_n (= F_{CO2}) exhibits a smaller response to increasing humidity deficit than g_s. Jacobs (1994) and Jacobs *et al.* (1995) used this result to parameterize humidity responses of g_s. They prescribed C_i/C_s as a linear function of the ambient humidity deficit D_s. Accounting for the effect of photorespiration on C_i, the following relationship was used:

$$\frac{C_i - \Gamma}{C_s - \Gamma} = f_0\left(1 - \frac{D_s}{D_{\max}}\right) \tag{3.35}$$

where Γ is the CO_2-compensation concentration, and f_0 and D_{max} calibration coefficients (see Appendix IV for details).

In the approach of Kim and Verma (1991a,b) the ratio $(C_i - \Gamma)/(C_s - \Gamma)$ was fixed at a constant maximum value. A maximum stomatal conductance, identified as g_s^0, is obtained by inserting this value in eq. 3.33. An empirical curvilinear humidity response function was applied to obtain the actual value of g_s, according to

$$g_s = g_s^0 \frac{1}{1 + b_D D_s} \tag{3.36}$$

in which b_D is a calibration coefficient, remaining to be specified. The value of $(C_i - \Gamma)/(C_s - \Gamma)$ is taken equal to 0.85 in the present analysis (Morison and Gifford, 1983; see also Appendix IV).

Winkel and Rambal (1990) experimentally determined the stomatal conductances of various grapevine species, and used an exponential humidity response function for g_s. Their expression for g_s was of the form

$$g_s = g_s^0 \exp(-D_s / D_r) \tag{3.37}$$

where again g_s^0 is used to indicate the value of the stomatal conductance obtained without including a humidity response, and D_r is another calibration coefficient.

- **Scaling up from leaf to crop**

For use in large scale meteorological applications, a one-layer description of the crop conductance must be derived from a model for g_s, using a weighing scheme for various microclimate classes of the canopy leaf population. Particularly the response of g_s to

absorbed PAR is highly non-linear. Leaves which are not directly illuminated by the sun contribute relatively much to the canopy photosynthesis, due to a very efficient use of light (Goudriaan, 1977). Following Baldocchi *et al.* (1987), g_s is calculated for two microclimate classes: the sunlit and shaded regimes. A simple weighing scheme using the sunlit and shaded leaf area, LAI_{sun} and LAI_{shad}, is applied to define an average crop conductance:

$$g_c = LAI_{sun} g_s(I_{a,sun}) + LAI_{shad} g_s(I_{a,shad}) \tag{3.38}$$

where I_a is the amount of absorbed PAR, and the subscripts *sun* and *shad* denote the sunlit and shaded regimes, respectively. Values of leaf temperature, ambient CO_2-concentration and humidity deficit are assumed similar for shaded and sunlit leaves.

Using the A_n-g_s model outlined in eqs. 3.33 - 3.35, and the weighing scheme in eq. 3.38 to determine the crop conductance g_c, the environmental parameters that need to be specified are LAI_{sun} and LAI_{shad}, $I_{a,sun}$ and $I_{a,shad}$, and leaf temperature, ambient CO_2-concentration and humidity deficit.

For the distribution of total leaf area *LAI* over sunlit and shaded fractions simple semi-empirical equations (e.g., Campbell, 1977) are succesfully applied for closed canopies. However, grouping of leaves in clusters – as is the practice in sparse canopies or row crops – makes these closed-canopy formulations invalid. In the present study the fraction of sunlit leaf area, $f_s \equiv LAI_{sun}/LAI$, was derived from field measurements (Figure 2.9), and will be further addressed in the discussion. Also the values of T_l, C_s and D_s were obtained from measured quantities, in a way explained in Appendix IV.

Norman (1982) proposed simple expressions to describe the flux densities of PAR reaching the sunlit and shaded leaves separately, as function of incoming PAR at reference height, *LAI* and solar zenith angle ζ. Assuming a random distribution of leaves over the canopy without azimuthal preference, and a spherical leaf angle distribution, the amount of absorbed PAR (I_a) for each class is given by

$$\begin{aligned} I_{a,shad} &= \alpha_l \, \mathrm{PAR}_{shad} \\ &= \alpha_l \left[\mathrm{PAR}_{dif} \exp(-0.5\, LAI^{0.7}) + 0.07\, \mathrm{PAR}_{dir} (1.1 - 0.1\, LAI) \exp(-\cos\zeta) \right] \end{aligned} \tag{3.39}$$

$$\begin{aligned} I_{a,sun} &= \alpha_l \, \mathrm{PAR}_{sun} \\ &= \alpha_l \left(\frac{0.5\, \mathrm{PAR}_{dir}}{\cos\zeta} + \mathrm{PAR}_{shad} \right) \end{aligned} \tag{3.40}$$

Here, PAR_{shad} and PAR_{sun} are the average flux densities of PAR reaching the shaded and sunlit leaves, and α_l is the leaf absorbtivity, taken as 0.8 (Kim and Verma, 1991a). Direct and diffuse PAR, denoted by the subscripts *dir* and *dif*, respectively, are assumed to be a constant fraction (0.47) of incoming direct and diffuse shortwave radiation (Goudriaan, 1977).

3.4.2 Site description and measurements

The analysis of the A_n-g_s model and the humidity response of the crop conductance is carried out using Mediterranean vineyard data measured during EFEDA-II. Measurements of *LAI*, f_s, g_s, total evaporation (E), average CO_2-concentration, friction velocity u_*, wind

speed u, air temperature (T_a) and specific humidity (q_a), and incoming shortwave and diffuse radiation (K and K_{dif}) were measured as outlined in the previous chapter. Leaf conductance data were averaged per hour to yield values of crop conductance g_c according to a weighing scheme similar to eq. 3.38 (see section 2.3.6). Leaf temperatures recorded by the diffusion porometer were arithmetically averaged per hour, separately for sunlit and shaded leaves. Also PAR measurements were recorded using the porometer sensor, held in approximately the same orientation as the leaf being monitored. Separate hourly averages of PAR were computed for shaded and sunlit leaves.

All meteorological measurements were averaged to hourly values, in correspondence with the porometry averaging interval. Timing between the energy balance and the porometry measurements was accurate within 1 minute.

3.4.3 Results

■ Calibration of the humidity functions

The A_n-g_s model as proposed by Jacobs (1994) and Jacobs *et al.* (1995) was calibrated during a field experiment carried out in 1991 in La Mancha, Spain, in the context of EFEDA-I. That site and vegetation were very similar to the location explored in the current study. For the calibration of the A_n-g_s model and the humidity response function (eq. 3.35), Jacobs (1994) used measurements taken with a steady state gas exchange unit, measuring the total CO_2-transport to a leaf, PAR, leaf temperature and D_s. He assumed the crop to be well supplied with soil moisture, owing to the large rooting depth of the vine plants. Since no explicit description of the dependence of g_s on soil moisture availability is considered, any possible effect of soil water depletion is implicitly included in his calibration of the model. The resulting calibration coefficients can be found in Appendix IV.

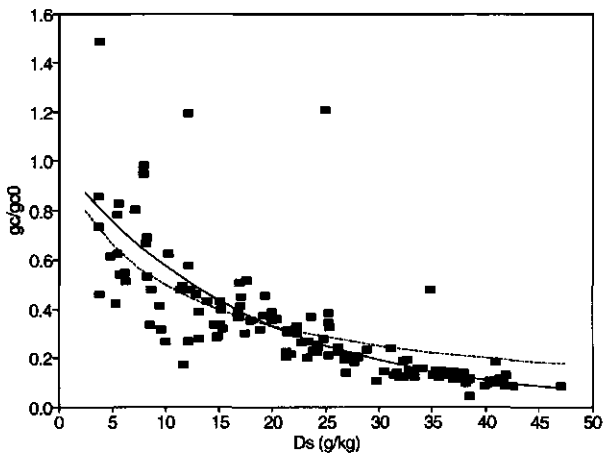

Figure 3.8: Measured values of g_c normalized with g_c^0 plotted against specific humidity deficit D_s. Also shown are the best-fit functions given by eqs. 3.36 (b_D = 0.121 (g/kg)$^{-1}$, - - -) and 3.37 (D_r = 17 g/kg, ——)

The calibration of the curvilinear (eq. 3.36) and exponential (eq. 3.37) humidity response functions was carried out directly at the canopy level. First, a maximum stomatal conductance, g_s^0, was computed for the sunlit and shaded leaves separately, and these were aggregated to a maximum crop conductance, g_c^0, using the weighing scheme of eq. 3.38.

Figure 3.8 shows a plot of observations of g_c normalized by g_c^0 plotted against D_s. The optimal curvilinear fit of eq. 3.36 was found to be represented by adopting b_D = 0.121 $(g/kg)^{-1}$, while the optimal value for D_r appearing in eq. 3.37 was found to be 17 g/kg. Both functions are also shown in Figure 3.8. The curvilinear function overestimates g_c/g_c^0 at high values of D_s, and underestimates this ratio at low humidity deficit. A better agreement is obtained when an exponential function is applied.

■ **The crop conductance from the A_n-g_s model**

Figure 3.9 shows a 1:1 plot of the measured and calculated crop conductance g_c, using the humidity response proposed by Jacobs (1994, eq. 3.35). From a linear regression through the origin, the model for g_c overestimates the experimental values on the average by 14%, and explains r^2 = 58% of the variance.

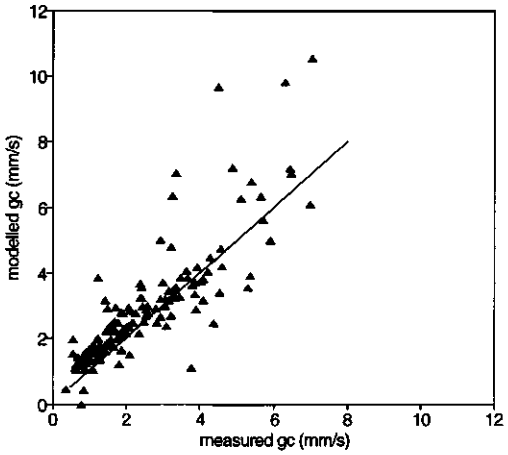

Figure 3.9: Measured and calculated values of crop conductance g_c, using the humidity response function of Jacobs (1994) (eq. 3.35)

A similar plot for the curvilinear function (eq. 3.36) results in a fairly low value for r^2 (30%). As expected, low values of g_c (corresponding to a high specific humidity deficit) are significantly overestimated, and this is compensated by an underestimation at higher conductances. A better agreement is obtained when the empirical curvilinear function is replaced by the simple exponential function (eq. 3.37). Using D_r = 17 g/kg, the model explains r^2 = 68% of the variance (figures not shown).

Figure 3.10 shows the diurnal variation of the observations and the three model variations for four different days, selected as to cover a wide range of days spread over the measurement period. It is clearly seen that g_c decreases with time, both at a diurnal and a seasonal time scale. The exponential fit and the expression of Jacobs (1994) show a close correspondence for most cases. The linear fit tends to overestimate g_c in the afternoon, particularly at later days.

3.4.4 Discussion and conclusions

Values of g_c, modelled using a photosynthesis approach and a response to ambient humidity proposed by Jacobs (1994) calibrated for a similar crop three years earlier, and by

adopting simple procedures to express PAR and D_s, showed a fair agreement with observed values of the crop conductance. Preliminary calculations showed that values of r^2 are much better than the performances of models using a statistical regression of g_c on D_s also calibrated in 1991. More attention to a comparison between the A_n-g_s model and a statistical approach will be paid in a subsequent study.

Particularly at small values of g_c the crop conductance predicted by the A_n-g_s model is somewhat overestimated. The model results are rather sensitive to the value of the ambient humidity D_s. The method to obtain D_s is associated with errors in measurements of E, q_a and u_*, and the assumptions concerning the turbulent exchange between the reference level and the leaf surface (Appendix IV).

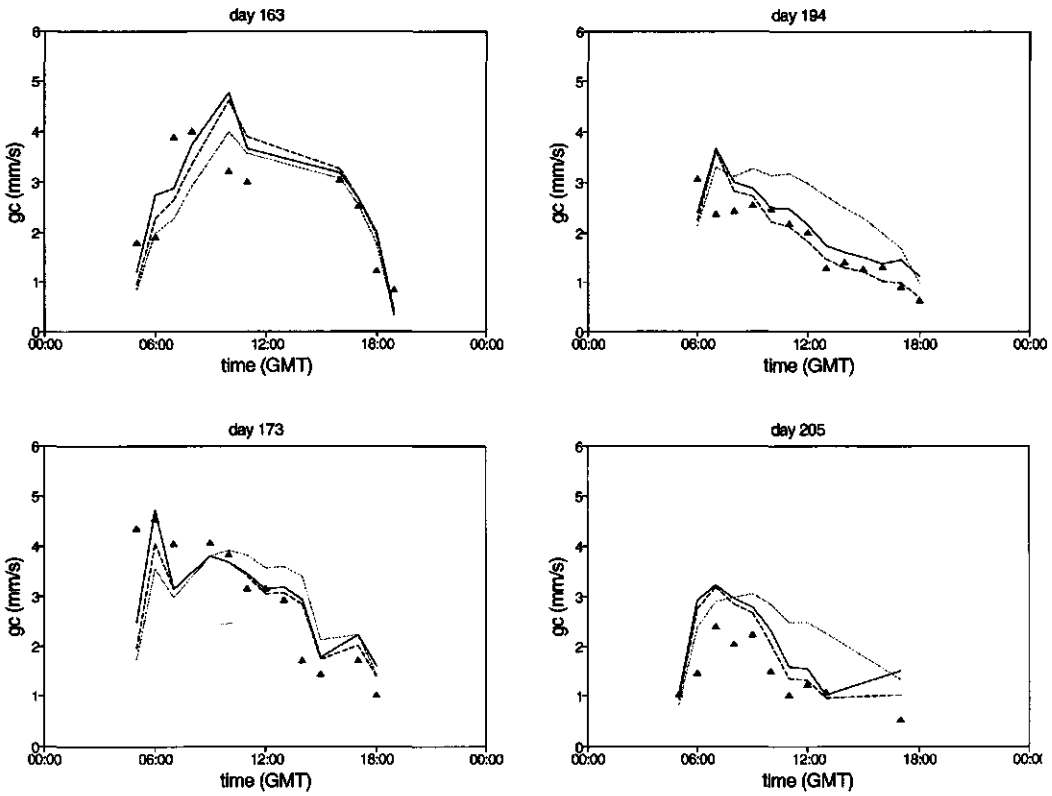

Figure 3.10: Measured and calculated values of crop conductance g_c, for DOY 163, 173, 194 and 205; ▲ observations; —— modelled g_c using the humidity response function of Jacobs (1994) (eq. 3.35); ····· the curvilinear humidity response function (eq. 3.36) with b_D = 0.121 (g/kg)$^{-1}$; - - - the exponential humidity response function (eq. 3.37) with D_r = 17 g/kg

Replacing modelled PAR by porometer observations did not result in a significant improvement of the correlation coefficient. The average overestimation of calculated values of g_c was reduced from 14% to 12% (figures not shown), in spite of the noticed underestimation by the PAR equations. The difference between modelled and measured PAR was especially present at high radiation levels, where the sensitivity of the photosynthesis

model to the amount of absorbed PAR rapidly falls off (see eq. 3 in Appendix IV). This implies that also the sensitivity of predicted values of g_c to the parameterization of intercepted PAR is less significant at high radiation levels.

Also, the measured values of g_c are subject to variability due to sampling errors. According to the porometer manufacturer the sampling error of a single porometry measurement is approximately 20%, owing to incorrect temperature or humidity registrations in the porometer sampling cell, or to improper field calibration. The error involved with scaling up leaf conductances to the canopy level depends on the sampled and true distribution of leaf conductances of a single plant, the representativity of the selected plants in the field, and the errors in the estimation of the leaf area index, fraction of sunlit leaves and the determination of leaf age. The coefficient of variance ($cv = \sigma(g_s) / \overline{g_s}$, where $\overline{g_s}$ is the average leaf conductivity) of the porometry measurements within a single averaging interval (1 hour) can serve as an indication of the error associated with the total crop conductance assessment. The *cv* increased from 0.35 ± 0.15 in the first half of the measurement period to 0.50 ± 0.25 in the second half.

Another possibly important source of error of the A_n-g_s model is associated with the calibrations carried out by Jacobs (1994). He assumed his crop to be well-watered, and soil moisture depletion was not included in the parameterization for g_c. However, a very low soil moisture content during long periods of time may affect the stomatal conductance negatively (Turner, 1991). There is accumulating evidence that stomatal response to soil water drought is governed by a change of the metabolic products in the xylem sap. This implies that soil water stress extending for a significant period will reduce the stomatal conductance of a crop. Soil moisture conditions may well have been different during the current experiment compared to the conditions reported by Jacobs (1994), and a shortage of soil water possibly reduced the actual crop conductance. In this situation, the model will overestimate the true conductance values. Unfortunately, soil moisture data necessary to test this hypothesis were not available.

A simpler approach to include the response of g_c to ambient humidity deficit, as proposed by e.g. Kim and Verma (1991a,b), required the derivation of a crop conductance not affected by an ambient humidity deficit. For this, a value of g_c was computed using $(C_i - \Gamma)/(C_s - \Gamma) = 0.85$ (see Appendix IV). Two different humidity response functions were optimized, using the current dataset rather than being tested independently. An optimal curvilinear fit to the measured conductance data was achieved for $b_D = 0.121$ $(g/kg)^{-1}$. This value is rather high compared to the range reported by Kim and Verma (1991b) for three tallgrass species (0.01 - 0.03 $(g/kg)^{-1}$). A strong humidity response of the vine species considered in this study is also revealed using the exponential function, which showed a better correspondence than the curvilinear fit. The value of the empirical coefficient $D_r = 17$ g/kg found from the present results also points at a strong humidity response compared to the results of Winkel and Rambal (1990), who report $D_r \approx 48$ g/kg for Carignane vine. They suggest that the stomatal humidity response is a species dependent characteristic, which might be linked to its geographical origin. Carignane – originating from the Aragon region in Spain with a strong semi-arid climate, and well-known for its hardiness – shows a relatively strong humidity response when compared to a species originating from the Rhone valley (Shiraz, $D_r \approx 222$ g/kg). A strong humidity response is likely to be favourable under

dry circumstances in order to avoid excessive water loss, and increases the water use efficiency of a crop. The even stronger humidity response encountered in the current study may be related to a stronger soil moisture stress, but this assumption can not be validated here.

In order to apply a photosynthesis model in large scale meteorological applications, a simple weighing procedure was adopted from Baldocchi *et al.* (1987), which requires an establishment of PAR absorbed by both shaded and sunlit leaves, and a factor representing the weight of each leaf class. In the current study the fraction of sunlit leaves, f_s, was obtained from field measurements. Practical formulations for f_s have been proposed for closed canopies (e.g., Campbell, 1977), but are invalid for sparse canopies. However, application of these formulations with effective leaf area indices can often result in reasonable descriptions. For instance, the simple equation of f_s proposed by Campbell (1977) overestimated observed values of f_s considerably when measured *LAI* (0.25 m^2/m^2) was inserted. A reasonable estimate of f_s was given by using a tenfold value for *LAI*.

The A_n-g_s model of Jacobs (1994) and Jacobs *et al.* (1995), incorporating effects of air humidity deficit on g_c via a modified C_i/C_s-ratio, is a relatively simple and promising approach for calculating the crop conductance g_c of species similar to the vines studied here. However, the sensitivity of g_c to ambient humidity varies widely between different plant species and even between vine cultivars. This variability imposes severe limitations on the use of uniform humidity response functions in any conductance model for large scale applications. The calibration carried out in 1991, however, seemed to be well applicable to the new 1994-dataset.

Monteith (1993, 1995b) and Mott and Parkhurst (1991) suggested that g_c should be a function of the crop evaporation rather than of the ambient humidity deficit. Monteith proposed to express the canopy conductance as function of the crop evaporation rate, using two scaling parameters, g_{max} and E_{max}:

$$\frac{g_c}{g_{\max}} = 1 - \frac{E_c}{E_{\max}} \qquad \textbf{(3.41)}$$

He hypothized that g_{max} is a function of the crop photosynthetic rate, and E_{max} is related to soil moisture. A possible strategy to obtain g_{max} is to use the A_n-g_s model described in this section under conditions where $D_s = 0$ and so $(C_i - \Gamma)/(C_s - \Gamma) = 0.85$. Based on the measured crop conductances described in this section, this assumption was used to explore the behaviour of E_{max}. However, owing to the sparse vegetation, relatively low values of the surface evaporation, and the lack of soil moisture measurements, the results were not fully conclusive. More evidence of eq. 3.41 is needed before it can be used in meteorological models.

3.5 Conclusions

In this chapter three aspects of surface exchange for a sparse canopy are discussed. The first aspect, the aerodynamic transfer between the surface and the atmosphere, has resulted in the formulation of a new set of aerodynamic resistances, based on Lagrangian theory. Also, these resistances are no longer parameterized by use of a fixed hypothetical

source at $d + z_{0m}$, but include an 'effectiveness weighing', which accounts for the effect of a vertical source variability. These resistances are presented in normalized forms, and scale with u_*. They are developed for a two-component surface model, and as such can be used to describe the exchange between the atmosphere and a sparse canopy. These resistances will be included in the one-dimensional simulations in chapter 6, and compared to existing formulations in a coupled SVAT-PBL model.

The survey of the surface albedo of the EFEDA-I measurement site has revealed a considerable variability, both in time (at diurnal and seasonal scale) and in space (at scales ranging between the diameter of individual plants and TMS-NS001 pixel size). An empirical regression was carried out to account for the temporal variation. The temporal changes at a seasonal time scale were rather low, probably owing to the counteracting effects of increasing vegetation cover and decreasing soil moisture content. In the remainder of this study, the effect of this temporal and spatial variability on the land surface-atmosphere interaction is not further investigated.

The A_n-g_s model of Jacobs (1994), describing the leaf stomatal conductance, was upscaled to the canopy level. The formulation of the canopy resistance from this work will be included in the sensitivity analysis in chapter 6.

4

A model is a mathematical interpretation of a physical process, rather than a second reality

Selected surface layer and boundary layer models

This chapter briefly describes the models used for the 'zero-dimensional' SVAT-intercomparison in chapter 5, and the sensitivity analysis with coupled SVAT-PBL models in chapter 6. As was outlined in the introduction of this thesis, components of various existing SVAT's will be combined in that sensitivity chapter. In spite of this, the existing surface models will be discussed here in their most original form, although a few modifications to authentic papers were employed. This particularly holds for the suggestions proposed by Van den Hurk and Beljaars (1995) to improve the new ECMWF surface scheme developed by Viterbo and Beljaars (1995). A separate section is dedicated to these suggestions.

After the discussion of the surface models in section 4.1, two models for the PBL are briefly outlined in section 4.2. A list of model limitations is discussed in section 4.3.

All models were extensively described in the original literature. In the following sections only the essentials will be presented.

4.1 Surface layer models for sparse canopies

Various parameterizations are currently in use in large scale GCM's or numerical weather prediction models. The degree of complexity varies from simple one-layer schemes inspired by the 'big-leaf' model (Monteith, 1965), to sophisticated multiple-source models (for instance, Sellers *et al.*, 1986; Dolman, 1993). Detailed multiple-level canopy models (Waggoner and Reifsnyder, 1968; Goudriaan, 1977; Raupach, 1989a, 1989b; El-Kilani *et al.*, 1994) are usually too complex to be used in large scale applications, owing to a large demand of input information and computer time. These models are not addressed here.

In the following sections the selected models are briefly described: a form of the big-leaf model, the ECMWF-surface scheme and its modifications, and the two-layer models of Deardorff (1978), Shuttleworth and Wallace (1985) and Choudhury and Monteith (1988). Some of these models do not include a specific description of the canopy resistance, r_s^c, but

rely on the parameterizations for r_s^c developed independently. The r_s^c-parameterizations of Viterbo and Beljaars (1995) and Choudhury and Monteith (1988) are discussed in the sections covering their surface models. The scheme proposed by Noilhan and Planton (1989) is treated in section 4.1.4, containing the model of Deardorff (1978). The parameterization of r_s^c along the lines of the photosynthesis-g_s model of Jacobs (1994) is presented previously in section 3.4. Also the implementation of Lagrangian diffusion theory (McNaughton and Van den Hurk, 1995) was discussed before (section 3.2), and this will not be repeated here.

4.1.1 The modified big-leaf model

The well-known one-layer 'big leaf' model (Monteith, 1965) simply describes evaporation and sensible heat exchange between a single surface and a reference level at height z_R close above. Strictly speaking, it is not applicable to sparse canopy surfaces, since it does not include a separate treatment of the various components of a sparsely vegetated surface. However, because of its simplicity it is present in various GCM's and NWP-models. For that reason it is included in the comparison study in chapter 6.

The original 'big leaf' model does not include a description of soil heat flux. For many sparse canopies this is a major term in the surface energy balance. In the formulation presented below, the soil heat flux is parameterized using a slightly modified so-called force-restore method.

The big-leaf model considers the energy balance of a surface (eq. 1.1), rewritten as

$$A = Q_* - G = H + \lambda E \tag{4.1}$$

where A is the available energy. Application of eq. 4.1 to a canopy assumes that no energy is stored or released within the canopy (either in the biomass or in the air within the canopy layer). Also, energy used for photosynthesis or respiration processes is ignored.

The turbulent fluxes of heat and water vapour are commonly expressed as ratios of a gradient of the scalar (temperature or water vapour density) and some resistance for turbulent exchange between the surface and z_R, denoted by r_a, according to

$$H = \rho c_p \frac{\theta_{sur} - \theta_a}{r_a} \tag{4.2}$$

and

$$\lambda E = \rho \lambda \frac{q_{sat}(T_{sur}) - q_a}{r_a + r_s^c} \tag{4.3}$$

where T_{sur} (or θ_{sur}) is an effective surface (potential) temperature (section 2.4.2), and θ_a and q_a are the potential temperature and specific humidity at the reference level z_R. Latent heat is supposed to be released from the surface through numerous stomatal pores present in canopy leaves. It is assumed that the specific humidity within these stomatal cavities is at surface temperature saturation, and in eq. 4.3 an additional resistance is included for the water vapour transport, being the 'surface resistance' r_s^c. This resistance allows for stomatal control of evaporation by plant canopies (Monteith, 1965), and must be explicitly

parameterized.

The aerodynamic resistance for heat and water vapour, r_a, consists of two parts:

$$r_a = r_a^a + r_a^h \tag{4.4}$$

The first, r_a^a, is a (stability dependent) exchange resistance between the reference level and the momentum roughness length, z_{0m}. For neutral conditions, the resistance is equal to the exchange resistance for momentum transfer. For stable and unstable conditions r_a^a is given by

$$r_a^a = \frac{1}{u_* \kappa}\left[\ln\left(\frac{z_R - d}{z_{0m}}\right) - \Psi_h\left(\frac{z_R - d}{L_v}\right) + \Psi_h\left(\frac{z_{0m}}{L_v}\right)\right] \tag{4.5}$$

where Ψ_h is a stability correction as function of the Monin-Obukhov length L_v (Beljaars and Holtslag, 1991).

The second part, r_a^h, is a (semi-empirical) excess resistance to account for the absence of bluff-body forces for scalar exchange (Garratt and Hicks, 1973). This latter resistance is equivalent to adopting a roughness length for scalars, z_{0h}, which is smaller than z_{0m}. The excess resistance is given by

$$r_a^h = \frac{1}{\kappa u_*}\left[\ln\left(\frac{z_{0m}}{z_{0h}}\right)\right] \tag{4.6}$$

where stability effects are ignored. Other parameterizations of r_a^h are based on the concept of a so-called leaf boundary layer resistance (Gates, 1980). More on this issue will be discussed below. At the outset we take r_a^h equal for heat and moisture exchange.

Net radiation is a (weak) function of the absolute surface temperature, T_{sur}, according to

$$Q_* = (1 - a)K^{\downarrow} + L^{\downarrow} - \varepsilon\sigma T_{sur}^4 \tag{4.7}$$

Incoming longwave and shortwave radiation, as well as the surface albedo and emissivity must be explicitly provided.

When a realistic description of the entire energy balance is needed, an expression for the soil heat flux G must be carried also. In this study the big-leaf model is extended by an equation for G, derived from the so-called 'force-restore' method (see section 4.1.4). G can be found from the rate of change of the surface temperature, T_{sur}, and a deep soil temperature, T_2:

$$G = \frac{\rho' C_h d_1}{2\sqrt{\pi}}\left[\frac{\partial T_{sur}}{\partial t} + \frac{2\pi\left(T_{sur} - T_2\right)}{\tau_1}\right] \tag{4.8}$$

where $\rho' C_h$ is the volumetric heat of the soil, d_1 is the e-folding depth of a diurnal

temperature wave, and τ_1 is the length of a single wave (see below). By rewriting the force-restore equation in this form, the surface energy balance equation can easily be solved by solving for T_{sur}. For small timesteps, only a small numerical difference exists with the original force-restore method, in which T_{sur} from the previous timestep is taken to solve the surface energy balance (see Appendix V).

For a given r_s^c and forcings at reference height, eqs. 4.1 - 4.8 can be solved iteratively for the surface temperature T_{sur} using the Newton-Raphson scheme (Jacobs and Brown, 1973; Appendix V). The stability correction in eq. 4.5 should be accounted for in another iteration loop, or computed by taking L_v from the previous time step.

This description of the big-leaf model is just one of the possible forms which are found in literature. Possible variations can be applied to the parameterization of soil heat flux (e.g., De Bruin, 1982), excess resistance (Kustas *et al.*, 1989), parameterization of incoming longwave radiation (Brutsaert, 1982), or stability corrections to aerodynamic resistance (Inclán and Forkel, 1995). Other workers included extensive schemes for surface albedo, canopy resistance, heat storage within the canopy and other issues. The formulation presented here serves the compatibility with other surface models, in order to be able to compare surface model components adequately (chapter 6).

4.1.2 The ECMWF surface scheme

■ Model description

The recently updated ECMWF surface scheme (Viterbo and Beljaars, 1995, replaced by VB95 hereafter) contains a rigorous treatment of the transport of heat and moisture within the soil. Like in the big-leaf model a single isothermal surface layer is defined, but with respect to evaporation a distinction is made between various surface fractions: open water, vegetation, bare soil and snow[1] (see Figure 4.1). This approach resembles the surface model of Noilhan and Planton (1989).

The heat transport in the soil is parameterized by means of a diffusion scheme:

$$\rho' C_h \frac{\partial T}{\partial t} = \frac{\partial}{\partial z}\left(\lambda_T \frac{\partial T}{\partial z}\right) \qquad (4.9)$$

where T is the soil temperature and λ_T the soil thermal conductivity. This equation is solved using a fully implicit solution scheme and discretization of the soil volume in four layers, of depth 0.07, 0.21, 0.72 and 1.89 m, respectively. The soil heat flux G is solved from the surface energy balance (see below) and provides the upper boundary condition. At the bottom of the simulation volume no heat flux is assumed to occur. Both $\rho' C_h$ and λ_T are allowed to vary with depth. $\rho' C_h$ is formulated according to eq. 2.21, while λ_T in layer i is parameterized according to Clapp and Hornberger (1978) as function of the soil water content in that layer, ω_i:

[1] Since snow was not included in the data sets we use, it is not considered here

$$\lambda_{T,i} = 3.8\,|\psi_{sat}|^{-1/\ln 10}\left(\frac{\omega_{sat}}{\omega_i}\right)^{-b/\ln 10} \tag{4.10}$$

ω_{sat} is the saturation moisture content, ψ_{sat} is the saturated matric potential and b the Clapp and Hornberger parameter. For very dry soils a minimum value is adopted for λ_T. The values of ψ_{sat}, ω_{sat} and b depend on the soil type, and are classified in 11 categories (Clapp and Hornberger, 1978). As suggested by Mahrt and Pan (1984), the heat flux at layer interfaces are computed with the "upstream" values for λ_T, that is, the highest conductivity in either of the two adjacent layers, to minimize truncation errors associated with the profile discretization.

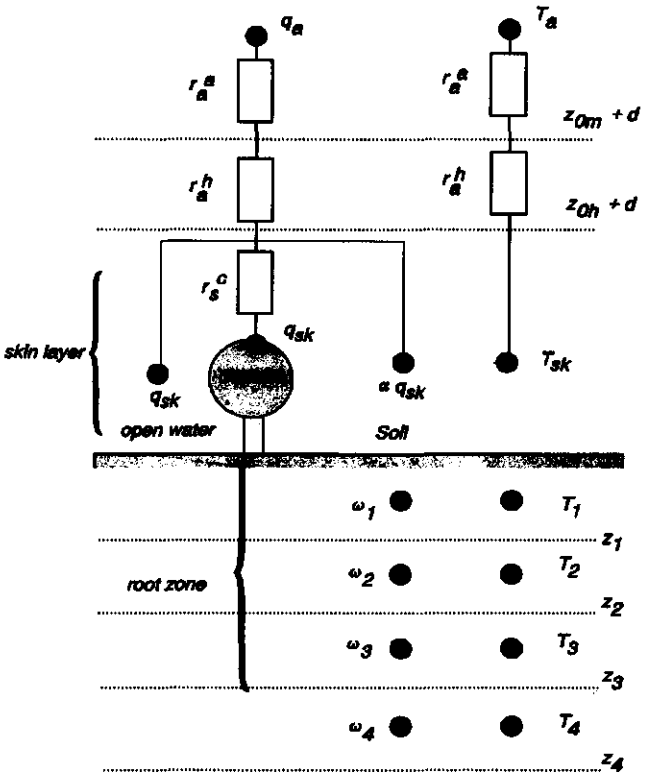

Figure 4.1: Schematic representation of the model of Viterbo and Beljaars (1995). For explanation, see text

Soil moisture transport is parameterized with a similar scheme, but here two additional processes cause a change of the moisture content in a certain layer: free drainage due to gravity, and root extraction by vegetation. The rate equation for soil moisture is given by

$$\rho_w \frac{\partial \omega}{\partial t} = -\frac{\partial}{\partial z}\left[-\rho_w\left(\lambda_H \frac{\partial \omega}{\partial z} - \gamma_H\right)\right] + \rho_w S_\omega \qquad (4.11)$$

In this equation, ρ_w is the density of liquid water, λ_H is the hydraulic diffusivity, γ_H the hydraulic conductivity and S_ω the root extraction of water. In each layer, λ_H and γ_H are also a function of water content, according to

$$\gamma_H = \gamma_{sat}\left(\frac{\omega}{\omega_{sat}}\right)^{2b+3} \qquad (4.12)$$

and

$$\lambda_H = \frac{b\,\gamma_{sat}|\psi_{sat}|}{\omega_{sat}}\left(\frac{\omega}{\omega_{sat}}\right)^{b+2} \qquad (4.13)$$

Again, a minimum value is adopted for both γ_H and λ_H, corresponding to the permanent wilting point of the soil, ω_{pwp}. The boundary conditions are provided by the infiltration of rain minus the bare soil evaporation at the top, and a free drainage at the bottom (taking $\partial\omega/\partial z = 0$).

The soil component of the model is coupled to the atmosphere by way of a so-called skin layer, which has no heat capacity of its own. This skin layer represents the heat transfer through the vegetation layer and loose organic material formed by litter or soil organisms. The skin layer has a uniform temperature, T_{sk}. The soil heat flux is parameterized empirically using an effective "conductivity", Λ:

$$G = \Lambda\,(T_{sk} - T_1) \qquad (4.14)$$

in which T_1 is the temperature of the top soil layer. T_{sk} is solved similar to the big-leaf model by considering the energy balance of the surface, which can be written as

$$(1-a)\,K^{\downarrow} + (1-\varepsilon)\,L^{\downarrow} - \varepsilon\sigma T_{sk}^4 = \rho c_p \frac{\theta_{sk} - \theta_a}{r_a} + \rho\lambda\left(x_s q_{sat}(T_{sk}) - x_l q_a\right) + \Lambda\,(T_{sk} - T_1) \qquad (4.15)$$

where x_s and x_l are resistance coefficients governed by the relative evaporation fractions of the surface, and their corresponding water transfer resistances (in the original scheme of VB95 the potential temperature at z_R was approximated as $T_a + g/c_p\,z_R$). The fraction of vegetation cover, σ_f, is a surface dependent parameter. The fraction of the surface covered with the skin reservoir, C_l, depends on the amount of intercepted dew and precipitation by the canopy leaves and soil surface. When snow may be ignored, the three evaporation fractions are the open water skin reservoir (C_l), the vegetation ($(1 - C_l)\,\sigma_f$) and bare soil ($(1 - C_l)\,(1 - \sigma_f)$). The resistance coefficients are simple weighted averages of the separate resistances according to

$$x_l = \frac{C_l}{r_a} + \frac{(1 - C_l)\,\sigma_f}{r_a + r_s^c} + \frac{(1 - C_l)(1 - \sigma_f)}{r_a} \tag{4.16}$$

$$x_s = \frac{C_l}{r_a} + \frac{(1 - C_l)\,\sigma_f}{r_a + r_s^c} + \frac{\alpha\,(1 - C_l)(1 - \sigma_f)}{r_a} \tag{4.17}$$

where r_s^c is the canopy resistance, and α the relative humidity at the soil surface. The total surface evaporation, E, is a weighted function of the evaporation rates from the skin reservoir (E_l), the canopy (E_c) and the bare soil (E_s):

$$E = C_l E_l + (1 - C_l)\left(\sigma_f E_c + (1 - \sigma_f) E_s\right) \tag{4.18}$$

In this formulation soil evaporation is treated using a so-called α-type resistance model (Kondo *et al.*, 1990). Rather than regulating soil evaporation by use of an extra soil evaporation resistance over the humidity gradient between the surface and the reference level (β-type resistance model), the relative humidity at the bare soil surface, α, is parameterized. In VB95, α is a semi-empirical function of the soil content in the upper soil layer:

$$\alpha = \begin{cases} 0.5\left[1 - \cos\left(\dfrac{\pi}{l_c}\dfrac{\omega_1}{\omega_c}\right)\right] & \omega_1 < l_c\,\omega_{fc} \\ 1 & \omega_1 \geq l_c\,\omega_{fc} \end{cases} \tag{4.19}$$

in which ω_c is a critical moisture content (in practice taken equal to the field capacity of the soil, ω_{fc}), and the factor l_c (set to 1.6) accounts for the difference between the average moisture content in the top soil layer and the moisture content near the surface. To avoid excessive dewfall for dry soils during daytime, the humidity gradient $\alpha q_{sat}(T_{sk}) - q_a$ is removed when $q_{sat}(T_{sk}) > q_a$ and $\alpha q_{sat}(T_{sk}) < q_a$ (Blondin, 1991).

The fraction of the surface covered with the skin reservoir, C_l, is determined by the depth of the skin reservoir, w_{dew}, given by

$$C_l = \min\left(1, \frac{w_{dew}}{w_{\max}}\right) \tag{4.20}$$

where $w_{\max}$ depends on the leaf area index LAI_* according to

$$w_{\max} = \left[\sigma_f LAI_* + (1 - \sigma_f)\right] W_{MAX} \tag{4.21}$$

Here, LAI_* refers to the leaf area per unit surface covered by vegetation, equal to LAI/σ_f. W_{MAX} is the maximum amount of water that can be retained on a leaf surface. The rate-equation for w_{dew} is governed by the rate of evaporation from the skin reservoir ($C_l E_l$) and

the interception, I, according to

$$\frac{\partial w_{dew}}{\partial t} = \frac{I + C_l E_l}{\rho_w} = \frac{C_l E_l}{\rho_w} + \frac{I}{\rho_w} \tag{4.22}$$

The dew reservoir can evaporate very fast into the atmosphere, giving numerical difficulties. A careful solution was proposed by VB95 in which the linear dependence of C_l on w_{dew} (eq. 4.20) is used. The interception of rain in the dew reservoir is calculated according to a simple bucket scheme, taking the unfilled space of the dew reservoir and convective or large-scale precipitation of rate P into account:

$$I = \min\left(0.25\,\sigma_f \frac{P}{k_p},\ \rho_w \frac{w_{\max} - w_{dew}}{\Delta t}\right) \tag{4.23}$$

The factor 0.25 accounts for the efficiency of interception of precipitation, and k_p is a precipitation heterogeneity coefficient, equal to 0.5 for convective precipitation and 1 for large scale precipitation. The remaining precipitation forms the throughfall rate, T, and is available for infiltration into the soil, I_s:

$$I_s = \mathrm{T} - E_s = P - I - E_s \tag{4.24}$$

where a reduction of soil infiltration due to soil evaporation is accounted for. Infiltration rates exceeding the maximum uptake capacity of the top soil layer is added to run-off.

The aerodynamic exchange between the surface and the reference level is similar for all surface fractions. VB95 assume an equal exchange for scalars and momentum between z_{0m} and z_R, but allow for a lower surface roughness z_{0h} for heat and scalars. The total aerodynamic resistance, r_a, appearing in eq. 4.15, is therefore given by eq. 4.4. r_a can also be expressed using the bulk transfer coefficient for heat, C_H, according to

$$r_a^a = \frac{1}{C_H u_a} \tag{4.25}$$

where u_a is the wind speed at reference height. C_H was solved using the stability functions Ψ_h of Beljaars and Holtslag (1991).

Finally, in VB95 the canopy resistance, r_s^c, is parameterized using a Jarvis-type model (Jarvis, 1976) according to

$$r_s^c = \frac{r_{s,\min}}{LAI_*} F_1(\mathrm{PAR})\, F_2(\overline{\omega}) \tag{4.26}$$

where $r_{s,\min}$ is a minimum stomatal resistance. The definition of LAI_* is equivalent to setting r_s^c(VB95) = $\sigma_f\, r_s^c$(big leaf) (see previous section). A dependence of r_s^c on air humidity or air temperature is not included. Dickinson *et al.* (1991) noted that there is no agreement among modellers for the water stress dependence, and the available empirical evidence does not allow for a general formulation. The functional dependence of r_s^c on PAR is expressed as

$$F_1(\mathrm{PAR}) = \left(1 - a_1 \ln \frac{a_2 + \mathrm{PAR}}{a_3 + \mathrm{PAR}}\right)^{-1} \tag{4.27}$$

where a_1, a_2 and a_3 are coefficients which may be related to canopy properties. PAR is estimated by taking $0.55\, K^{\downarrow}(1 - a)$. The dependence on soil humidity is similar to the formulation proposed by Noilhan and Planton (1989), reading

$$\frac{1}{F_2(\overline{\omega})} = \begin{cases} 0 & \overline{\omega} < \omega_{pwp} \\ \dfrac{\overline{\omega} - \omega_{pwp}}{\omega_{fc} - \omega_{pwp}} & \omega_{pwp} < \overline{\omega} < \omega_{fc} \\ 1 & \overline{\omega} > \omega_{fc} \end{cases} \tag{4.28}$$

In eq. 4.28 $\overline{\omega}$ is defined as

$$\overline{\omega} = R_1 \omega_1 + R_2 \omega_2 + R_3 \omega_3 \tag{4.29}$$

where R_i is the relative root extraction in layer i. $\overline{\omega}$ and S_ω (eq. 4.11) are parameterized by setting $R_1 = R_2 = R_3 = 1/3$, thereby defining an effective rooting depth of 1 m.

Eq. 4.15 is solved by linearizing T_{sk}^4 using a Taylor expansion and $q_{sat}(T_{sk})$ using a value of $\partial q_{sat}/\partial T$ at the value of T_{sk} of the previous timestep. The ECMWF-scheme uses C_H from the previous time step explicitly, and an implicit solver for the temperature at the new time level (Beljaars, 1992).

4.1.3 Impact of some simplifying assumptions in the new ECMWF-surface scheme[2]

Embedded in a global model, the new surface scheme presented by VB95 is designed to describe the surface fluxes over a wide range of possible vegetation covers and time scales. In order to avoid excessive data and computatial requirements, it is sometimes necessary to simplify the parameterization of the transfer of scalars and momentum to and from the surface.

One of the simplifications included in their scheme was the representation of the surface by a single layer with uniform temperature. This layer is referred to as a 'skin layer'. Four different grid box fractions with respect to evaporation are accounted for: bare soil, dry vegetation, an open water skin reservoir filled with dew and intercepted water, and snow (not treated here). The evaporation rate of each of these fractions is computed using a humidity gradient between a reference level and the appropriate surface component (see above).

In practice, the temperature of a non-uniformly vegetated surface can exhibit large differences between e.g. the vegetation and the bare soil component of the surface. In conditions of a well-irrigated vegetation stand only partially covering the surface and high

[2] Adapted from Van den Hurk and Beljaars (1995)

sensible heat release by the bare ground, adopting a single surface temperature for both the vegetation and the bare ground can lead to a significant overestimation of the canopy evaporation rate. Also, the predicted soil evaporation rate is often strongly overestimated for a few hours after a period with rain, when canopy is also present. The temperature of the canopy component rapidly increases once the intercepted water is evaporated, and this temperature increase unrealistically enhances the simulated evaporation rate of the bare ground.

A second simplification employed by VB95 is the use of an effective conductivity for heat transfer through the skin layer. This skin conductivity, Λ (units W/m^2K), defines the temperature difference between the top soil layer and the skin layer, and accounts for the heat flow into the soil component. A uniform value of 7 W/m^2K was chosen as to realize a reasonable amplitude of the diurnal cycle of the ground heat flux, following Beljaars and Betts (1992).

This section explores the consequence of these two simplifications for the sensible and latent heat fluxes over partially vegetated regions. First, the original scheme is compared to a slightly modified form, in which the temperatures are defined separately for the relevant surface components. The performance and practical consequences of this modification are evaluated using data collected during FIFE-1987 (Sellers *et al.*, 1988) and EFEDA-1991 (Bolle *et al.*, 1993). Second, a suggestion for a physical interpretation for Λ is made, and its value is evaluated experimentally. For this purpose, again EFEDA-1991 data are considered.

- **The skin layer temperature**

In order to avoid the unrealistic coupling between different surface fractions (e.g., bare soil and vegetation) through a single skin temperature, it is necessary to allow this skin temperature to be different for the bare soil, the vegetation and wet surface fractions. Once the vegetation temperature is allowed to differ from the bare ground temperature, excessive canopy evaporation under dry conditions is readily avoided. In practice, vegetation can remain much cooler than bare ground, because it can sustain evaporation by accessing water from deeper soil layers. Multiple source models, as presented for instance by Dolman (1993), allow for these temperature differences by using the Penman-Monteith concept (Monteith, 1981) separately for the canopy elements and the underlying soil.

The scheme of VB95 solves the skin temperature T_{sk} implicitly by considering the energy balance of the surface (eq. 4.15), in which the soil heat flux G is given by eq. 4.14. The total sensible and latent heat fluxes H and λE can be deduced from eq. 4.15 and are specified according to

$$H = \rho C_H u_a \left(c_p T_{sk} - c_p T_a - g z_R \right) \tag{4.30}$$

and

$$\lambda E = \lambda \rho \left(x_s q_{sat}(T_{sk}) - x_l q_a \right) \tag{4.31}$$

where the original formulation is used for the potential temperature at z_R.

Obviously, the values for T_{sk} found from eqs. 4.15, 4.30 and 4.31 will depend on the relative surface fractions covering the grid box. When the crop resistance differs from 0 and the relative humidity at the soil surface < 1, T_{sk} will depend on C_l and σ_f. For instance, with $C_l = 1$ the entire grid box has a wet skin reservoir, and the skin temperature will adjust to a potential evaporation rate ($r_s^c \rightarrow 0$, $\alpha \rightarrow 1$). In cases where $C_l = 0$ and $\sigma_f = 1$ (vegetation only) the skin temperature will be lower than when $\sigma_f = 0$ (bare ground only), owing to the larger evaporation capacity of vegetation.

A straightforward strategy to compute the temperatures of the different surface fractions is to solve eq. 4.15 separately for each component, by choosing appropriate values for x_l and x_s. The final grid box averaged energy flux is then computed from the energy fluxes and temperatures from each component according to the same weighting scheme as presented in eq. 4.18. A similar strategy is adopted in the "tile"-approach by Koster and Suarez (1992), albeit that in their model the energy balance in each tile is solved by using a simplified form of the two-component model SiB (Sellers *et al.*, 1986).

For practical applications two issues need further attention: the stability dependence of C_H, and the solution of the surface temperature from the linearization around the previous timestep.

An important issue is the treatment of the aerodynamic resistance between the surface and the lowest atmospheric grid point, $r_a = 1/C_H u_a$. Since the value of C_H depends on atmospheric stability — and therefore on the sensible heat flux — its value is expected to be different for the separate surface fractions when local energy balances differ. In the VB95 model the transfer from the different surface fractions is computed independently, using a uniform value of C_H for all fractions. The independent treatment of surface fractions is reasonable if the surface fractions are large enough to have internal boundary layers that do not merge below the lowest model level. For patchy surfaces with small horizontal scales, it would be necessary to introduce an extra node in the resistance network somewhere between the surface and the lowest model level (Blyth, 1995), but such a concept is difficult to handle in a global model without appropriate data sets.

In line with VB95 it would be appropriate to parameterize the transfer coefficient C_H separately for each surface fraction. In that context, the stability correction in C_H for each fraction is dependent on its exchange of sensible heat with the reference level. If additional storage of parameters between subsequent time steps should be avoided, the value of C_H can no longer be estimated from the previous time step, and for each fraction the energy balance should be solved iteratively in order to determine C_H. However, in general the stability functions in C_H are relatively unimportant in the parameterization of sensible and latent heat exchange between the surface and the atmosphere, and therefore a first approximation may be sufficient. The dependence of C_H on atmospheric stability can be expressed using an average sensible heat flux, which is obtained from the separate energy balance solutions and a weighting scheme defined by eq. 4.18. A major practical advantage is, that we can proceed deriving C_H from the previous time step and avoid iterations for determination of the surface temperature and the surface energy balance for each surface component.

When the temperatures of the individual surface components show significant differences (as can be the case for a sparsely vegetated surface with evaporation from

plants), the linearization of $\partial q_{sat}/\partial T$ at a (weighed) average value of T_{sk} from the previous timestep can introduce significant errors. Obviously, similar errors are introduced if a linearization around the reference temperature is carried out and the surface temperature differs significantly from this value (McArthur, 1990). The error can be minimized by storing all three surface temperatures separately rather than a weighed average between two subsequent time steps. Alternatively, for each component the surface temperature can be initialized with the weighed average from the previous time step, and a (small) number of iterations is needed in order to update $\partial q_{sat}/\partial T$ and to find the actual value of the surface humidity. The number of iterations will depend on the actual temperature differences, but generally can be limited to 2 or 3.

In the following we will demonstrate the implication of solving separate surface temperatures by adopting two iterations to solve the surface energy balance and find its temperature. The calculations are initialized using the average sensible heat flux and surface temperature from the previous time step, as is currently applied in the ECMWF surface scheme. In a subsequent section this numerical strategy will be compared to a fully iterative approach for solving the surface energy balance.

■ Case studies for the temperature differentiation

Two case studies demonstrate the effect of discerning between the different grid box fraction temperatures: a case regarding a drying surface after rain (measurements from FIFE), and the simulation of a series of diurnal courses of the evaporation of a sparse vineyard canopy surface (measurements taken during EFEDA).

Table 4.1: Surface parameters for the FIFE-1987 test case

parameter	symbol	value
roughness length for momentum	z_{0m}	0.3 m
roughness length for heat	z_{0h}	0.03 m
surface fraction covered with vegetation	σ_f	0.85
surface albedo	a	0.168
longwave emissivity	ε	0.996
initial soil temperature	T	291.4 K
initial soil humidity	ω	field capacity

A drying surface after rain

The original model of VB95 was validated with several data sets, including the data collected during the FIFE-1987 experiment (Sellers *et al.*, 1988). During this experiment micrometeorological parameters were measured during 168 days, from May until October 1987. Data were collected above a tallgrass prairie in rolling terrain. Half hourly averages of temperature, wind speed and air humidity at reference height, as well as incoming longwave and shortwave radiation are available. During four intensive field campaigns (IFC's) eddy correlation data of sensible and latent heat flux density were collected, together with net radiation and soil heat flux density. The observations from all available stations

were averaged to obtain a single time series by Betts and Ball (1992).

Both the original and the modified scheme were used to simulate the surface fluxes for the entire experimental period. All model settings (including soil type and root profile) were taken as in the original paper. Values of some surface specific parameters can be found in Table 4.1. The soil moisture profile was initialized at field capacity, and a vertically uniform temperature profile was taken as initial profile.

For comparison with measured fluxes, a situation is selected in which the surface is drying after a period of rain. For the present study the simulations for days 176 and 177 are chosen. Unlike the intercomparisons in VB95, we focus on diurnal variations of measured and predicted surface fluxes.

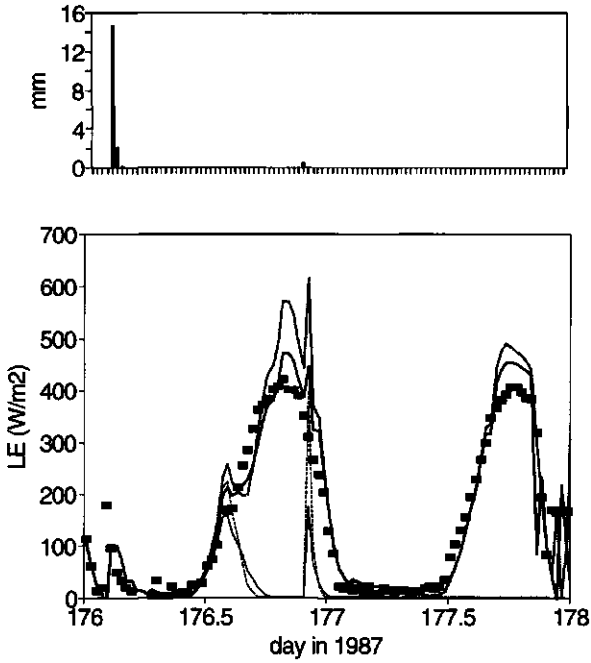

Figure 4.2: (Lower panel:) Observed (■) and simulated (heavy lines) total evaporation for FIFE-1987, days 176 and 177. Simulations are carried out with both the original VB95 model (·····) and the new version with different temperatures for different surface fractions (——). Also shown are the simulated evaporation from the skin reservoir, $C_l\ \lambda E_l$ (thin lines) and observed precipitation (upper p

Figure 4.2 shows the simulated and observed total evaporation for the selected days. Also precipitation is shown, and the calculated evaporation from the skin-reservoir, λE_l. The new scheme reduces the overestimation of λE by approximately 50%, especially for day 176. Also the pronounced peaks caused by the skin evaporation are reduced, although not entirely removed. As was discussed by VB95, the skin reservoir is very shallow (< 0.7 mm), and can fill up and evaporate within a single time step. However, in their scheme the value of C_l is computed from the skin reservoir content in the previous time step. The result is that skin evaporation does not take place during the first time step of filling the reservoir by interception. Too large time steps can result in simulation of a excessive peak transpiration. The choice of the fairly large timestep used here (1800 s; equivalent to the time step in the

ECMWF model) causes the remaining part of the overestimation of the evaporation, visible in Figure 4.2.

The new solution for the surface temperature has a pronounced effect on the partitioning of the evaporation over the ground surface and the canopy. Figure 4.3 shows the simulated bare soil and canopy evaporation rates, given by $(1 - C_l)(1 - \sigma_f)\lambda E_s$ and $(1 - C_l)\sigma_f \lambda E_c$, respectively. Since the soil is wet just after a rainy period, the bare soil evaporates at a nearly potential rate, which has a strong feedback to the surface temperature. The old scheme simulates a maximum weighted soil evaporation of about 300 W/m^2. For the bare ground fraction (equal to 15% when $C_l = 0$), this is equivalent to 2000 W/m^2! The reason is that the dominating vegetated part enforces its higher surface equilibrium temperature on the bare soil fraction. Allowing for different temperatures of the soil and the canopy component causes a reduction of 50% of the soil evaporation, whereas the canopy evaporation is enhanced by approximately 10% around noon.

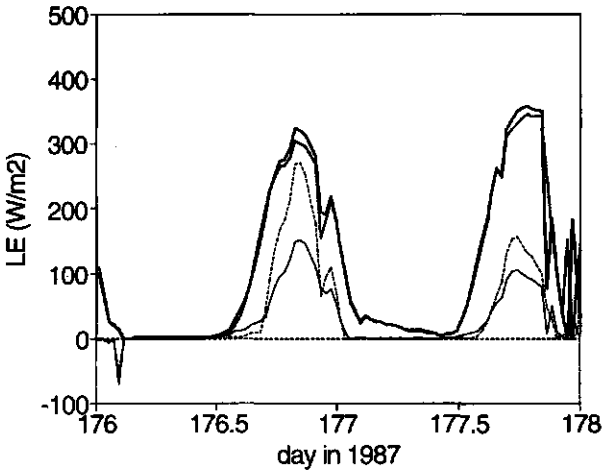

Figure 4.3: Simulation of the canopy evaporation, $(1 - C_l)\sigma_f \lambda E_c$ (thick lines) and soil evaporation, $(1 - c_l)(1 - \sigma_f)\lambda E_s$ (thin lines) for the original model (·····) and new version (——)

A sparsely vegetated vineyard

The model of VB95 was also run for a sparsely vegetated Mediterranean vineyard area for five consecutive days in June 1991. Data were collected in the Tomelloso area during the EFEDA-I intensive measurement campaign (Bolle *et al.*, 1993). The fraction of area covered by vegetation was about 12% in the considered period, and the Leaf Area Index did not exceed 0.3 m^2/m^2. Since dew and precipitation were absent in this period, the fraction of area covered by the skin reservoir (C_l) was zero all time. The soil consisted of sandy loam material and the top layer was covered with stones and very dry. The plants extracted water from deeper soil layers (> 1 m), and canopy evaporation could be sustained in spite of the very dry top soil.

Energy balance measurements were obtained as indicated in section 2.4.3. Surface temperatures were obtained from an infrared sensor moving along the cable at 3 m height

(section 2.2.3). The crop resistance r_s^c was inferred from measured values of total evaporation and canopy temperature. Evaporation from the underlying soil was assumed zero, and aerodynamic resistances in the pathway between the canopy and the reference height were parameterized according to Choudhury and Monteith (1988). Sene (1994) showed that the final value of r_s^c is not sensitive to the exact values of these aerodynamic resistances. More details about the experimental setup can be found in section 2.2.

For the settings of most model parameters the suggestions made by VB95 were followed. The original treatment of the crop resistance (eqs. 4.26 - 4.28) was replaced by the formulation of Choudhury and Monteith (1988), calibrated to match the current data (see Figure 4.4). The physical soil parameters were quantified according to the sandy loam soil type cited by Noilhan and Planton (1989). Surface albedo was taken 0.29 at all times, obtained from field observations. The apparent conductivity of the skin layer (Λ) was taken 7 W/m^{2}K, and the drag coefficient C_H was computed using z_{0m}/z_{0h} = 200, following Van den Hurk *et al.* (1995). These adaptations were necessary to predict a reasonable value of the surface temperature and the soil heat flux.

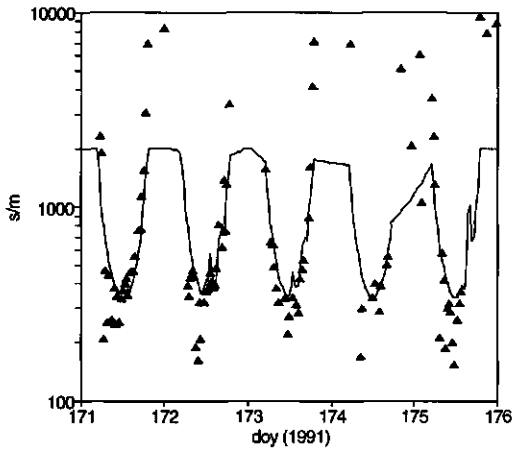

Figure 4.4: Values of the crop resistance for 5 days during EFEDA-91; ▲: data inferred from measured total evaporation; —— predictions using a calibrated model of Choudhury and Monteith (1988)

Figure 4.5 shows observations and simulations with the original scheme of bare soil temperature (4.5A), plant temperature (4.5B) and total latent heat flux (4.5C). Simulations with both the original and the modified scheme are shown. For the original model, the simulated temperatures of the canopy and the bare soil are represented by the average skin temperature.

The total soil heat flux and average surface temperature are hardly affected by the new parameterization (figures not shown). The surface temperature is dominated by the bare ground component, since the area fraction of vegetation was very limited (Figure 4.5A). However, the impact of the new temperature scheme on the total evaporation rate (4.5C) is significant, and a reduction of almost 50% is caused by adopting the new scheme. The reduction of the evaporation is balanced by a slight increase of the sensible heat flux, consistent with a closed surface energy balance.

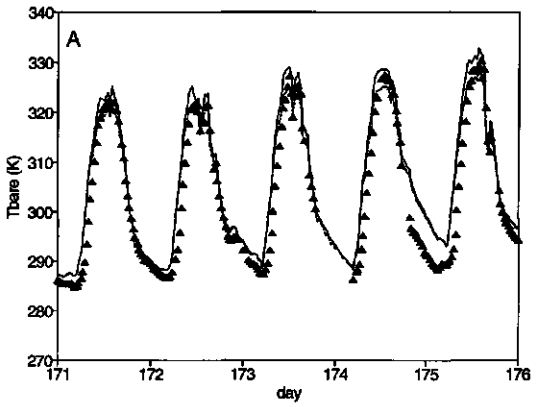

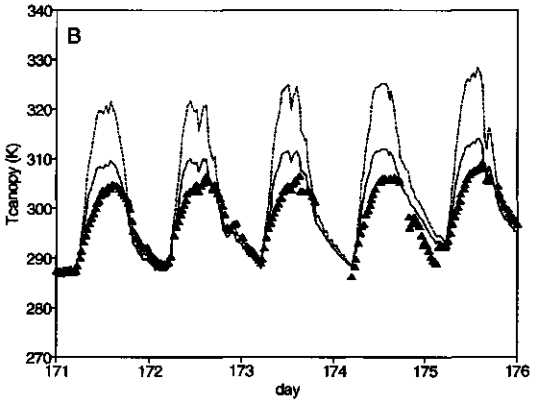

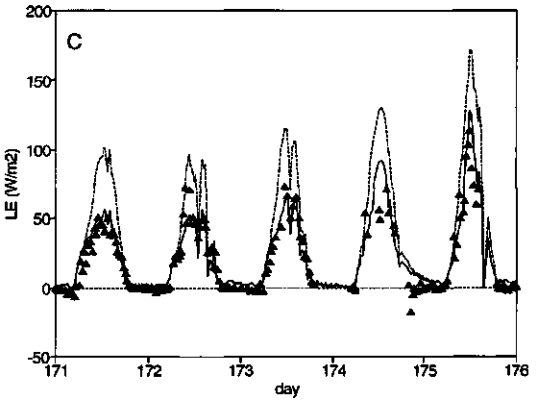

Figure 4.5: (A) Bare soil temperature, (B) canopy temperature and (C) total latent heat flux for the EFEDA-91 case. Shown are observations (▲) and model simulations with the original (·····) and new (——) formulation

Effect of the numerical scheme on the energy balance solution

During the second (EFEDA) case, occasions with high sensible heat fluxes and surface temperatures often occurred. Therefore this is a good case to demonstrate the effect of

numerical approximations of C_H, as outlined previously. We confined ourselves to the modified scheme, in which the surface temperatures are solved separately for each surfacefraction. Three strategies are compared:

(1) as applied above, that is, computing C_H by use of an average sensible heat flux from the previous time step, and solve the energy balance of each surface fraction by means of 2 iteration rounds

(2) same procedure, but with only a single iteration round, and

(3) same procedure, with iterations until convergence.

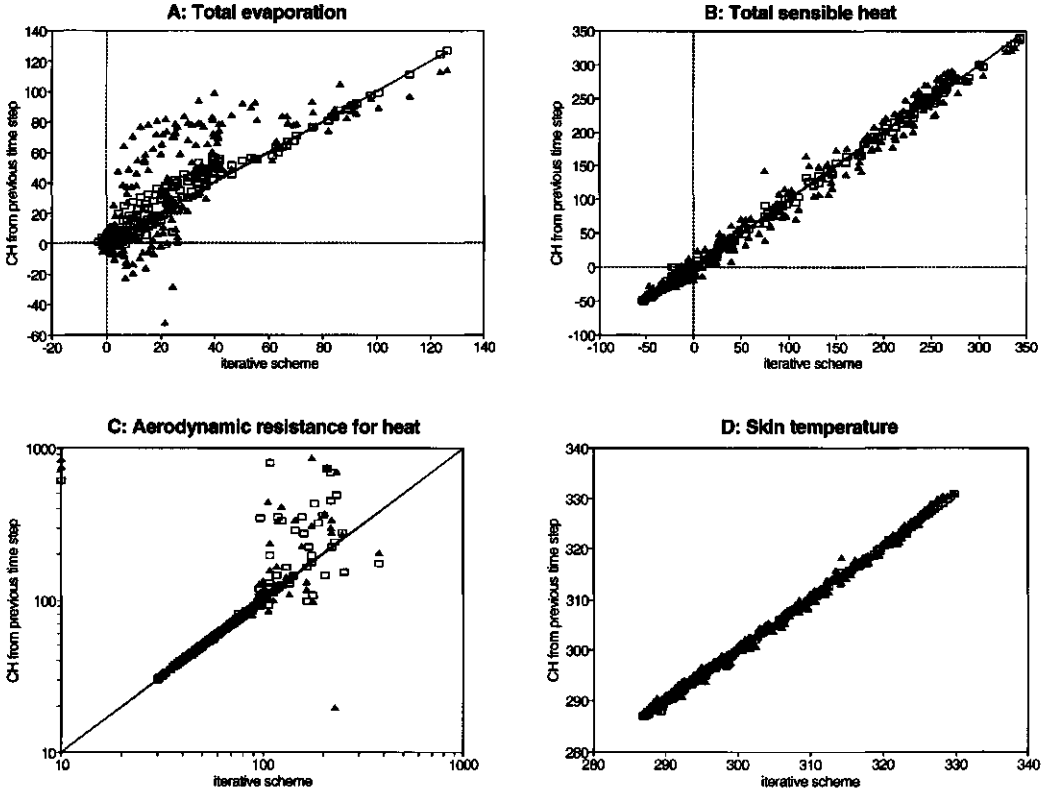

Figure 4.6: EFEDA-1991 simulations of (A) total evaporation, (B) total sensible heat flux, (C) aerodynamic resistance and (D) average skin temperature, computed by means of a fully iterative scheme for each surface fraction (x-axis), and an explicit correction of r_a for stability effect using sensible heat fluxes from the previous time step, with 1 (▲) and 2 (□) iterations (y-axis)

Figure 4.6 shows the results in terms of simulated total evaporation (4.6A), total sensible heat (4.6B), aerodynamic resistance r_a (4.6C) and bare soil temperature (4.6D). A clear difference is present between procedures (1) and (2) for especially the simulated latent heat flux. Ignoring the error involved with the linearization of $\partial q_{sat}/\partial T$ (procedure (2)) results in serious deviations compared to the fully iterative scheme (3). The deviations are particularly large for relatively low values of λE, which occur just after sunrise and before sunset when the rate of change of the surface temperature is large. Smaller deviations are

present for the sensible heat and bare soil temperature.

It is also evident from Figure 4.6 that a significant reduction of the deviation between an iterative and an explicit formulation is obtained by allowing for an extra iteration round (procedure (1)). The total evaporation, sensible heat and bare soil temperature agree now very well with the iterative approach. The aerodynamic resistance computed using C_H from the previous time step differs from the iterative solution for only a small number of high values of r_a, which occur under stably stratified conditions with small sensible heat fluxes. The large deviations shown in Figure 4.6C (on a logarithmic scale) are not found in the plots for sensible heat and bare soil temperature. The parameterization of the turbulent fluxes appears to be rather insensitive to the way stability effects are incorporated in C_H.

■ **The numerical value of the skin conductivity**

In the model of VB95, the apparent skin conductivity, Λ, is defined as the heat flux through the vegetation layer per degree temperature difference between the skin layer and the upper soil layer (see eq. 4.14). For calculations on the global scale, VB95 treat Λ as a fixed coefficient, with a value of 7 W/m^2K (Beljaars and Betts, 1992). However, considerably different values may be expected for different types of surfaces.

For densely vegetated canopies, the value of Λ includes the heat conductivity of the canopy elements, the air within the canopy layer, and the top soil layer. Complicated processes like aerodynamic transport within the canopy layer and heat conduction through the stems inhibit an easy quantitative assessment of Λ. However, since the presence of the vegetation will insulate the soil thermally from the atmosphere, Λ may be expected to be small.

On the other hand, when vegetation is sparse or absent, the skin temperature is dominated by the (underlying) soil. In that case, the temperature difference appearing in eq. 4.14 is proportional to the soil temperature gradient immediately below the surface, which may be significant, especially for dry soils. Eq. 4.14 can be compared to an ordinary conductivity equation for soil heat flow, of the form

$$G = -\Lambda\, \Delta T = -(\Lambda\, \Delta z)\frac{\Delta T}{\Delta z} \approx -\lambda_T \frac{\partial T}{\partial z} \qquad \textbf{(4.32)}$$

where ΔT is equal to $T_1 - T_{sk}$. From this equation, the apparent heat conductivity Λ can be interpreted as a physical conductivity by multiplication with a reference depth. The temperature difference defined by eq. 4.14 can be treated as a real gradient through division by the same depth. Thus, for bare soils $\Lambda\, \Delta z$ is proportional to the soil thermal conductivity λ_T, which depends on type and moisture content of the top soil.

A similar approach was followed by Mahrt and Pan (1984), who chose Δz to be the centre of the model top soil layer, that is, $z_1/2$. In cases of steep non-linear temperature gradients near the surface, significant truncation errors are introduced when z_1 is chosen too large. Therefore, a better choice for Δz would be the depth where the real temperature profile equals the temperature of the model top soil layer, T_1. In principal this will not be a constant depth. At times where the soil heat flux density is large, steep temperature profiles with an exponential shape are present, and Δz is expected to be closer to the surface than $z_1/2$.

The EFEDA-dataset, described above, provides a useful test-case to determine a value for Λ for a typical Mediterranean sparse canopy surface. Simulations of soil heat flux density were carried out using VB95, in which soil physical and aerodynamic parameters were selected as before. In order to examine the effects of the choice for Λ in the present ECMWF-scheme, sensitivity experiments were carried out with three different values of Λ, namely 7, 14 and 20 W/m^2K.

Figure 4.7 shows the simulated and measured soil heat flux G for the 5 consecutive days in June 1991. Clearly, the default value of 7 W/m^2K yields an underestimation of G of approximately 60% at all times. Λ = 20 W/m^2K gives an optimal simulation. The intermediate value of 14 W/m^2K results in only a slight underestimation of G (<20%, on the average). As a consequence of the surface energy balance equation the sensible and latent heat fluxes are reduced by several tens of W/m^2 at most when Λ is increased from 7 to 20 W/m^2.

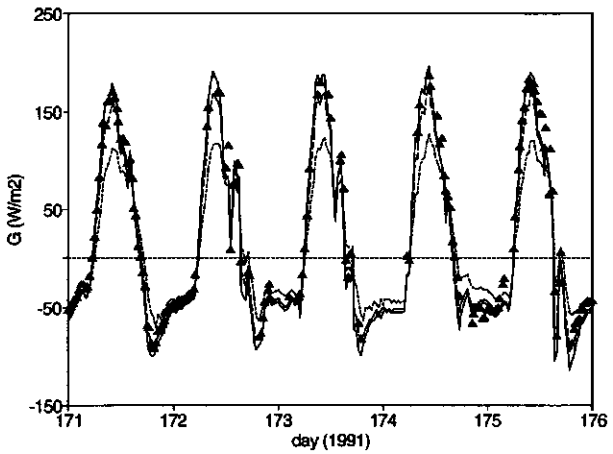

Figure 4.7: Measured (•) and simulated (lines) values of the soil heat flux for the EFEDA-1991 case. Simulations include Λ = 7 (·····), 14 (- - -) and 20 (——) W/m^2K

Also shown are the simulated temperatures of the skin layer and the first soil layer obtained using Λ = 7 and 20 W/m^2K (Figures 4.8A and 4.8B, respectively). Observations of the temperature of the upper soil layer were derived by an arithmetic average of the temperatures at z = 0.03 and z = 0.05 m. The effect of Λ on the skin temperature is only moderate. The skin temperature is a key parameter in the entire energy balance solution (eq. 4.15), and is only to a small extent determined by the heat flow into the soil. The prediction of the temperature of the first soil layer, however, is much improved when Λ = 20 W/m^2K is used.

■ Discussion and conclusions

This section considers two types of simplifications applied in the new ECMWF surface scheme: a uniform skin layer temperature, and a constant value of the skin layer conductivity for all surface types.

A simple scheme is presented to allow the different surface fractions (bare soil, dry vegetation and a skin reservoir of intercepted water) to adopt temperatures that are in

equilibrium with their state of evaporation, as in the Penman-Monteith concept (Monteith, 1965). The three surface temperatures are solved according to the original scheme by first regarding each of the fractions as if fully covering the grid box, and then average the resulting fluxes and surface temperatures using a similar weighting as used for the evaporation (eq. 4.18). By initializing each surface fraction energy balance solution using the average skin temperature from the previous time step, and employing a second iteration to minimize the error involved with linearization of $\partial q_{sat}/\partial T$, no additional information needs to be stored between subsequent time steps. This numerical scheme is shown to have virtually identical results as a full iteration for each surface fraction energy balance.

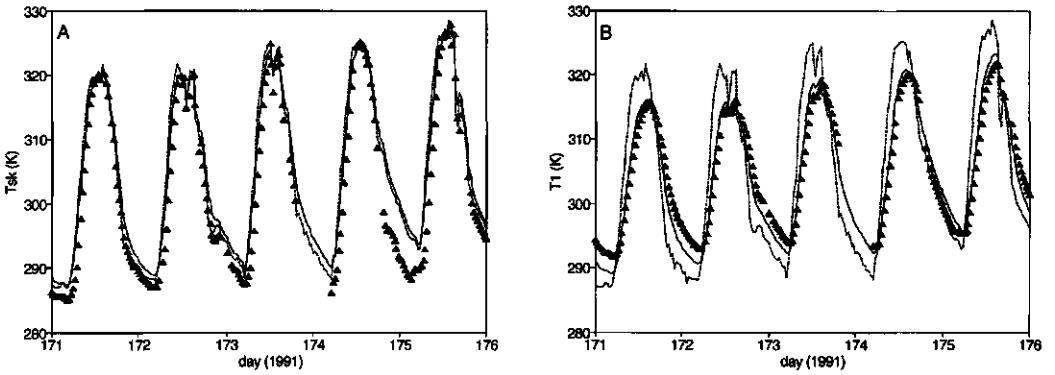

Figure 4.8: Observed (▲) and simulated (lines) values of (A) the skin temperature, and (B) temperature of the top soil layer. Simulations include $\Lambda = 7$ (·····) and 20 (——) W/m^2K

This procedure is somewhat different from the dual source models presented by e.g. Deardorff (1978), Shuttleworth and Wallace (1985) or Choudhury and Monteith (1988). In their models, an interaction between the bare soil and vegetation takes place directly by computing a temperature and humidity deficit within the canopy layer, and computing fluxes from either of these components through this canopy layer node. Blyth (1995) presented a more general concept by placing this node at some level between the surface and the lowest model layer, which serves as a reference height for the surface forcings.

A major disadvantage of this concept for large scale meteorological models is the data requirement. The values of the resistances between this node and the various surface fractions need to be parameterized, and cannot be expected to be of similar magnitude for all vegetation types or degrees of coverage (McNaughton and Van den Hurk, 1995). In the current ECMWF-scheme the aerodynamic transfer between the surface and the reference level allows no direct interaction between various surface fractions, since the fluxes from each component are treated as purely additive. However, in a surface layer model coupled to a model for the rest of the atmosphere, the surface fluxes will affect the meteorological forcings at the reference height via boundary layer interaction. This feedback serves as an indirect interaction mechanism between the surface fractions.

In the original scheme, the computation of the surface evaporation (eq. 4.18) is

conceptually almost[3] similar to defining a single surface resistance for evaporation, weighted by the various grid box fractions (see eqs. 4.16 and 4.17). Based on numerical simulations over heterogeneous terrain, Blyth *et al.* (1993) argue that an average resistance defined in this way will underestimate an *effective* surface resistance, which is defined by the ratio of the humidity gradient to the average flux in the grid box. This effective resistance should be obtained by weighting the surface resistances in a grid box by the various fluxes rather than by the grid box fractions. In the new scheme, however, the effective resistance is no longer solely determined by the grid box fractions, but takes differences between humidity gradients of the various fractions also into account. By definition, a single surface resistance yielding the same average flux is now equal to the effective resistance, weighted by the fluxes from the various grid box fractions. Obviously, this is only applicable to the fractions which are actually considered in the surface model: the influence of a variability of different crop resistances for patches of different vegetation types within a grid box (Koster and Suarez, 1992) is only implicitly included in the parameterization of r_s^c present in VB95.

In a case study where the behaviour of a drying vegetated surface wetted by rain was simulated, the new scheme considerably altered the partitioning of latent heat flux over the vegetation and the soil. In the original scheme maximum soil evaporation was of the same order as the canopy evaporation, in spite of the fact that only 15% of the surface was not vegetated. The new scheme reduced the soil evaporation by 50%, and enhanced the canopy evaporation slightly.

A case study carried out using a dataset collected over a sparsely vegetated dry vineyard with negligible soil evaporation showed a significant reduction of the canopy evaporation. The simulations of total evaporation carried out with the new scheme matched observations rather well, while the original scheme caused an overestimation of approximately 100%. Obviously, a similar change of the simulated canopy evaporation could also be forced by changing the value of the surface resistance, r_s^c. However, it merely is the purpose of this demonstration to show the effect of the assumption of the uniform surface temperature used by VB95, rather than to verify all components of their model. The present case shows this assumption to have a significant impact on the canopy evaporation rate.

In general, solution of the surface temperature for separate surface components reduces evaporation of those components which are cooler than their surroundings. In the FIFE-dataset, the soil evaporation was significantly reduced, whereas evaporation by the vegetation was reduced for the Spanish simulation.

Also the parameterization of the soil heat flux by use of a skin conductivity Λ, assumed constant for all vegetation types, was evaluated using data collected during EFEDA-1991. It was shown that for the limit of a bare soil surface, Λ is proportional to the soil thermal conductivity λ_T. The coefficient of proportionality is a reference depth Δz. Mahrt and Pan (1984) proposed to choose Δz as the centre of the top soil layer, but for steep non-linear temperature gradients this depth may be chosen closer to the surface.

For the dry Mediterranean vineyard, soil temperature and soil heat flux data showed

[3] A deviation from this concept is caused by treating the evaporation from the bare soil component using the relative humidity α, rather than defining a soil evaporation resistance

that $\Lambda = 20$ W/m^{2}K is a better estimate than the presumed value of 7 W/m^{2}K. For this case, the thermal conductivity of the upper soil levels was estimated at 0.3 W/mK (Verhoef *et al.*, 1995). Using $\Lambda = 20$ W/m^{2}K, Δz would be approximately 1.5 cm.

The value of $\Lambda = 7$ W/m^{2}K was obtained from soil heat flux densities observed at a meadow grass land site near Cabauw, The Netherlands (Beljaars and Betts, 1992). The difference with the value found from the EFEDA-1991 data is presumably associated with the different insulation properties of the vegetation types at both sites. Whilst the sparse vineyard canopy had a low degree of vegetation cover (~12%) hardly providing a barrier for heat transfer between the soil and the atmosphere, the grass vegetation near Cabauw more effectively insulated the underlying soil. These two values found for Λ possibly mark the likely range of values for most surface types. Including experimental evidence for tall vegetations (forests) or completely bare surfaces (deserts) might further extend this range. However, in order to limit the global input requirement, a simple differentiation between the two values of Λ — preferably based on grid box vegetation cover — would provide a significant improvement of current parameterizations.

For surface flux predictions at seasonal or even annual time scales, the exact determination of the soil heat flux is not too crucial. The diurnal average soil heat flux is generally small compared to the total net radiative energy supply. However, the diurnal course of G affects the predicted diurnal latent and sensible heat flux patterns. For various applications these diurnal patterns have a considerable impact (e.g., prediction of temperature at screen height, timing of development of convective clouds, studies of atmosphere-surface feedback processes etc.), and a correct estimate of G may be significant.

4.1.4 The two-layer model of Deardorff

Unlike the surface schemes discussed above, the surface model of Deardorff (1978, referred to as D78) treats sensible and latent heat fluxes separately for the vegetation elements and the underlying soil. It was one of the first two-layer models, presented in a paper actually comparing various parameterizations of surface temperature related to soil heat flux density. Deardorff's model is the base of the Biosphere-Atmosphere Transfer Scheme (BATS), developed by Dickinson *et al.* (1986, 1993) for application in GCM's. In the version included here a few minor parameterizations were replaced as recommended by Dickinson *et al.* (1986). A schematic lay-out of Deardorff's model is shown in Figure 4.9.

The basic concept of D78 consists of a solution of the energy balance of the canopy elements and the soil surface separately. Ignoring heat storage in the vegetation and energy consumption by photosynthesis, the canopy energy balance is given by

$$K_c^{\downarrow} - K_c^{\uparrow} + L_c^{\downarrow} - L_c^{\uparrow} = H_c + \lambda E_c \qquad (4.33)$$

At the soil surface the energy balance is

$$K_s^{\downarrow} - K_s^{\uparrow} + L_s^{\downarrow} - L_s^{\uparrow} = H_s + \lambda E_s + G \qquad (4.34)$$

In eqs. 4.33 and 4.34 the subscripts c and s denote canopy and soil fluxes, respectively.

The partitioning of net radiation over the canopy and the soil surface is specified by

use of a vegetation coverage factor σ_f. Unlike the later two-component models (see next section), D78 does not entirely rely on a solution of the Penman-Monteith equation, but on a direct solution of the surface flux equations by using prognostic equations for the surface temperature and humidity. This prognostic equation is derived from the force-restore method for the temperature and humidity of the soil surface.

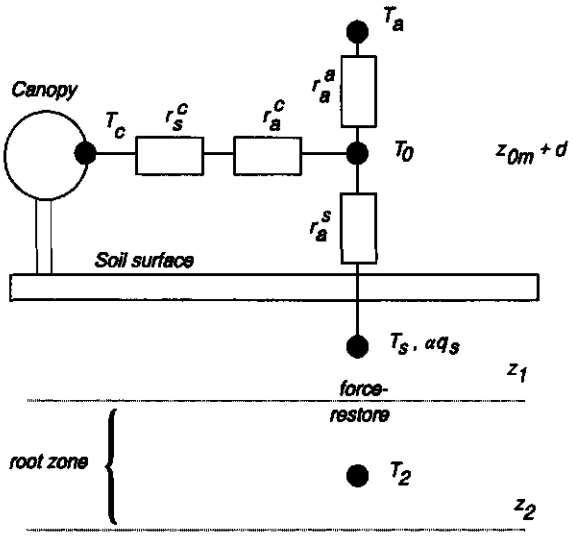

Figure 4.9: Schematic layout of the model of Deardorff (1978). For explanation of symbols: see text

Incoming shortwave radiation is distributed over the canopy and soil proportional to σ_f, according to

$$\begin{aligned} K_c^{\downarrow} &= \sigma_f K^{\downarrow} \\ K_s^{\downarrow} &= (1 - \sigma_f) K^{\downarrow} \end{aligned} \tag{4.35}$$

The canopy is not transparent to shortwave radiation. The reflected shortwave radiation is calculated using a separate canopy and ground albedo, a_c and a_s:

$$\begin{aligned} K_c^{\uparrow} &= a_c K_c^{\downarrow} \\ K_s^{\uparrow} &= a_s K_s^{\downarrow} \end{aligned} \tag{4.36}$$

Net longwave radiation of each component is determined by the atmospheric emission (distributed similarly as for shortwave radiation) and longwave exchange between the canopy and soil. The canopy emits longwave radiation upwards and downwards, and absorbs radiation emitted by the atmosphere and the ground:

$$L_c^{\downarrow} - L_c^{\uparrow} = \sigma_f \left[\varepsilon_c L^{\downarrow} + \frac{\varepsilon_c \varepsilon_s}{\varepsilon_c + \varepsilon_s - \varepsilon_c \varepsilon_s} \sigma T_s^4 - \frac{\varepsilon_c + 2\varepsilon_s - \varepsilon \varepsilon_s}{\varepsilon_c + \varepsilon_s - 2\varepsilon_c \varepsilon_s} \varepsilon_c \sigma T_c^4 \right] \tag{4.37}$$

in which the same subscript conventions apply as before. The longwave radiation components at the ground surface are given by

$$L_s^{\downarrow} = (1 - \sigma_f)\,\varepsilon_s L^{\downarrow} + \sigma_f \frac{\varepsilon_c \sigma T_c^4 + (1 - \varepsilon_c)\,\varepsilon_s \sigma T_s^4}{\varepsilon_c + \varepsilon_s - \varepsilon_c \varepsilon_s} \tag{4.38}$$

$$L_s^{\uparrow} = (1 - \sigma_f)\left[\varepsilon_s \sigma T_s^4 + (1 - \varepsilon_s) L^{\downarrow}\right] + \sigma_f \frac{\varepsilon_s \sigma T_s^4 + (1 - \varepsilon_s)\varepsilon_c \sigma T_c^4}{\varepsilon_s + \varepsilon_c - \varepsilon_s \varepsilon_c} \tag{4.39}$$

These relatively complicated equations simulate the longwave radiation exchange between two parallel plates, representing the canopy and the soil surface.

The transfer of heat and water vapour from each of the two surface components takes place via a common node in the resistance network (see Figure 4.9), representing the temperature and specific humidity of the air within the canopy layer, θ_0 and q_0 respectively. Here, a potential rather than an actual temperature is used. Since θ_0 and q_0 are affected by fluxes from both the soil surface and the canopy, a direct interaction between these two sources is allowed. The aerodynamic exchange of heat between the canopy elements and the canopy air is parameterized as

$$H_c = \Gamma_b \rho c_p \frac{\theta_c - \theta_0}{r_a^c} \tag{4.40}$$

where Γ_b is a factor accounting for sensible heat exchange from non-evaporating parts. The sensible heat exchange from the soil surface is given by

$$H_s = \rho c_p \frac{\theta_s - \theta_0}{r_a^s} \tag{4.41}$$

Here, the transfer coefficient formulations in D78 are expressed as a resistance formulation, comparable to the resistances in the other two-layer models. An equivalent formulation is used for the exchange of water vapour from the soil surface, written as

$$E_s = \rho \frac{q_s - q_0}{r_a^s} \tag{4.42}$$

The specific humidity at the soil surface, q_s, is treated similarly to VB95, that is, by expressing a surface relative humidity as a function of the soil moisture content of the top soil layer. In D78 the factor l_c appearing in eq. 4.19 to account for humidity gradients in the top soil layer, is set to unity.

The water vapour flux from the canopy is formulated somewhat differently, since it accounts for the evaporation from both intercepted water and from the canopy leaves. Analogous to eq. 4.42, a potential evaporation, E_c^{pot}, is first defined as

$$E_c^{pot} = \rho \frac{q_c - q_0}{r_a^c} \tag{4.43}$$

where $q_c = q_{sat}(T_c)$. The actual canopy evaporation, E_c, is a fraction ξ of E_c^{pot}. ξ depends on the stomatal resistance r_{st}, the leaf boundary layer resistance r_b and the relative amount of intercepted water, w_{dew}/w_{max}, given by

$$\xi = 1 - \delta \left[\frac{r_{st}}{r_{st} + r_b} \right] \left[1 - \left(\frac{w_{dew}}{w_{max}} \right)^{2/3} \right] \tag{4.44}$$

where $\delta = 0$ when condensation is occuring ($q_0 \geq q_c$) and unity otherwise. Unlike in VB95, a power function is used to express a higher dew evaporation rate when the dew reservoir gets empty, which in practice correponds to the formation of droplets on leaves with a large surface area. Combination of eqs. 4.43 and 4.44 yields the total canopy evaporation, E_c:

$$E_c = \xi E_c^{pot} \tag{4.45}$$

Only the transpiration by the leaves, E_t, is extracted from the soil water reservoir (see below), and is specified as

$$E_t = \delta \left[E_c^{pot} \frac{r_b}{r_{st} + r_b} \right] \left[1 - \left(\frac{w_{dew}}{w_{max}} \right)^{2/3} \right] \tag{4.46}$$

The canopy sensible and latent heat exchange are determined by an iterative solution of the canopy temperature, θ_c. A Newton-Raphson iteration scheme is used to solve T_c and θ_c from eqs. 4.37 - 4.45, for specified values of θ_0, q_0, T_s and radiative input.

The temperature at the soil surface, θ_s, is calculated by use of the force-restore method (Bhumralkar, 1975). The absolute surface temperature, T_s, is determined by a forcing heat supply from the surface (G) and a restoring thermal diffusion from below, depending on the temperature of the lowest slab, T_2:

$$\frac{\partial T_s}{\partial t} = \frac{2\sqrt{\pi}\, G}{\left(\rho' C_h d_1\right)_s} - \frac{2\pi (T_s - T_2)}{\tau_1} \tag{4.47}$$

τ_1 is the length of the diurnal wave (24 hrs). d_1 is equal to the depth of the diurnal temperature wave, and depends on the thermal diffusivity and volumetric heat content of the soil. Gradients of these thermal properties may be induced by a variation of soil moisture content with depth. Following Deardorff (1978), these gradients are accounted for by application of an empirical weighting over the two soil layers:

$$\left(\rho' C_h d_1\right)_s = r'\left[\left(\rho' C_h\right)_1 \sqrt{k_1 \tau_1}\right] + \left(1 - r'\right)\left[\left(\rho' C_h\right)_2 \sqrt{k_2 \tau_1}\right] \tag{4.48}$$

where r' is a coefficient equal to $0.30 + 0.05\omega_1/\omega_2$, and k_i is the thermal diffusivity (equal to $\lambda_T/\rho' C_h$) in layer i. T_2 can be estimated using the e-folding depth of the annual temperature wave, d_2:

$$\frac{\partial T_2}{\partial t} = \frac{G}{\left(\rho' C_h\right)_2 d_2} \tag{4.49}$$

with d_2 given by $\sqrt{k_2 \tau_2}$ and $\tau_2 = 365\ \tau_1$.

The force-restore method is based on the solution of the surface temperature for a periodic surface forcing, assuming that the thermal properties of the soil are constant with depth. Dickinson (1988) derived slightly modified force-restore expressions for a surface forcing which consists of higher harmonics (induced by for instance shading by clouds or surface elements). However, as he pointed out, the impact of the higher harmonics on the surface temperature is quickly damped, and can be ignored in most cases. He also considered non-homogeneous soils, of which soils covered with layers of snow or litter are extreme examples. Although the implications of this heterogeneity for a proper solution for T_s may be significant, these modifications are not considered here.

The soil moisture content of the top soil layer is also described using a force-restore parameterization, calibrated for various soil types by Noilhan and Planton (1989). The surface forcing is formed by the balance between the surface precipitation rate, P_s (given by $(1 - \sigma_f)P$), soil evaporation, E_s, and a fraction R_1 of the total canopy transpiration, E_t. The rate of change of the soil moisture content in the top layer is given by

$$\frac{\partial \omega_1}{\partial t} = \frac{C_1}{\rho_w z_{1,w}}\left(P_s - E_s - R_1 E_t\right) - \frac{C_2(\omega_1 - \omega_{equ})}{\tau_1} \tag{4.50}$$

The depth of the upper slab, $z_{1,w}$, is an arbitrary normalization depth, set to 0.1 m. Deardorff (1978) chose $R_1 = 0.1$, but we follow Noilhan and Planton (1989), ignoring transpiration extraction from the top layer. C_1 and C_2 are soil type specific coefficients depending on soil moisture content, porosity and isothermal water vapour transport. The coefficient C_1 is specified as

$$C_1 = \frac{2 z_{1,w}}{\sqrt{\frac{\tau_1}{\pi c_w}\left(\lambda_H(\omega_1) + \frac{K_T(\omega_1)}{\rho_w}\right)}} \tag{4.51a}$$

while C_2 is expressed using a calibration coefficient C_{2ref} depending on soil type as

$$C_2 = C_{2ref}\left(\frac{\omega_2}{\omega_{sat} - \omega_2 + \omega_1}\right) \tag{4.51b}$$

in which c_w is the hydraulic capacity (equal to $\partial\omega/\partial\psi$), K_T the isothermal water vapour diffusivity and ω_1 a small numerical value to limit C_2 at saturation. K_T is estimated as

$$K_T = \frac{\tau p}{p - e_{sat}(T_s)} \frac{D_v g e_{sat}(T_s)}{(R_v T_s)^2} (\omega_{sat} - \omega_1) \tag{4.52}$$

with D_v the molecular diffusivity of water vapour, $\tau = 0.66$ a tortuosity factor, and R_v the gas constant for water vapour (Braud *et al.*, 1993). The value of C_1 is limited to the value at $\omega_s = \omega_{sat}$. Noilhan and Planton (1989) give a simplified equation for C_1, in which isothermal water vapour diffusion is not included. In the current study, eq. 4.51a is used for C_1 instead.

An equilibrium lower soil moisture content, ω_{equ}, replaces ω_2 in eq. 4.50, to account for gravity effects. ω_{equ} is defined as

$$\omega_{equ} = \omega_2 - \omega_{sat}\left[a_{equ}\left(\frac{\omega_2}{\omega_{sat}}\right)^{p_{equ}}\left(1 - \left(\frac{\omega_2}{\omega_{sat}}\right)^{8p_{equ}}\right)\right] \tag{4.53}$$

In eq. 4.53 a_{equ} and p_{equ} are calibration coefficients, determined for various soil categories by Noilhan and Planton (1989).

The time dependent equation for the soil water content in the lowest soil layer is written as

$$\frac{\partial\omega_2}{\partial t} = \frac{1}{\rho_w z_{2,w}}\left(P_s - E_s - E_t\right) \tag{4.54}$$

$z_{2,w}$ is the depth of the bulk soil moisture reservoir, and must be specified explicitly.

The depth of the dew reservoir, w_{dew}, is determined as function of the intercepted precipitation, the collection of dew and the evaporation from the dew reservoir. Interception I is assumed to be equal to the precipitation falling on the part of the surface covered by canopy elements. w_{dew} thus changes according to

$$\frac{\partial w_{dew}}{\partial t} = \sigma_f P - \left(E_c - E_t\right) \qquad 0 \le w_{dew} \le w_{\max} \tag{4.55}$$

where $w_{\max}$ remains to be specified. Dew water collection exceeding the maximum reservoir depth is added to the soil precipitation rate, P_s.

Originally, D78 obtained θ_0 as a weighted average of the temperatures at the reference level, θ_a, of the canopy, θ_c and of the bare soil surface, θ_s. The weighting factors were assumed to be fixed. A value of q_0 was obtained similarly. Dickinson *et al.* (1986) replaced this formulation by a weighting over the resistances connected by the node within the canopy:

$$\theta_0 = \frac{\theta_a / r_a^a + \Gamma_b \theta_c / r_a^c + \theta_s / r_a^s}{1/r_a^a + \Gamma_b / r_a^c + 1/r_a^s} \qquad (4.56)$$

The aerodynamic resistance above the canopy, r_a^a, is expressed using the bulk transfer functions of Louis (1979). By choosing the roughness length for momentum, z_{0m}, to coincide with the within-canopy resistance node, the solution of r_a^a is similar to eq. 4.5. The excess resistance in the one-layer models formally corresponds to a combination of the extra resistances r_a^c and r_a^s in the two-layer models (see figure 4.9). D78 describes the bulk boundary layer resistance, r_a^c, equivalent to a leaf boundary resistance according to

$$r_a^c = \frac{r_b}{LAI} = \frac{1}{LAI\, 0.01 \sqrt{u_*/l_w}} \qquad (4.57)$$

where l_w is a characteristic leaf dimension. Eq. 4.57 is derived from Nusselt number scaling arguments, accounting for the difference between momentum and heat transfer. The value of the numerical coefficient (0.01 $m/s^{0.5}$) accounts for a development of an internal boundary layer on both sides of a flat leaf (Gates, 1980; see Appendix III).

In D78 the aerodynamic resistance between the bare ground and the canopy layer, r_a^s, is specified according to

$$r_a^s = \frac{1}{C_H [\sigma_f u_0 + (1 - \sigma_f) u_a]} \qquad (4.58)$$

where u_0 is a characteristic wind speed within the canopy. The original parameterization for u_0 of D78 was replaced by taking $u_0 = u_*$, as in the BATS-scheme. In the original D78 and BATS schemes, the bulk drag coefficient C_M was taken instead of C_H, assumed equal for momentum and heat.

The formulation of r_a^s shows an inconsistency, due to the empirical nature of its definition. A consequence of eq. 4.58 is that for $\sigma_f < 1$, r_a^s depends on the choice of the reference height z_R via its dependence on u_a, rather than solely on the aerodynamic transfer within the canopy layer. Unreported comparisons between r_a^s parameterized by D78 and by Choudhury and Monteith (1988, see next section) show that both values approximate each other in the EFEDA vineyard case for z_R = 25 m, but that the D78 parameterization gives a value approximately half as high as the Choudhury and Monteith value for z_R = 3 m (Van den Hurk *et al.*, 1995; section 5.2.2). Dickinson *et al.* (1986) chose a reference height of 1.3 m above grass land. In a newer version of BATS (Dickinson *et al.*, 1993), the dependence of r_a^s on z_R was avoided by taking $[0.004\, u_*]^{-1}$, where the numerical coefficient is a fixed value of the transfer coefficient between the soil surface and the inside canopy air layer.

The leaf stomatal resistance in D78 depends on intercepted shortwave radiation and soil moisture content only. In the current study, it was replaced by the parameterization present in BATS and proposed by Noilhan and Planton (1989). r_{st} depends also on vapour pressure deficit and leaf temperature, and is given by a Jarvis-type model according to

$$r_{st} = r_{s,\min} \frac{F_1}{F_2 F_3 F_4} \tag{4.59}$$

in which

$$F_1 = \frac{1+f}{f + \dfrac{r_{s,\min}}{r_{s,\max}}} \tag{4.60}$$

with $f = 0.55\, K^{\downarrow}/LAI\, K_{ref}$ and K_{ref} a reference value,

$$F_3 = 1 - g_D (q_c - q_0) \tag{4.61}$$

with g_D a species-dependent coefficient,

$$F_4 = 1 - 0.0016 \left(298 - T_c\right)^2 \tag{4.62}$$

and F_2 given by eq. 4.28 with $\overline{\omega} = \omega_2$.

4.1.5 The two-layer models of Shuttleworth & Wallace and Choudhury & Monteith

■ Model description

Shuttleworth and Wallace (1985, denoted as SW85) proposed a two-layer model similar to D78, but based on a solution of the Penman-Monteith equation for both the canopy and the underlying soil. The Penman-Monteith equation implicitly solves for the surface temperature by linearizing $\partial q_{sat}/\partial T$ and combining the equations for H, λE and the total amount of available energy. This strategy allows a direct computation of the surface fluxes, without the need to define a surface temperature.

A resistance network sketched in Figure 4.10 is designed, and just like for D78 the within-canopy temperature and vapour pressure are affected by the fluxes of each component.

SW85 considered the partition of available energy, A (eq. 4.1), into sensible and latent heat, by using the concept of surface resistance for both the canopy and the soil evaporation. Unlike in D78, A is assumed known. The energy budgets for the canopy and soil are given as

$$A_c = Q_{*,c} = H_c + \lambda E_c \tag{4.63}$$

and

$$A_s = Q_{*,s} - G = H_s + \lambda E_s \tag{4.64}$$

The partitioning of net radiation over the canopy and the soil components is parameterized by applying Beer's extinction using an extinction coefficient β_r:

$$Q_{*,s} = Q_* \exp\left(-\beta_r LAI\right) \tag{4.65}$$

Implicitly it is assumed that the radiation absorbing material (the canopy leaves) are

homogeneously distributed over the canopy layer, both horizontally and vertically. Dolman (1993) adapted this simple partitioning by allowing for an exponential extinction in only a part of the grid box, equivalent to defining a fraction of vegetation cover. Furthermore, he allowed the presence of an understorey of vegetation, which was assumed to have the same temperature as the underlying soil, for simplicity. These modifications were not included in the current study.

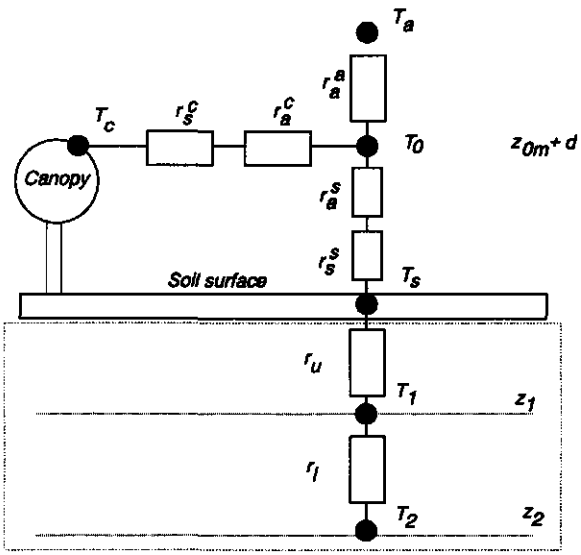

Figure 4.10: Schematic layout of the models of Shuttleworth and Wallace (1985) and Choudhury and Monteith (1988). The components enclosed by the dashed box apply to the Choudhury and Monteith formalism only. For explanation of symbols: see text

SW85 elaborated the expressions for the canopy- and soil evaporation drawing up separate PM-equations for each component, and eliminating the within-canopy water vapour pressure deficit, D_0. The total evaporation is given by

$$\lambda E = C_c PM_c + C_s PM_s \tag{4.66}$$

in which the coefficients PM_s and PM_c are given by

$$PM_c = \frac{\Delta A + \dfrac{\rho c_p D - \Delta r_a^c A_s}{r_a^a + r_a^c}}{\Delta + \gamma\left(1 + \dfrac{r_s^c}{r_a^a + r_a^c}\right)}, \qquad PM_s = \frac{\Delta A + \dfrac{\rho c_p D - \Delta r_a^s A_c}{r_a^a + r_a^s}}{\Delta + \gamma\left(1 + \dfrac{r_s^s}{r_a^a + r_a^s}\right)} \tag{4.67}$$

r_s^s is the soil resistance for evaporation, equivalent to r_s^c. The coefficients C_c and C_s in eq. 4.66 are functions of the resistances in the network of Figure 4.10, written as

$$C_c = \left[1 + \frac{R_c R_a}{R_s(R_c + R_a)}\right]^{-1}, \quad C_s = \left[1 + \frac{R_s R_a}{R_c(R_s + R_a)}\right]^{-1} \tag{4.68}$$

where

$$\begin{aligned} R_a &= (\Delta + \gamma)\, r_a^a \\ R_s &= (\Delta + \gamma)\, r_a^s + \gamma\, r_s^s \\ R_c &= (\Delta + \gamma)\, r_a^c + \gamma\, r_s^c \end{aligned} \tag{4.69}$$

The resistances are parameterized somewhat differently than in D78. The aerodynamic resistance above the canopy, r_a^a, includes a stability correction of the form proposed by Choudhury *et al.* (1986):

$$r_a^a = \frac{1}{\kappa^2 u_a} \ln\left(\frac{z_R - d}{z_{0m}}\right)^2 \left(1 + 5g(z_R - d)(T_0 - T_a)/(T_a u_a^2)\right)^{-x} \tag{4.70}$$

with $x = 2$ for stable and 0.75 for unstable conditions, respectively. The resistance to the soil, r_a^s, is obtained by integration of a (hypothetical) exponential profile of the eddy diffusivity within a dense canopy ($LAI \geq 4$) between the surface and the level $z_{0m} + d$, indicated by the node in the resistance network. The final value of r_a^s was found by a linear interpolation between a full canopy cover and a bare soil. Alternatively, Choudhury and Monteith (1988, denoted as CM88) parameterized r_a^s by defining the effective source level, $z_{0m} + d$ dependent on the canopy density and crop height, using the numerical simulations of Shaw and Pereira (1982). Their final formulation of r_a^s is written as

$$r_a^s = \frac{h \exp(n)}{n K(h)} \left[\exp\left(\frac{-n z_0'}{h}\right) - \exp\left(\frac{-n (d + z_{0m})}{h}\right)\right] \tag{4.71}$$

where z_0' is the roughness length of the underlying soil, n an eddy-diffusivity extinction coefficient, and $K(h)$ the eddy-diffusivity at crop height h, given as $\kappa u_* (h - d)$. The roughness length and displacement height of a canopy with leaf area index LAI is fitted on the simulations of Shaw and Pereira (1982) by the expressions

$$z_{0m} = \begin{cases} z_0' + 0.3\, h \sqrt{X} & 0 \leq X \leq 0.2 \\ 0.3\, h \left(1 + \dfrac{d}{h}\right) & 0.2 < X \leq 1.5 \end{cases} \tag{4.72a}$$

and

$$d = 1.1\,h \ln\left(1 + X^{1/4}\right) \tag{4.72b}$$

with X given by $C_d\,LAI$, where C_d is the leaf drag coefficient. Shuttleworth and Gurney (1990) showed that this formulation did not differ significantly from the parameterization of SW85.

CM88 also use a vertical integration of the canopy wind profile to parameterize the bulk boundary layer resistance, r_a^c. Considering an exponential wind profile described by use of an attenuation coefficient α_u (Cionco, 1972), the bulk boundary layer resistance is given by

$$r_a^c = \left\{ LAI \left(\frac{0.02}{\alpha_u} \right) \sqrt{\frac{u(h)}{l_w}} \left[1 - \exp\left(-\frac{\alpha_u}{2} \right) \right] \right\}^{-1} \tag{4.73}$$

No equivalent resistance is present in the pathway between the canopy air and the soil surface. In the limit of a completely bare soil, the absence of an extra resistance for scalars implies that momentum and scalars are exchanged at the same rate, and so $z_{0m} = z_{0h}$.

Unlike SW85, CM88 also specify the canopy resistance. It is assumed to be a function of LAI and shortwave radiation only, according to

$$r_s^c = \left[g_{cut} LAI + g_1 K^{\downarrow} \left(1 - \exp(-\beta_r LAI) \right) \right]^{-1} \tag{4.74}$$

in which g_1 is a coefficient expressing the sensitivity of r_s^c to sunlight.

Apart from a different parameterization of some of the resistances in SW85, CM88 conceptually differs by including explicit expressions for the soil heat flux and soil evaporation resistance. In their model, two soil layers are discerned: an unsaturated zone close to the surface, and a saturated soil layer at a depth below the surface (see Figure 4.10). Evaporation of soil water takes place at the intersection between the two soil layers. The energy balance at the bare soil surface is therefore given by

$$Q_{*,s} = H_s + G_0 \tag{4.75}$$

where G_0 is the soil heat transport downward from the surface. At the evaporation front the energy balance equation reads

$$\lambda E_s = G_0 - G \tag{4.76}$$

Both G_0 and G are parameterized using a resistance formulation and a temperature gradient:

$$G_0 = \rho c_p \frac{T_s - T_1}{r_u} \tag{4.77}$$

and

$$G = \rho c_p \frac{T_1 - T_2}{r_l} \tag{4.78}$$

where ρc_p appears in eqs. 4.77 and 4.78 for numerical simplicity, and T_1 is the temperature at the layer interface, rather than the temperature of the upper slab. The upper and lower exchange resistances are functions of the thermal properties of the soil and the corresponding layer depth, according to

$$r_u = \rho c_p \frac{z_1}{\lambda_T(\omega_1)} \tag{4.79}$$

$$r_l = \rho c_p \frac{z_2}{\lambda_T(\omega_{sat})} \tag{4.80}$$

where λ_T is treated as function of the soil moisture content (at saturation in the lowest soil layer). The introduction of these resistances enabled CM88 to develop and additional PM-equation for the soil evaporation, by writing

$$\lambda E_s = \left(\frac{\rho c_p}{\gamma}\right) \frac{e_{sat}(T_1) - e_0}{r_a^s + r_s^s} \tag{4.81}$$

and linearizing e_{sat} between T_0 and T_1. r_s^s is a resistance for water vapour transport through the upper (dry) soil layer, equivalent to SW85. An expression of r_s^s, proposed by CM88, includes a dependence on D_v and a tortuosity τ:

$$r_s^s = \frac{\tau z_1}{p D_v} \tag{4.82}$$

Various (semi-)empirical expressions for r_s^s exist (for instance, Camillo and Gurney, 1986; Dolman, 1993). Often this so-called β-type evaporation scheme (Kondo *et al.*, 1990) is used in combination with a relative humidity in the soil pores, α_p, rather than assuming the air in the pores to be saturated (Van de Griend and Owe, 1994). α_p is a function of the matric potential ψ according to (Philip, 1957):

$$\alpha_p = \exp(g\psi / R_v T) \tag{4.83}$$

In CM88, α_p is assumed to be unity.

The depth of the upper soil layer, z_1, increases as soil evaporation proceeds. For a constant value of ω_{sat} in the saturated zone, the depth of the upper soil layer progresses according to

$$E_s = \omega_{sat} \frac{dz_1}{df} \tag{4.84}$$

The entire set of equations describing the energy balance at both the soil and the canopy surface is rather complicated and not repeated here.

A major physical drawback of the resistance parameterization of the soil heat flux is that heat storage in the upper soil layer is ignored. A resistance equation as eq. 4.78 requires that the heat flow is constant over the resistance pathway. In atmospheric heat transport this requirement is roughly met, due to the low specific heat capacity of air. However, the specific heat capacity of soil cannot be regarded to be negligible, and a constant flux is hardly present, especially in soil layers close to the surface. A second point of criticism is the assumption of a saturated zone near the surface. This situation may often occur in agricultural farmland, where the soil water table is controlled to optimize crop production. However, Mediterranean sparse canopies are usually characterized by a significant water stress, and a saturated water table will seldom be found close to the surface in these areas. These issues will be further adressed in section 5.3.

■ **Numerical stability of PM-type two-component models**

Studies with coupled surface-PBL models carried out with surface models based on the PM-equation consistently revealed problems with numerical stability. Three aspects related to surface temperature are responsible for this problem: net radiation, stability correction of r_a^a and soil heat flux.

In a PM-type two component model both the canopy and bare soil temperature are implicitly obtained by linearizing $\partial q_{sat}/\partial T$. The models are diagnostic rather than prognostic, and don't include time derivatives of for instance the canopy and bare soil temperatures. Thus, with respect to the solution of the canopy and soil temperature, PM-models are fully implicit, and therefore numerically very stable. However, when for instance a dependence of net radiation on surface temperature is to be carried out, the equations describing Q_* and its partitioning should be incorporated in an implicit mode as well, in order to gain advantage of the fully implicit character of the PM-model. Unfortunately, the two layer models carry a large number of equations to solve for the surface temperatures and fluxes, even with prescribed values of Q_*, G and r_a^a. Including implicit dependences of these parameters on surface temperature is therefore a cumbersome job. Particularly under stable conditions, when aerodynamic resistances are large, these surface temperatures are very sensitive to the exact values of the sensible heat fluxes from the canopy layer to the canopy and soil component. As these sensible heat fluxes are to a large extent determined by net radiation, an unstable set of equations is readily obtained when an explicit formulation is used for Q_*. Similar arguments are valid for including a stability correction in r_a^a, or describing soil heat flux, for instance by use of a force-restore method (as in the modified big-leaf model, section 4.1.1).

Although Dolman (1993) claims his PM-type surface model to be designed for application in GCM's, he tested it using measured values of Q_* and G. Similar tests were carried out by SW85 and CM88. However, to serve as surface description scheme in GCM's a surface model should include a parameterization of these quantities. Dolman and Ashby

(personal communication) are currently developing a numerical surface scheme in which the multiple source surface model of Dolman (1993) is coupled to an implicit diffusion scheme to describe heat and water fluxes in the soil. The implicit soil scheme describes a temperature profile at time step $n + 1$ using adjacent temperatures in the same time step. Dolman and Ashby are extending the numerical solution matrix for the soil temperatures with two extra layers, situated at the canopy layer and the reference level above. The matrix coefficients for the exchange between these two above-surface layers include the exchange resistances for aerodynamic transport and available energy. The air temperatures are solved at the implicit time step $(n + 1)$, and can numerically be attached to the soil scheme. By the time of finalizing this thesis a complete version of this algorithm was not yet available.

4.2 Treatment of the planetary boundary layer

In this study the development of the planetary boundary layer is described in relation to the diffusion of heat, moisture and momentum in the lowest layers of the atmosphere. Two turbulence regimes are considered: a fully convective regime during daytime (the mixed layer), and a stable nocturnal PBL. Other stability regimes (Holtslag and Nieuwstadt, 1986) are not considered in this study. For each regime profiles of the turbulent diffusivity are constructed, based on appropriate scaling parameters.

The diffusion problem is solved by taking the surface fluxes as the lower boundary condition. During daytime, entrainment processes at the top of the PBL are also incorporated. The boundary layer depth, z_i, is explicitly evaluated from the simulated virtual temperature profiles. The numerical diffusion scheme proposed by Troen and Mahrt (1986) is used to solve the diffusion equations. The full model is described by Jacobs (1994), and below only a brief summary is given. For the convective PBL a simple slab model is also used in chapter 6, and this model is described briefly in section 4.2.2.

4.2.1 A numerical diffusion scheme for the planetary boundary layer

Fluxes of momentum and scalars in the PBL are parameterized using a simple local first order closure scheme:

$$\overline{w's'} = -K_s\left(\frac{\partial s}{\partial z} - \gamma_s\right) \tag{4.85}$$

In this equation s denotes a constituent ($s = m$ for momentum, h for heat and q for humidity), K_s an eddy-diffusivity and γ_s a countergradient correction term, introduced by Deardorff (1972). γ_s accounts for transport contributions from large turbulent structures, and its impact is shown to be considerable for particularly highly convective conditions (Holtslag *et al.*, 1995).

For the daytime PBL, the eddy-diffusivities and countergradient corrections proposed by Holtslag and Moeng (1991) are used. K_s is a function of the free convection velocity scale w_*, the boundary layer height z_i, and the entrainment ratio R_s, which represents the ratio of the flux at the PBL-top to the surface flux of constituent s. w_* is defined by

$$w_* \equiv \left[\frac{g\, z_i}{\overline{\theta}_v} \overline{w'\theta'_{v_0}} \right]^{1/3} \tag{4.86}$$

γ_s is a function of w_*, the surface heat flux and the profile of $\overline{w'^2}$, which was described using an expression proposed by Lenschow *et al.* (1980).

Both K_s and γ_s were fitted on LES simulations carried out by Moeng and Wyngaard (1984, 1989). These simulations indicated that the pressure covariance term and the turbulent transport term in the scalar flux equation differed by a constant value. This indication was used to parameterize γ_s. Holtslag and Moeng (1991) suggested that the parameterization of K_s and γ_s could be applied to both the heat and scalar flux equations. However, strictly spoken the parameterization is valid in only a limited PBL-height range, approximately between 0.1 and 0.8 z_i. Jacobs (1994) argued that the difference between the pressure covariance term and the turbulent transport term in the scalar flux equation may well be constant in the centre of the PBL, but that this breaks down near the top, where the entrainment of humidity is generally positive. This causes the pressure covariance term in the scalar flux equation ($\sim \overline{q'\theta'_v}$) to be positive rather than negative (Stull, 1988). He therefore evaluated γ_q at $z/z_i = 0.4$, and kept this countergradient term constant throughout the entire PBL.

The LES simulations of Moeng and Wyngaard (1984) were carried out for two classical situations: a positive scalar flux at the surface combined with a negative flux at the top of the PBL (typical for temperature transport), and a positive scalar flux at both the bottom and the top of the PBL (representative for humidity transport). A distinction between bottom-up and top-down processes was carried out by simulating a situation with a negative scalar flux at the PBL-top only. The difference between this transport and the typical temperature transport enabled the definition of the bottom-up transport term for temperature. A similar set-up for discerning between top-down and bottom-up processes for moisture would consist of a LES simulation with a positive flux at the PBL-top only. This simulation was not carried out by Moeng and Wyngaard (1984). An improvement of the parameterization of γ_q could possibly be achieved by performing these additional LES exercises (Michels and Holtslag, priv. communication). However, this aspect is beyond the scope of this study, and we adopt the recommendations of Jacobs (1994) for further calculations.

For the description of K_s in the nocturnal PBL we followed the original suggestions of Troen and Mahrt (1986). K_s is expressed using a different velocity scale, w_s, given by

$$w_s \equiv \frac{u_*}{\phi_m \left(\frac{z}{L_v} \right)} \tag{4.87}$$

in which ϕ_m is a stability function (Holtslag *et al.*, 1990). A smooth interpolation between nocturnal and daytime diffusivity profiles is carried out by using w_*/u_* as indicator.

During each timestep the boundary layer height z_i is diagnosed using a bulk-

Richardson approach:

$$z_i = \frac{Ri_c \overline{\theta}_v \left| V(z_i) \right|^2}{g\,(\theta_v(z_i) - \theta_s)} \tag{4.88}$$

In this equation, Ri_c is a critical Richardson number, which is a measure for the largest stability where turbulence can still exist. Ri_c is taken to be 0.25. Furthermore, V is the horizontal wind speed, and θ_s a measure of the temperature excess of the thermals, parameterized using the surface buoyancy flux and the temperature at the $z = z_R$. In all cases a minimum value of $0.175\ \kappa\, u_*/f$ is taken for z_i, which is a suggested value of the near-neutral PBL-height scale, including the effects of geostrophic wind shear (Koracin and Berkowicz, 1988). f is the Coriolis parameter, equal to $2\Omega\sin\Phi$.

The entrainment ratio R_s is evaluated from the calculated flux profile in past time steps. R_h is defined as the ratio of the *minimum* heat flux to the surface flux. Generally, the level where the heat flux is minimum (z_{min}) is found slightly below z_i. As pointed out by Jacobs (1994), the entrainment ratio for humidity is prone to numerical fluctuations when evaluated at the same level as R_h. Therefore, R_q was specified as $\overline{w'q'}(z = 0.8\, z_{\min}) \,/\, \overline{w'q'}_0$. Both R_h and R_q are set to zero for stable conditions. In order to increase numerical stability new values for R_h and R_q are evaluated only every ten minutes of simulation.

During every time step the wind profile is adjusted by a geostrophic forcing, determined by the geostrophic wind speed V_g. Numerical experiments have shown that this geostrophic forcing can yield strong oscillations of the wind field with a frequency $\sim f$ and amplitude $\sim V_g$. For these reasons the geostrophic acceleration was only applied at levels within the PBL. Also, the wind, temperature and humidity profiles above the PBL were unchanged in the simulations.

4.2.2 Slab-model for the convective PBL

Tennekes (1973) and Driedonks (1981, 1982a) discuss the treatment of the convective boundary layer by use of a so-called slab model. The model treats the boundary layer as a box heated from both below and above. Air within that box is instantaneously mixed, and its average temperature θ_m is a function of the net heat supplied both from below and from above, and of the height of the box. Driedonks (1981) derived analytical expressions for the sensitivity of z_i and θ_m to the total amount of sensible heat released by the surface, and to the initial profile of θ. A simple heat entrainment closure was adopted. McNaughton and Spriggs (1986) applied the approach of Driedonks to describe evaporation into a convective boundary layer.

The slab model elaborated by Driedonks (1981) describes the growth of the PBL as

$$\frac{dz_i}{dt} = \frac{\overline{w'\theta'_v}_e}{\Delta\theta_v} \tag{4.89}$$

where $\Delta\theta_v$ is the inversion strength at the top of the boundary layer, and $\overline{w'\theta'_v}_e$ is an entrainment buoyancy flux at the top of the PBL.

A simple closure of $\overline{w'\theta'_{v_e}}$ is not easy to give, since sensible and latent heat transport both contribute to this term. However, for a dry convective boundary layer, $\overline{w'\theta'_{v_e}} \approx \overline{w'\theta'}_e$. A simple closure consists of relating $\overline{w'\theta'}_e$ to the surface heat flux, $\overline{w'\theta'}_0$, according to

$$\overline{w'\theta'}_e = R_h \overline{w'\theta'}_0 \tag{4.90}$$

Tennekes (1973) also considered the contribution of mechanical turbulence to the entrainment flux, but this is ignored here. By definition of the integrated surface heat flux as

$$I(t) \equiv \int_0^t \overline{w'\theta'}_0(t')\,dt' \tag{4.91}$$

Driedonks (1981) expressed the development of z_i as

$$z_i^2 = \frac{(1 + 2R_h)\left(I - \delta_0^{\theta}\right)}{0.5\,\gamma_\theta} \tag{4.92}$$

where δ_0^{θ} is the initial heat content, given by $z_{i0}\Delta\theta_0 - 0.5\gamma_\theta z_{i0}^2$, and γ_θ is the temperature slope above the PBL. This expression predicts that for a constant value of γ_θ and R_h the PBL height increases as function of $I^{1/2}$.

Similarly, the value of the mixed layer temperature, θ_m, can be expressed as function of z_i, for a given value of γ_θ and R_h:

$$\theta_m(t) = \theta_{00} + \gamma_\theta \frac{1 + R_h}{1 + 2R_h} z_i(t) \tag{4.93}$$

where θ_{00} is the value of θ when γ_θ is extrapolated to $z = 0$. The rate equation for the temperature jump $\Delta\theta$ is given by

$$\Delta\theta = \gamma_\theta \frac{R_h}{1 + 2R_h} z_i \tag{4.94}$$

The dependence of the specific humidity of the PBL on the total integrated surface latent heat flux J, defined as

$$J(t) = \int_0^t \overline{w'q'}_0(t')\,dt' \tag{4.95}$$

is a more complex function. The rate of change of the mixed layer specific humidity, q_m, is written as (Driedonks, 1981; McNaughton and Spriggs, 1986)

$$\frac{dq_m}{dt} = \frac{\left(\overline{w'q'}_0 + \Delta q \frac{dz_i}{dt}\right)}{z_i} \tag{4.96}$$

The second term between brackets in eq. 4.96 indicates the transport of moisture at the top of the PBL. A *de*trainment is simulated if the specific humidity jump Δq is negative. The entrainment rate dz_i/dt is given by eq. 4.89, while Δq is equal to

$$\Delta q = q_{00} + z_i \gamma_q - q_m \tag{4.97}$$

where q_{00} and γ_q have the same meaning as θ_{00} and γ_θ. Δq also changes as time proceeds, and an analytical expression for dq_m/dt is not easy to give. In chapter 6, eq. 4.96 will be solved numerically by taking Δq, calculated from eq. 4.97, from the previous time step.

4.3 Limitations to the coupled 1-dimensional atmospheric model

The study reported in this thesis is designed to evaluate the sensitivity of the predicted PBL-development to the parameterization of the underlying (sparsely vegetated) surface. Later in this study computer simulations will be compared to field measurements (chapters 5 and 6). However, the conclusions to be drawn are confined to the processes that are included in the simulations. It is therefore of interest to pay some attention to the physical processes which were *not* included in the models described above. These may play a role in the complex surface-atmosphere interaction which is the subject of this study.

First of all, the coupled SL-PBL model is essentially **one-dimensional**. Computations are carried out and compared to data under the assumption that the forcings apply to a homogeneous fetch of unlimited horizontal dimension. In practice, advection of warm dry air has modified the measured profiles considerably for many days (see section 6.5.1). The radiosoundings also revealed the existence of a clear and persistent sea wind as far as the Tomelloso area (Bessemoulin, priv. communication).

A second limitation of the model is that processes associated with **clouds** are not included. Especially the radiative properties may be of importance for the net radiation at the surface or the temperature profiles in higher air layers.

Third, **longwave radiative cooling** was not regarded. This process in practice results in a decrease of the temperature of the air near the surface of 1 - 2 K per 24 hrs (Garratt, 1992). Stronger cooling takes place near the surface than at higher altitude, which causes the development of a slightly stable stratification in the residual layer during nighttime, when vertical mixing is absent. This stable lapse rate limits the growth speed of the convective PBL, and ignoring this process may lead to an overestimation of this growth speed. However, the exact rate of the cooling in each layer depends on the distribution of greenhouse gases in the air masses above and below the particular layer, of which water vapour and CO_2 are present in the highest concentrations.

Also, large scale processes like **subsidence** were not included. This process is caused by descending air motions in the centre of high pressure areas, and reduces the boundary layer height.

The entrainment equations in both the numerical and the slab model regard **buoyant turbulence only**. Turbulence induced by for instance wind shear near the top of the PBL is not included.

Furthermore, sensitivity analyses in chapters 5 and 6 were confined to simulation periods of five days at most. This is a rather **short time scale** for considering parameterization effects on for instance soil moisture content. Shao *et al.* (1994) compared various soil moisture parameterizations of land surface schemes, and suggest that datasets of at least one year are required for an adequate model evaluation.

Finally, the one-dimensional origin of the model simulations does not allow to include **pressure effects on wind flow** or the **influence of baroclinicity (thermal winds)**. For instance, the Coriolis force can result in a very strong oscillation of the wind speed within the PBL (see above). In the real world, these oscillations will probably be damped due to the building up of high pressure areas, which will change the geostrophic wind direction. This damping effect was not accounted for, and the simulated wind profiles appeared to be rather unrealistic in some occasions. However, note that one-dimensional simulations are essentially inadequate for investigations of the wind profile and its changes in time, since the horizontal motion of air is a two-dimensional problem. We therefore pay only little attention to simulated wind profiles.

5

If you think about a problem during the night, and think about it again the next morning, you get different answers

An intercomparison of three soil/vegetation models for a sparse vineyard canopy[1]

For GCM's the lower boundary condition is often provided by a Soil-Vegetation-Atmosphere-Transfer (SVAT) model. As pointed out in the introduction section of this study, the description of the exchange processes between the surface and the atmosphere is of great influence on the long term predictions of these larger scale models.

Obviously, a SVAT intended to provide the lower boundary condition in GCM's needs to be able to describe a wide range of surface types, varying from completely vegetated to sparsely vegetated or completely bare surfaces. Sparse canopy surfaces exhibit rather demanding features with respect to the exchange of momentum, scalars and heat between the surface and the atmosphere. Here, we focus on three aspects: aerodynamic exchange, soil heat flux and surface evaporation.

For the aerodynamic exchange, a difference is made between the exchange of momentum and of scalars as heat, water vapour, CO_2 or trace gases. Surface roughness elements acting as a momentum sink are usually parameterized by extrapolation of the wind profile to a hypothetical sink level at height $d + z_{0m}$. Both parameters depend on the presence of roughness elements, characterized by the surface fraction being covered, and the spacing and height of the elements. Measurements and theoretical considerations reveal a difference between the exchange rates of scalars and momentum. The transport of water vapour, heat or trace gasses is considered less efficient than momentum transport in most cases, owing to the absence of bluff-body forces for scalar exchange (Thom, 1972; Beljaars and Holtslag, 1991). Models treating the surface as a single homogeneous layer impose an 'excess' resistance for scalars to account for this effect, equivalent to adopting a different roughness length for scalars, z_{0h} (section 2.4.2). Experimental quantification of this roughness length has been carried out for many surface types, particularly using radiometric

[1] Adapted from Van den Hurk *et al.* (1995)

surface temperature measurements (Garratt, 1978; Huband and Monteith, 1986; Kustas *et al.*, 1989).

For sparse canopies the interpretation of z_{0h} is far from straightforward. The heat exchange takes place at various levels, and the source distribution is determined by various environmental parameters, such as radiation, canopy evaporation, or forced convection. Two-layer models avoid the definition of a single source level by parameterizing the sensible and latent heat exchange at two separate levels: the canopy and the underlying substrate. The absence of bluff-body forces for scalar exchange is accounted for by additional resistances within the canopy layer. The turbulent exchange of sensible and latent heat between the canopy, the substrate and the air above are treated separately. Parameterization of these resistances is carried out by adopting assumptions about the turbulent exchange within the canopy layer and the effective sink level. This level can either be a fixed function of the canopy height (Shuttleworth and Wallace, 1985), a more complex function of leaf area index (Choudhury and Monteith, 1988), or crop density (Raupach, 1992). However, turbulence characteristics within the canopy layer are rather complex and not easily defined using simple parameters (McNaughton and Van den Hurk, 1995).

Blyth and Dolman (1995) used a two-layer model to explore the value of z_{0m}/z_{0h} for a sparse canopy. The apparent aerodynamic resistance for heat transfer, r_a, was deduced from the simulated total sensible heat flux density H, the air temperature T_a, and a mean surface temperature $\overline{T}_{sur}$, according to (see also eq. 2.35)

$$r_a = \rho c_p \frac{\overline{T}_{sur} - T_a}{H} \tag{5.1}$$

$\overline{T}_{sur}$ was obtained from a linear interpolation of the model predictions of canopy temperature T_c and ground temperature T_s:

$$\overline{T}_{sur} = \sigma_f T_c + (1 - \sigma_f) T_s \tag{5.2}$$

The value of z_{0h} is then obtained from eq. 2.36. The resulting roughness length for heat appeared to be no function of the surface itself (as is the case for z_{0m}), but it showed a clear variation with radiation, wind and even vapour pressure deficit. Apparently, the variation of the distribution of the heat sources causes the variation of z_{0h}. Similar results were obtained experimentally by Kustas *et al.* (1989), Verhoef (1995), and in section 2.4.2.

The second issue of interest for sparse canopy surfaces is the treatment of the soil heat flux density. Under conditions where a significant part of the radiant energy reaches the bare soil, a relatively large part of this energy is associated with heating and cooling of the upper soil layers. An accurate description of long term thermal dynamics of such a sparse canopy surface requires a proper description of the heat transfer into the soil. Since for strongly irradiated, dry soils large temperature gradients can be present near the surface, the description of the soil heat flux is likely to depend on the selected number and thickness of the soil layers, and the parameterization of the thermal conductivity of the soil.

The third issue involves evaporation from a sparse canopy surface and dewfall onto it. The water vapour transport from a sparse canopy surface into the atmosphere is a

mixture of transpiration from the canopy elements and evaporation from the bare soil component or from intercepted water. During the process of dew formation, water vapour is transported downward from the atmosphere (dewfall), or it condensates immediately after being released by the underlying soil (dewrise).

This section is dedicated to a comparison of various SVAT schemes using a common dataset collected over a sparse vineyard canopy surface for five consecutive days, with particular attention to the issues addressed above. The SVAT schemes include a one layer model currently in use in the ECMWF global weather prediction model (Viterbo and Beljaars, 1995, VB95) and two dual-source models, published by Choudhury and Monteith (1988, CM88) and Deardorff (1978, D78). In each of these models the algorithms to describe soil heat flux density and aerodynamic transfer are based on different physical concepts (see chapter 4 for a description of these models).

The intercomparison serves two purposes. First, a qualitative and quantitative evaluation of these different process treatments is of interest as these algorithms are often applied in large scale atmospheric models. Second, the results will be used to construct a reference SVAT, to be used in the coupled PBL-SVAT simulations in the next chapter.

Both in nature and in the model simulations the governing parameters show many complex feedbacks, and individual processes can not easily be investigated in an isolated way. Model errors related to one process of the transfer between surface and atmosphere can cause significant discrepancies for the description of other processes. Despite this feature, the comparison between the models and the observations will be separated into three process categories: soil heat flux density, aerodynamic exchange of heat, and evaporation and soil water balance.

1 Description of data, model settings and used forcings

5.1.1 Collected data

Data were collected during the regional scale EFEDA experiment (Bolle *et al.*, 1993) in a dry, semi-arid sparsely vegetated vineyard near Tomelloso, La Mancha, Spain. A detailed description of the site and vegetation is given in section 2.2.

Measurements consisted of both forcings and flux densities to validate model results. Atmospheric forcings were measured at a reference level of 2.95 m height, and consisted of air temperature, air humidity, horizontal wind speed, incoming and reflected shortwave radiation and net radiation. Longwave downward radiation $L^{\downarrow}$ was parameterized by closing the surface radiation balance, eq. 2.1. In this equation, the values of global radiation ($K^{\downarrow}$) and net radiation (Q_*) were measured, the albedo (a) and longwave emissivity (ε_s) were taken as in the simulations (see below), and an effective surface temperature ($\overline{T}_{sur}$) was taken from measurements using an infrared sensor mounted at 3 m above the soil surface on a cable and moved along a transect of 35 m. The transect included both canopy elements and bare soil. Individual canopy and bare soil temperatures were extracted from the record of temperatures. Soil temperatures were measured at five levels between 0.03 and 0.50 m depth. Energy fluxes were selected from the available data as outlined in section 2.4.3. Corrections to these fluxes are discussed in Appendix II.

Aerodynamic roughness z_{0m} and zero plane displacement d were determined from

wind profile measurements at four levels between 1.5 and 10.0 m. These quantities changed considerably due to the vegetation growth (see section 2.4.1).

Soil moisture measurements were carried out at a few days before and during the comparison period by the Dept. of Water Resources of the Wageningen University, using TDR at 0.10 m intervals to 0.50 m depth (Droogers *et al.*, 1993). Leaf resistance to water vapour transport was measured from sunrise until sunset once every two days by use of a dynamic diffusion porometer. After extensive quality control on data and calibration (Jacobs, 1994), a crop resistance was obtained by averaging the measurements using a weighing based on leaf age and light exposure (section 2.2.7). Measurements of leaf area index, *LAI*, and fraction of vegetation cover, σ_f, were taken as described before.

5.1.2 Forcings and specific model settings

The simulations were carried out using observations taken between 19 June (DOY 170) 20:00 GMT, and 24 June (DOY 175) 24:00 GMT. For each model the simulation time step was 600 s, and observations averaged to half hour intervals were interpolated to match the time discretization.

All three models use measured values of temperature, wind speed and humidity at a reference height above the canopy, and initial soil temperature and soil moisture profiles. Observations of total net radiation were used as input for CM88, and shortwave and longwave incoming radiation for VB95 and D78. However, during the nocturnal periods following DOY 173 and 174 some data are missing due to failure of the measurement system. Linear interpolation was used to estimate missing data. Initial soil moisture and temperature profiles can be found in Table 5.1, for each of the models. Temperatures and moisture contents in soil layers deeper than measured were assumed to be identical to the values at 0.50 m depth at the starting time of the simulation. Figure 5.1 displays the atmospheric forcings.

To make the comparison of the models as straightforward as possible, most model settings were adjusted to give similar surface and vegetation specifications. However, since all models treat several parameters differently, some choices had to be made. A summary of all model settings can be found in Table 5.2.

- **VB95**

In the original paper of VB95 universal functions describing the physical properties of the soil are used for each soil type. However, we adjusted these parameters according to the suggestions made by Noilhan and Planton (1989) for a sandy loam soil type (see Table 5.2). The surface albedo was fixed at the measured value 0.29 for both the vegetation and soil components, and for the longwave emissivity a value of 0.98 was taken (Bolle and Streckenbach, 1993). In the operational ECMWF version of VB95, the aerodynamic roughness length is a specified quantity for each grid box. Here, calculated aerodynamic roughness and zero plane displacement were taken. The value of z_{0m} increased from 0.035 m at DOY 171 to 0.043 m at DOY 175, whereas d was kept constant at 0.35 m in this limited time range. Note that these values are relatively small, regarding the observed canopy height exceeding 0.80 m at all times (Wieringa, 1993). A different aerodynamic roughness for heat was calculated, using $z_{0m}/z_{0h} = 200$. Note that this value is an order of magnitude larger than the value

suggested by Braud *et al.* (1993), who simulated the energy balance of a similar sparsely vegetated vineyard using the scheme of Noilhan and Planton (1989). Since the sensible heat flux is the dominant term of the surface energy budget for a dry sparse canopy surface, the choice for z_{0m}/z_{0h} will reflect the difference between the mean level of the momentum sink (the canopy elements) and the heat source (the underlying bare soil). The apparent conductivity of the skin layer was kept at the suggested value of 7 W/m^2K. Since exact information about the root distribution was not available, the rooting depth of the vegetation was defined according to the original suggestion (1 m, with water extracted equally from the top three layers). The response of the canopy resistance to light and soil moisture was parameterized according to VB95. In the simulation period *LAI* increased from 0.29 m^2/m^2 on DOY 171 to 0.35 m^2/m^2 on DOY 175, whereas σ_f increased from 0.10 to 0.12 in the same period.

Table 5.1: Initial values of soil moisture and soil temperature for each model

Parameter	Depth (m)	D78	CM88	VB95
Soil temperature (K)	0	293.09	293.09	293.09
	0.07			302.96
	0.10		303.21	
	0.28			298.66
	0.50	296.09	296.09	
	1.00			296.09
	2.89			296.09
Soil moisture content (m^3/m^3)	0.07			0.07
	0.10	0.07		
	0.28			0.08
	0.50	0.15		
	1.00			0.15
	2.89			0.15

- **CM88**

CM88 uses principally net radiation, wind speed, humidity and air temperature as forcing functions. For this comparison, the deep soil temperature was taken from measurements at 0.50 m depth, rather than taking it as constant. The absence of a saturated zone near the surface made a formal justification for choosing the value of the depth of the top soil layer, z_1 impossible. z_1 was taken to be 0.40 m, to get a high soil evaporation resistance corresponding to a small soil evaporation expected from a dry soil surface. For the thermal conductivity in the top layer a value of 0.3 W/mK was adopted, and in the bottom layer 0.5 W/mK, following Verhoef *et al.* (1995). Directly measured values of *LAI* and crop height, *h*, were adopted. Roughness length and displacement were computed as function of *LAI* and *h*, assuming a leaf drag coefficient of 0.2 (Choudhury and Monteith, 1988). Characteristic leaf size, necessary for computing the crop boundary resistance r_a^c, was 0.05 m. Since explicit calibration coefficients of the response function for stomata to radiation

are not given by CM88, the function was calibrated using porometry measurements taken at several days in the measurement period (see Table 5.2).

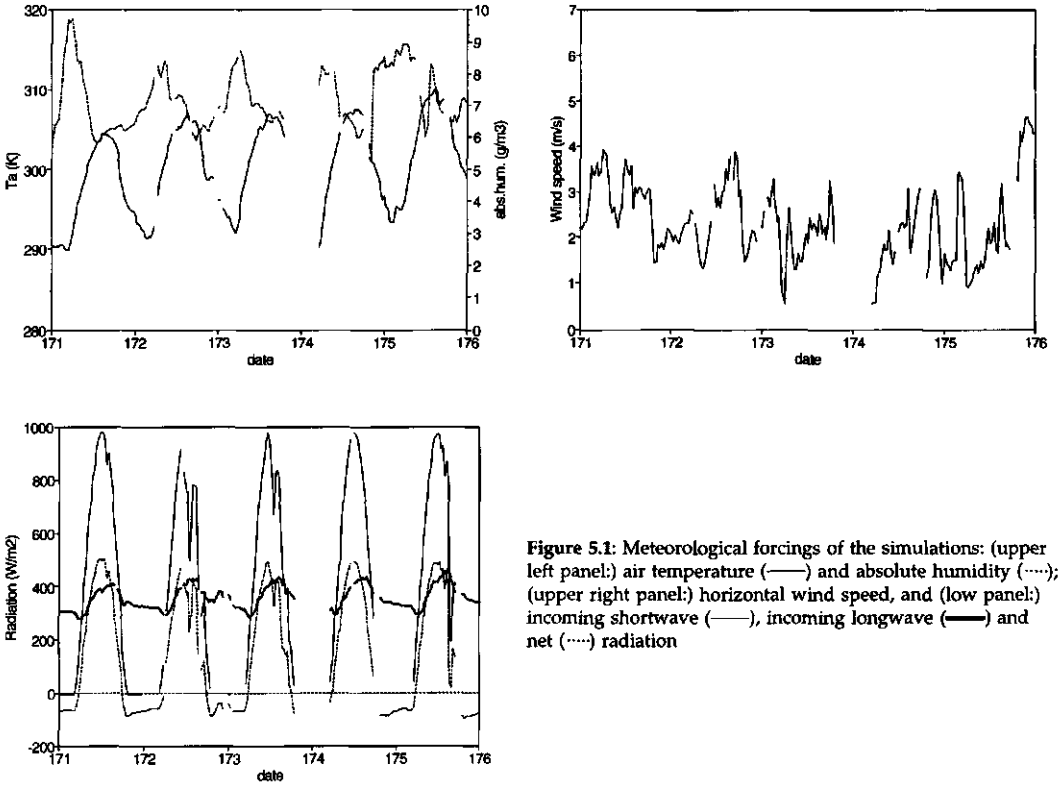

Figure 5.1: Meteorological forcings of the simulations: (upper left panel:) air temperature (——) and absolute humidity (·····); (upper right panel:) horizontal wind speed, and (low panel:) incoming shortwave (——), incoming longwave (▬▬) and net (·····) radiation

■ D78

For D78, z_{0m} and d were computed using the same formulation as CM88. The thickness of the top soil layer was fixed at 0.1 m, and the deep soil temperature varied with a seasonal cycle as suggested in the original paper. The crop resistance was parameterized as function of radiation, air temperature, atmospheric humidity and soil moisture, following the general suggestions made by Noilhan and Planton (1989).

Similar soil physical quantities were taken as for VB95, that is, the sandy loam soil type (see Table 5.2). The surface albedo was fixed at the observed value (0.29), and the surface longwave emissivity was taken the same as in VB95 (0.98 for both plants and soil).

5.2 Simulations with the SVAT-schemes

The sparse canopy surface for which the simulation was carried out has some pronounced properties with respect to the partition of energy over the various components. First, unlike in case of densely vegetated surfaces, the soil heat flux density is an important component of the surface energy balance for the current data set. Due to the small relative area covered by the plants (maximum 12%), approximately 30% of the total daytime net

radiation was used to heat the soil. The daily averaged soil heat flux density was approximately 20 W/m^2, indicating a temperature increase in deeper soil layers at this time of the year.

Second, the surface net radiation is hardly used for evaporation (< 10% of net radiation, generally), but a clear distinction between the canopy and the underlying soil is present in terms of latent and sensible heat exchange and surface temperature. Sensible heat (about 60% of net radiation) was released mainly by the warm substrate, whereas the evaporation, which was dominated by the canopy, caused the vegetation to be significantly cooler than the surrounding bare soil.

Third, the large rooting depth enabled the vegetation to transpire in spite of a very dry top soil. Stomatal responses to the moisture content in the top soil layer are expected to be small.

The models faced the challenge of simulating these features. The simulations will be compared with attention focused on three aspects: soil heat flux density, sensible heat transfer between the surface and the atmosphere, and evaporation in combination with soil moisture budget.

Table 5.2: Model parameter values

Parameter	symbol	eq(s).	D78	CM88	VB95
General configuration					
time step (s)	t	-	600	600	600
depth of soil layers (m)	z_1	-	0.10	0.40 (start)	0.07
	z_2		0.50	0.50	0.28
	z_3		-	-	1.00
	z_4		-	-	2.89
Vegetation dimensions					
crop height (m)	h	4.71 - 4.72	1	1	-
Leaf Area Index	LAI	multiple	0.29 - 0.35	0.29 - 0.35	0.29 - 0.35
fraction vegetation cover	σ_f	multiple	0.10 - 0.12	0.10 - 0.12	0.10 - 0.12
characteristic leaf size	l_w	4.57, 4.73	0.05	0.05	-
Aerodynamics					
roughness length (m)	z_{0m}	4.5, 4.70, 4.71	f(LAI, h, C_d)	f(LAI, h, C_d)	0.035 - 0.043
displacement height (m)	d	4.5, 4.70, 4.71	f(LAI, h, C_d)	f(LAI, h, C_d)	0.35
soil roughness length (m)	z_0'	4.71	0.01	0.01	-
roughness length for heat (m)	z_{0h}	4.6	-	-	$z_{0m}/200$
leaf drag coefficient	C_d	4.72	0.2	0.2	-
reference height (m)	z_R	4.5, 4.70	2.95	2.95	2.95
non-evaporating parts factor	Γ_b	4.40, 4.56	1.1	-	-
extinction coefficient for wind speed	α_u	4.73	-	3	-
extinction coefficient for eddy diffusivity	n	4.71	-	2.5	-

Parameter	symbol	eq(s).	D78	CM88	VB95
Radiation					
soil albedo	a_s	4.15, 4.36	0.29	-	0.29
canopy albedo	a_c	4.15, 4.36	0.29	-	0.29
surface emissivity	ϵ_s	4.15, 4.37 - 4.39	0.98	-	0.98
extinction coefficient for net radiation	β_r	4.65, 4.74	-	0.7	-
Canopy resistance					
minimum crop resistance (s/m)	$r_{s,min}$	4.26, 4.59	125	-	240
maximum crop resistance	$r_{s,max}$	4.60	5000	-	-
cuticular conductance (m/s)	g_{cut}	4.74	-	0.0005	-
change of conductance per unit shortwave radiation (m/s / W/m^2)	g_1	4.74	-	$4\ 10^{-6}$	-
coefficients for PAR-response	a_1 a_2 a_3	4.27	-	-	0.19 1128 30.8
reference shortwave radiation (W/m^2)	K_{ref}	4.60	100	-	-
humidity response coefficient (Pa^{-1})	g_D	4.61	0.00025	-	-
maximum dew reservoir depth (mm)	w_{max}	4.20, 4.23, 4.44, 4.46	0.8	-	0.8 f(LAI, σ_f)
Soil parameters					
skin conductivity (W/m^{2}K)	Λ	4.14	-	-	7
averaging coefficient for soil surface relative humidity	l_c	4.19	1	-	1.6
thermal conductivity top soil layer (W/mK)	λ_{T1}	4.9, 4.48, 4.79	f(ω_1)	0.3	f(ω_1)
thermal conductivity other soil layers, i (W/mK)	λ_{Ti}	4.9, 4.49, 4.80	f(ω_i)	0.5	f(ω_i)
Retention curve coefficient	b	4.10, 4.12, 4.13	4.90	-	4.90
saturated soil moisture (m^3/m^3)	ω_{sat}	4.10, 4.12, 4.13, 4.51, 4.53, 4.84	0.472	0.472	0.472
field capacity (m^3/m^3)	ω_{fc}	4.19, 4.28	0.354	-	0.354
wilting point (m^3/m^3)	ω_{pwp}	4.28	0.075	-	0.075
tortuosity	τ	4.52, 4.82	0.66	2	-
saturated hydraulic pressure (m)	Ψ_{sat}	4.10, 4.13	-0.25	-	-0.25
saturated hydraulic conductivity (m/s)	γ_{sat}	4.12	$3.41\ 10^{-5}$	-	$3.41\ 10^{-5}$
coefficients for ω_{equ}	a_{equ} p_{equ}	4.53	0.219 4	-	-
coefficient for force-restore humidity transport	C_{2ref}	4.51	1.8	-	-

5.2.1 Soil heat flux density

Figure 5.2 gives the measured and simulated soil heat flux density for DOY 171 - 175. As can be seen, the differences between the model predictions are very large. D78, using a force-restore method to compute the soil heat flux density, gives a very good agreement with observations. A small underestimation is present early in the comparison period. The relatively slow response of the deep soil temperature to surface forcings results in a clear phase shift of the soil heat flux density compared to net radiation (detailed in Figure 5.3), which is well simulated by D78.

Also VB95 simulates a maximum soil heat flux density somewhat before local noon, albeit less pronounced than D78. The soil heat flux density is on average about 30% too small compared to the observations. This underestimation is not caused by a discrepancy between the observed substrate temperature and the simulated skin layer temperature (Figure 5.7). Obviously, the chosen value of the skin conductivity, Λ, plays a significant role in this aspect.

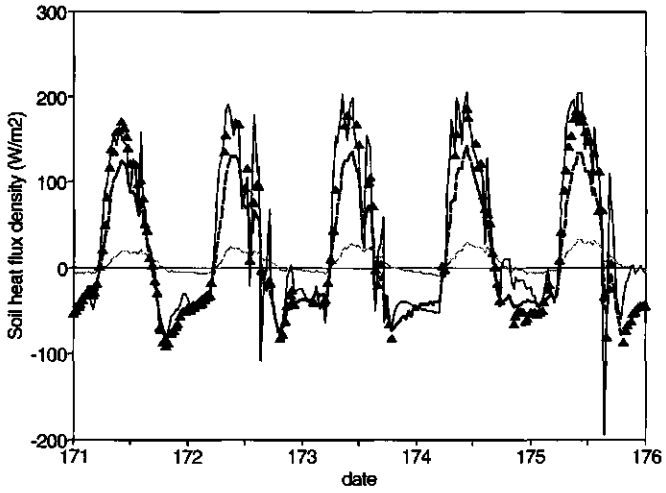

Figure 5.2: Soil heat flux density for all comparison days. ▲ observations; —— D78; - - - VB95; ····· CM88

The soil heat flux density predicted by CM88 is much too small compared to the observations, in spite of using measured values of the thermal conductivity in the two soil layers (see Table 5.2). The underestimation is almost a factor 10, and is too large to be related to the choice of the initial dry soil layer depth (z_1). Taking z_1 0.01 m rather than 0.40 m at the first time step increases the soil heat flux only by a few percent (figures not shown). Also, a phase shift with respect to the local noon is not simulated by CM88 (see Figure 5.3). Only by increasing the thermal conductivity to unlikely high values (exceeding 5 W/mK for the top soil layer) can the maximum of the simulated soil heat flux be matched to the maximum of the observed values, but not at the right time with respect to the local noon. The reason for the discrepancy between model and data is the absence of a heat capacity in the upper soil layer. The use of a resistance to regulate the heat flux in CM88 implies that no heat loss occurs in this layer. Hence, the soil heat flux will always respond immediately to the forcing

at the surface, and a phase shift will not be present in the calculations.

As a result of the underestimation of the predicted soil heat flux density by CM88, a large part of the net radiation is available for λE and H, and causes a clear overestimation of these two terms. This overestimation is reflected in the plot of the simulated substrate temperature, shown in Figure 5.4, which is high compared to the radiometric observations of the bare soil temperature.

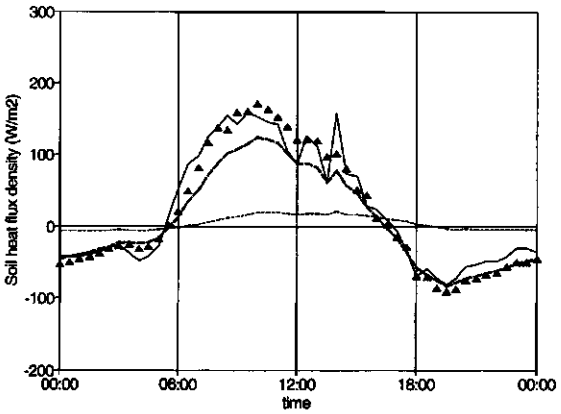

Figure 5.3: Measured and simulated soil heat flux density for DOY 171; ▲ observations; —— D78; - - - VB95; ····· CM88

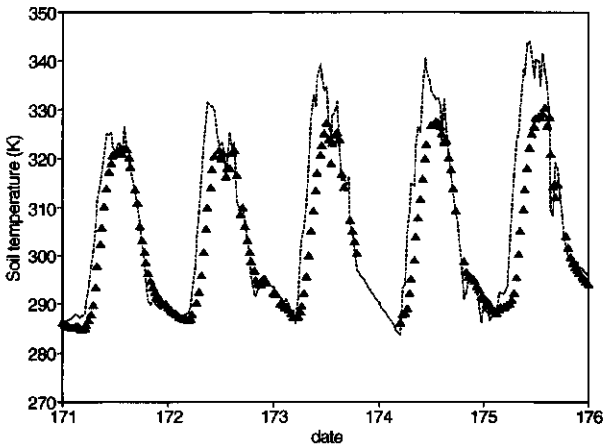

Figure 5.4: Measured (▲) and simulated (·····) bare soil temperature. Only simulations by CM88 with computed soil heat flux densities are shown

The overestimation of the prediction of H and λE makes a comparison of the parameterization of e.g. the aerodynamic exchange by CM88 with other models impossible. With respect to this aerodynamic exchange a fair comparison between CM88 and D78 is particularly useful, since these models use different formulations for aerodynamic resistances in a similar resistance network (Figures 4.9 and 4.10). Therefore, in the following the computed soil heat flux computation in CM88 is replaced by values of G as computed by D78 which are very close to the observations (Figure 5.2). A comparison of H and λE from CM88 and VB95 is somewhat biased by the difference of G computed by D78 and VB95, and

must be carried out with caution. The soil evaporation in CM88 is treated as before, using a resistance for water vapour transfer at the soil surface interface which increases as soil evaporation progresses. A model of this form is essentially comparable to the model presented by Shuttleworth and Gurney (1990), who adapted the original two-layer model of Shuttleworth and Wallace (1985) with the parameterization of the aerodynamic parameters according to CM88.

5.2.2 Sensible heat exchange and surface temperature

For the surface considered the aerodynamic exchange of heat between the surface and the reference level is dominated by the contribution of the bare soil component. This exchange can be separated in two segments for each model: a transfer above the canopy equivalent to momentum transfer, and an extra resistance to account for the difference between heat and momentum transport. In VB95 this difference is accounted for by taking $z_{0m}/z_{0h} > 1$, while in CM88 and D78 this extra resistance consists of r_a^c and r_a^s (see Figures 4.9 and 4.10).

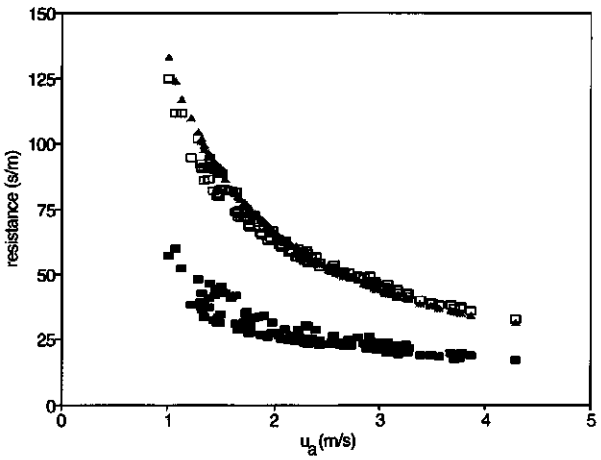

Figure 5.5: Aerodynamic resistance within canopy for D78 and CM88, and excess resistance for VB95, as function of measured wind speed at reference level. Only simulation points are shown for which $H > 0$; ■ D78; □ VB95; ▲ CM88

The aerodynamic resistance above the canopy, r_a^a, is a function of the reference wind speed, the roughness length z_{0m} and a stability correction. The estimation of z_{0m} from LAI and h as applied in CM88 and D78 resulted in a value of 0.082 cm at DOY 171, slowly increasing to 0.095 cm at DOY 175, exceeding the observed roughness length by a factor two. The measured friction velocity, u_*, was overestimated by CM88 and D78, and reproduced very well by VB95 (figure not shown). The latter was to be expected from the adoption of measured values of z_{0m}. The slightly different stability corrections in CM88 and D78 hardly resulted in different values of u_* and r_a^a.

Figure 5.5 shows the values of the aerodynamic resistance between the soil and the canopy layer (r_a^s, for D78 and CM88) and the excess resistance applicable for $z_{0m}/z_{0h} = 200$ for VB95, for unstable conditions. A clear difference between CM88 and D78 is present in the values adopted for r_a^s, CM88 giving a value roughly twice as high as D78. The CM88 parameterization corresponds closely to the excess resistance adopted by VB95 for daytime

situations. The implications of the parameterization of r_a^s and the excess resistance are demonstrated well by the relationship between the bare soil temperature and the total sensible heat flux density, since the sensible heat released by the canopy is only a small part of the total sensible heat exchange. CM88 and VB95 succeed very well in predicting both the total sensible heat flux density (Figure 5.6) and the bare soil temperature (Figure 5.7). D78 underestimates the bare soil temperature by at most 7 K around noon, and overestimates the sensible heat flux density by up to 100 W/m^2. A small part of this overestimation is associated with an enhanced net radiation due to lower surface temperatures.

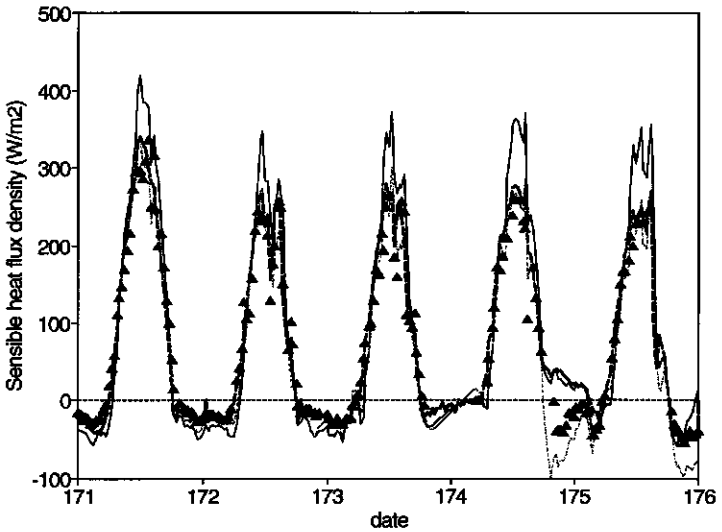

Figure 5.6: Measured and simulated total sensible heat flux density; ▲ observations; —— D78; - - - VB95; ····· CM88

The performance of VB95 is very good for both sensible heat flux and surface temperature, since values of z_{0m} and z_{0h} were obtained from field measurements. A small overestimation of the sensible heat flux density is present for the first simulation day. Obviously, the choice for the value of z_{0m}/z_{0h} is an important parameter for a proper description of the sensible heat transfer between the surface and the atmosphere. An evaluation of z_{0m}/z_{0h} using measured soil and canopy temperatures reveals a clear variation as time proceeds, both diurnally and for the five consecutive days (Figure 2.13). A similar figure appeared by using the model of CM88 as outlined in eqs. 5.1 - 5.2 and 2.36. A clear increase during the day can be seen, which can be interpreted as a reduction of the effective level of the sensible heat source as the bare ground gets warmer. Taking $z_{0m}/z_{0h} = 200$ for the whole period appears a good estimate for all days except the first.

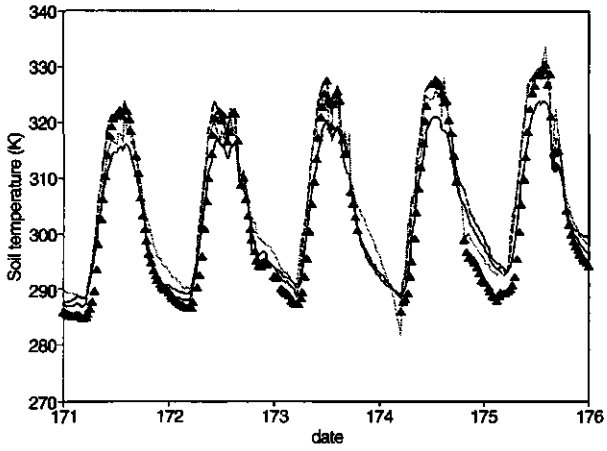

Figure 5.7: Measured and simulated bare soil temperature for CM88 and D78, and skin temperature for VB95; ▲ observations; —— D78; - - - VB95; ····· CM88

5.2.3 Evaporation and soil water budget

VB95 and D78 underestimate the total evaporation during the entire comparison period, while CM88 gives a small but consistent overestimation (Figure 5.8). The evaporated water originates almost entirely from the canopy in CM88, since soil evaporation is limited to low values by selecting a large top soil layer depth (Figure 5.9). Unlike CM88 and VB95, D78 computes a significant soil evaporation in the early hours after sunrise. The strong diurnal variation of the moisture content in the top soil layer, ω_1 (Figure 5.10) causes the humidity at the soil surface to reach values which are higher than the humidity in the canopy layer, giving rise to pronounced soil evaporation. Once the top soil layer has lost enough water to for the relative humidity at the soil surface to drop below the canopy specific humidity, q_0, soil evaporation suddenly ends.

Due to the different vertical resolution of the numerical schemes used to describe the soil moisture content adopted by VB95 and D78, the dynamics of the top soil moisture content, ω_1, differs significantly for both models. In D78 ω_1 is much lower than the moisture content in the bulk soil layer, while this difference is small in VB95 (Figure 5.10). As a result, diurnal variations of ω_1 are strongly damped in VB95. The calculated soil moisture content in the root zone decreases much stronger in VB95 than in D78, in spite of a similar canopy evaporation rate (see below). The stronger decrease in VB95 is a direct result of the simulation of water drainage to lower soil layers, not accounted for in D78. For longer term predictions these different approaches can lead to significant differences in predicted soil moisture content in the root zone. Unfortunately, the measurements of ω were taken only once during the comparison period, and these values were used to initialize the model runs. Therefore, a detailed comparison between model runs and observations is not possible.

The canopy evaporation rate is predicted rather differently by the various models. Since the crop resistance is usually approximately an order of magnitude larger than the other resistances in the pathway between the canopy and the reference level, the parameterization of r_s^c is of critical importance for the prediction of the canopy evaporation. Figure 5.11 shows values of computed crop resistances, combined with porometry data.

Also shown are values of r_s^c obtained from measured evaporation rates and leaf temperatures, by assuming zero soil evaporation and adopting parameterizations for r_a^c and r_a^a according to CM88. The values of r_s^c predicted by CM88, which are a function of incoming radiation only and calibrated using measurements, obviously agree best with both directly measured and inferred values. The formulations for soil moisture stress and response to air humidity adopted by VB95 and D78 result in higher values for r_s^c. The crop resistance in VB95 is higher than in D78, partially owing to the different choices for the minimum crop resistance (Table 5.2). In spite of this difference, the canopy evaporation rates of the two models are similar (Figure 5.8). In VB95 the surface humidity is considerably higher than the humidity at the canopy surface in D78 during daytime, due to the uniform high skin layer temperature.

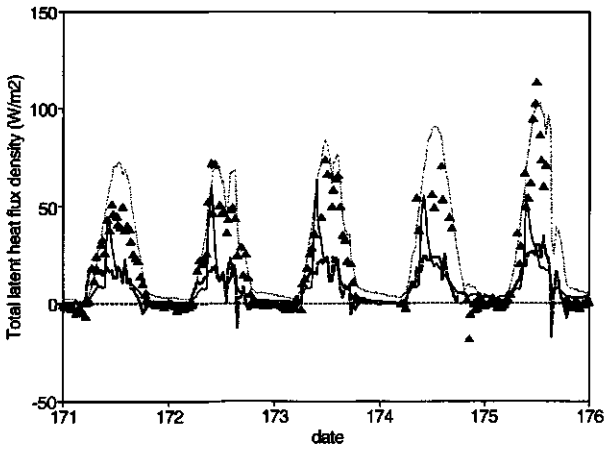

Figure 5.8: Measured and simulated total latent heat flux density; ▲ observations; —— D78; - - - VB95; ····· CM88

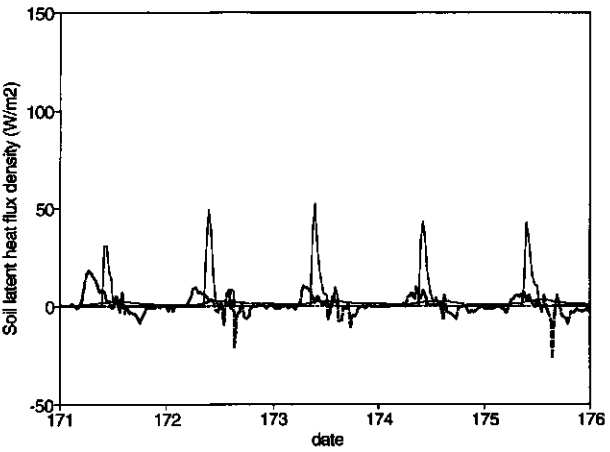

Figure 5.9: Simulated soil evaporation; ▲ observations; —— D78; - - - VB95; ····· CM88

Another reason for the difference in canopy evaporation between D78 and CM88 is the difference in parameterization of net radiation absorbed by the vegetation (Figure 5.12).

The exponential extinction formulation adopted by CM88 gives higher values for the energy available to the canopy than the explicit solution of the separate soil and canopy energy balances as modelled by D78. Hence, a higher canopy evaporation rate will be predicted by CM88 when all other variables remain unchanged.

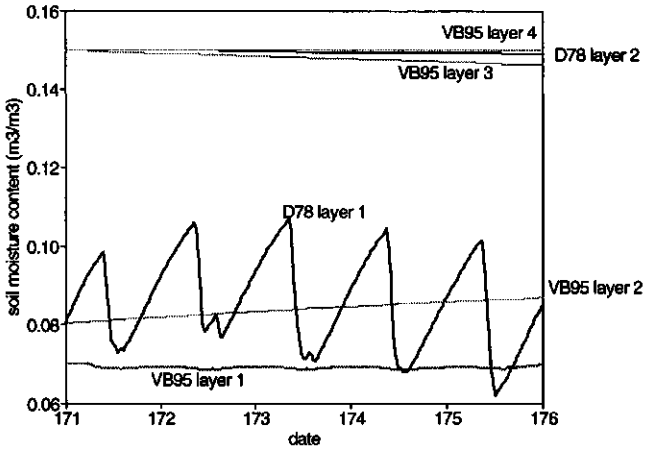

Figure 5.10: Simulated soil moisture content by D78 (——) and VB95 (·····) at levels as indicated

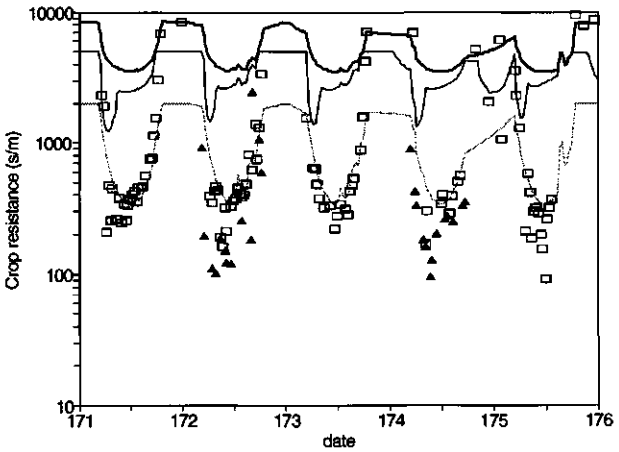

Figure 5.11: Simulated and observed values of the canopy resistance, r_s^c; Observations are carried out using porometry (▲) and inferred from measured total latent heat flux density (□); —— D78; ═══ VB95; ····· CM88

5.3 Discussion and conclusions

A comparison of three schemes for describing the exchange of momentum, heat and water vapour at the atmosphere-surface interface for a sparse canopy surface shows a wide range of predicted results. In particular predicted values of soil heat flux density and surface evaporation vary widely.

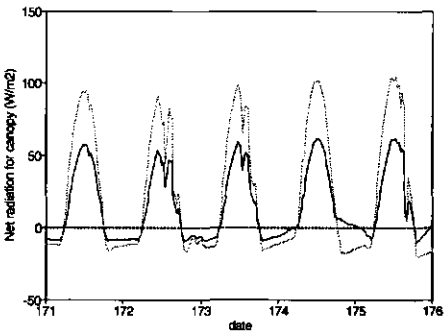

Figure 5.12: Amount of net radiation absorbed by canopy layer parameterized by D78 and CM88; —— D78; ····· CM88

With respect to the soil heat flux density, the parameterization of D78 gives the best results compared with data. The simple resistance approach of CM88 underestimates the soil heat flux density by almost an order of magnitude, due to neglecting dynamic heat storage in the upper soil layer. A dynamic heat storage, ΔG, can be implemented in the model of CM88, while solving the temperatures at the surface and at the interface between the two soil layers, at depth z_1. The heat necessary to change the temperature of the upper soil layer could be considered simply by assuming that the temperature of the top soil layer changes uniformly with depth during the simulation time step. This approach is similar to the computation of the heat storage in a well-mixed water reservoir (see Keijman, 1974). However, the effect of ΔG on the total soil heat flux density strongly depends on the choice for z_1, since the well-mixed criterion is used. In a real soil this criterion is never met, and a good estimate of G will only be achieved by a smart choice for z_1, without the possibility for providing a universal solution.

VB95 also underestimates soil heat flux density, by approximately 30%. Much of this underestimation is due to the choice of the value for the apparent heat conductivity of the skin layer, Λ. For a dense canopy, the presence of the vegetation will thermally isolate the soil from the atmosphere, and Λ may be expected to be small. For a sparse canopy, however, this temperature difference can be regarded as proportional to the soil temperature gradient immediately below the surface. Obviously, a value of Λ could be chosen corresponding to the soil type under investigation which would give a better prediction of G. A value of 17 rather than 7 W/m^2K would be a more appropriate estimate for Λ in the current situation (section 4.1.3).

In all tested models the surface temperature plays a key role, since it regulates important processes such as soil heat flux, sensible and latent heat flux, and net radiation. CM88 predicts high sensible heat fluxes in the original form, since surface temperatures are strongly overestimated when too little heat is transported into the soil. However, when the soil heat flux density was forced to values simulated by D78, their parameterization of the aerodynamic exchange within the canopy (using the resistance labelled r_a^s) appeared to give better results of the surface temperature than the formulation used by D78. In CM88, the total exchange resistance for heat between the bare soil and the reference level resembles the value included in VB95, which was based on field measurements of roughness length, surface temperature and sensible heat flux. D78 prescribes a value of r_a^s which is about half

as high as CM88, and consequently underestimates the bare soil temperature. Note that r_a^s as parameterized according to eq. 4.58 depends on the choice of z_R, taken 2.95 m here.

The parameterization of aerodynamic transfer of heat is especially important for a sparse canopy like the vineyard under investigation, where during daytime high sensible heat fluxes from the bare ground component occurred. The heat transfer is dominated by the soil component, but it is governed by many meteorological parameters in the partitioning of available energy between the soil and the vegetation. From the current exercise it can be seen that when the aerodynamic transfer between the atmosphere and a sparsely vegetated surface is treated as an excess resistance for heat, its value cannot be expected to be constant, as was discussed earlier by Kustas *et al.* (1989), Verhoef (1995) and Blyth and Dolman (1995). However, for the limited simulation period investigated in this study a constant value of $z_{0m}/z_{0h} = 200$ as applied in VB95 yields satisfactory results with respect to both surface temperature and sensible heat flux density.

The crop resistance for evaporation is best described by CM88, where a calibrated function of incoming radiation was used to describe r_s^c. The dependence of r_s^c on soil moisture content cannot be expected to be realistically described by either D78 or VB95, which assume a much smaller root zone than found in our field. Also the response of stomatal aperture to ambient humidity deficit is not fully resolved, and is an issue of discussion. Under dry and warm conditions several plant species seem to develop a specific survival mechanism, and respond differently to air humidity than plants from which the expression of Noilhan and Planton (1989) was obtained (Monteith, 1995b).

The partition of radiant energy over the vegetation and the underlying substrate is solved differently by CM88 (adopting radiant extinction) and D78 (solving separate energy balances for the two surface components). The extinction parameterization was originally developed for closed canopies, and is expected to deviate significantly from real radiative interception for a vegetation stand with widely separated plants. On the other hand, drawing up separate radiation balances does not take all edge effects into account. Which of the parameterizations is to be preferred can only be supported by detailed measurements and modelling efforts, and will most likely be different for each type of vegetation.

For large scale applications a land surface scheme necessarily needs to describe accurately a wide range of land surface types, covering the full transition from densely vegetated to completely bare. From the current study, a general conclusion can be made that for a rather sparsely vegetated surface none of the three models compared can be regarded to be the 'ideal' land surface scheme. Each of the schemes involved in this test has some superior qualities compared to the others, but also shows significant deficiencies when applied to a very sparse canopy. For the surface for which this comparison was run, a combination of parts from each of the models will likely give optimal results. Following the conclusions above such a combined model would consist of a soil heat flux parameterization using the force restore method, an aerodynamic exchange process simulated using the resistance formulation of CM88, and a canopy resistance parameterization that realistically accounts for stomatal responses to soil moisture content and air humidity. Such a model will be used as a reference in the next chapter, and will be outlined in more detail.

6

Nature is always numerically stable

Sensitivity of the planetary boundary layer to surface description

This chapter describes the influence of the description of the surface on the planetary boundary layer. The issue of atmospheric sensitivity to the description of land surface processes is not new (see, e.g., Garratt, 1993). Detailed studies were carried out previously addressing PBL-sensitivity to surface albedo, roughness, crop resistance or soil moisture content (Troen and Mahrt, 1986; McNaughton and Spriggs, 1986; Jacobs and de Bruin, 1992). In these studies the value of one or more of the surface parameters was varied, and the resulting range of predicted atmospheric variables was evaluated. Similar exercises were carried out with land-surface parameterization schemes providing the lower boundary conditions in GCM's (a list of these is included in the introduction section of this thesis).

By coupling land-surface models to larger scale atmospheric models, these studies included the effect of atmospheric feedback, as outlined in chapter 1. Their focus was to evaluate the sensitivity of the atmosphere to land-surface characteristics. They did so by adopting rather extreme ranges of surface parameters, considered to describe the largest possible atmospheric sensitivity to surface parameterization. For instance, the sensitivity study of Charney *et al.* (1977) investigates the effect of changing the albedo for some areas from 0.14 to 0.35. Jacobs and De Bruin (1992) and Sato *et al.* (1989) investigated the effect of describing the surface evaporation by means of a (simple) biophysical model, instead of using a simple bucket scheme.

The current study focuses on the response of the PBL to the physical parameterization of the fluxes between the atmosphere and a specified surface, a sparse Mediterranean canopy. The parameterization of surface fluxes from such a surface type has made significant progress in the recent past. The main question that arises is the degree of sophistication that needs to be included in the surface schemes, in order to obtain a realistic description of the PBL dynamics. An optimum choice must be made between numerical simplicity on one hand, and physical correctness on the other.

The current study focuses on the manner of describing the surface processes themselves, rather than changing values of specific surface parameters. The PBL-sensitivity to different physical parameterizations of various surface processes is investigated, rather than the effect of varying the surface coefficients. All included physical parameterizations are designed to give a description of the surface exchange processes as realistic as possible, using known characteristics of a specified surface. The parameterizations differ in complexity or in theoretical foundation.

The strategy adopted here makes use of a coupled one-dimensional surface-PBL model. Using the zero-dimensional comparison study, reported in the previous chapter, a reference SVAT scheme is chosen. Next, the description of various components of this reference SVAT are replaced with alternative parameterizations, and the effect of this replacement on the computed state of the overlying PBL is the subject of analysis.

This strategy differs in two aspects from the zero-dimensional comparison study presented in the previous section:

(1) instead of using atmospheric forcings measured at reference height, a coupled SVAT-PBL model is used here. This allows description of the atmosphere-surface feedbacks, which will affect the PBL-sensitivity to the surface description

(2) a reference model is defined, and components of this model are exchanged. In the previous section complete models were compared which differed from each other in many aspects. By changing single surface model components only, an attempt is made to disentangle the complex coupled processes simulated simultaneously in a full surface scheme.

Obviously, the results of this approach will partly depend on the choice of reference model, on the simulated surface, and on the calibration of the various SVAT components. The coupling between various surface processes (for instance, the effect of soil heat flux on surface temperature and consequently on soil evaporation) will be different for different types of surfaces or different ways of representing surface processes. However, the complexity of the process interactions makes a reduction of the total number of degrees of freedom inevitable, and emphasis is put on a single sparse canopy surface. In order to maintain a certain degree of generality of the sensitivity study, a number of the prescribed surface parameters were varied in some cases.

The sensitivity study is carried out for two sets of forcings and initializations: a synthetic set and a measured set. The synthetic dataset includes two initial PBL-profiles, chosen to represent climate zones in which sparse canopies are often found: a dry Tropical profile (DRY) and a more humid Mid Latitude Summer profile (MLS). DRY is considered to represent Mediterranean conditions in the dry growing season. MLS is included to represent conditions which may be considered typical for agricultural crops with incomplete vegetation cover, early in the summer.

The measured set of initial profiles and forcings is obtained from measurements taken during the EFEDA-I campaign in June 1991. This set of model calculations is included in order to evaluate the ability of the coupled SVAT-PBL model to describe actually measured data, and to evaluate the sensitivity of this description to the surface parameterization. It also adds to the sensitivity study by adopting initial profiles showing a pronounced

presence of a residual layer, which often occured during EFEDA. The initial profiles are obtained from a radiosounding carried out by CNRM, and the geostrophic and radiative forcing are taken from measured quantities. A control run with measured surface fluxes is included to provide insight in the skill of the uncoupled PBL-scheme for the present case.

An 'honest' intercomparison of parameterizations can only be carried out when the various schemes are calibrated to describe a similar surface. Due to the different theoretical backgrounds of the included schemes, this is not always straightforward. In all cases the surface schemes were calibrated using data described in earlier sections.

First a summary of the reference model and variations thereupon will be presented in section 6.1. Also the calibration of the model components is outlined. Then the setup of the sensitivity analysis using the artificial input is discussed (section 6.2). The results of this analysis are presented separately for daytime (convective) conditions (section 6.3) and nighttime (stable) conditions (section 6.4). The results-sections are followed by a model comparison applied using measured data. For this last analysis a selection of an adequate comparison period had to be made. This selection and the data used are presented in section 6.5. Section 6.6 concludes this sensitivity chapter.

6.1 Model specification

The scientific backgrounds of the surface model components were discussed before (section 4.1). Here, a brief summary is given. In most cases the calibration of the models is similar as in the previous chapter (Table 5.2). Where appropriate, additional commentary is given. The numerical schemes used to solve the coupled models are discussed in Appendix V.

6.1.1 The reference model

The sensitivity of the PBL to the surface paramaterization is basically a sensitivity to simulated surface flux densities. Therefore, an appropriate selection criterion for a parameterized lower boundary condition is to select a SVAT describing the observed fluxes optimally. In the conclusions of the previous chapter it was suggested that, using measured forcings, the surface fluxes were optimally simulated by the Deardorff model, where aerodynamic resistances were parameterized according to Choudhury and Monteith (1988), and a realistic crop resistance was included. Verhoef (1995) tested a SVAT of this kind for a Sahelian savanna and tigerbush surface. The reference model consists of the following parts (see Table 6.1 for a summary):

- *surface components:* two surface components are distinguished: the canopy elements and the underlying soil. A relative fraction of surface covered with vegetation is used for calculating energy fluxes of each of these components. Each component is allowed to obtain its own temperature and surface humidity.
- *soil temperature:* the force-restore method (eq. 4.47) is used to describe the soil surface temperature T_s. Basic parameters determining the temperature change of the top soil layer are the specific heat of the soil, the temperature of the lowest layer (assumed to vary according to an annual wave) and the soil heat flux density.
- *net radiation:* shortwave and longwave incoming radiation are specified. Net

radiation for each surface component is obtained by using its temperature to specify emitted longwave radiation. Albedo and longwave emissivity are specified coefficients. In contrast to the simulations in chapter 5, the longwave emissivity of the plants was taken to be 0.90 rather than 0.98.

- *surface fluxes:* canopy evaporation is calculated by defining a fraction of the potential evaporation using the ratio of leaf stomatal and leaf boundary layer resistances. Soil evaporation is parameterized by specifying a relative humidity of the soil surface, as function of the soil moisture content of the top soil layer. Soil heat flux is the remainder of the energy balance at the soil.
- *aerodynamic exchange:* the aerodynamic resistances are calculated following Choudhury and Monteith (1988). The resistance above the canopy is similar for momentum and heat. Bulk boundary layer and within-canopy aerodynamic resistance are functions of leaf area index, roughness length of the soil, and surface roughness and displacement height. Measured values of z_{0m} and d were used instead of the canopy roughness characteristics calculated by Shaw and Pereira (1982).
- *soil moisture:* as for temperature, a two layer force-restore method is used. Soil hydraulic properties are described as proposed by Clapp and Hornberger (1978).
- *canopy resistance:* a simple scheme proposed by Choudhury and Monteith (1988) is used, which describes r_s^c as function of *LAI* and total shortwave radiation only. The response of r_s^c to shortwave radiation is calibrated using field data.

6.1.2 Model variations

The case 'big-leaf'

In the case 'big-leaf' the two-component surface source is replaced by a single 'big-leaf' approach, in which the surface consists of a single source with uniform temperature. The energy balance of the surface is solved with the incoming radiation terms specified. As in the reference case the force restore-method is used to describe G, but this time the soil heat flux is evaluated from a known value of the surface temperature, rather than the other way round (eq. 4.8). The same lower boundary conditions in the soil apply as in the reference case. An excess resistance for scalars is used, by taking $z_{0m}/z_{0h} = 200$. The surface longwave emissivity was fixed at 0.98.

The case 'isotherm'

In the case 'isotherm' the surface source consists of a single layer with a uniform temperature, as in the big-leaf approach. However, various fractions are discerned with respect to the evaporation rate: a skin reservoir with open water (filled with dew and intercepted water), an evaporating plant canopy and an evaporating bare soil. The surface description in this case resembles the treatment employed in the ECMWF-surface scheme (Viterbo and Beljaars, 1995) and the model of Noilhan and Planton (1989). Net radiation, sensible and soil heat flux density, and an excess resistance used to discern between momentum and scalar transfer, are treated as in the case 'big leaf'.

The case '3 fracs'

The case '3 fracs' was included as to evaluate the effect of the temperature

Table 6.1: Variations of the surface model

Variation code	sources at surface	partition of radiation	aerodynamic exchange	crop resistance	soil heat and water fluxes	remarks
reference	canopy and soil	D78	CM88	CM88 (calibrated)	force-restore	
big leaf	big-leaf	-	excess resistance			
isotherm	VB95	-	excess resistance			
3 fracs	VB95 (non isothermal)	-	excess resistance			
aero D78			D78			
aero MH95			MH95			
r_c CO_2				assimilation		
r_c VB95				VB95		
r_c fix				fixed		
r_c big CO_2	big-leaf			assimilation		
soil VB95					VB95	
soil r_s^s					λE_s using r_s^s	$\partial\omega/\partial t$ and $\partial T/\partial t$ from force-restore
soil CM88	CM88	SW85 (modified ext.coeff.)	Louis (1979)		CM88	Q_* from reference, no iteration for r_a^a

differentiation in the VB95 model in a coupled mode (see section 4.1.3). The surface energy balance is computed separately for each surface fraction (open water, canopy and bare ground), and the final fluxes of λE, H, Q_* and G as well as the temperature of the upper soil layer and the aerodynamic resistances are computed by averaging the resulting quantities weighted by the appropriate surface fractions (eq. 4.18).

■ **The case 'aero D78'**

The aerodynamic resistance within the canopy, computed assuming an exponential decay of the eddy-diffusivity, is replaced by a simple drag partition scheme proposed by Deardorff (1978) in the case 'aero D78'. An effective canopy wind is obtained by interpolation between the reference wind and u_*, and an iterative stability correction is applied. For consistency with results reported in section 5.2.2, in the coupled surface layer-PBL models r_a^s is evaluated using eq. 4.58, in which u_a and C_H are evaluated at a height of 2 m above the canopy top (that is, at 3 m for the EFEDA sparse vineyard canopy). Also the leaf boundary resistance is treated simpler than in the reference model, by not taking wind speed gradients within the canopy into account.

- **The case 'aero MH95'**

In the case 'aero MH95' the aerodynamic resistances both within and above the canopy defined by Choudhury and Monteith are replaced by the resistances proposed by McNaughton and Van den Hurk (1995), which are based on Lagrangian principles (see section 3.2.3). The values are chosen to represent a uniform source profile (Beta-distribution with $p = q = 1$), the value of σ_w/u_* at $z = 0$ equal to 0.15, and the wind profile extinction coefficient α_u equal to 3 (see Tables 3.2 and 3.3). For the normalized near-field resistor $\Re_n$ the suggested value of 0.36 was applied. Note that the value of the normalized aerodynamic resistance above the canopy corresponds to a reference height of $2h$. The resistance was extrapolated to the reference level z_R according to

$$\Re_1(z_R) = \Re_1(2h) + \frac{1}{\kappa} \ln\left(\frac{z_R}{2h}\right) \tag{6.1}$$

Actual resistances were obtained by dividing the normalized values by u_*. Values of u_* were obtained from u_a by using the Dyer-Hicks stability corrections for the pathway between z_R and $2h$ (see Appendix V).

- **The case 'r_c CO_2'**

The case 'r_c CO_2' replaces the parameterization of the crop resistance by the assimilation routine of Jacobs (1994), scaled up to the canopy level (section 3.4).

- **The case 'r_c VB95'**

In the case 'r_c VB95' the crop resistance is described by the multiregression model of Viterbo and Beljaars (1995). In this model, the crop resistance is only affected by the shortwave radiation and soil moisture (see eqs. 4.26 - 4.28). No dependence on ambient humidity deficit is included. The calibration is carried out according to the suggestions made by VB95. For $\overline{\omega}$ the value of ω_2 is used.

- **The case 'r_c fix'**

In the case 'r_c fix' the crop resistance is replaced by a fixed value, independent of any meteorological condition. This value is obtained using a weighted average of a diurnal cycle of values of r_s^c simulated in the reference model.

- **The case 'r_c big CO_2'**

As in the case 'r_c CO_2' the assimilation routine of Jacobs (1994) and discussed in section 3.4 is used to describe the surface resistance, but this time the surface model is replaced by the big-leaf scheme (case 'big-leaf'). This case is included to demonstrate the effect of a surface resistance with a strong response to environmental conditions.

- **The case 'soil VB95'**

The 'soil VB95' case is dedicated to the exploration of the effect of replacing the force-restore method in the reference case by the 4-layer soil model as used in the ECMWF-surface model (VB95). In this approach the variation of the soil temperature and soil moisture

content are solved for four layers, using a numerical solution of a set of diffusion equations. Thermal and hydraulic conductivity depend on soil type and moisture content, and are parameterized with similar relations as in the reference model. The soil heat flux and soil evaporation forcing the temperature and moisture changes are treated as in the reference model. A zero heat flux and free water drainage are imposed as lower boundary conditions, and the total simulation depth is taken equal to the original ECMWF land surface scheme, that is, 2.89 m (see Table 6.7). In the VB95 model, the surface temperature forcing of the soil volume is situated in a skin layer without heat capacity (section 4.1.2). For large soil heat fluxes, a considerable temperature difference may occur between this skin layer and the centre of the upper slab, at depth 3.5 cm. In order to employ a proper coupling between the surface energy balance and the soil heat flux here, a very thin slab (1 mm) is added on top of the diffusion scheme. The temperature of this slab is considered to be equal to the skin temperature, from which net radiation and sensible heat flux are calculated. The soil moisture transport is simulated with the original 4-layer diffusion scheme, and the thermal soil properties of the upper thin layer are evaluated using the soil moisture content of the upper slab of 7 cm depth. Water extracted by vegetation is taken from the upper three layers only. As in the reference model, soil surface relative humidity is calculated by using eq. 4.19 but with the layer coefficient l_c set to 1.6, as suggested by VB95.

- **The case 'soil $r_s^{s\prime}$'**

The case 'soil $r_s^{s\prime}$' represents an alternative description of soil evaporation. The relative humidity at the soil surface is calculated according to the formulation of Philip (1957, eq. 4.83). The matric potential ψ is obtained from the soil moisture content in the top layer, using the Clapp and Hornberger (1978) parameterization, given by

$$\psi_1 = \psi_{sat}\left(\frac{\omega_1}{\omega_{sat}}\right)^{-b} \tag{6.2}$$

A soil evaporation resistance, r_s^s, is included in the pathway of water vapour from the surface to the canopy airstream. We used a fixed value of 2000 s/m, as suggested by Shuttleworth and Wallace (1985) for dry soils. This value is close to the high-end of the range span by the clear diurnal course reported by Van de Griend and Owe (1994), who measured r_s^s of the EFEDA test site using a respiration chamber. Soil moisture transport is treated similarly as in the reference case, that is, using a force-restore method.

- **The case 'soil CM88'**

In the case 'soil CM88' the soil heat flux is computed using the scheme of Choudhury and Monteith (1988), that is, using a heat exchange resistance and a temperature difference between the surface and an intermediate level under the surface. Also soil evaporation is treated using a resistance formulation, as by CM88. The change of the deep soil temperature is calculated as in the reference model. Also the soil moisture content of the two layers are computed using the force-restore algorithm, in spite of the CM88-assumption that the lowest soil layer is water-saturated. The depth of the upper soil layer is initialized at 0.1 m, and changes as soil evaporation proceeds.

In CM88, the computation of the soil heat flux density and soil evaporation are imbedded in a rather complicated set of equations. These equations solve the temperature and humidity at the bare soil surface, the canopy surface, the airstream within the canopy and at the layer intersection within the soil, as well as the fluxes of water vapour and heat in between these levels (see section 4.1.5). For the 'soil CM88' case the entire CM88 algorithm replaces the D78 surface model. As discussed before (section 4.1.5), the two-layer canopy models based on the Penman-Monteith concept suffer from numerical instability when stability corrections are incorporated or when net radiation and soil heat flux are parameterized as function of the canopy or soil temperature. Therefore, net radiation is taken from the reference simulations. Its partition over soil and canopy is computed by using the exponential extinction (eq. 4.65), with an extinction coeffient β_r set to 0.45. This value results in a partition nearly similar to the reference model. The parameterization of the aerodynamic resistance above the surface is carried out using the non-iterative scheme of Louis (1979), in order to minimize numerical stability problems. In this way a steady state solution of the surface energy balance is obtained, which is a consequence of replacing the force-restore method by the CM88 strategy. The flux densities above the ground are affected by the alternative prediction of the surface temperature, but their computation follows practically the same physical treatment as in the reference model.

Table 6.2: Configuration of comparison groups. Also given are code letters and numbers for the surface models and surface types, respectively, for later reference

group	surface models	model code	surface types	surface code
surface representation	reference	a	sparse vineyard canopy	1
	case 'big-leaf'	b	sparse vineyard canopy $\sigma_f = 0.4$	2
	case 'isotherm'	c	sparse vineyard canopy $\sigma_f = 0.7$	3
	case '3 fracs'	d	sparse vineyard canopy $\sigma_f = 1.0$	4
soil heat and water flux	reference	a	sparse vineyard canopy on sandy loam	1
	case 'soil VB95'	l	sparse vineyard canopy on sandy clay	5
	case 'soil CM88'	m		
	case 'soil r_s^5	n		
aerodynamic exchange	reference	a	sparse vineyard canopy	1
	case 'aero D78'	e	tigerbush	6
	case 'aero MH95'	g	forest	7
canopy resistance	reference	a	sparse vineyard canopy	1
	case 'r_c CO_2'	h		
	case 'r_c VB95'	i		
	case 'r_c fix'	j		
	case 'r_c big CO_2'	k		

6.2 Set-up of the sensitivity analysis

6.2.1 Basic strategy

Many of the surface processes show complex interactions. An investigation of all possible combinations of selected model variations, initializations and surface land types may seem appropriate since it will include all these interactions, but in practice is not useful due to the large amount of quantities that must then be evaluated. Therefore, a set of four

relevant groups of parameterizations were defined, and separately discussed: a *source representation* group, a *soil heat and water flux* group, an *aerodynamic exchange* group, and a *canopy resistance* group. Each of these groups contains a number of model combinations and land surface types. A 36 hour run with a coupled surface-PBL model is carried out for each of the relevant surface types using a prescribed radiative forcing. Two different initial PBL-profiles are taken for each of the runs. First the four different groups containing the model combinations and land surface types will be briefly discussed. Table 6.2 summarizes the layout of the various groups. The next sections pay attention to the definition of the evaluated SL- and PBL-parameters, and to the forcing and initial profiles adopted in the simulation runs.

The *source representation* group is designed to evaluate the importance of recognizing separate sources of heat and water vapour in case of a sparse canopy surface. For that purpose, four different surface model combinations are included: the reference model, and the cases 'big-leaf', 'isotherm' and '3 fracs'. The surface is parameterized as a sparse vineyard canopy as encountered during the EFEDA experiment. Parameter values for this default surface are found in Table 6.3. Furthermore, a range of degrees of vegetation coverage is allowed, ranging from 0.11 (the default value) to 1.0.

Table 6.3: Default parameter values for sparse vineyard canopy. Only listed are the parameters which are changed in the sensitivity analysis. Remaining surface parameter values can be found in Table 5.2.

parameter	symbol	value		
		vineyard	tigerbush	forest
Leaf Area Index per unit plant surface	LAI_*	3 m^2/m^2	3 m^2/m^2	3 m^2/m^2
roughness length momentum	z_{0m}	0.04 m	0.44 m	0.40 m
roughness length scalars (for one-layer cases)	z_{0h}	z_{0m}/200 m	z_{0m}/200	z_{0m}/200
displacement height	d	0.45 m	2.00 m	5.10 m
crop height	h	1 m	4 m	8 m
fraction vegetation cover	σ_f	0.11	0.33	0.25
soil type		sandy loam (see Table 6.4)		
reference		this study	Dolman *et al.*, 1992	Garratt, 1978

The *soil heat and water flux* group pays attention to the effect of various parameterizations of soil heat flux and soil evaporation. Again four different model combinations are included: the reference model and the cases 'soil VB95', 'soil CM88' and 'soil $r_s^{s'}$'. The intercomparison is carried out for a sparse vineyard canopy on two different types of soil: the default sandy loam, and a denser sandy clay soil. Parameter values of these soil types can be found in Table 6.4.

The *aerodynamic exchange* group investigates the different parameterizations of the aerodynamic resistances in the two-component model. Three different cases are compared here: the reference model, and the cases 'aero D78' and 'aero MH95'. The sensitivity analysis is carried out for three different vegetation types: the default sparse vineyard canopy, a

Table 6.4: Soil parameters for different soil types

soil type	ψ_{sat} (m)	b	a	p	C_{2ref}	γ_{sat} (m/s)	ω_{sat} (m^3/m^3)	ω_{pwp} (m^3/m^3)	ω_{fc} (= ω_c) (m^3/m^3)
sandy loam	-0.25	4.9	0.219	4	1.8	$3.41\ 10^{-5}$	0.472	0.075	0.354
sandy clay	-0.15	10.4	0.139	8	0.3	$2.15\ 10^{-6}$	0.426	0.075	0.320

sparse tigerbush vegetation in semi-arid areas (Dolman *et al.*, 1992) and a moderately dense forest canopy (Garratt, 1978). Aerodynamic parameter values for these surface types can be found in Table 6.3.

The *canopy resistance* group explores different canopy resistance models with varying complexity. In this group five different canopy resistance parameterizations are included. The reference model includes a dependence of r_s^c on *LAI* and shortwave radiation only (the calibrated simple formulation of CM88). The case 'r_c VB95' adopts also a dependence on soil moisture content. 'r_c CO_2' and 'r_c big CO_2' are treated using the photosynthesis model, and include dependences on ambient humidity deficit, radiation and leaf temperature. The last case, 'r_c fix' excludes any dependence by treating r_s^c as a fixed parameter. The practical formulation of the canopy resistance is usually carried out by using an extensive species specific calibration. Many species could be investigated and included in the surface description. However, to serve simplicity and comparability with other parts of this study the work is confined to the default sparse vineyard canopy. For the two photosynthesis models (cases 'r_c CO_2' and 'r_c big CO_2') the calibration coefficients as found by Jacobs (1994) were adopted (see section 3.4). Table 6.5 lists the relevant coefficient values for the resistance models.

6.2.2 Specification of considered SL- and PBL-parameters

The coupled SVAT-PBL model used for this study was designed to describe diurnal variations of energy and momentum fluxes. As a result, the PBL-temperature, humidity content and height vary with time.

In order to quantify the PBL-sensitivity to the surface parameterization a set of relevant parameters must be specified which allows an objective intercomparison of the various model components. Furthermore, we are interested in differences between the effects of various model components on these parameters, compared to a specified reference set of model components. Therefore, a sensitivity of parameter x to the surface parameterization is defined as

$$\xi_x = \frac{x(m_i) - x(m_r)}{x(m_r)} \qquad (6.3)$$

where $x(m_i)$ is the PBL-parameter computed with model variation m_i, and m_r is the reference model variation. For the parameters indicating a temperature or specific humidity a sensitivity as expressed by eq. 6.3 is not very meaningful, and these are expressed as an absolute difference with the value computed by the reference model. For an evaluation of absolute values of $x(m_i)$, Appendix VI lists the values of x calculated with the reference model.

Table 6.5: Coefficient values for the various canopy resistance models

model	coefficient	symbol	value
reference (CM88)	cuticular conductance	g_{cut}	0.0005 m/s
	change of conductance per unit shortwave radiation	g_1	4 10^{-6} m/s / W/m^2
	radiation extinction coefficient	β_r	0.7
photosynthesis model	maximum humidity deficit	D_{max}	58.2 g/kg
(cases 'r_c CO_2' and 'r_c big CO_2')	slope of C_i/C_s with changing humidity deficit	f_0	0.916
	maximum C_i/C_s	f	0.85
	plant type *	C3	
'r_c VB95'	minimum stomatal resistance	$r_{s,min}$	240 s/m
	maximum stomatal resistance	$r_{s,max}$	5000 s/m
	shortwave radiation coefficients	a_1	0.19
		a_2	1128 W/m^2
		a_3	30.8 W/m^2
'r_c fix'	fixed value of stomatal resistance	r_{st}	500 s/m

* Values of physiological parameters for C3 plants can be found in section 3.4 and Appendix IV

The choice of the relevant parameters must reflect the basic physical characteristics of the surface-PBL system. For daytime conditions the selected parameters are the surface energy balance components (Q_*, H, λE and G) and amounts of entrained sensible and latent heat during daytime, the mixed layer temperature, -specific humidity, -wind speed and -height, and the change of the total soil moisture content in the soil simulation volume. In order to avoid a tedious and unorganized intercomparison some data reduction is desirable. Energy balance parameters as well as entrained heat fluxes are averaged to daytime (6 - 18 GMT) and nighttime (18 - 6 GMT) values. Parameters describing the state of the PBL and the change of the bulk soil moisture content are evaluated at fixed simulation time intervals.

Since the fluxes of sensible and latent heat were very small during the nighttime simulations, a relative difference of these quantities is not very meaningful. Instead, for discussion of the nighttime simulations we selected the minimum temperature at reference height as a characteristic parameter, which is strongly associated with the nighttime cooling due to forced convection and the initial temperature profile when the night begins. The associated parameters that are presented are the specific humidity at the same reference level, and the PBL-height, all at the same time where the minimum reference temperature was recorded (around sunrise). Table 6.6 summarizes the chosen parameters.

6.2.3 Radiative forcings and initial profiles

The simulations all started at 4 GMT for a hypothetical DOY 174, and were executed for 36 hours with a time step Δt of 3 minutes. The shortwave radiative forcing was expressed as a function of zenith angle ζ using the semi-empirical turbidity formulation (Holtslag and Van Ulden, 1983)

$$K^{\downarrow} = 1041 \cos\zeta - 69 \tag{6.4}$$

The incoming longwave radiation is parameterized using the formulation of Brutsaert (1982):

$$L^{\downarrow} = \varepsilon_a \sigma T_a^4 = 1.24 \left(\frac{e_a}{T_a} \right)^{1/7} \sigma T_a^4 \tag{6.5}$$

with e_a expressed in hPa and T_a in Kelvin. In these synthetic cases the radiative forcing (both shortwave and longwave) were parameterized assuming the absence of clouds.

Table 6.6: Basic PBL-surface parameters included in the sensitivity analysis

Parameter	symbol	defined as
daytime net radiation	Q_*^D	average Q_* between t = 6 GMT and t = 18 GMT (day 174)
daytime sensible heat flux	H^D	as Q_*^D
daytime latent heat flux	λE^D	as Q_*^D
daytime soil heat flux	G^D	as Q_*^D
daytime entrained sensible heat flux	H_t^D	as Q_*^D
daytime entrained latent heat flux	λE_t^D	as Q_*^D
boundary layer height at 6 hours intervals	z_i^t	z_i at t = 12, 18 GMT (day 174) and t = 6 GMT (day 175)
soil moisture change compared to 6 GMT, day 174	$\Delta\omega^t$	$D\ [\Sigma\ \omega_i(t) - \Sigma\ \omega_i(0)]$ for t = 18 GMT (day 174 and 175) *
PBL-potential virtual temperature at 6 hours intervals	θ_v^t	average $\theta_v(t, z)$ between 0.1 z_i and 0.9 z_i, for t = 18 GMT (day 174)
PBL-specific humidity at 6 hours intervals	q^t	as θ_v^t
minimum nighttime reference temperature	θ_v^{min}	minimum value of $\theta_v(z_R)$ between t = 0 and 6 GMT, day 175
minimum nighttime reference specific humidity	q^{min}	$q(z_R)$ at the same time as θ_v^{min}

* D is the depth of the lowest soil moisture layer in the model's soil simulation volume

The first of the two artificial initial PBL profiles, labeled Mid Latitude Summer (MLS), was taken from Ellingson *et al.* (1991), both for θ_v and q. They used and listed standard atmospheric profiles derived by McClatchey *et al.* (1971) to intercompare longwave radiation codes in climate models. The second profile, labeled DRY, was inspired on the EFEDA-I radiosoundings of CNRM. The θ_v-profiles measured early in the season very much resembled the so-called Tropical profile presented by Ellingson *et al.* (1991), shown in Figure 6.1. However, as an example of θ_v-profiles observed later during the campaign, the profile of 23 June (DOY 174) 1991, 4:10 GMT is also shown in Figure 6.1. A clear residual layer is present in

the profile of θ_v. The exact shape of this profile was shown to have many appearances in the later EFEDA-season. For reasons of representativeness, the Tropical θ_v-profile was chosen for the DRY profile. However, the associated humidity profile, shown by the dashed curve in the right panel of Figure 6.1, was very humid compared to the conditions encountered during EFEDA. Therefore, for the DRY humidity profile a 'representative' artificial humidity profile, based on several observed humidity profiles taken during the entire EFEDA season, was drawn by eye. The typical shape of this artificial profile is clearly present in the observations of 23 June, shown also.

For the calculations, only profile levels below z = 5 km were considered, and the vertical resolution of the model was nearly corresponding to the resolution of the observations taken during EFEDA. A small number of data points were omitted, and a total number of 82 model levels was left, the lowest being at z_R = 25 m. The grid box size increased further from 25 m in the lowest part of the model to 85 m near the top.

In all cases the air pressure at the surface was kept at standard pressure (1013.5 hPa). The geostrophic forcing was provided by assuming a constant geostrophic wind of 5 m/s. The horizontal wind speed was kept at a constant (geostrophic) value for z > 1000 m, and was extrapolated to the surface according to a neutral logarithmic profile. Also an initial profile of the CO_2 concentration was specified, affected by the cases where an active source or sink of CO_2 was modelled, that is, in the cases 'r_c CO_2' and 'r_c big CO_2'. An initial value of 340 ppm at all levels was specified.

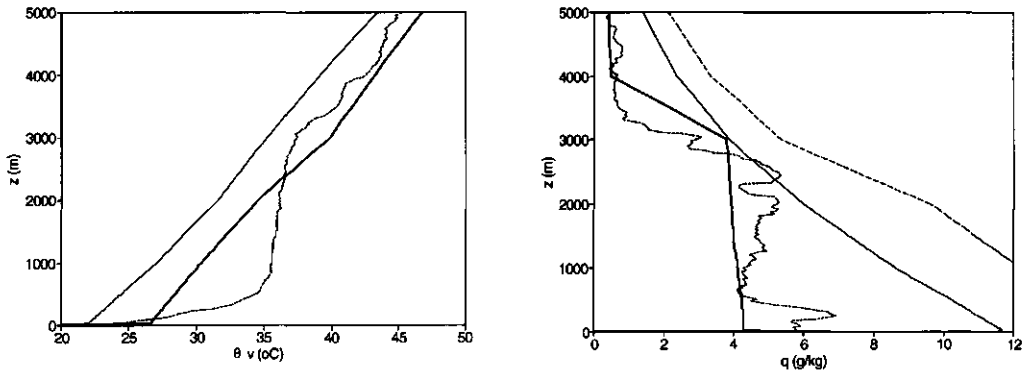

Figure 6.1: Initial profiles of θ_v (left) and q (right); ——: MLS, taken from Ellingson *et al.* (1991) for both θ_v and q, and ——: DRY, taken from the Tropical profile of Ellingson *et al.* (1991) for θ_v and drawn by eye for q. Also shown are the measured profiles of 23 June 1991, 4:10 GMT (·····) and the Tropical humidity profile presented by Ellingson *et al.* (1991) (- - -)

An initial soil temperature and moisture profile were obtained from EFEDA-I field measurements, taken at DOY 174, 4:00 GMT. These values were used for all initializations, and can be found in Table 6.7.

6.3 Results of the sensitivity analysis for daytime conditions

Only the simulation results for the first daytime period (6:00 - 18:00 GMT) are presented here. A separate subsection (6.3.5) summarizes the sensitivity results for

Table 6.7: Initial soil moisture and temperature profiles

depth (m)	temperature (°C)	moisture content (m^3/m^3)
all models except case 'soil VB95'		
0 - 0.10 *	15.8	0.07
0 - 0.60 *	24.0	0.15
soil model case 'soil VB95'		
0 - 0.001 **	15.8	
0.001 - 0.07	21.3	0.07
0.07 - 0.28	26.1	0.08
0.28 - 1.00	24.0	0.15
1.00 - 2.89	24.0	0.15

* these soil depths apply to the moisture budget only; the depths for the thermal force-restore method are equal to the depth of the diurnal and annual temperature wave, respectively (section 4.1.4)

** the upper soil layer only applies to the temperature diffusion; soil moisture in that layer is equal to the soil moisture in the second soil layer, and not computed separately

convective conditions, by comparison of all model simulations with a simple slab-model, which is partly analytical.

6.3.1 The surface representation group

The surface representation group contains runs from the cases 'reference', 'big leaf', 'isotherm' and '3 fracs', simulating vineyard canopies with σ_f equal to 0.11, 0.4, 0.7 and 1.0, and initialized with DRY and MLS profiles (see Table 6.2).

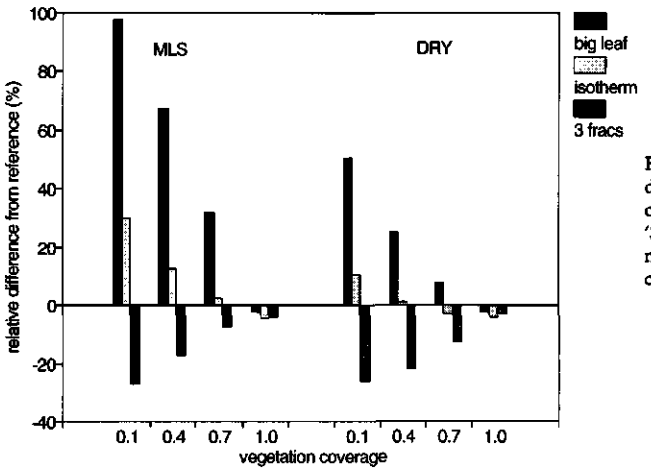

Figure 6.2: Differences in predicted daytime evaporation, λE^D, for the cases 'big leaf', 'isotherm' and '3 fracs' relative to the reference model. The fraction of vegetation cover σ_f varied between 0.1 and 1.0

- **Surface parameters**

The most pronounced effect of treating the surface as a single isothermal source of heat and water vapour is the prediction of the average daytime evaporation, λE^D (Figure

6.2). The case 'big leaf' clearly results in a significant increase of λE^D, and this effect is most pronounced when when σ_f is small. For larger amounts of vegetation cover the difference between the two-component model and the big-leaf approach decreases, and the average surface temperature driving the surface evaporation in the case 'big leaf' converges towards the canopy temperature in the reference model. For $\sigma_f = 1$, almost no difference between the two cases remains. Minor differences persist due to the different parameterization of the aerodynamic resistances in the two models.

The initialization has a clear impact of the sensitivity of λE^D to the model choice: the differences between case 'big leaf' and the reference are much larger for MLS than for DRY. The same holds for the case 'isotherm'. However, from Figure 6.2 it is also obvious that the latter case resembles the reference two-component model much more than the 'big leaf' case. The division of the surface into separate fractions with respect to evaporation reduces the effect of the uniform surface temperature, which is approximately identical in both cases. The reduction is caused by an artificial enhancement of the aerodynamic resistance in the 'isotherm' case. The surface evaporation for the case 'big leaf' is given by

$$E = \rho \frac{q_{sat}(T_s) - q_a}{r_s^c + r_a} \tag{6.6}$$

while E in the case 'isotherm' (assuming a negligible evaporation from the skin reservoir) is equal to

$$E = \sigma_f \rho \frac{q_{sat}(T_s) - q_a}{\sigma_f r_s^c + r_a} + (1 - \sigma_f) \rho \frac{\alpha q_{sat}(T_s) - q_a}{r_a} \tag{6.7}$$

For a zero soil evaporation (which applies to very dry top soil and can be obtained by taking $\alpha = q_a / q_{sat}(T_s)$), eq. 6.7 reduces to

$$E = \rho \frac{q_{sat}(T_s) - q_a}{r_s^c + r_a/\sigma_f} \tag{6.8}$$

For small values of r_a the cases 'isotherm' and 'big leaf' are nearly similar, and the total evaporation is mainly regulated by the canopy resistance. However, owing to the relatively large excess resistance included in r_a, the cases differ significantly by the enhancement of r_a by a factor $1/\sigma_f$.

When different temperatures for the different surface fractions are allowed (case '3 fracs'), the surface scheme simulates a lower evaporation than the reference model in all cases. This reduction is less when σ_f increases.

The sensitivity of the total daytime sensible heat flux, H^D, to the surface representation is shown in Figure 6.3. In all cases, the cooler surface temperature results in a decrease of H^D. The sensitivities are limited to 35% for the MLS initialization, and 25% for DRY. The largest response of H^D is generally not found in cases of almost bare soil or complete vegetation cover, but occurs in between these limits. In spite of the large relative difference of λE^D for $\sigma_f = 0.1$, the relative sensitivity of H^D is small for all cases, due to the

low absolute value of λE^D, and the consequently small redistribution of available energy towards H. For large values of σ_f the difference between the formulation of an average surface temperature by a single- or dual source model vanishes, and the impact of the surface representation on H^D is consequently also small. The relatively high response of H^D for intermediate values of σ_f is the result of a balance of these two effects. The differences between the cases '3 fracs' and the reference model are mainly caused by a small phase shift of the simulated sensible heat flux, rather than different maximum values.

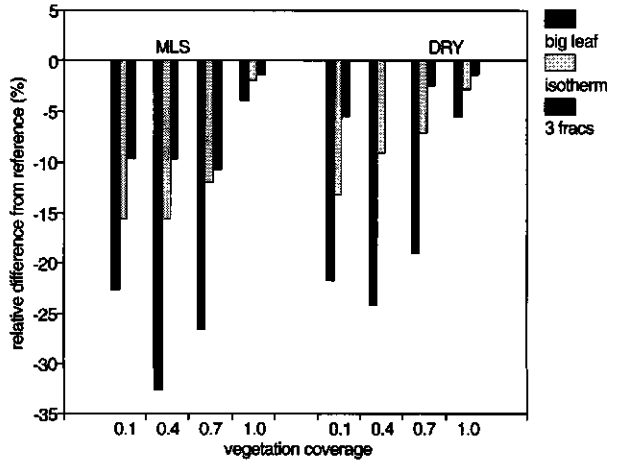

Figure 6.3: As Figure 6.2, for daytime sensible heat flux, H^D

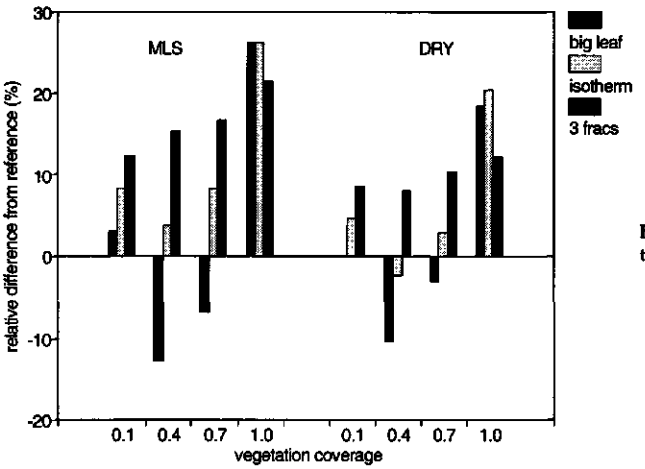

Figure 6.4: As Figure 6.2, for the total daytime soil heat flux, G^D

The response of the daytime soil heat flux G^D, shown in Figure 6.4, is somewhat different. The difference between the one-layer surface models and the reference are relatively small for $\sigma_f < 1$, but are generally higher for $\sigma_f = 1$. Common to all models that regard the surface as a single layer is the absence of simulating a sensible heat flux between the soil and the canopy. This tends to increase the soil heat flux. However, it must be noted

that the absolute values of G^D calculated by the reference model are rather small: 42 and 49 W/m^2 for the MLS and DRY initializations, respectively (Appendix VI).

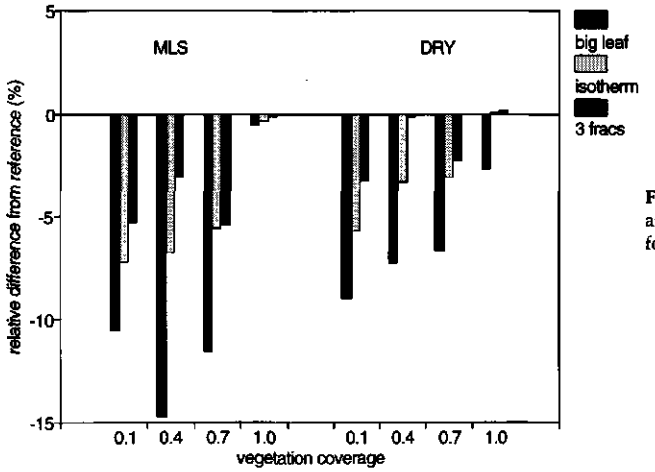

Figure 6.5: Boundary layer height at 18:00 GMT, 1st simulation day, for the cases explained in Figure 6.2

■ **Boundary layer parameters**

The effect of the surface representation on the boundary layer height at 18:00 GMT, shown in Figure 6.5, follows roughly the pattern exhibited by the sensible heat flux response (Figure 6.3). The PBL-height simulated by the reference model reaches approximately 1630 ± 60 m for MLS and 1520 ± 130 m for DRY. The close match between z_i^{18} and H^D is a direct result of the small entrainment of heat (see below). The results of z_i^{18} at the next day show a similar response (figures not shown), although the simulated PBL-heights are some 600 m or so higher. A rapid PBL-growth is simulated in a near-neutral residual layer for the second simulation day.

The entrainment of heat is fairly low in all cases. Both initializations result in a daytime average heat entrainment of -5 W/m^2 on the average. Due to the low absolute values of H_t^D, relative differences are rather meaningless and not shown. Moisture is in all cases transported out of the PBL rather than entrained into it, and the rate of this so-called detrainment is strongly related to σ_f. The different surface representations don't give rise to large moisture detrainment differences for the MLS initialization, but a significantly higher detrainment is simulated by the case 'big leaf' for an initial DRY-profile (Figure 6.6). The strong surface evaporation results in a large moisture gradient across the top of the PBL (see Figure 6.7), and this enhances the moisture flux. Owing to the steep humidity gradient above the PBL (Figure 6.1), the compensating effect of a slightly lower PBL height is small. This is not the case for the large humidity gradient in the MLS initialization. In spite of a significant increase of PBL humidity (Figure 6.8), the entrainment is low. Here the small reduction of z_i resulted in a stronger reduction of the humidity gradient across the PBL-top, as illustrated in Figure 6.7.

Apart from the cases where the surface evaporation is low ($\sigma_f = 0.1$), the response of q^{18} (Figure 6.8) resembles the pattern of λE^D (Figure 6.2). The largest differences occur for the case 'big leaf', where an increase of up to 1.2 g/kg is simulated.

Finally, the impact of the surface representation on the mixed layer temperature at 18 GMT is very well explained from the differences in surface sensible heat flux, shown before. The small entrainment of heat causes a fairly strict response of θ_v^{18} to H^D (figure not shown).

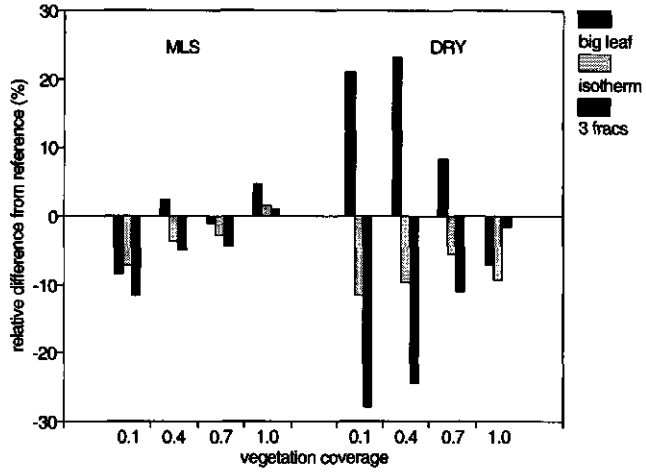

Figure 6.6: Differences in total daytime moisture entrainment, λE_t^D, for the cases as shown in Figure 6.2

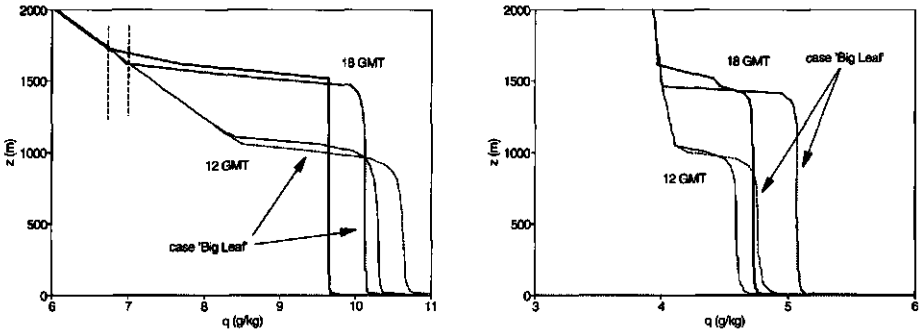

Figure 6.7: Profiles of specific humidity simulated for $\sigma_f = 0.1$ by the reference case (solid lines) and the case 'big leaf' (dashed lines) for times 12:00 GMT (normal) and 18:00 GMT (thick); Left: MLS initialization; Right: DRY initialization. The dashed vertical lines in the left panel indicate the change of the humidity gradient across the PBL-top due to the change of z_i, at 18:00 GMT. A similar change is not shown for the DRY simulation, since it very small

6.3.2 The soil heat and water vapour flux group

In the soil heat and water vapour flux group four model variations are compared for two soil types: sandy loam and sandy clay. The model variations include the cases 'reference', 'soil VB95', 'soil r_s^{s}' and 'soil CM88'.

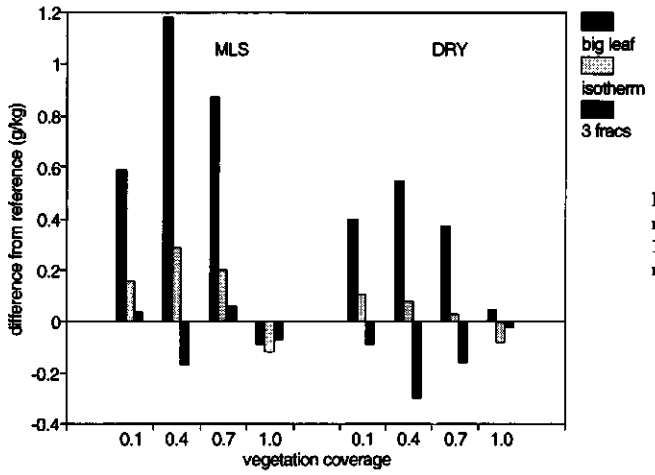

Figure 6.8: Absolute differences in mixed layer specific humidity at 18:00 GMT, q^{18}, for the surface and model variations as in Figure 6.2

■ Surface parameters

The partition of net radiation over sensible, latent and soil heat is simulated rather differently by the various model variations. Large differences are present for the simulation of daytime soil heat flux (Figure 6.9). For both initializations the values of G^D predicted by the case 'soil VB95' are approximately 40% lower than the reference case for sandy loam soil, and 20% lower for sandy clay soil. Both the reference model and the case 'soil VB95' derive G as a residual of the surface energy balance. They also adopted a similar lowest boundary condition (no soil heat flux below the simulation volume), and equal physical expressions for λ_T. In spite of this, the bare soil temperature is generally higher for 'soil VB95' than in the reference case. This causes the sensible heat flux to be higher than for the reference model, which has a negative feedback on the soil heat flux.

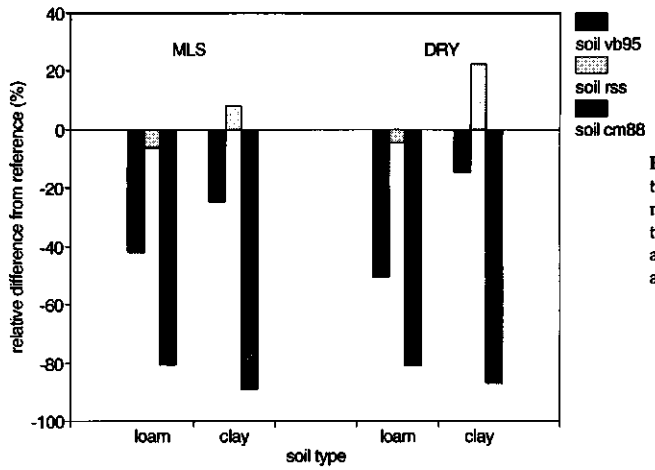

Figure 6.9: Differences in predicted total daytime soil heat flux, G^D, relative to the reference model, for the model cases 'soil VB95', 'soil $r_g^{S'}$ and 'soil CM88', for sandy loam and sandy clay soil types

A major difference between the cases 'soil VB95' and 'reference' is also depicted in Figure 6.10, where the total daytime surface evaporation is shown. For the sandy loam soil type the two cases result in nearly identical amounts of evaporation, but for sandy clay the reference model simulates 20% - 60% more evaporation than 'soil VB95'. One of the reasons for this difference is the layer coefficient l_c (eq. 4.19), equal to 1.0 for the reference model and 1.6 for the case 'soil VB95'. The coefficient efficiently reduces the surface relative humidity to below the minimum level q_0, for which soil evaporation is allowed. In the reference case this reduction is not included, and a significant part of the total evaporation originates from the bare soil component.

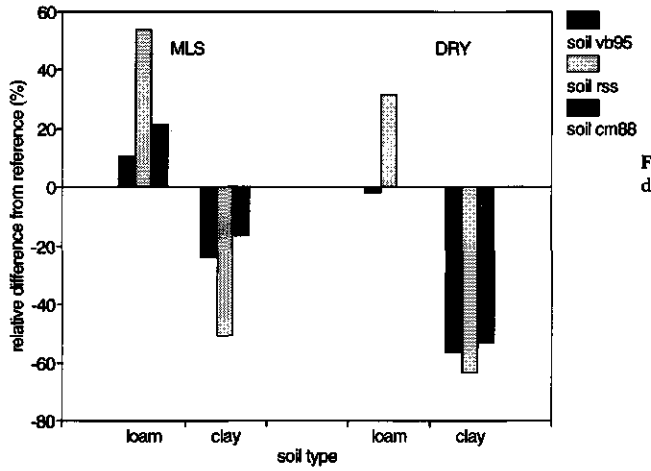

Figure 6.10: As Figure 6.9, for the daytime evaporation λE^D

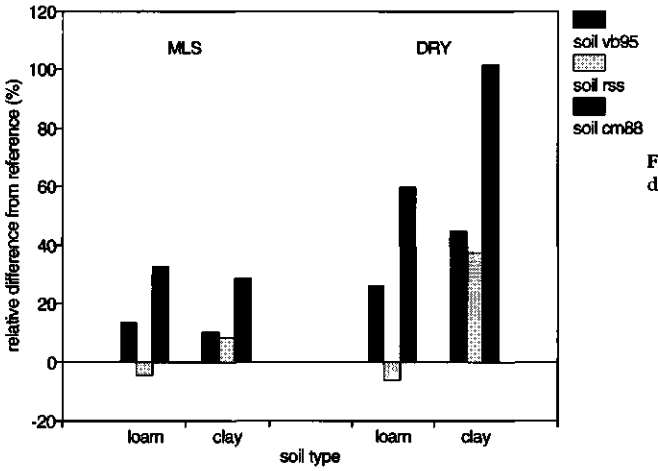

Figure 6.11: As Figure 6.9, for the daytime sensible heat flux H^D

Also the cases 'soil $r_s^{s'}$' and 'soil CM88' simulate a lower surface evaporation for sandy clay, the largest deviation of ± 60% present for 'soil $r_s^{s'}$'. For sandy loam, 'soil $r_s^{s'}$' predicts an evaporation rate which is ± 60% higher than the reference model. The difference

is entirely caused by an enhanced soil evaporation of 'soil $r_s^{s\prime}$'. In this model, two factors regulate the soil evaporation: the soil resistance r_s^s, and the relative humidity in the soil pores close to the surface, given by eq. 4.83. This relative humidity is evaluated from the soil moisture content in the top soil layer, which has a depth of 10 cm in the current simulations. However, the soil moisture content shows a significant gradient close to the ground, and is considerably lower in the top 1 cm than averaged over 10 cm. Van de Griend and Owe (1994) report ω values of typically 0.02 m^3/m^3 of the top 1 cm of the soil, measured at the EFEDA-I test site. This is small compared to the initial value of 0.07 m^3/m^3, as adopted for the simulations (Table 6.7). Furthermore, Kondo *et al.* (1992) point out that eq. 4.83 is invalid close to the surface. An equilibrium situation, as assumed by Philips (1957) equation, is violated near the surface due to evaporation. This also leads to an overestimation of the surface relative humidity by case 'soil $r_s^{s\prime}$'.

The soil heat flux is nearly similar for both the reference model and the case 'soil $r_s^{s\prime}$' (Figure 6.9). The resistance formulation merely affects the surface evaporation, which is only a minor part of the surface energy balance here. Similar arguments can be put forward for the total daytime sensible heat flux (Figure 6.11).

The extremely low value of G^D as simulated by the case 'soil CM88' was noticed before already (section 5.2.1). The effects of this low soil heat flux on the sensible heat flux (Figure 6.11) is evidently large. Up to 100% more sensible heat (DRY-initialization, sandy clay) is released into the atmosphere compared to the reference model.

- **Boundary layer parameters**

The high sensible heat fluxes simulated by the case 'soil CM88' have a major effect on the PBL-height. Also the mixed layer temperature is significantly enhanced (Figure 6.12). For the cases 'soil VB95' and 'soil $r_s^{s\prime}$' the increase of θ_v^{18} is limited to ± 0.8 K, but 'soil CM88' results in an increase of 1.5 - 2.5 K in all cases. As before, the coupling between differences in θ_v^{18} and z_i^{18} to differences in H^D is strong, due to the low amounts of entrained heat.

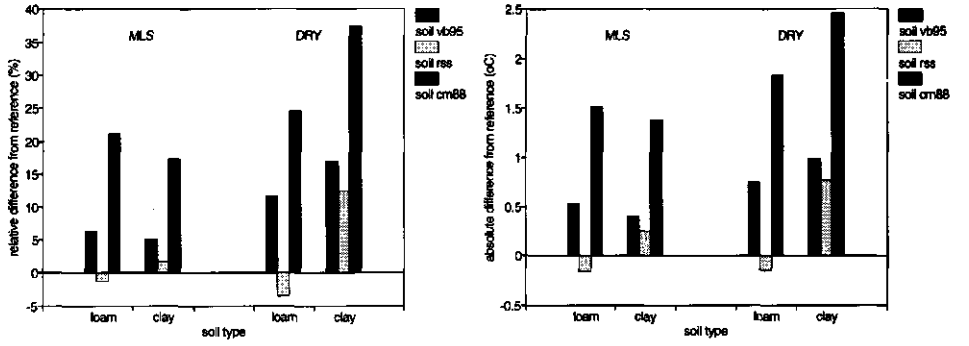

Figure 6.12: (left:) Relative differences in predictions of PBL-height; (right:) Absolute differences in predictions of mixed layer temperature at 18:00 GMT for the soil types and model cases as in Figure 6.9

The effects of the strong evaporation rate for sandy loam in the case 'soil $r_s^{s\prime}$', and the weak evaporation in all cases for sandy clay, are shown in Figure 6.13, where the mixed layer specific humidity is plotted. The dry simulations for sandy clay are shown evidently in

this figure. More striking is the strong reduction of q^{18} for the case 'soil CM88' for both soil types, where for sandy loam a slight increase of surface evaporation was predicted (Figure 6.10). The large boundary layer height, combined with an increase of the moisture detrainment by 40 - 50% (Figure 6.13, MLS), together are responsible for this feature.

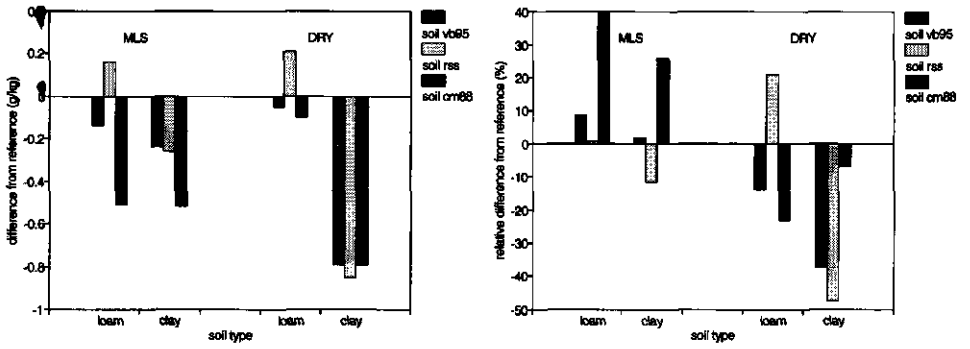

Figure 6.13: (left:) Mixed layer specific humidity, q^{18}; (right:) Daytime moisture entrainment, λE_l^D

6.3.3 The aerodynamic exchange group

The aerodynamic exchange group contains simulations over the reference vineyard surface, a tigerbush and a forest. Simulations are carried out with the reference model and by means of the variations 'aero D78' and 'aero MH95'.

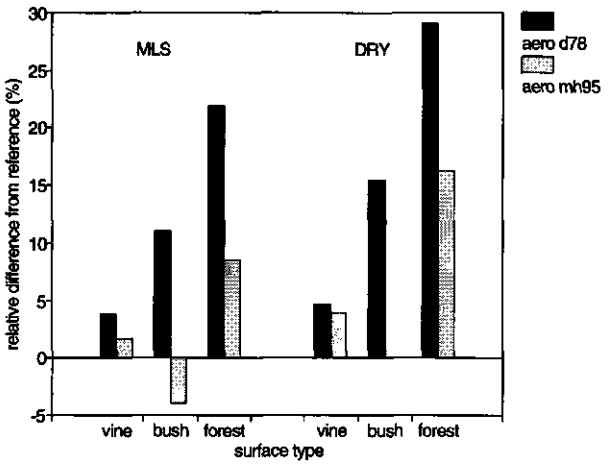

Figure 6.14: Different predictions of daytime sensible heat flux, H^D, compared to the reference model for the cases 'aero D78' and 'aero MH95', for various surface types

- **Surface parameters**

The different parameterizations of the aerodynamic resistances particularly affect the simulated total daytime sensible heat flux (Figure 6.14). The differences from the reference model are different for both model variations, and generally increase as the canopy becomes rougher and taller. For the case 'aero D78' a gradual increase of ξ_{H^D} is a result of the effect of particularly d on the aerodynamic resistance within the canopy in the reference model,

expressed by eq. 4.71. The zero-plane displacement has only a limited effect on the value of r_a^s in the case 'aero D78' (by way of the quantification of u_*), and this resistance is much smaller than in the reference model (typically 75% for the forest vegetation type). Also the case 'aero MH95' simulates smaller aerodynamic resistances, but these are parameterized independent on the surface roughness parameters. The difference between this case and the reference model are therefore again dominated by the effect of z_{0m} and d on r_a^s in the reference model. Unlike the gradual increase of ξ_{H^D} from vineyard to forest using 'aero D78', the case 'aero MH95' shows a minimum value of ξ_{H^D} for the intermediately rough tigerbush surface.

The differences in H^D are fully compensated by opposite differences in the daytime soil heat flux (figures not shown): in all cases net radiation and evaporation were simulated nearly similarly.

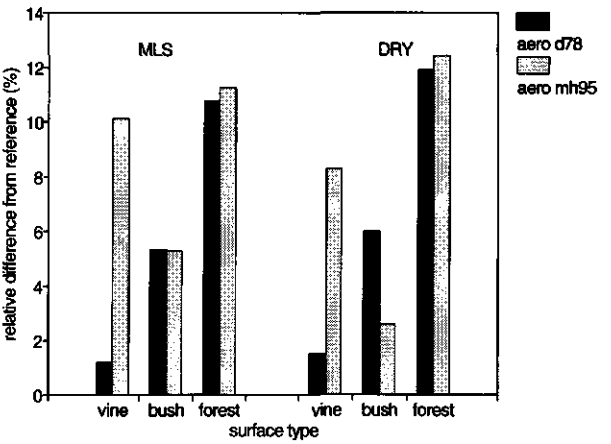

Figure 6.15: Boundary layer height at 18:00 GMT for the same simulations as shown in Figure 6.14

■ **Boundary layer parameters**

The different predictions of daytime sensible heat flux lead to a remarkable difference in boundary layer height at 18:00 GMT (Figure 6.15). The behaviour of z_i^{18} is very similar to the change in surface heat flux for the case 'aero D78'. However, for the case 'aero MH95' z_i^{18} shows a much stronger response to variations in H^D. A similar picture is presented in Figure 6.16, where the PBL temperature at 18:00 GMT is shown. The reason for the discrepancy between H^D and z_i^{18} is the increased entrainment of heat, simulated by the case 'aero MH95'. In the reference model the heat entrainment flux is typically -5 W/m^2, but for the case 'aero MH95' it is up to five times as large, approximately -25 W/m^2. This is caused by a complex interaction of parameterizations in the coupled models. The low aerodynamic resistances in 'aero MH95', and the absence of stability corrections in the range below $2h$, are associated with relatively large friction velocities near the surface (figures not shown). An increase of u_* results in an increase of the variance of the vertical velocity, $\overline{w'^2}$. This reduces the countergradient correction $\gamma_{h'}$ which increases the modified temperature gradient used to calculate the vertical heat flux in eq. 4.85. Since during daytime u_* is not a

scaling parameter in the PBL eddy diffusivity, the vertical heat flux is increased at heights where γ_h plays a significant role, that is, near the top of the PBL. As a result, the boundary layer grows faster, particularly at early times after sunrise, and its temperature becomes higher.

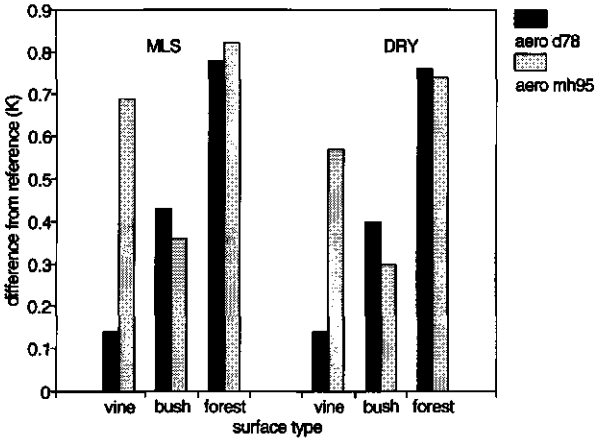

Figure 6.16: As Figure 6.14, for θ_v [18]

6.3.4 The canopy resistance group

In the canopy resistance group five different parameterizations are intercompared for a 'standard' vineyard surface: the reference model (calibrated version of CM88), and the cases 'r_c CO_2', 'r_c VB95', 'r_c fix' and 'r_c big CO_2'.

- **Surface parameters**

The parameter that is primarily affected by the parameterization of the canopy resistance is the total daytime evaporation, shown in Figure 6.17. The case 'r_c CO_2' yields a total evaporation which is 80% higher than is computed by the reference model for the relatively cool and moist MLS initialization. For DRY the difference is 40%. This behaviour in fact shows the response of r_s^c, as computed by the photosynthesis model, to ambient humidity deficit: the MLS initialization puts a smaller constraint on the crop conductance than a warmer and dry initial profile (DRY). The parameterizations embedded in the cases 'r_c VB95' and 'r_c fix' give values of λE^D which are approximately 50% and 10% lower than the reference, respectively. The close correspondence between case 'r_c fix' and the reference model is mainly due to the choice of the fixed value of r_s^c, being equal to the daily average of the parameterization in the reference model. For the case 'r_c VB95' a strong soil moisture response is included in the parameterization of r_s^c, which results in relatively high values owing to the low soil moisture content in the simulations.

The large reduction of the predicted daytime evaporation by case 'r_c big CO_2' is somewhat surprising, given the increases of λE^D by both cases 'big leaf' (Figure 6.2) and 'r_c CO_2'. The reason for the strong reduction of λE^D is the pronounced response to the ambient humidity deficit, present in the photosynthesis model for r_s^c. The high leaf temperature — which is a consequence of the isothermal source description in a big leaf model — enforces

a high ambient humidity deficit. This imposes a strong limitation to the canopy conductance, thereby reducing the evaporation rate. The case 'r_c big CO_2' produces relatively high evaporation rates just after sunrise and just before sunset, but the evaporation rate during midday reduces to low values (figures not shown).

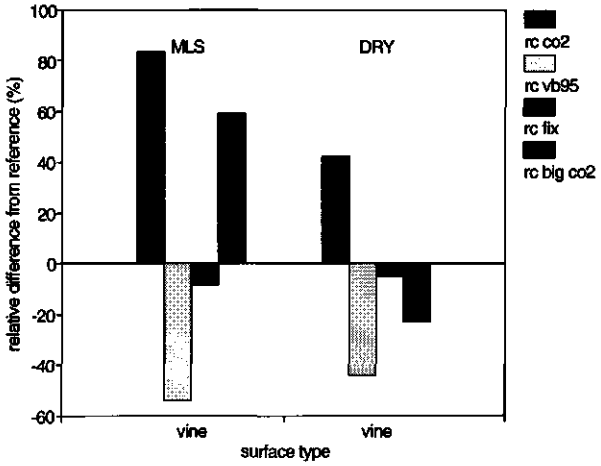

Figure 6.17: Differences in predicted total daytime evaporation, λE^D, compared to the reference model, for the case 'r_c CO_2', 'r_c VB95', 'r_c fix' and 'r_c big CO_2', for the reference vineyard surface

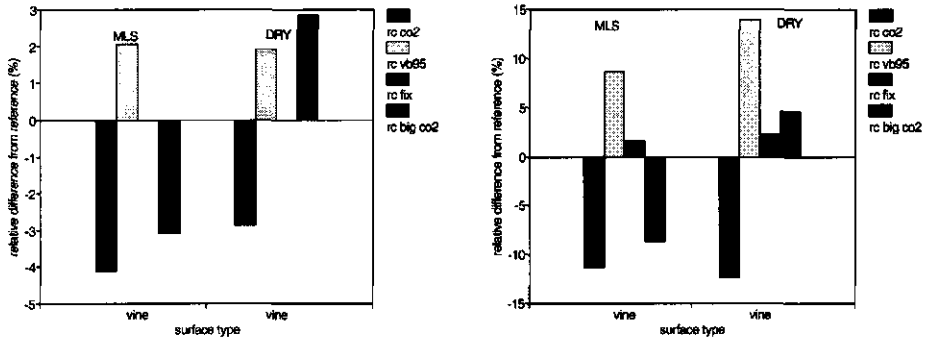

Figure 6.18: (Left:) Daytime soil heat flux, G^D; (Right:) Daytime sensible heat flux, H^D, for cases as in Figure 6.17

The impact of the cases in the canopy resistance group on the other energy budget terms is smaller: the soil heat flux changes by less than 5% in all cases. Changes in the sensible heat flux are limited to 15% (for the case 'r_c CO_2' with the DRY initialization), and tend to compensate most of the effects of r_s^c on λE^D (Figure 6.18).

■ **Boundary layer parameters**

The effect of the choice for the computation algorithm for r_s^c on the PBL height at 18:00 GMT follows closely the response of the daytime sensible heat. It is inversely proportional to the computed latent heat totals. The effect of these two processes on the

average specific humidity in the mixed layer is shown in Figure 6.19. As expected, a slight increase is present for the 'r_c CO_2' cases.

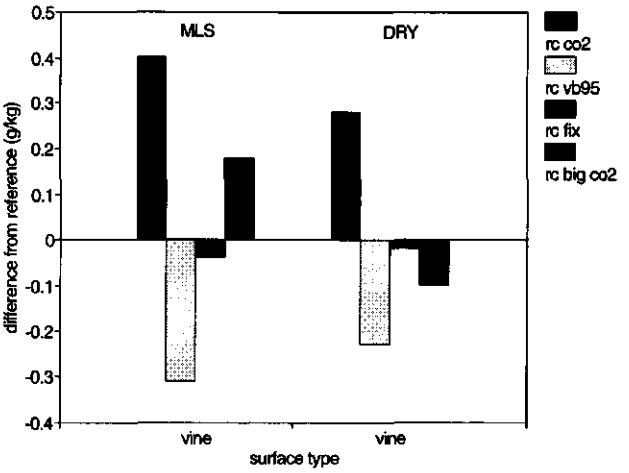

Figure 6.19: As Figure 6.17, for the differences in PBL specific humidity, q^{18}

A somewhat more unexpected picture is shown in Figure 6.20, where the differences of the predicted total moisture entrainment compared to the reference are plotted. A 40% increase of moisture detrainment is simulated by the case 'r_c CO_2', for DRY only. The background of this increase is related to the timing of the simulated surface evaporation. The case 'r_c CO_2' calculates the peak evaporation well before noon, which results in an early rise of the specific humidity of the PBL. A larger difference between q^{12} and the specific humidity of the free atmosphere above is present for this case than for the reference model. This gradient enhances the simulated transport of moisture out of the PBL. The absolute effect of this extra detrainment on q^{18} is relatively small.

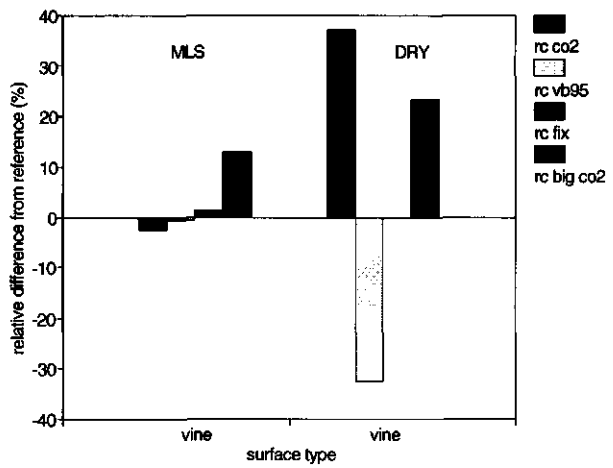

Figure 6.20: Differences in moisture daytime entrainment, λE_i^D, for the same simulations as in Figure 6.17

6.3.5 PBL-sensitivity and an analytical approach

The different surface parameterizations described above cover a considerable range of predicted sensible and latent heat totals. Assuming that the collection of these surface schemes represents the current state of the art of the parameterization of sparse canopy surfaces, this range of surface energy totals can be regarded to span a likely range of PBL predictions. A summary of the PBL-sensitivity can thus be obtained by plotting the most relevant PBL-parameters as function of the surface energy budgets as computed by the various surface models.

A similar sensitivity analysis was carried out by Driedonks (1981, 1982b), using the simple slab model of Tennekes (1973) (section 4.2.2). For the sensitivity of z_i and θ_m to the integrated surface heat flux I, analytical expressions were developed. For the sensitivity of q_m to the integrated surface evaporation J, no analytical expressions were derived, and the value of q_m at 18:00 GMT was computed numerically with the slab model. Here we compare the values of z_i^{18}, θ_m^{18} and q_m^{18} as function of I and J calculated with this simple slab model, to the results of similar sensitivities as computed by the series of coupled SVAT-PBL models described above. For comparison with the analytical model for the dynamics of the PBL-temperature, the mixed layer temperature θ^{18} rather than the virtual temperature θ_v^{18} is obtained from the numerical simulations. The values of θ_{00}, q_{00}, γ_θ and γ_q were obtained for each of the initial profiles (Figure 6.1), and are listed in Table 6.8. In all cases δ_0^q and δ_0^θ were taken zero, as the simulations started at the time where $\Delta\theta$, Δq and z_{i0} were small.

Table 6.8: Values of θ_{00}, q_{00}, γ_θ and γ_q for the initial profiles labeled MLS and DRY

quantity	MLS	DRY
θ_{00} (°C)	19.80	25.66
q_{00} (g/kg)	11.70	4.34
γ_θ (°C m^{-1})	$5.33\ 10^{-3}$	$4.08\ 10^{-3}$
γ_q (g/kg m^{-1})	$-2.85\ 10^{-3}$	$-2.10\ 10^{-4}$
height range for determination γ (m)	200 - 2000	200 - 2000

■ **PBL-height as function of surface heat flux**

Figure 6.21 shows the values of z_i^{18} plotted against the integrated daytime surface virtual heat flux I, calculated as $12 \times 3600 \times H^D/\rho c_p$, for all coupled SVAT-PBL simulations. Also shown is the analytical expression (eq. 4.92), with entrainment coefficient values of 0.2 and 0.0. The datapoint labels refer to the model runs specified in Table 6.2 on page 172.

For both initializations the results from the coupled models show a consistent increase of z_i^{18} with increasing I. At low values of I, z_i^{18} reaches relatively high values, compared to the predictions of the slab model. This is partly caused by an absence of the effect of the virtual component on the entrainment flux, which is not included in the simple slab model. Adopting an entrainment ratio of $R_h = 0.2$ results in a correspondence with the numerical simulations at low values of I. For higher values of I, the analytical model describes the coupled model runs slightly better for $R_h = 0.0$ than for $R_h = 0.2$. The simulated daily averaged entrainment coefficients were in most cases equal to approximately 0.1, which is consistent with the analytical expression. However, the entrainment ratios found

here are rather low, and this will be discussed in section 6.6.

A few outliers are present. For the MLS profile *g1*, *g6* and *g7* (model case 'aero MH95') show a higher PBL-height at 18 GMT than model combinations with comparable values of I. The reason for this - higher values of friction velocity combined with enhanced heat entrainment - was discussed above already, and causes a resemblance with the analytical solution using $R_h \approx 0.2$ (figure not shown). For the DRY-initialization only the datapoint labelled *g1* shows a similar behaviour.

For the MLS initialization, $\partial z_i^{18}/\partial I \approx 0.12$ K^{-1} (estimated from Figure 6.21), while for DRY this sensitivity is approximately equal to 0.15 K^{-1}.

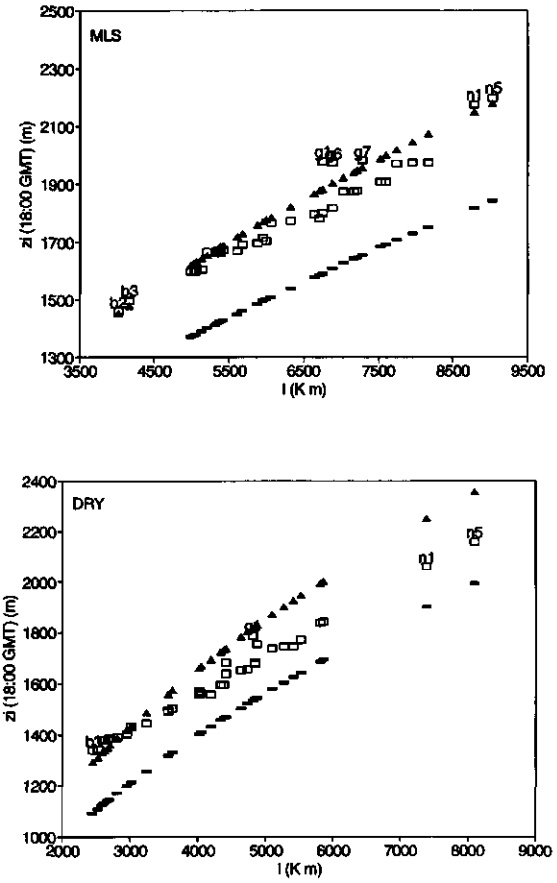

Figure 6.21: PBL-height at 18:00 GMT plotted against integrated surface heat flux I for the 2 initializations MLS and DRY: □ model cases; ▲ analytical solution with $R_h = 0.2$; – analytical solution with $R_h = 0.0$. Labels refer to model cases and surface types explained in Table 6.2 on page 172

■ **PBL-temperature as function of surface heat flux**

The relationship between θ^{18} and I, plotted in Figure 6.22, shows up as a nearly straight line. The analytical expressions are particularly insensitive to the value of R_h. The analytical solutions and the numerical model runs result in a nearly similar dependence of θ^{18} on I, although the numerical models tend to be slightly less sensitive to I. Overall, the sensitivity $\partial\theta^{18}/\partial I \approx 5.9\ 10^{-4}$ m^{-1} for MLS and $6.7\ 10^{-4}$ m^{-1} for DRY. Again, these sensitivities were derived by eye from Figure 6.22.

As for the sensitivity of z_i^{18} to I, the model runs $g1$ - $g7$ lie out of the range. The enhanced entrainment due to the large mechanical contribution causes heating of the PBL, which exceeds the heating rate expected from the surface contribution solely.

■ **PBL-humidity and surface water vapour flux**

The numerical prediction for q^{18} using the slab model as function of the integrated surface moisture flux, $J = 12 \times 3600 \times \lambda E^D / \lambda\rho$, is shown in Figure 6.23, together with the simulations from the coupled models. The scatter for both models is larger than for the former two relationships. In the slab model, the expression for q^{18} includes an independent variable dz_i/dt, which is a function of I. This independent variable is not present in the thermal relationships. Furthermore, the relative contribution of water vapour transport near the top of the PBL is significant and of the same order as the surface evaporation.

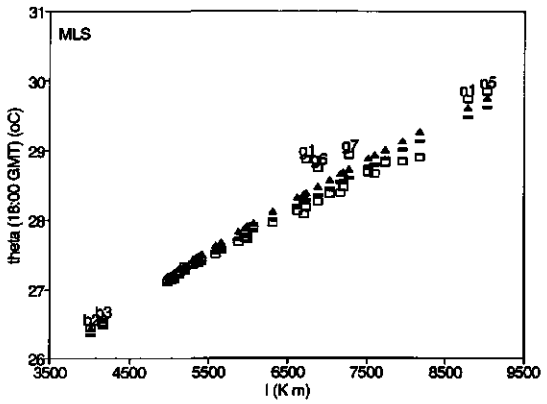

Figure 6.22: As Figure 6.21, for the relationship between θ^{18} and I

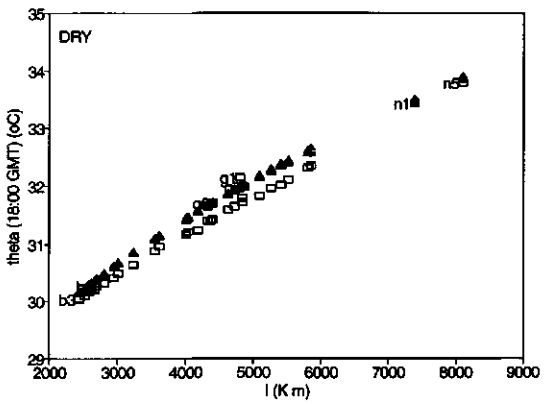

Clearly, q^{18} generally increases as J increases, and the two models result in a similar response. A linear regression for all datapoints yields a sensitivity $\partial q^{18}/\partial J$ equal to 8.12 10^{-4} m^{-1} for MLS, and 8.27 10^{-4} m^{-1} for DRY.

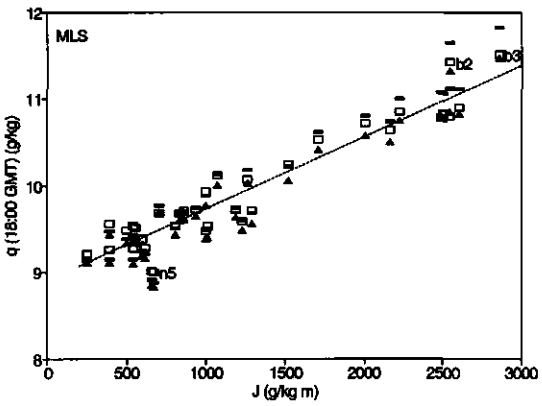

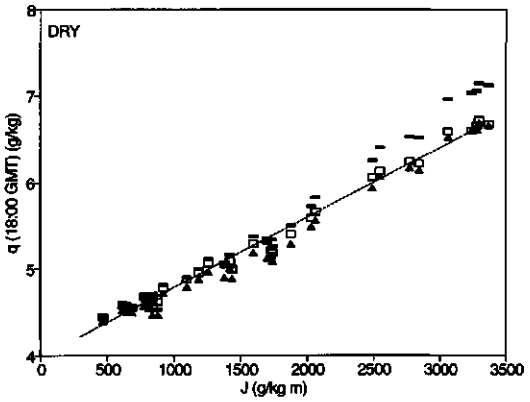

Figure 6.23: As Figure 6.21, for the relationship between q^{18} and J. The dashed lines show the linear regressions of q^{18} predicted by the combined models as function of J

6.4 Results of the sensitivity analysis for nighttime conditions

For nighttime conditions only a limited parameters is evaluated (see Table 6.2): the minimum temperature at reference height (θ_v^{min}), and the specific humidity at reference height (q^{min}) and the boundary-layer height (z_i^{min}) at the same time.

6.4.1 The surface representation group

For all simulations in the surface representation group, the minimum temperature at reference height occurs just before sunrise (after ± 24 hours of simulation). For all parameterizations in the surface representation group, θ_v^{min} is considerably higher than for the reference model (Figure 6.24). The reason for this difference is the parameterization of the temperature at z_{0m}, which affects the stability correction in the aerodynamic resistance between the surface and the reference level. Accounting for two separate surface sources, as adopted in the reference model, generally yields lower values for θ_0 during nighttime. The differences are particularly evident for a surface having an intermediate vegetation cover, and temperature differences of up to 3.5 °C may be the result, as shown in Figure 6.24.

A large difference is also present for the specific humidity at reference level, just

before sunrise (Figure 6.25). Here a pronounced influence of σ_f is present. The origin of the different values of q^{min} differs from the origin for the temperature variability. Here, the single layer models sustain a small evaporation during the night. This evaporated moisture quickly becomes trapped in the very shallow boundary layer.

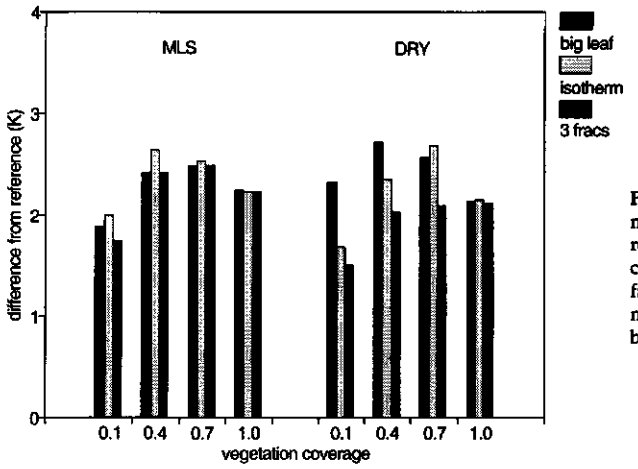

Figure 6.24: Differences of minimum nighttime temperature at reference level, θ_v^{min} for the model cases 'big leaf', 'isotherm' and '3 fracs' compared to the reference model, for values of σ_f ranging between 0.1 and 1.0

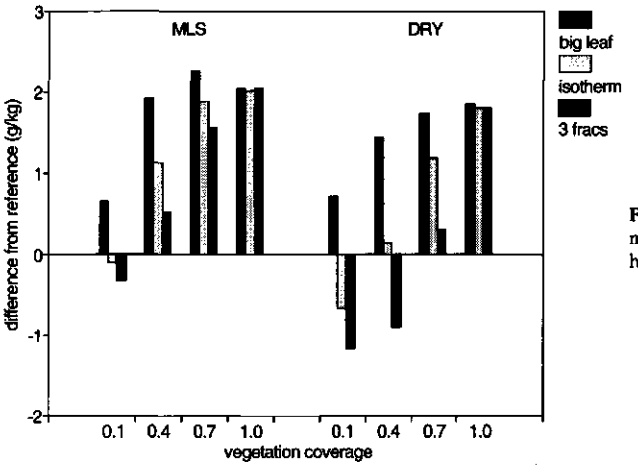

Figure 6.25: As Figure 6.24, for the minimum reference specific humidity, q^{min}

The differences in aerodynamic resistances, noticed above, also have an impact on the simulated friction velocity. This shows up in the simulations as a variation of the PBL-height just before sunrise (Figure 6.26). However, since the absolute values of z_i are rather low (± 50 m), and the number of simulation layers within the nighttime PBL is limited to 4 or 5, these relative figures are not very significant. The DRY simulations give rise to smaller differences than MLS.

6.4.2 The soil heat and water vapour flux group

In the case 'soil $r_s^{s'}$ the bare soil temperature reaches a lower value than in the

reference model for a clay soil. The result is a significantly lower air temperature just before sunrise (Figure 6.27). For 'soil VB95' this is the case for the sandy clay soil type. In this figure the results for case 'soil CM88' are omitted, since some meaningless values were simulated here due to a lack of numerical stability.

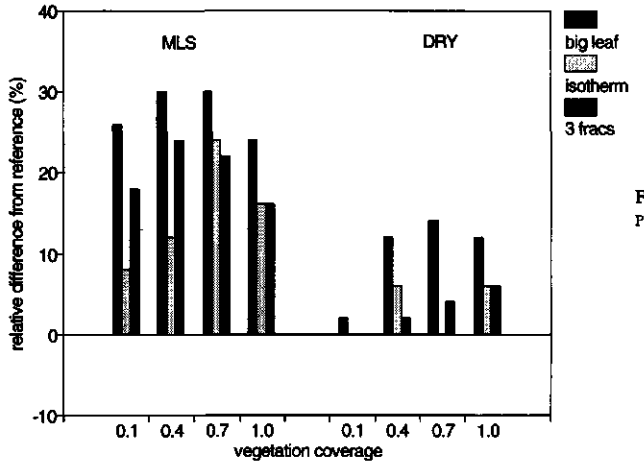

Figure 6.26: As Figure 6.24, for the PBL-height at 6:00 GMT, z_i^6

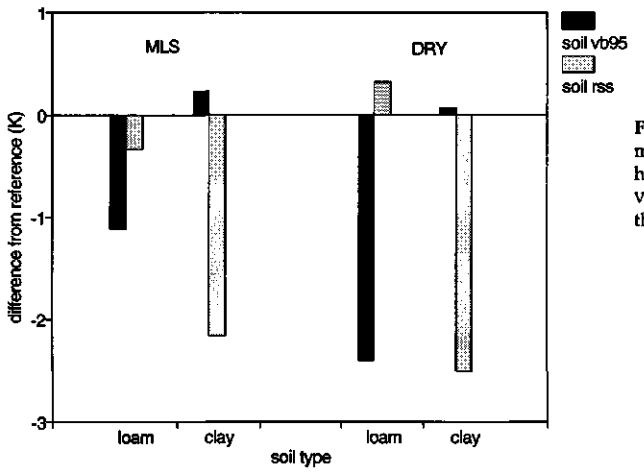

Figure 6.27: Difference of minimum temperature at reference height, θ_v^{min}, for model cases 'soil VB95' and 'soil $r_s^{s'}$', compared to the reference model

6.4.3 The aerodynamic exchange group

The observed temperature differences found above are less pronounced in the aerodynamic exchange group (Figure 6.28). A cool reference temperature, simulated by case 'aero MH95', is evident for the DRY-initialization. The absence of a stability correction on the aerodynamic resistances below $z = z_R$ plays a major role here. A significant reduction of the wind speed gradient between $z = z_R$ and $z = z_{0m}$ is simulated by the case 'aero MH95', since r_a^a is hardly increased by a stability correction.

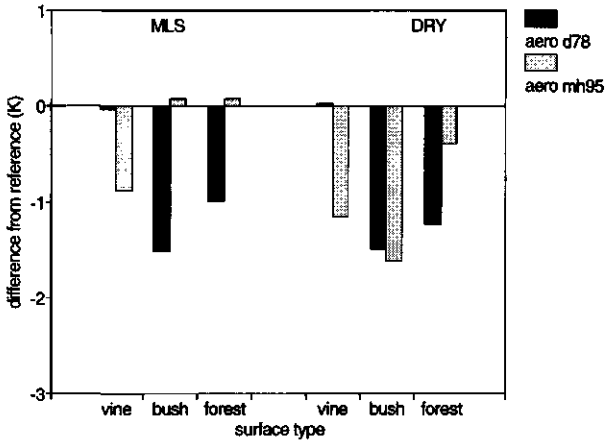

Figure 6.28: Differences of the minimum reference temperature, θ_v^{min} for the model cases 'aero D78' and 'aero MH95' compared to the reference model, for various surface types

6.4.4 The canopy resistance group

The issue of the increased reference humidity shown in the surface representation group is obviously also related to the parameterization of the canopy resistance: imposing a nighttime value of $r_s^c \rightarrow \infty$ will effectively remove all nighttime evaporation, and the difference between the various surface models is likely to vanish. A significant difference with the reference model is only present for the case 'r_c fix', which adopts a lower canopy resistance than any of the other cases (Figure 6.29).

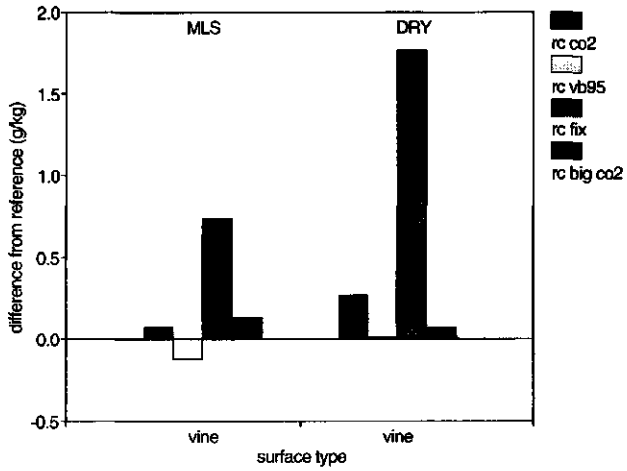

Figure 6.29: Differences in predicted early morning specific humidity, q^{min}, for the cases 'r_c CO_2', 'r_c VB95', r_c fix' and 'r_c big CO_2', compared to the reference model

6.5 Simulations using EFEDA-observations

The sensitivity analysis described above was carried out using rather idealized radiative and geostrophic forcings and initial PBL-profiles. However, the measurements carried out during the EFEDA-I experiment allow an evaluation of the performance of the

various coupled models to simulate observed atmospheric quantities. Therefore, an additional set of model runs was carried out which used the forcings and initializations obtained from field measurements. Data for initialization of the PBL-model, for the atmospheric forcings and for comparison of simulations are collected during EFEDA-I, in the Tomelloso vineyard area in June 1991 (section 2.2).

Rather than expressing model results in terms of deviations from a reference model, the simulations were compared to a PBL-run using actually measured surface fluxes as lower boundary condition. The surface fluxes were synthesized from a number of stations in the Tomelloso area. This dataset was prepared by colleagues from CNRM using the EFEDA-I database.

This section starts with the selection of a simulation period. As was discussed in section 4.3 a one-dimensional atmospheric model encounters severe limitations for the description of the state of an atmospheric column, when horizontal advection importantly determines the state of that column. Analysis of the data collected during the EFEDA campaign revealed a strong advection on many days. A very strong sea-wind effect caused a sharp rotation of the wind direction near Barrax, some 100 km from the Tomelloso location. Also the radiosonde profiles near Tomelloso showed that advection played an important role. Obviously, interpretation of PBL-simulations is particularly difficult when the data are affected by mechanisms not included in the model. A selection of data modified as little as possible by non-simulated advection effects is therefore useful.

Based upon this selection, the initial profiles and atmospheric forcings are presented. A control run is carried out (section 6.5.3), which consists of the PBL-model using the measured surface fluxes. In section 6.5.4 simulations are carried out in which the various surface model combinations provide the lower boundary conditions. Mutual differences are expressed relative to the control run, and discussed.

6.5.1 Selection of the simulation period

In order to get a first impression of the influence of advection, it was tested whether the measured atmospheric profiles obeyed conservation of heat. For this purpose the simple slab model for the PBL (Driedonks, 1981) was used for a selection of a simulation period. A sufficient correspondence between observed mixed layer temperature and θ_m-predictions from this simple model using observed values of $\overline{w'\theta'}_0$ indicates that the PBL-temperature profile is well adapted to the heat released from the local surface and entrained from the atmosphere above. Obviously, a model of this form only gives an indication of the importance of advection, since subsidence and radiative heating are not included, and the entrainment closure assumption in eq. 4.90 cannot be expected to be universal.

For all days where radiosonde measurements were available, the slab model was used to estimate the mixed layer temperature. The mixed layer temperature is rather insensitive to the specification of the heat entrainment ratio R_h, and therefore serves as a better indicator than z_i, whose prediction is strongly dependent on the choice for R_h (Driedonks, 1982b). Surface heat flux was taken from the CNRM database (see below), and z_i was estimated from the soundings as the level of the lowest temperature inversion and specific humidity jump (see section 2.2.7). Observed values of θ_m were simply obtained by averaging the temperature profile below $z = z_i$. From the entire set, observations taken at

day 174 showed the best correspondence with the model, and this day was selected to serve as test case.

Figure 6.30 shows a comparison between observed and parameterized mixed layer temperatures for this day. Note that the observed PBL-temperatures are still approximately 2 °C warmer than predicted, which was noticed also by Jacobs (1994). This must be kept in mind during the interpretation of simulations in the following.

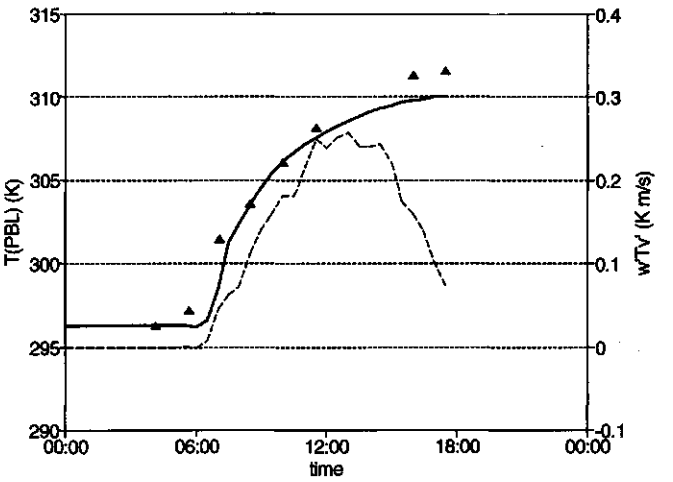

Figure 6.30: Observed (▲) and simulated (——) mixed layer temperature (left axis) for DOY 174, 1991. Simulations are carried out using the slab model with $R_h = 0.2$ and the measured surface heat flux (- - -, right axis)

6.5.2 Initialization and forcing

As before, a 36 hour simulation was carried out using Δt = 3 minutes. The initial PBL-profile was taken from the radiosonde measurements collected at day 174, 4:10 GMT (Figure 6.1). The vertical resolution was also taken similar as before.

The geostrophic wind U_g was taken from the radiosonde observations. The wind profile showed considerable vertical gradients over the entire depth of the simulation at all times, presumably due to thermal winds (baroclinicity). A definition of U_g as a simple average in a specified height range was considered to be rather unrepresentative for the general forcing. Rather, a visual inspection of all available wind profiles was carried out to estimate the geostrophic wind speed. In each wind profile a level between 1 and 4 km was selected where the wind speed could be regarded to represent the average wind speed in a layer above the PBL. The geostrophic wind was linearly interpolated between the times of the radiosonde measurements. The resulting geostrophic wind decreased gradually from 6 m/s on 23 June, 0:00 GMT to 2 m/s on 25 June, 0:00 GMT.

The observed surface fluxes for the control run with the PBL-model were compiled by CNRM. Area averaged surface fluxes were obtained by averaging measurements carried out by various scientific groups in the Tomelloso area, after a carefull quality inspection. A similar averaging procedure was followed to obtain area averaged temperature, absolute humidity and wind speed at 2 m above the surface. Due to the poor performance of most

sensors measuring evaporation, λE was obtained by closing the energy balance using the area averaged net radiation, soil heat flux and sensible heat flux density. Measurements of WAUMET were included in all quantities. Figure 6.31 shows the resulting energy balance components for days 174 and 175. The measured shortwave and longwave incoming radiation were used as energy forcings for the coupled models.

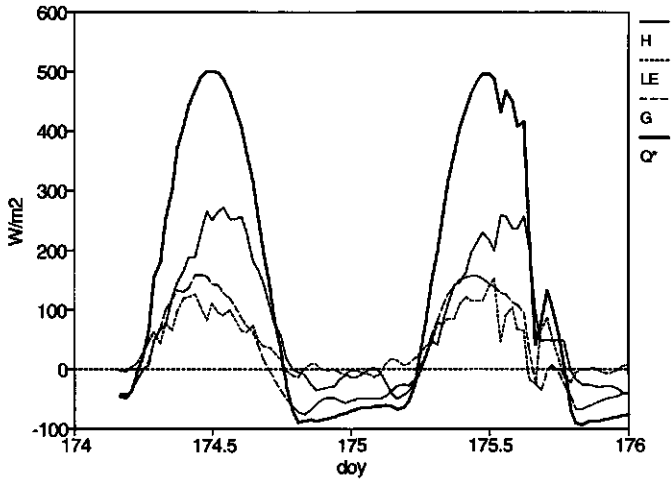

Figure 6.31: Mean energy balance components assembled from measurements at DOY 174 and 175 from various groups operating in the Tomelloso area

The surface momentum flux, $\overline{u'w'}_0$, was not taken from this assembled data base, since a rather poor numerical resolution (1 significant number) was used. Instead, the measurements taken by WAUMET using the sonic anemometer at 4.35 m height (Table 2.1) were used. The total momentum flux was divided over $\overline{u'w'}$ and $\overline{v'w'}$ assuming that the angle between geostrophic wind and surface stress was 40° at all times. The results of the one-dimensional simulations reported below are unsensitive to this rotation angle.

6.5.3 Control run

A control run of the PBL-model was carried out using the area-averaged surface fluxes as lower boundary conditions, over the period between day 174, 4:00 GMT and day 175, 16:00 GMT.

Figure 6.32 shows the measured and simulated boundary layer height, z_i. The measured values were obtained using the same formulation as in the model, to avoid methodological differences. The correspondence for the first day is very well. During the night no observations were available, but the results seem quite reasonable. The sudden increase and decrease around 4:30 GMT at day 175 is associated with a peak in the surface momentum stress (figure not shown), which has an unknown origin so far.

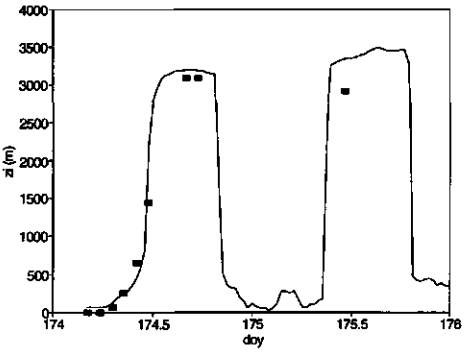

Figure 6.32: Simulated (——) and observed (■) PBL-height

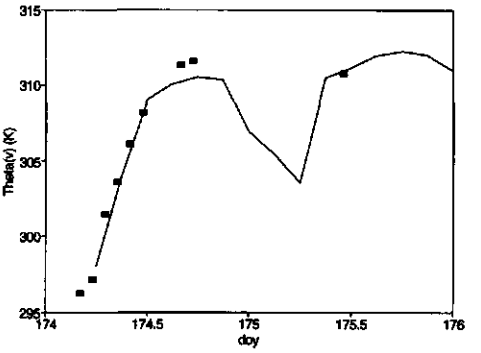

Figure 6.33: Simulated (——) and observed (■) mixed layer potential virtual temperature, θ_v^t

Also the mixed layer temperature (Figure 6.33) shows a good correspondence between data and simulations. θ_v^t closely corresponds to simulations with the slab model (Figure 6.30), since a similar surface forcing was used. The entrainment ratio for heat, R_h (Figure 6.34) shows a large diurnal variation. On the average the value is somewhat smaller than -0.2, as adopted in the slab model, during both days. The small value for the second day is well explained by the small temperature gradient in the entrainment layer, which is entirely a residual from the previous day, without modification by radiative cooling.

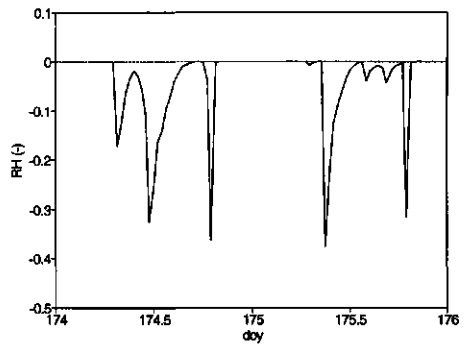

Figure 6.34: Simulated heat entrainment ratio, R_h

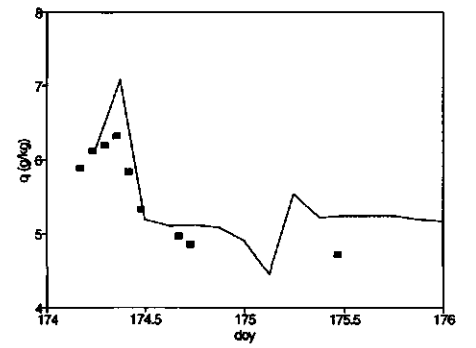

Figure 6.35: Simulated (——) and observed (■) mixed layer specific humidity, q^t

The mixed layer specific humidity (Figure 6.35) is slightly overestimated during the first day. Most likely, the difference between model and data has the same origin as the difference between modelled and simulated mixed layer temperature, where the data show a higher value than the model runs. Advection of dry warm air has influenced the radiosonde data.

The simulated wind profiles show a strong deviation from the observations (Figure 6.36). A clear geostrophic maximum is present at a height of about 2.5 km in the initial profile, and this air stream is rather well mixed into the PBL at the end of the first day. This

mixing, together with the geostrophic forcing, causes a marked overestimation of the wind speed in the entire PBL, already a few hours after the simulation starts. The poor vertical mixing occurring during nighttime caused a significant decrease of the wind speed near the surface, where friction reduces the wind speed.

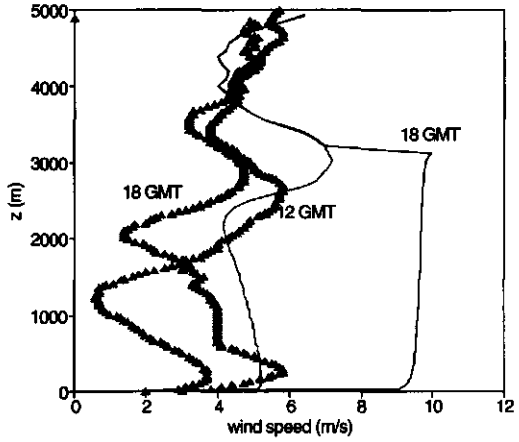

Figure 6.36: Observed (▲) and simulated (——) horizontal wind profiles for t = 12 GMT and t = 18 GMT

In general, the PBL-model is quite well capable to simulate the main characteristics of the observed boundary layer dynamics, apart from the horizontal wind speed profile. During daytime, the PBL warms up, by heating both from below and from above. A rapid growth takes place around noon, stopping at about 14:00 GMT. However, the large gap in the radiosonde measurement sequence around noon leaves the PBL-growth rate unresolved. Similar measurements carried out in the Belmonte area, some 100 km from Tomelloso, give rise to suspect the actual growth rate to be somewhat less rapid than suggested by the model simulation. Michels and Jochum (1995) report a PBL-depth of approximately 2000 m at 14:00 GMT, DOY 174. Moreover, aircraft measurements taken around 13:00 GMT above Tomelloso at a height of 2500 m show turbulence patterns which are typical for a residual layer, rather than for a fully developed convective layer. Large scale advection or subsidence may have reduced the PBL-growth speed. Both observations and simulations indicate the development of a nocturnal boundary layer from about 18:00 GMT onwards. The height of this nocturnal PBL changed only slightly as the night proceeded, and was affected mainly by the momentum flux. The predictions for the second day are more suggestive, since only one measured PBL-profile is available around noon. An overestimation of the PBL-depth is likely to be caused by the absence of radiative cooling in the residual layer.

6.5.4 Results of the sensitivity analysis

As before, a difference is made between the surface parameters (surface energy balance and soil moisture) and PBL-parameters (height, mixed layer state variables and entrainment fluxes).

■ **Surface parameters**

The various parameterizations of a sparse vineyard canopy on a sandy loam soil resulted in considerable differences of predicted surface energy balance partitioning. In the following figures the measured quantities serve as reference.

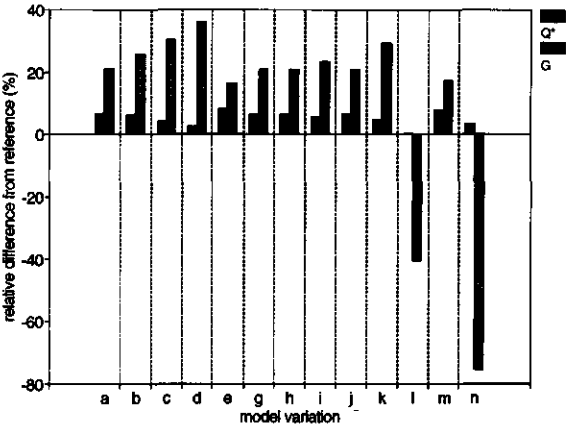

Figure 6.37: Relative differences in predicted daytime net radiation and soil heat flux, compared to the reference run using observed fluxes. Simulations are carried out for a standard vineyard surface using measured initialization and forcings. Model variation codes are as explained in Table 6.2 on page 172

The dominance of the common incoming radiative forcing on the total daytime net radiation, Q_*^D, causes the relative differences between the various model variations to be limited to 5% at most (Figure 6.37). Most models compute a slightly higher net radiation than measured. An exception is the model case *l* ('soil VB95'), which predicts a lower net radiation as a result of a higher surface temperature.

The daytime soil heat flux shows a much larger variability, in particular for the cases *l* = 'soil VB95' and *n* = 'soil CM88' (Figure 6.37). The large underestimation of the CM88 resistance parameterization (*n*) was already noticed. Compared to the measured soil heat fluxes the reference model (*a*) predicts G^D values which are ± 20% too high, while the case 'soil VB95' gives too low values. The latter feature is probably caused by an underestimation of the thermal conductivity, λ_T, near the surface. For the current soil moisture content, λ_T approached its minimum value of 0.171 W/mK. Verhoef *et al.* (1995, section 2.4.4) found values about twice this figure for DOY 174 using the amplitude method. The empirical weighting of λ_T over both soil layers in the reference force-restore model (eq. 4.48) apparently compensated this underestimation. The impact of increasing λ_T was not investigated.

The consequence of the soil heat flux parameterization for the daytime sensible heat flux is evident from Figure 6.38. A significant increase of H^D is simulated by the *n* = 'soil CM88' case, whereas all other parameterizations confine the differences to approximately 20%. Also the correspondence between measured H^D and simulated with the reference model (*a*) is good, albeit that the reference model overestimates H^D by 5%. Quite more pronounced are the differences in simulated daytime latent heat flux. As expected, the

isothermal big-leaf approach (b = 'big-leaf') results in a significantly larger evaporation than the reference. This overestimation is not present in the c = 'isotherm' case, where the canopy evaporation originates from a small part of the grid box only. A very low evaporation rate is calculated by the case i = 'r_c VB95', in which a dependence of r_s^c on soil moisture and radiation is adopted. The underestimation of λE^D is approximately 60%, apparently owing to an overestimation of the crop resistance. A comparison of modelled values of r_s^c with EFEDA-II porometry data showed this overestimation to be particularly present at high radiation levels, thus in cases where the restriction function for ω plays a significant role. However, a field calibration using soil moisture measurements in order to evaluate the r_s^c-expression of VB95 was not possible. The cumulative evaporation computed with the reference model is 20% lower than the observed fluxes. The quality of the measurements may be disputed, regarding the energy balance closure method used to obtain the data.

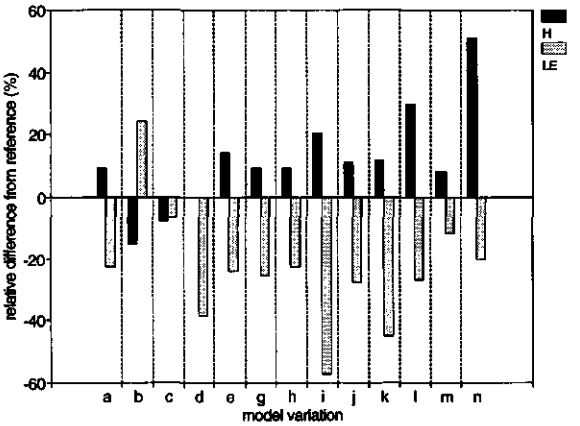

Figure 6.38: As Figure 6.37, for the daytime simulations of sensible and latent heat

The change of the soil moisture volume follows the evaporation pattern closely (Figure 6.39). By the end of the first simulation day a larger soil water depletion occurs when surface evaporation is higher. A similar behaviour is present for the second simulation day. The cases b = 'big-leaf' and m = 'soil r_s^{sl}' both show an enhanced soil moisture depletion compared to the reference, owing to a larger cumulative evaporation.

■ **Boundary layer parameters**

The different predictions in boundary layer height are shown in Figure 6.40. Here, values of z_i at two times on day 174 are shown. A striking feature is that the differences are particularly present for the mid-day (12 GMT) values of z_i. The final PBL-height by the end of the afternoon (18 GMT) is similar for all model variations. The surface parameterization has a significant effect on the time at which the PBL shows the fastest growth. The value of z_i at t = 12 GMT roughly marks two different groups of simulations: one group with an early PBL growth, which are the model variations with relatively high sensible heat flux values (Figure 6.38), and one group of model variations by which rapid PBL-growth is postponed by a few hours. The case n = 'soil CM88' shows a relatively early start of PBL-growth, governed by the

very high sensible heat flux simulated by this model variation. Both groups eventually reach approximately the same PBL-height, which is presumably strongly determined by the sharp inversion at $z \approx 3$ km (Figure 6.1).

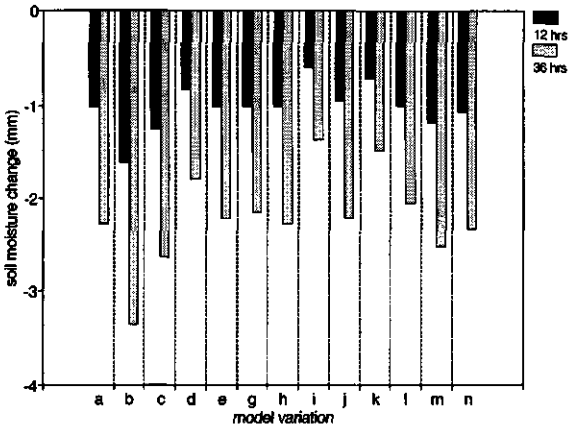

Figure 6.39: Change of the total soil moisture content after 12 and 36 hours of simulation, for the model variations indicated in Figure 6.37. In this figure the simulated soil moisture depletion is plotted rather than a relative depletion compared to the reference run.

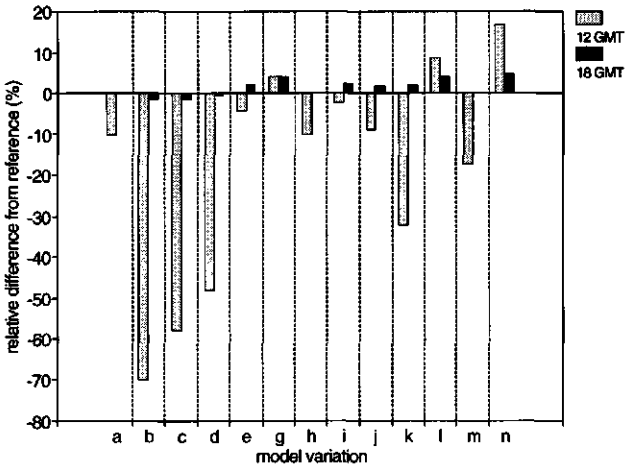

Figure 6.40: Differences in predicted PBL-height at 12:00 and 18:00 GMT for the model variations shown in Figure 6.37, compared to the reference model

The predicted values of the PBL-height during the next day hardly show the timing differences demonstrated above. The near-neutral residual temperature profile allows a very rapid PBL-growth well before noon. The final value of z_i reaches approximately 3400 m in most cases. Again, the final value of z_i is only partially determined by the exact value of the sensible heat flux, that shows similar differences as on day 174 (figures not shown).

The mixed layer potential virtual temperature is more closely related to the predicted sensible heat flux from the surface (Figure 6.41). The model variations causing a rapid PBL-

growth result in a higher mixed layer temperature by the end of the day. The boundary layer temperature simulated by case n = 'soil CM88', in which 50% more sensible heat is transported towards the PBL during daytime, ends up being 1.1 K warmer than the situation using observed surface fluxes. The value of z_i in this same case is only 4% higher. Also the case g = 'aero MH95', results in a PBL which is approximately 0.5 K warmer, but here the total daytime surface sensible heat was only 9% higher than for the reference case. The additional source of heat is provided by an enhanced entrainment of heat (Figure 6.42). The small value of the average heat entrainment in the reference case (-16 W/m^2 between 6 and 18 GMT) makes the relative difference for the sensible heat entrainment of case g = 'aero MH95' (± -40 W/m^2) rather large.

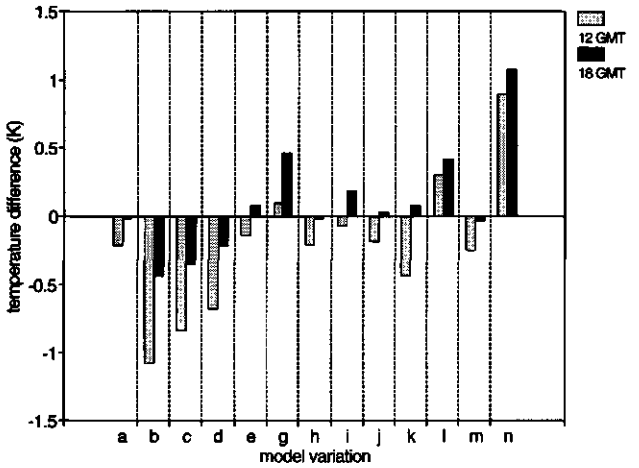

Figure 6.41: As Figure 6.40, for the mixed layer temperature

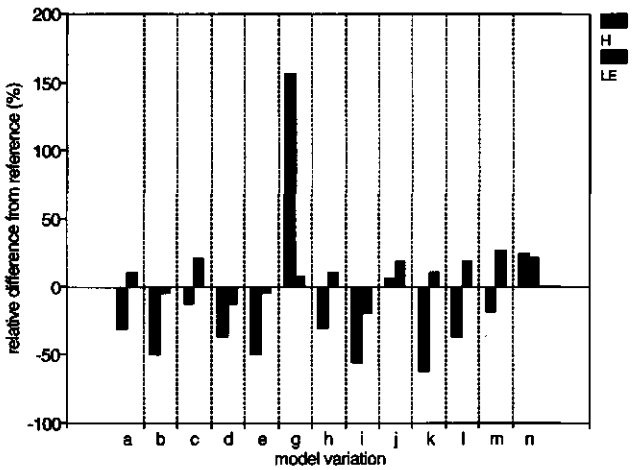

Figure 6.42: Relative differences in predicted daytime entrainment fluxes for heat and moisture, compared to the reference model

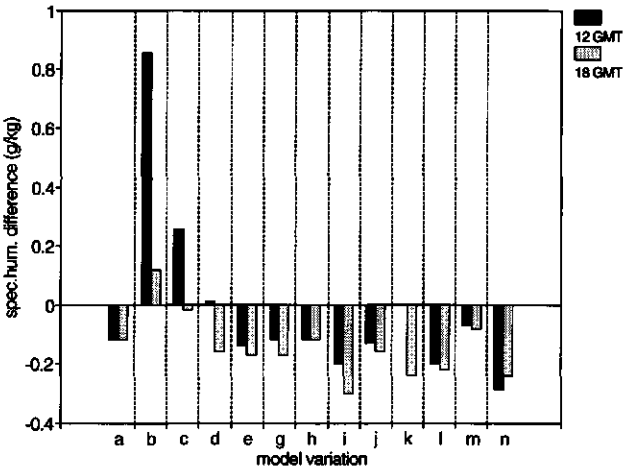

Figure 6.43: As Figure 6.40, for the mixed layer specific humidity

The specific humidity of the mixed layer around sunset (q^{18}) shows a relatively small variation (Figure 6.43). Obviously, the big-leaf case (*b*) results in a pronounced increase of q^{18} compared to the reference case, while the case *n* = 'soil CM88' results in a significant reduction (> 0.2 g/kg), in spite of the only moderate reduction of λE^D and increase of the entrainment water vapour flux.

6.6 Discussion and conclusions

We recall that the investigation of the sensitivity of the PBL to the surface parameterization is carried out by comparing the results of various surface models, coupled to a PBL-model. The experiments focused on the implication of the choices for physical parameterizations of separate model components. This was carried out by construction of a reference model, and replacing its components by alternative parameterizations. The PBL-sensitivity was expressed in terms of a change of simulated quantities compared to the reference model. This strategy leads to an investigation of the sensitivity of the PBL to the selection of surface models, rather than to the selection of surface types or parameter values. A second aim of the study was to describe Mediterranean sparse canopy conditions. To include a certain generality, some variations were employed in the initial temperature- and air humidity profiles, in the vegetation (cover and type), and in soil type.

Despite these restrictions, a large number of degrees of freedom remained. Many physical processes interact, and the results will often not be transferrable to other conditions. Also, the range of available land surface models is much larger than covered by this investigation. Different conclusions could possibly be drawn when alternative parameterizations would have been included.

First we will summarize the main features of the results shown in this chapter. In a separate section the practical implications for application of SVAT's in meteorological models well be discussed. A final section contains considerations with respect to future research.

6.6.1 Differences of model parts

We have compared various model components divided into four categories: surface representation, aerodynamic exchange, soil heat and moisture transfer, and canopy resistance.

In the *surface representation group* it is found that the 'big leaf' case gives a much higher evaporation than any of the other schemes included. The total daytime evaporation was also considerably higher than the observed latent heat flux. A significant overestimation of λE^D by 'big leaf' is to be expected in cases of partial vegetation cover. Adopting a single surface source results in a surface temperature weighted to relatively high values of the warm bare soil component. This high surface temperature leads to an overestimation of the surface specific humidity of the evaporating surface.

Two solutions to this problem were included here. The first, proposed by Noilhan and Planton (1989), is to discern between a vegetated and a bare surface fraction, identified by σ_f. This was embedded in the case 'isotherm'. For a zero soil evaporation, the surface evaporation formulations in 'big leaf' and 'isotherm' are equal except for and artificial enhancement of the aerodynamic resistance r_a in 'isotherm' (eq. 6.8). When r_a is not insignificant compared to r_s^c, this leads to a reduction of λE^D. For the present simulations, the aerodynamic resistance included a relatively large excess resistance, and this caused the desired reduction of λE^D. A more fundamental solution is to solve the energy balance of each surface fraction separately, as was first proposed by Deardorff (1978). This leads to a much more realistic lower surface temperature for the vegetation component. This solution was adopted in the reference case and in the case '3 fracs'. As expected, the λE^D-differences between a big-leaf model, the surface fraction models and the two-component scheme vanish for $\sigma_f \rightarrow 1$.

Within the boundary layer the overestimation of λE^D leads to an enhanced detrainment of moisture. This detrainment is strongly linked to the shape of the specific humidity profile and to the PBL growth. In the DRY simulations, the 'big leaf' case reduces PBL growth, giving rise to higher humidity concentrations within the PBL and stronger humidity gradients at the top of it. This finally leads to an increase of the moisture detrainment by up to 25% compared to the reference model.

The various parameterizations in the *soil heat and water vapour flux group* give rise to considerable differences in simulated soil heat flux and evaporation. The largest effect is the underestimation of G by the case 'soil CM88'. The soil model in CM88 ignores heat storage in the upper soil layer, and predicts values of G^D which are up to 80% lower than the reference force-restore model. The associated energy surplus is used to heat the air in the atmosphere, and this has a clear impact on both PBL height and -temperature.

Compared to the reference model, the four-layer diffusion scheme employed in the case 'soil VB95' predicts a generally higher soil temperature during daytime, which results in a larger sensible heat and lower soil heat flux. The difference in predicted G^D compared to the reference model is 30 - 40%. In the zero-dimensional intercomparison between the models of D78 and VB95 carried out in chapter 5, the different surface temperature predictions was explained from a difference in aerodynamic resistance above the surface. The intercomparison reported in this chapter was executed with similar aerodynamic

resistances for both models, and the same difference (albeit somewhat smaller) appears. We must conclude that the different solutions for the surface temperature are mainly caused by the difference in soil heat flux parameterization.

The force-restore method, embedded in the reference model, gives an exact solution of the thermal diffusion equation for a homogeneous soil with a single harmonic surface forcing (Dickinson, 1988). In the reference model a difference in thermal properties of the top and the lower soil layer is accounted for by an empirical weighing as depicted in eq. 4.48, but a gradient of these parameters is not included. The four-layer diffusion scheme allows for both inhomogeneous soil and multiple wave lengths in the surface forcing. The initial soil moisture profile imposed in the current analysis leads to a pronounced thermal conductivity gradient in case of sandy loam soil. This feature may explain the different G^D-predictions by the cases 'soil VB95' and the reference model. Indeed, the difference between these two cases is much smaller in case of sandy clay. In that case, the adopted initial soil moisture profile leads to a similar value of the thermal conductivity for both models (equal to the minimum value of 0.171 W/mK) throughout the entire soil volume. A comparison of model simulations with EFEDA data suggest a clear underestimation of 'soil VB95', which is probably related to a too low value of the soil thermal conductivity.

Also, with respect to evaporation the models in this group show a considerable variability. This variability is mainly caused by the differences in predicted soil evaporation. The differences between the included models are not consistent, but depend strongly on the soil type. For sandy loam, the case 'soil $r_s^{s\prime}$' gives a high soil evaporation compared to all other schemes. Referring to the very dry top soil as encountered during the EFEDA campaign, the large soil evaporation simulated by 'soil $r_s^{s\prime}$' is unlikely. Under conditions of high surface temperature, the simulated soil evaporation is rather sensitive to the surface relative humidity, α. The formulation of Philip (1957), used for case 'soil $r_s^{s\prime}$', probably gives too high values near the surface (Kondo *et al.*, 1992). Furthermore, the soil moisture content in the top layer from which ψ and α are derived must be regarded as an average of the ω-profile in the entire layer. Choosing a too deep layer ensures large truncation errors, and this probably also plays a role in the overestimation of the soil evaporation by case 'soil $r_s^{s\prime}$'. However, it should be noted that the absolute values of λE^D are small.

The picture is entirely different for a sandy clay soil. In this case the reference model appears to predict a significant soil evaporation, exceeding the canopy evaporation during daytime. In contrast to the sandy loam soil type, a large difference between the reference and the case 'soil VB95' now occurs. Both models treat soil evaporation similarly by defining a surface relative humidity from the top layer soil moisture content, except for the value of a layer averaging coefficient l_c in eq. 4.19. Increasing l_c from 1 (reference case) to 1.6 (case 'soil VB95') results in a clear reduction of the soil evaporation. Given the dry initialization of the soil, we feel that this reduction results in more realistic simulations. The choice to take $l_c = 1.6$ applies to an upper soil layer of 7 cm depth, and is compatible with numerical simulation results carried out by Mahrt and Pan (1984). However, VB95 rightly point at the empirical nature of the coefficient l_c. More on this issue is discussed below.

The different behaviour of soil evaporation simulated by the reference force-restore model for the two soil types was also noted by Kondo *et al.* (1992). They simulated a drying bare soil with both a multi-layer diffusion scheme and a force-restore scheme. The latter

showed a sudden decrease of the surface soil water content after 10 days of simulation. As they explained, the water transport capacity of the lower soil layer is a steep function of the soil moisture content. When ω drops below a critical value, the upward water transport is severely limited and the upper layer dries out. In the simulations of the current study, the sandy loam profile of the relative soil moisture content, ω/ω_{sat}, is lower than for the sandy clay, and shows a similar low surface soil moisture content.

The differences found here are considerably higher than reported by Mahfouf and Noilhan (1991), who compared both α-type and β-type soil evaporation schemes. Their comparison was carried out for a silty clay loam soil with a higher initial moisture content than in this study. The soil thermal and hydraulic properties are extremely strong functions of the soil moisture content under dry conditions, and this makes a comparison very sensitive to the specification of the initial soil moisture profile. The current study focussed on these dry semi-arid conditions, but could be extended by including a somewhat wider range of moisture and soil type conditions.

The *aerodynamic exchange group* considers the PBL-sensitivity to the parameterization of the inside-canopy aerodynamic resistance, r_a^s. The establishment of a proper balance between the bare soil temperature and the total sensible heat flux is greatly determined by the parameterization of r_a^s, or its equivalent in terms of the specification of a roughness length for heat (section 2.4.2). The reference model, using the parameterization of CM88, gives the highest value of r_a^s and correspondingly the lowest sensible heat flux. The resistance formulation based on Lagrangian principles, case 'aero MH95', gives a very low r_a^s and high H, which seems related to the poor knowledge of the true diffusivity profiles right down near the surface. The semi-empirical BATS-formulation in 'aero D78' is situated in between these two. The differences were particularly obvious for the rougher and denser canopies. Based on the EFEDA-measurements, the reference model gives an optimal balance between surface temperature and sensible heat flux, and is superior to both alternative parameterizations.

As a consequence of the low value of r_a^s by case 'aero MH95', also the momentum transfer between the surface and the atmosphere was increased compared to the reference model, appearing as an increased friction velocity, u_*. The relatively large mechanical turbulence contributed much to the growth of the PBL. This effect augmented the difference in PBL-height between the case 'aero MH95' on one hand, and the other parameterizations on the other. During nighttime, the momentum transfer in 'aero MH95' is extra enhanced compared to the other cases owing to the absence of a stability correction between $z = z_{0m}$ and $z = z_R$. In particular the 'aero MH95' simulations of the tall forest vegetation type reveal a strong increase of the nighttime PBL-height.

An increased momentum flux between a vineyard canopy and the atmosphere is also to be expected if the observed roughness length, implemented in all coupled models, is replaced by the formulation proposed by CM88. This formulation is based on the numerical experiments of Shaw and Pereira (1982), and gives an apparent overestimation of z_{0m} of nearly a factor two compared to wind profile measurements (section 2.4.1). The observed roughness length was rather low: z_{0m}/h was ~0.05. Similar values were reported by Sene (1994) for a vineyard in the same area, and by Garratt (1978) for a sparse forest canopy type.

The intercomparisons carried out in the *canopy resistance group* give rise to a large range in predicted surface evaporation. In absolute sense the impact of choosing a canopy resistance model is limited owing to the low value of σ_f adopted here. For more complete vegetation covers the differences are more significant.

A common feature to canopy resistance parameterizations is that they need independent calibration. Data collected during EFEDA-I were used to calibrate the reference formulation, proposed by CM88, and the photosynthesis-r_c models in 'r_c CO_2' and 'r_c big CO_2'. The value of r_s^c in 'r_c fix' was obtained from the reference model, and thus indirectly also calibrated with the same dataset. Only the parameterization in 'r_c VB95' was not calibrated using the collected observations, and these expressions resulted in a too low evaporation rate compared to the observations and the reference model simulations.

However, a significant difference between model variations is also caused by differences in included environmental responses in the various models. In the reference case r_s^c only depends on incoming shortwave radiation. Comparing the predicted daytime evaporation to the observed quantities (section 6.5) reveals an underestimation of approximately 20%. But, as noticed before, the quality of the λE-data leaves the possibility that measured evaporation rates are too high. The correspondence between the reference model and the observations taken at the WAUMET site is better (section 5.2).

The daytime evaporation predicted by the photosynthesis-r_c model proposed by Jacobs (1994) and Jacobs *et al.* (1995), present in the case h = 'r_c CO_2', is significantly larger than the reference model, especially for the cool and moist MLS initialization. The model was calibrated under conditions corresponding to the DRY profile, and a rather strong response to ambient humidity deficit is included. This humidity response causes a strong reduction of r_s^c under MLS conditions and gives rise to higher values of λE^D. The humidity response is so strong, that the overestimating effect of adopting a single surface temperature as in the case 'big leaf' is greatly compensated by the associated rise in ambient humidity deficit (case 'r_c big CO_2'). Furthermore, the case 'r_c CO_2' simulates an evaporation peak at about 10 GMT. This causes a considerable increase in the total daytime moisture flux at the top of the PBL. Before noon the PBL is still low, and the moisture accumulation below the inversion gives a strong humidity gradient across the PBL top.

The average ratio of the entrainment virtual heat flux to the surface flux, R_h, is approximately 0.1 for the EFEDA simulations of DOY 174. The simulations using artificial initial profiles show a similar figure. The value of R_h found here is not necessarily a physical quantity, as it is derived from the numerical simulation of a turbulent diffusion process, according to Troen and Mahrt (1986) and Holtslag and Moeng (1991). Since R_h follows from the development of the turbulent fluxes in the past, and also enters the formulation of the turbulent diffusivity, a negative feedback in the model may result in a reduction of R_h. Also, the present PBL-model does not include the contribution of wind shear above the PBL to the growth of the turbulent layer. However, the dependence of K_h on R_h is not very strong, and the model also succeeds in a reasonable simulation of observed PBL-temperatures under conditions of poor advection. This indicates that the estimates of R_h contain some realism, and allow an intercomparison with other studies. Driedonks (1981) and Tennekes (1973) suggest $R_h \approx 0.2$ for most cases. Betts and Ball (1994) found $R_h = 0.44$ for the FIFE radiosoundings. In this dataset, larger values (0.55) where found from an analysis of the θ_v-

budget of the PBL, while lower values (0.32) resulted from an analysis of observed θ_v-jumps and PBL-growth. As they comment, the former method is rather sensitive to advection, while the latter method suffers from the exclusion of the influence of subsidence on PBL-growth. However, the sensitivity analysis of Driedonks (1982b) clearly demonstrates a limited sensitivity of mixed layer temperature to the value of R_h, and this might partially explain the high value found by Betts and Ball (1994), using the θ_v-budget. Also Culf (1992) found $R_h \approx 0.5$ by comparing PBL height observations with the slab model of Tennekes (1973) using data collected over the Sahel. He argues that again advection might have played an unknown role in his data. The average value of 0.1 found here seems rather low compared to these studies. A final statement about the significance of this result is hard to give, since simulations and data on only a single day have been used to obtain the value of R_h. A more careful analysis of the other soundings and an averaging over the entire period should be carried out to evaluate the value of R_h.

The initial temperature profile of DOY 174 clearly showed the presence of a residual layer reaching a height of approximately 3 km. A strong temperature inversion at this height prevented the PBL from a significant growth beyond this level for the given surface heat flux. This strongly developed residual layer yielded a limited heat entrainment ratio in the simulations. The entrainment ratio for moisture is much larger, but shows a great variability due to the small surface flux of moisture.

6.6.2 Practical considerations for SVAT's

An important question arising from the comparison study is what practical consequences can be extracted from it.

From the *surface representation group* we concluded that a sparse canopy must be described by use of at least two separate components, a vegetation and a bare soil component. The surface energy balance is quite well reproduced by either the reference two-component model or the case '3 fracs' (section 4.2.1), which both allow a separate temperature for the bare soil and the vegetation component of the surface. Soil heat flux is still too high for both these model variations, compared to area-averaged measurements from the CNRM database.

The *soil heat and water vapour flux group* is less conclusive. The overestimation of G^D by the reference model is accompanied by a clear underestimation in the case 'soil VB95', but which of them should be preferred is not clear. As outlined by Dickinson (1988), the force-restore method is efficient but shows shortcomings in case of inhomogeneous soils and irregular surface forcing. Based on these physical aspects, a multilayer diffusion scheme to simulate soil heat fluxes should be preferred in semi-arid areas, where strong soil moisture gradients are very common. The four-layer scheme present in the latest ECMWF surface model (Viterbo and Beljaars, 1995) probably provides a good optimum between numerical efficiency and physical accuracy. Warrilow *et al.* (1986) pointed out that the choice of four soil layers with an exponentially increasing layer depth ensures a proper coupling between the diurnal and the seasonal variations. However, the parameterization of the soil heat flux as proposed by Viterbo and Beljaars (1995) may be improved by allowing a range of effective conductivity values, Λ (section 4.1.3).

For soil evaporation it is more difficult to come to a conclusion from a shortrange

intercomparison as employed here. The schemes included show a wide range of surface evaporation rates. For the sandy loam soil, as encountered during EFEDA, the reference model or the soil resistance model (case 'soil r_s^{s}') yield total evaporation rates close to the observed values. However, the observations are probably too high, and the correspondence between the two model types is far from ideal for an other soil, i.e. sandy clay. The soil surface relative humidity as described by eq. 4.19 using l_c = 1.6 reduces the soil evaporation to nearly zero, as would be expected from the dry top soil layer encountered during EFEDA. The adjustment of the expression for α using this coefficient is yet rather empirical, as suggested by VB95, and needs further analysis. The albedo-observations (section 3.3) suggest some diurnal variation of the soil moisture content in the top soil layer, being highest around sunrise. Some evaporation should be expected at these times, but none of the models simulated these details. The skill of the models highly depends on the accuracy of the initial soil moisture profile, which may have been too poor, particularly for the soil moisture content in the very top soil layer.

The *aerodynamic exchange* from the underlying bare soil to the free atmosphere is a particularly relevant parameter for sparse canopy, where a large portion of the sensible heat originates from the bare soil component. The aerodynamic transfer has a clear impact on the surface temperature, which in turn affects radiative, physiological and aerodynamic processes. From this study we found that the parameterization of CM88 gives optimal results for the EFEDA vineyard. A disadvantage in CM88 is the need for information about the canopy height, which is often not available in global applications. The concept of a fixed excess resistance, or roughness length for heat, is simpler to apply. However, observations of the soil temperature show a clear diurnal pattern of this excess resistance. They also show that for the present surface type the ratio of z_{0m} and z_{0h} should be chosen significantly higher than 10, as employed by for instance VB95, or even 20, as proposed by Braud *et al.* (1993).

The *canopy resistance models* compared in the current study have only a minor effect on the total surface energy balance, owing to the low degree of vegetation cover. The photosynthesis model in case 'r_c CO_2' has a very strong humidity response, but, as discussed in section 3.4, does not contain a dependence on soil moisture content. The parameterization in 'r_c VB95', on the other hand, includes a soil moisture effect which results in a relatively high crop resistance. Again, the choice for the optimal model for the canopy resistance is not univocally obvious from the present study. The physical origin of the photosynthesis model, and its skill to describe field data rather well, makes it a very attractive alternative to the traditional statistical models. However, attention must be paid to the response of r_s^{c} to soil moisture, which for long term simulations is probably more important for the total crop evaporation than a response to air humidity (Monteith, personal comm.).

6.6.3 Guidance for future research

From this study it is clear that many physical viewpoints have been proposed in order to assess the lower boundary condition for atmospheric models. It is also clear that different models give rather different predictions. Until now, no general consensus exists about which SVAT provides the 'best' surface flux predictions for global applications.

In that context a very important research program currently running is the Program for Intercomparison of Land-surface Parameterization Schemes (PILPS; Henderson-Sellers *et al.*, 1993, 1995). This program aims to 'improve the understanding of current and future land-surface parameterization schemes used to represent regional to continental scale, by documentation of current models, acquisition of appropriate data sets for model intercomparison, identification of model inadequacies and propose solutions to these' (Henderson-Sellers and Brown, 1992). The PILPS program is scheduled to last 7 years, and is separated into various phases: (0) model documentation, (1) stand-alone tests with synthetic forcings, (2) stand-alone tests with observed data, (3) coupled intercomparisons with a selected 3-D model, and (4) coupled intercomparison with a range of 3-D models. The research program is unique in its completeness of both existing SVAT schemes and considered topics, and greatly will contribute to the quantification of surface model variability.

The required quality of a SVAT depends on the application foreseen. For large scale applications in GCM's or NWP models the SVAT must cover a great range of surface types and time scales. An important feature is a realistic description of moisture transport on a diurnal and seasonal (annual) timescale, and the parameterization of soil evaporation is a major issue for semi-arid conditions. Similarly, the quality of the global fields of surface characteristics (albedo, roughness, soil type, vegetation cover) determines the skill of the SVAT's to a large extent, and this needs attention as well.

Appendix I: List of symbols and acronymns

- **acronymns**

BATS	Biosphere-Atmosphere Transfer Scheme
CM88	Choudhury and Monteith (1988)
CNRM	Centre National de Réchèrches Météorologiques, Toulouse
COP	Copenhagen University
D78	Deardorff (1978)
DOY	Day Of Year
ECHIVAL	European project on Climatic and Hydrological Interactions between the Vegetation, the Atmosphere and the Land Surface
ECMWF	European Centre for Medium-range Weather Forecasting
EFEDA	ECHIVAL Field Experiment in Desertification-threatened Area
EPOCH	European Programme on Climate and Natural Hazards
FIFE	First ISLSCP Field Experiment
GCM	General Circulation Model
GMT	Greenwich Mean Time
HAPEX	Hydrological Atmospheric Pilot EXperiment
HIRLAM	High Resolution Limited Area Model
ISLSCP	First International Satellite Land Surface Climatology Project
KNMI	Royal Netherlands Meteorological Institute
LNF	Localized Near-Field theory
MH95	McNaughton and Van den Hurk (1995)
MLS	Mid-Latitude Summer (initial PBL-profile)
NP89	Noilhan and Planton (1989)
NWP	Numerical Weather Prediction
PAR	Photosynthetic Active Radiation
PBL	Planetary Boundary Layer
PILPS	Project for Intercomparison of Land surface Parameterization Schemes
PM	Penman-Monteith (equation)
SIB	Simple Biosphere model
SL	Surface Layer
SVAT	Soil-Vegetation-Atmosphere Transfer
SW85	Shuttleworth and Wallace (1985)
TDR	Time Domain Reflectometry
VB95	Viterbo and Beljaars (1995)
VU	Free University of Amsterdam
WAUHBH	Wageningen Agricultural University, Dept. of Hydrology
WAUMET	Wageningen Agricultural University, Dept. of Meteorology
WMO	World Meteorological Organization
WSC	Winand Staring Centre

- **Symbols**

A available energy (W/m^2)
$A^{\downarrow\uparrow}$ allwave radiation (W/m^2)
A_c available energy for canopy (W/m^2)
A_d drip area (m^2)
A_l average leaf area single leaf (m^2)
A_m asymptotic value of A_n (kg/m^2s)
$A_{m,max}$ maximum value of A_m (kg/m^2s)
A_n photosynthetic rate (kg/m^2s)
A_p areal surface of soil heat flux plate (m^2)
A_s available energy for soil (W/m^2)
A_T amplitude temperature wave (K)
A_x, A_{wx} spectra functions
a surface albedo; coefficient in PBL-model; coefficient for longwave emittance (W/m^2K^4)

a_∞ canopy albedo for $LAI \rightarrow \infty$
a_0 albedo at noon
a_1, a_2, a_3 coefficients in r_s^c model of VB95
a_c canopy albedo
a_{equ} calibration coefficient for ω_{equ}
a_{hor} albedo for canopy with horizontal leaves
a_i effective area for T_{sur} (m^2)
a_s bare soil albedo
a_{sph} albedo for canopy with spherically distributed leaves
B^{-1} $1/\kappa \ln z_{0m}/z_{0h}$
B_x, B_{wx} spectra functions
b characteristic plant width (m); Clapp and Hornberger coefficient; coefficient in PBL-model; coefficient for longwave emittance
b_b, b_t coefficients in PBL-model
b_D coefficient for humidity dependence of g_s $(g/kg)^{-1}$
$\mathbb{C}$ soil heat content (J/m^2)
C scalar concentration (kg/m^3); cloud cover (-)
C_1, C_2, C_{2ref} coefficients for soil moisture transport in force-restore scheme
C_a specific heat air (J/kgK)
C_b average concentration near leaf (kg/m^3)
C_c average concentration within canopy layer (kg/m^3); coefficient in SW85
C_d leaf drag coefficient
C_f far-field concentration (kg/m^3)
C_H transfer coefficient for heat and scalars
C_h specific heat of soil (J/kgK)
C_i internal CO_2-concentration (kg/m^3)
C_l fraction of surface covered with skin reservoir
C_M bulk drag coefficient for momentum
C_n near-field concentration (kg/m^3)
C_o specific heat organic material (J/kgK); relative oxygen concentration (%)
C_R drag coefficient roughness element; reference concentration (kg/m^3)
C_S substrate drag coeficient
C_s specific heat of mineral (J/kgK); concentration at ground surface (kg/m^3); external CO_2-concentration (kg/m^3); coefficient in SW85
C_T^2 temperature structure parameter ($K^2 m^{-2/3}$)
C_v average far-field concentration (kg/m^3)
C_w specific heat water (J/kgK); spectra function
c coefficient for d; specific scalar concentration (kg/kg)
c_0, c_1, c_2 coefficients in description for σ_w and T_l
c_d coefficient for d
c_g coefficient for g
c_i internal specific concentration (kg/kg)
c_m regression coefficient for m_d
c_p specific heat for dry air at constant pressure (J/kgK)
c_s external specific concentration (kg/kg)
c_w hydraulic capacity (m^{-1})
c_{x1}, c_{x2}, c_{sx} coefficient for similarity method ($x = T$, q, u)
c_λ correction factor for λ_p
D characteristic plant spacing (m); vapour pressure deficit at reference height (Pa); molecular diffusion coefficient (m^2/s)
D_0 canopy water vapour deficit (Pa)
D_a humidity deficit at reference height (kg/kg)
D_{max} reference humidity deficit for humidity response in A_n-g_s model (kg/kg)
D_p plant density (m^{-2})
D_r calibration coefficient in humidity response of g_s (g/kg)
D_s ambient humidity deficit (kg/kg)
D_v molecular diffusivity for water vapour (m^2/s)
d displacement height (m)
d_1, d_2 depth of soil layer i (m)
d_{31} crosstalk coefficient
d_{33} attenuation coefficient
d_p diameter of soil heat flux plate (m)
d_s beam path length (m)
E evaporation rate (kg/m^2s)
E_c canopy evaporation (kg/m^2s)
E_c^{pot} potential canopy evaporation (kg/m^2s)
E^D daytime average of surface evaporation (kg/m^2s)
E_l leaf evaporation rate (kg/m^2s); evaporation from skin reservoir (kg/m^2s)
E_{max} maximum evaporation rate (kg/m^2s)
E_s soil evaporation (kg/m^2s)
E_t leaf transpiration (kg/m^2s)
E_t^D daytime average moisture entrainment (kg/m^2s)
e water vapour pressure (Pa)
e_0 water vapour pressure in canopy air (Pa)
e_a water vapour pressure at reference level (Pa)
e_{sat} saturated water vapour pressure (Pa)
F moisture flux in soil (kg/m^2s)
F_c canopy flux density profile (kg/m^2s)
F_{CO2} CO_2-flux density (kg/m^2s)
F_h average canopy flux density (kg/m^2s)
F_s ground flux density (kg/m^2s)
F_t total flux density (kg/m^2s)
F_x flux density of x (kg/m^2s)
f Coriolis parameter (s^{-1}); normalized frequency (s^{-1}); humidity function of C_i/C_s
f_0 ratio of C_i/C_s at $D_s = 0$
f_d fraction of diffuse radiation
f_s fraction of sunlit leaves
G soil heat flux density (W/m^2)
G_0 soil heat flux density at surface in CM88 (W/m^2)
G^D daytime average soil heat flux density (W/m^2)
$G_{i,t}$, $G_{i,b}$ soil heat flux density at top and bottom of layer i (W/m^2)
g gravity acceleration (m/s^2); function for a_s
g_0 regression coefficient for g
g_1 calibration coefficient in crop resistance according to CM88 (m/s / W/m^2)
g_b dimensionless concentration in PBL-model

g_{c_0} crop conductance (m/s)
g_c^0 g_c at $D_s = 0$ (m/s)
g_{cut} cuticular conductance (m/s)
g_D humidity response of r_s^c in NP89
g_m mesophyll conductance (m/s)
g_{max} maximum crop conductance (m/s)
g_s stomatal conductance (m/s)
$g_{s,CO2}$ stomatal conductance for CO_2-exchange (m/s)
g_{s_0max} maximum g_s (m/s)
g_s^0 g_s at $D_s = 0$ (m/s)
g_t dimensionless concentration in PBL-model
H sensible heat flux density (W/m^2)
H_c canopy sensible heat flux (W/m^2)
H^D daytime average sensible heat flux density (W/m^2)
H_s soil sensible heat flux (W/m^2)
H_t^D daytime average heat entrainment (W/m^2)
h canopy height (m)
I interception (kg/m^2s); integrated surface buoyancy flux (K m); beam intensity; absorbed PAR (W/m^2)
I_0 reference beam intensity
I_s infiltration (kg/m^2s)
J integrated surface latent heat flux (g/kg m)
K, K_χ eddy-diffusivity (m^2/s) ($x = h$ for heat, m for momentum, e for water vapour, c or s for scalars)
$K^{\downarrow\uparrow}$ incoming, reflected shortwave radiation (W/m^2)
$K_{b\downarrow\uparrow}$ bottom-up diffusivity (m^2/s)
$K_c^{\downarrow\uparrow}$ incoming, reflected shortwave radiation for canopy (W/m^2)
K_{dif} diffuse radiation (W/m^2)
$K_e^{\downarrow}$ extraterrestrial shortwave radiation (W/m^2)
K_{ref} coefficient in r_s^c model (W/m^2)
$K_s^{\downarrow\uparrow}$ incoming, reflected shortwave radiation for soil (W/m^2)
K_T isothermal water vapour diffusivity (m^2/s)
K_t top-down diffusivity (m^2/s)
k soil thermal diffusivity (m^2/s)
k_{bl} extinction coefficient for black leaves
k_i absorption coefficient for gas i
k_n near-field kernel function
k_p precipitation coefficient
k_r extinction coefficient
k_v water vapour absorbtion coefficient
$L^{\downarrow\uparrow}$ incoming/outgoing longwave radiation (W/m^2)
$L_{8\text{-}14}^{\downarrow}$ incoming longwave in 8-14 μm band (W/m^2)
$L_c^{\downarrow\uparrow}$ incoming/outgoing longwave radiation for canopy (W/m^2)
$L_s^{\downarrow\uparrow}$ incoming/outgoing longwave radiation for soil (W/m^2)
L_u cup-anemometer response length (m)
L_v Monin-Obukhov length (m)
LA Leaf Area (m^2)
LAD Leaf Area Density (m^2/m^3)
LAI Leaf Area Index (m^2/m^2)
LAI_* LAI/σ_f
l tube length (m)
l_c layer-averaging coefficient for α
l_w characteristic leaf dimension (m)
M_λ longwave emittance (W/m^2)
m_a molecular weight of dry air
m_d assymetry function for a_s
m_{d0} regression coefficient for m_d
m_o molecular weight of oxygen
m_v molecular weight of water
N number of leaves
Nu Nusselt number (ratio l_w/δ)
n eddy-diffusivity extinction coefficient; number of samples; frequency (s^{-1})
n_0 cut-off frequency (s^{-1})
n_s sampling frequency (s^{-1})
P total precipitation rate (kg/m^2s)
Pr Prandtl number (ratio dynamic viscosity and thermal diffusivity of air)
P_s surface precipitation rate (kg/m^2s)
p air pressure (Pa); parameter in β-distribution; sensor averaging length (m)
p_0 standard air pressure (Pa)
p_{equ} calibration coefficient for ω_{equ}
Q_{10} reference value in dimensionless response function
Q_* net radiation (W/m^2)
Q_*^D daytime average net radiation (W/m^2)
$Q_{*,c}$ canopy net radiation (W/m^2)
$Q_{*,s}$ soil net radiation (W/m^2)
q specific humidity (kg/kg); parameter in β-distribution
q_*^{ML} characteristic humidity scale in convective PBL (kg/kg)
q_0 within canopy specific humidity (kg/kg)
q_{00} humidity profile extrapolated to $z = 0$ (kg/kg)
q_a reference specific humidity (kg/kg)
q_c canopy surface specific humidity (kg/kg)
q_m average q in PBL (kg/kg)
q^{min} average q in PBL just before sunrise (kg/kg)
q_s soil surface specific humidity (kg/kg)
q_{sat} saturated specific humidity (kg/kg)
q^t average PBL specific humidity at time t (kg/kg)
R molar gas constant (m^2/s^2 K)
$R_1, R_2, ..$ root extraction fraction
R_a coefficient in SW85
R_c coefficient in SW85
R_d dark respiration (kg/m^2s)
R_h heat entrainment ratio
R_q moisture entrainment ratio
R_s coefficient in SW85; scalar entrainment ratio
R_v gas constant for water vapour (m^2/s^2 K)
$\Re$ dimensionless resistance
Re Reynolds number
Re_c critical Reynolds number
Ri_c critical Richardson number
r reflection coefficient; mixing ratio
$r_{1,2}$ space coordinate (m)

r_a aerodynamic resistance (s/m)
r_a^a aerodynamic resistance for scalars between z_{0m} and z_R (s/m)
r_a^h excess resistance (s/m)
r_a^c bulk boundary layer resistance (s/m)
r_a^s aerodynamic resistance in two-layer model between soil surface and within canopy node (s/m)
r_b leaf boundary resistance (s/m)
r_l lower soil resistance in CM88 (s/m)
r_n near-field resistance (s/m)
r_s^c canopy or crop (stomatal) resistance (s/m)
r_s^s soil resistance for evaporation (s/m)
r_{st} leaf stomatal resistance (s/m)
$r_{s,min}$, $r_{s,max}$ coefficients in r_s^c model
r_t tube radius (m)
r_u upper soil resistance in CM88 (s/m)
r_x plant radius (m)
rh porometer relative humidity
S source strength (kg/m^{3}s)
s $\partial q_{sat}/\partial T$; sensor separation (m)
S_ω root extraction (kg/m^{2}s)
S_h canopy source strength (kg/m^{3}s)
S_{xy} (co-)spectral distribution function
T_0 temperature in canopy layer (K)
$T_1, T_2, ..$ soil temperature in layer i (K); reference temperatures in Q_{10}-response function (°C)
T_a reference air temperature (K); analog-to-digital transfer function
T_b sensor body temperature (K)
T_c canopy temperature (K)
T_d first-order digital high-pass filter transfer function
T_l Lagrangian time scale (s); leaf temperature (K)
T_n data-acquisition net transfer function
T_p sensor line averaging transfer function
T_r sensor dynamic response transfer function
T_s soil temperature (K)
T_{sk} skin layer temperature (K)
T_{son} sonic temperature (K)
T_{sur} effective surface temperature (K)
T_t tube damping transfer function
T_u horizontal averaging vector transfer function
T_v virtual temperature (K); low-pass filter transfer function
T_w wet-bulb temperature (K); vertical averaging vector transfer function
T_{xy} (co-)spectral transfer function for $x'y'$
t time (s)
u horizontal wind speed (m/s)
u_* friction velocity (m/s)
u_0 within canopy wind speed (m/s)
u_a reference wind speed (m/s)
u_g geostrophic wind component (m/s)
u_t tube air speed (m/s)
V volume of plant (m^3); Voltage (V)
V_c speed of sound (m/s)
v horizontal wind speed (m/s)
v_g geostrophic wind component (m/s)
W_{MAX} coefficient for w_{max} (mm)
w vertical wind speed (m/s)
w_* convective velocity scale (m/s)
w_{dew} amount of intercepted water (mm or kg/m^2)
w_{max} maximum amount of intercepted water (mm)
w_s characteristic velocity scale in PBL-model (m/s)
X $C_d LAI$
x constituent
x_a volume fraction of air
x_l resistance coefficient in VB95 (m/s); sensor longwave gain (V per W/m^2)
x_o volume fraction of organic material
x_s volume fraction of soil; resistance coefficient in VB95 (m/s); shortwave gain (V per W/m^2)
x_w volume fraction of water
z_R reference height for canopy models, or lowest model level for PBL-model (m)
z height (m)
z_{0m} roughness length for momentum (m)
z_{0h} roughness length for heat and salars (m)
z_0' roughness length of soil (m)
$z_{1,w}, z_{2,w}$ soil layer depth for water transport (m)
z_i boundary layer height (at time t) (m)
z_s particle release height (m)

■ **Greek letters**
α surface relative humidity; horizontal angle
α_d time coefficient in first-order filter
α_l leaf absorbtivity
α_p shape factor for soil heat flux plates
α_u wind speed extinction coefficient
β solar elevation; rotation angle
β_R C_R/C_S
β_r radiation extinction coefficient
β_s sheltering factor for r_b
Γ compensation concentration (kg/m^3)
Γ_b coefficient for non-evaporating parts in D78
γ psychrometer constant (Pa/K)
γ_b bottom-up countergradient correction (m^{-1})
γ_H hydraulic conductivity (m/s)
γ_h $u(h)/u_*$
γ_q humidity gradient above PBL (m^{-1})
γ_s scalar countergradient correction (m^{-1})
γ_{sat} saturated hydraulic conductivity (m/s)
γ_t top-down countergradient correction (m^{-1})
γ_{θ_v} temperature gradient above PBL (K/m)
δ step function; thickness of leaf boundary layer (m)
Δ $\partial e_{sat}/\partial T$
Δ_l optical depth
ε m_v/m_a; emissivity
ε_0 maximum quantum use efficiency (kg/J PAR)
ε_a longwave emissivity of air
ε_b sensor body emissivity
$\varepsilon_c, \varepsilon_s$ canopy or surface longwave emissivity
ε_i initial quantum use efficiency (kg/J PAR)
ε_T sensor setting for ε

ζ zenith angle; spectra function
η roughness density
θ potential temperature (K); vertical wind angle (rad)
θ_* temperature scale (K)
θ_*^{ML} mixed layer temperature scale (K)
θ_0 within canopy potential temperature (K)
θ_a reference potential temperature (K)
θ_c canopy surface temperature (K)
θ_m average PBL-temperature (K)
θ_s soil surface potential temperature (K); temperature excess of convective thermal (K)
θ_{sk} potential skin layer temperature (K)
θ_{sur} average surface potential temperature (K)
θ_v^t average PBL potential virtual temperature at time t (K)
θ_v^{min} average PBL potential virtual temperature just before sunrise (K)
$\theta_{v_{00}}$ temperature profile extrapolated to $z = 0$ (K)
Λ skin conductivity (W/m^2K)
λ latent heat of water vapour (J/kg); wave length (m)
κ Karman constant (0.4)
λ_H hydraulic diffusivity (m^2/s)
λ_T soil thermal conductivity (m^2/s)
λ_a thermal conductivity of air (W/mK)
λ_p condictivity of soil heat flux plate (W/mK)
μ cos ζ
ν kinematic molar diffusivity (m^2/s)
ξ fraction of potential canopy evaporation; spectra function
ξ_x sensitivity parameter for x
$\rho_{(a)}$ density of dry air (kg/m^3)
ρ' soil bulk density (kg/m^3)
ρ_l reflectance of leaves
ρ_o density of dry matter (kg/m^3)
ρ_s density of soil (kg/m^3)
ρ_v water vapour density (kg/m^3)
ρ_w density of liquid water (kg/m^3)
ρ_x scalar concentration (kg/m^3)
σ Stefan-Bolzmann coefficient
σ_f fractional vegetation cover
σ_x standard deviation of x
T throughfall (kg/m^2s)
τ momentum flux density ($kg/m\ s^2$); tortuosity parameter; return-to-isotropy time scale (s)
τ_1 diurnal time scale (24 hrs)
τ_2 annual time scale (365.25 days)
τ_c sensor time constant (s)
τ_d digital filter time scale (s)
τ_l leaf transmittance
ϕ dimensionless source profile; azimuth
ϕ_h integrated stability correction for heat and scalars
ϕ_m integrated stability correction for momentum
φ effectiveness weighting for r_b
Ψ_h stability correction; profile influence function
ψ soil matric potential (m)
ψ_{sat} saturated soil matric potential (m)
ω_c critical soil moisture content for α (m^3/m^3)
ω_i soil moisture content in layer i (m^3/m^3)
ω_i^* implicit form of ω_i (m^3/m^3)
ω_{equ} equilibrium soil moisture content (m^3/m^3)
ω_{pwp} wilting point soil moisture content (m^3/m^3)
ω_{fc} field capacity soil moisture content (m^3/m^3)
ω_{sat} saturated soil moisture content (m^3/m^3)

Appendix II: Instrumental aspects and data processing

Sensing the atmosphere or the soil is almost inevitably associated with introduction of errors. The errors can be associated with flow distortion, sensing in a limited frequency or spatial domain, sensor calibration affected by environmental conditions and some other factors. The corrections applied to the eddy-correlation measurements, soil heat flux, surface temperature and radiation are discussed in this section.

1 Low-pass filtering (detrending)

The covariances measured by the eddy-correlation technique are often affected by trends in the signal which don't have a turbulent origin. Diurnal variations of air temperature and humidity, wind velocity changes due to a change of the wind direction, or the influence of sudden cloud cover changes on the average air temperature are examples of non-turbulent contributions to the eddy-correlation covariances. The same applies to fast-response variance measurements, used for instance to determine fluxes from the variance method (section 2.2.4). Therefore, some kind of detrending must be applied to filter out the low-frequency part of the measured spectrum of the constituents of interest. The frequency below which fluctuations have to be removed (the high-pass cut-off frequency) strongly depends on the mechanism causing the non-turbulent contribution to the quantity fluctuations. Different opinions are circulating about the preferred choice of the cut-off frequency and the detrending algorithm. However, these choices sometimes play a non-trivial role in the determination of the final detrended covariances from raw time series.

Van den Hurk (1995) explored the effect of various detrending algorithms on the computed variances and covariances of simultaneously measured series of the horizontal and vertical wind speed, u and w, respectively. He used a dataset collected during the EFEDA-II eddy-correlation intercomparison. Various artificial trends were added to an original trendless time series. The variances and covariances were computed using various averaging algorithms currently applied by different experimentalists. The artificial trends were selected as to cover a range of likely trends occurring in the real world.

The results often showed a large impact of the choice of the detrending algorithm, depending on the combination of added artificial trend and algorithm employed. The differences were particularly significant for corrections on σ_u^2, and less significant for $\overline{u'w'}$ and $\overline{w'T'}$.

This section discusses various detrending algorithms, and describes the algorithms employed during the EFEDA-I and EFEDA-II measuring campaigns.

- **Description of detrending methods**

The *linear detrend* defines the mean of a constituent as the linear regression of the variable against time. The fluctuation part of the quantity x is equal to the value of x minus the value of the regression line at the same time. The time scale of the fluctuations that must be removed is proportional to the length of the averaging interval over which the regression is computed. A linearly detrended variance of x is assessed by subtracting the signal-time covariance from the raw variance:

$$\sigma^2_{x,\mathrm{det}} = \overline{x'x'} - \overline{x't'} = \sigma^2_x - \left(\frac{1}{n}\Sigma xt - \frac{1}{n}\Sigma x \frac{1}{n}\Sigma t \right) \qquad \text{(II.1)}$$

where n is the number of samples, and the subscript *det* indicates detrended variance.

The *first-order digital filter* approaches a running mean by defining the average of x as

$$\overline{x}_i = \alpha_d \overline{x}_{i-1} + (1 - \alpha_d)\, x_i \qquad \text{(II.2)}$$

in which α_d is given by $\exp(-1/(\tau_d n_s))$, and τ_d is a time constant. The fluctuating part of the quantity x is obtained by subtracting the mean from the total quantity, which yields from eq. II.2

$$x_i' = x_i - \overline{x}_i = \alpha_d(x_i - x_{i-1}) + \alpha_d x_{i-1}' \qquad \text{(II.3)}$$

τ is the timescale of the fluctuations which must be removed from the signal. In operational systems as the Hydra (Shuttleworth *et al.*, 1988) τ = 200 s. However, longer time scales must be included to describe the low-frequency contributions to $\overline{u'u'}$, originating from eddies of the scale of the boundary layer height (Panofsky *et al.*, 1977). Some experimentalists use τ = 600 s. Moore (1986) derived correction factors to account for the effect of high pass-filtering on the (undesired) removal of turbulent fluctuations. These correction factors are discussed below.

Simpler approaches describe the trend in a signal by computing *separate means for short intervals*, shorter than the averaging time of 30 minutes. Fluctuations of the quantity x in a specific sub-interval are then defined as the deviation from the mean in that sub-interval. The (co)variance applicable to the entire interval is given by the arithmetic average of the covariances obtained in the various sub-intervals.

The *centred running mean* with averaging time τ computes the average of constituent x at time t from an interval extending from $t - \tau/2$ to $t + \tau/2$. A circular buffer containg all data in this interval must be retained and updated for each new time step.

A very time-consuming but well defined filtering technique uses a *Fourier transformation* to transform samples within a specified averaging interval to the frequency space. Specified transfer functions are used to remove undesired frequencies, and afterwards an inverse Fourier transform converts the series back into a time series. This method must be applied for each (co)variance separately. The Fourier method was not included in the comparison study of Van den Hurk (1995).

Which averaging method is best depends on the nature of the trend in the average signals. Diurnal trends can be removed effectively with both the linear and 1st order detrend. Sudden signal changes due to, for instance, cloud overpass are followed better by the recursive filter, although the filtered signal lags behind. By application of a higher order filter (Krikke, 1994b) or the running mean removal, this lagging is avoided. Application of higher order filters introduces concern about the high degree of non-natural information in the 'cleaned' signal. Linear detrends are favourable when the signal shows large variations with only a small average trend. Recursive filtering will remove too much of the true variation in that case, especially when the time constant for the recursive filtering is chosen too small.

- **Detrending methods employed**

During EFEDA-I all fast-response signals were linearly detrended over an half-hour interval. The slow-response signals were first linearly detrended within 10 minute intervals. These 10 minute averages were arithmetically averaged to 30 minute intervals.

The eddy-correlation software used during EFEDA-II originally executed a digital 1st order filter. This algorithm was later replaced by a linear detrend over a fixed 30 minute interval. The slow-response measurements were not detrended at all.

2 Eddy-correlation corrections

Eddy correlation corrections can be divided into three categories. Rotation corrections consider tilted streamlines due to terrain or mast tilt and flow distortion by the sensor. Frequency response corrections assess the problem of the limited frequency range actually being sensed, which is generally smaller than the inertial subrange. The third group of corrections consider various aspects of the fast response sensing system: vector averaging by cup anemometers, Webb-correction, virtual temperature and light-absorption by non-relevant gases.

- **Rotation corrections**

Ideally the wind flows parallel to the Earth's surface from a steady direction. Moreover, the transport of momentum in the lateral direction ($\overline{v'w'}$) can be ignored. Deviations from this ideal behaviour are caused by tilted sensors, sloping terrain in upwind direction, and flow distortion by the array. Wyngaard (1988) points out that the rotation corrections usually carried out are not sufficient to account for flow distortion errors. It is not difficult to show that a flow distortion caused by a sensor can actually *add* motion to the free wind stream, whereas rotation only *redistributes* the motions over the three components. Wyngaard (1988) defines an attenuation or amplification

coefficient of wind in the vertical direction (d_{33}), and a crosstalk coefficient of horizontal wind components into the vertical direction (d_{31}). The undisturbed covariance $\overline{wx}$ can be computed from

$$\overline{w_m x_m} \;/\; \overline{wx} \;=\; 1 + d_{33} + d_{31}\left(\frac{\overline{ux}}{\overline{wx}}\right) \tag{II.4}$$

where the subscript m refers to the measured vertical flux density. Both coefficients must be specified using an undisturbed free wind stream. For a vertically symmetric array d_{33} is rather insignificant compared to d_{31}. Since carefull attention is paid to twisting the sonic arrays into the mean wind, vertical symmetry of the array, and data selection as function of relative wind direction, the rotations discussed next are considered to serve as a proper correction to flow distortion as well.

The coordinate rotation applied here is the one proposed by McMillen (1988). The algorithm consists of 3 rotations:

- a horizontal rotation to align the u-component with the mean horizontal wind $\overline{U}$, thus rotating $\overline{v}$ to zero
- a vertical rotation to align the mean wind perpendicular to the streamline, thus forcing $\overline{w}$ to be zero
- a rotation along the u-axis to force the lateral momentum flux $\overline{v'w'}$ to zero. This rotation defines the vertical flux densities normal to the streamline rather than to the geopotential, which is of importance when the streamline inclines with respect to the local surface due to upwind terrain slopes. This rotation must be applied with care, since it is not always well defined, particularly under low wind speed conditions.

The rotation algorithm consists of a set of matrix multiplications. The first two rotations can be solved explicitly. Let α be the angle between $\overline{u}$ and $\overline{U}$, and θ be the vertical tilt, defined by

$$\theta \;=\; \arctan\left(\frac{w}{\sqrt{u^2 + v^2 + w^2}}\right)$$

The rotation matrix for the first two rotation, $M_{1,2}$, now becomes

$$M_{1,2} = \begin{vmatrix} \cos\alpha\cos\theta & \sin\alpha\sin\theta & \sin\theta \\ -\sin\theta & \cos\alpha & 0 \\ -\cos\alpha\sin\theta & -\sin\alpha\sin\theta & \cos\theta \end{vmatrix} \tag{II.5}$$

This matrix can be applied to both the mean wind values and the fluctuating parts:

$$\begin{pmatrix} u_2 \\ v_2 \\ w_2 \end{pmatrix} = M_{1,2}\begin{pmatrix} u \\ v \\ w \end{pmatrix}, \qquad \begin{pmatrix} u_2' \\ v_2' \\ w_2' \end{pmatrix} = M_{1,2}\begin{pmatrix} u' \\ v' \\ w' \end{pmatrix}$$

These rotations could be carried out with both the raw samples before calculating the covariances, and to averaged raw covariances. Let us consider rotation over α only, and define $a = \cos\alpha$ and $b = \sin\alpha$. Then the rotation of a covariance $\overline{x'y'}$ over α is given by

$$\begin{aligned} \overline{x_r' y_r'} &= \overline{(ax' + by')(-bx' + ay')} = \overline{-ab\,x'^2 + (a^2 - b^2)x'y' + ab\,y'^2} \\ &= -ab\,\overline{x'^2} + (a^2 - b^2)\,\overline{x'y'} + ab\,\overline{y'^2} \end{aligned} \tag{II.6}$$

where the subscript r denotes the rotated covariance. However, when additional non-linear transformations on x' or y' are carried out (such as detrending using a first- or higher order digital filter), the execution of these matrix transformations before or after computation of the covariances leads to different results (Krikke, 1994b). In that case it is recommended that the rotation operation is carried out on the raw data, rather than on the computed covariances.

The third rotation is carried out along the (rotated) u_2-axis. The matrix M_3 is given by

$$M_3 = \begin{vmatrix} 1 & 0 & 0 \\ 0 & \cos\beta & \sin\beta \\ 0 & -\sin\beta & \cos\beta \end{vmatrix} \qquad \text{(II.7)}$$

The angle β over which the rotation must be carried out is found iteratively by specifying $\overline{v_3'w_3'}$ from eq. II.7 and forcing it to zero:

$$\begin{aligned} \overline{v_3'w_3'} &= -\sin\beta\cos\beta\overline{v_2'v_2'} + \sin\beta\cos\beta\overline{w_2'w_2'} + (1 - 2\sin^2\beta)\,\overline{v_2'w_2'} \\ &= \left(\overline{v_2'v_2'} - \overline{w_2'w_2'}\right)\left[-\sin\beta\cos\beta + \frac{(1 - 2\sin^2\beta)\,\overline{v_2'w_2'}}{\overline{v_2'v_2'} - \overline{w_2'w_2'}}\right] \end{aligned} \qquad \text{(II.8)}$$

This leaves the need to find β for which the term between square brackets is zero. This is made possible by introduction of a factor K, defined as

$$K = \frac{\overline{v_2'w_2'}}{\overline{v_2'v_2'} - \overline{w_2'w_2'}}$$

Now eq. II.8 can be solved iteratively for β, using

$$\sin\beta = \frac{-\cos\beta \; +/- \; \sqrt{\cos^2\beta + 8K^2}}{4K} \qquad \text{(II.9)}$$

and $\cos^2\beta + \sin^2\beta = 1$. Usually three or four iterations are necessary to find β.

- **Frequency response corrections**

The turbulent flux density can be measured using eddy-correlation, provided that fluctuations in the frequency range in which turbulent transport takes place are all sensed. In practice, this condition is hardly met due to a limited frequency response of the sensors and the data acquisition system, averaging over a path rather than taking a point value, separation between sensors for different quantities, and filtering applied. For each of these effects a theoretical co-spectral transfer function can be computed, which is unity for all frequencies for an ideal system. Convolution of this loss factor with the actual turbulent spectrum of the considered quantity gives a fraction of the true covariance that is actually sensed. Application of this method to really measured spectra will not be of much significance, since these spectra show the shortcomings of the sensor configuration we were looking to correct for. Therefore, theoretical spectra are used. The flux loss ΔF_{xy} is then defined by

$$\frac{\Delta F_{xy}}{F_{xy}} = 1 - \frac{\int_0^\infty T_{xy}(n)\, S_{xy}(n)\, \mathrm{d}n}{\int_0^\infty S_{xy}(n)\, \mathrm{d}n} \qquad \text{(II.10)}$$

where n is the frequency, T_{xy} the net co-spectral transfer function, and S_{xy} the theoretical co-spectral distribution function. In the present analysis integration is carried out over a range of $0.001 < n < 100$ Hz.

Moore (1986) worked out most of the frequency response correction for a Hydra flux measurement station (Shuttleworth *et al.*, 1988). His work provided the basis for the correction algorithm developed here. The special corrections applicable to closed path sensors as the LICOR6262 have been obtained from Leuning and Moncreiff (1990). An overview of these corrections is also given by Moncreiff *et al.* (1995).

Digital sampling at limited frequency

An analogue to digital sampling acquisition method causes aliasing of spectral contributions exceeding the Nyquist frequency. The effective transfer function for an analog-to-digital sampling system, $T_a(n)$, is given by

$$T_a(n) = 1 + \left(\frac{n}{n_s - n}\right)^3 \qquad n \leq n_s/2 \qquad \textbf{(II.11)}$$

with n_s the sampling frequency. For eq. II.11 it is assumed that aliasing is reduced by prefiltering the raw signal at $n = n_s/2$, causing negligible co-spectral power above the Nyquist frequency. In spite of the limited application of low-pass filtering, eq. II.11 was adopted (see Figure II.1 for an example).

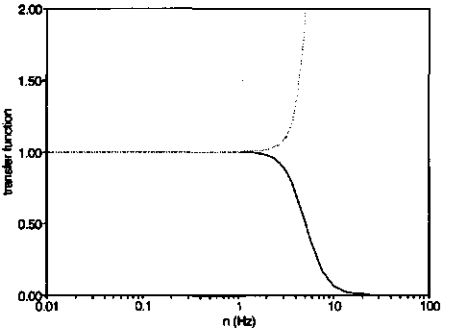

Figure II.1: Examples of the low-pass filtering transfer function T_v (——) and the analog-to-digital transfer function T_a (·····) for n_s = 10 Hz

Low-pass filtering

Low-pass filtering is applied to prevent aliasing, or folding frequencies higher than the Nyquist frequency $n_s/2$ into lower frequencies (Stull, 1988). Electronic filtering using a 4rd order Chebychev filter was only applied to w-signals during EFEDA-I, from day 19 onwards, and not at all during EFEDA-II. The transfer function $T_v(n)$ is given by

$$T_v(n) = \left[1 + \left(\frac{n}{n_0}\right)^4\right]^{-1} \qquad \textbf{(II.12)}$$

where n_0 is the cut-off frequency (at $n_s/2$). The time constant of the filter is given by $1/2\pi n_0$. Obviously, when no low-pass filtering is applied $T_v = 1$. An example of T_v is shown in Figure II.1.

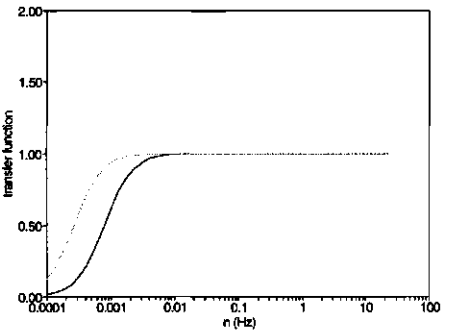

Figure II.2: Example of the high-pass filtering transfer function T_d for n_s = 10 Hz; shown are τ_d = 200 s (——) and 600 s (·····)

High-pass filtering (detrending)

The transfer function $T_d(n)$ for a first order digital filter is to a very good approximation given by

$$T_d(n) = \frac{(2\pi n \tau_d)^2}{1 + (2\pi n \tau_d)^2/\alpha_d} \qquad n \leq n_s/2 \qquad \textbf{(II.13)}$$

An example is shown in Figure II.2 for τ_d = 200 and 600 s.

For linear detrending the choice of the interval length is very similar to choosing a time constant

τ_d for a running mean interval. However, for the linear detrending algorithms employed during both EFEDA campaigns no frequency response correction was applied.

Sensor response and tube damping

The dynamic response of many sensors can be described by a simple first-order gain function:

$$T_r(n, \tau_c) = \left(1 + (2\pi n)^2 \tau_c^2\right)^{-1/2} \qquad \textbf{(II.14)}$$

where τ_c is the time constant of the instrument. For most instruments this correction was neglected. Only the home-made thermocouples, the cup anemometers and the LICOR6262 were considered to have a low enough time constant to affect the measured frequency spectrum. The thermocouple time constants were estimated to be 0.5 s (as concluded from inspection of measured energy spectra, but higher than 0.1 s as cited by Van Asselt *et al.*, 1991). For the LICOR6262 0.2 s was taken. The time constant of the cup anemometers was given by L_u/u, where L_u was the response length (estimated as 1.2 m; Jacobs, personal comm.) and u the horizontal wind speed. An example is depicted in Figure II.3.

A special case of damping of fluctuations is caused by the tube transporting the air from the sonic anemometer volume to the LICOR6262 gas analyzer. Leuning and King (1992) present a transfer function T_t given by

$$T_t(n) = \begin{cases} \sqrt{\exp(x / 6Du_t)} & \dfrac{2\pi n r_t^2}{D} < 10 \\ 1 & \text{elsewhere} \end{cases} \qquad \textbf{(II.15)}$$

where x is given by $-(\pi\, n\, r_t)^2\, l$, r_t the tube radius, l the tube length, D the diffusivity of the gas being analyzed and u_t the air speed in the tube. Eq. II.15 is strictly valid in cases where the flow within the tube may be considered to be laminar, and density fluctuations at all frequencies travel down the tube with the same velocity, u_t. Based on expressions presented by Philip (1963), Leuning and King (1992) state that this applies to frequencies for which $2\pi n r_t^2/D < 10$. For turbulent flow they propose the following transfer function

$$T_t(n) = \sqrt{\exp\left(-160 Re^{-1/8} r_t n^2 l / u_t^2\right)} \qquad Re > Re_c \qquad \textbf{(II.16)}$$

where Re_c is a critical Reynolds number, equal to ± 2300, and Re is given by $2u_t r_t/\nu$. Figure II.4 shows an example for both equations. For the corrections applied during EFEDA-II the laminar expression (eq. II.15) was used, where r_t was 0.0015 m, l = 4 m and u_t approximately 5 m/s.

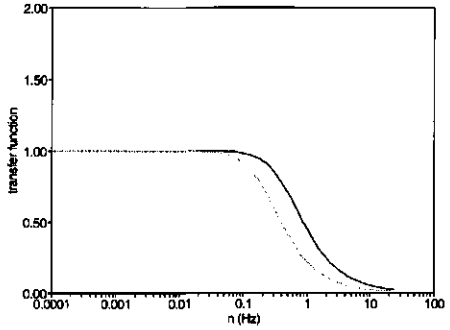

Figure II.3: Example of the sensor response transfer function T_r for n_s = 10 Hz; shown are τ_c = 0.1 s (——) and 0.5 s (·····)

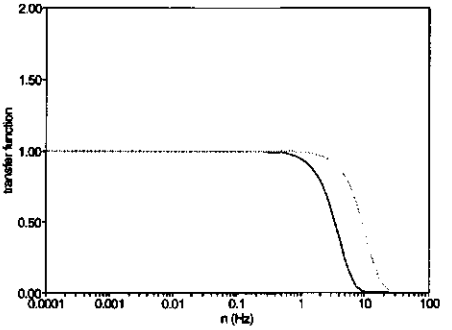

Figure II.4: Example of the tube damping transfer function T_t; shown are eq. II.15 for laminar flow (——) and eq. II.16 for turbulent flow (·····). In both cases n_s = 10 Hz, l = 4 m, r_t = 0.0015 m, u_t = 5 m/s and $D = D_0$ = 2.56 10^{-6} m^2/s

Sensor line averaging

In most cases a scalar quantity is measured over a (finite) path length rather than at a single point. The effect of the spatial averaging involved can be described very well by

$$T_p(p) = \frac{1}{2\pi f}\left(3 + \exp(-2\pi f) - 4\,\frac{1-\exp(-2\pi f)}{2\pi f}\right) \qquad \textbf{(II.17)}$$

where f is the normalized frequency $n\,p/u$, p being the averaging distance. Spatial averaging is relevant for all sensors. However, the effect on the temperature measured using a thermocouple is considered small enough to ignore a correction for this. The averaging path for the sonic temperature is equal to that of the vertical wind, and will be discussed hereafter. For the closed-path analyzer the averaging path is determined by the length of the gas chamber (0.15 m).

For the development of eq. II.17 it is assumed that the averaging path is perpendicular to the average mean wind, which is true for each wind direction when the averaging path is oriented vertically. This applied to the configuration of the Lyman-α and thermocouple sensors during EFEDA-I. The Krypton in operation during EFEDA-II, however, was mounted horizontally. Graphical examination of the full formulation of eq. II.17 given by Moore (1986) did not give rise to correct for this (see Figure II.5).

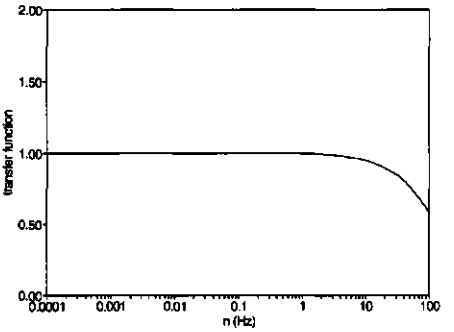

Figure II.5: Example of the transfer function for sensor line averaging for scalars, T_p, for p = 0.025 m and u = 5 m/s

The effect of spatial averaging on measurements of vector quantities is different to that for scalar quantities. Moore (1986) gives a simplified transfer function for the vertical wind component, based on findings of Kaimal *et al.* (1968). The transfer function T_w for averaging the vertical velocity over a path with distance p reads

$$T_w = \frac{2}{\pi f}\left(1 + \frac{\exp(-2\pi f)}{2} - \frac{3\left(1-\exp(-2\pi f)\right)}{4\pi f}\right) \qquad \textbf{(II.18)}$$

For the horizontal wind components a general function as eq. II.18 is not possible to give, since it depends on sensor geometry and wind direction. Two different generalizations were carried out for the two experiments. For EFEDA-II eq. II.18 was adopted for both the scalar and the horizontal wind quantities. The data of EFEDA-I were corrected using the original equations of Kaimal *et al.* (1968) and some assumptions about the instrumental configuration elaborated by Verhoef (priv. communication). For a symmetrical orthogonal set of transducers (as for the Kaijo Denki DAT310 device), the transfer functions were computed for a horizontal wind from a direction of 45° compared to each component. Then the sensor averaging transfer function can be reduced to a single function T_u:

$$T_u = \left(\frac{\sin\pi f}{\pi f}\right)^2 \qquad \textbf{(II.19)}$$

No attempt was made to investigate the assumptions leading to this formulation. For the DAT310 devices p = 0.20 m for all wind components, while p = 0.10 m for the Gill sonic anemometer. Figure II.6 provides an example of T_w and T_u.

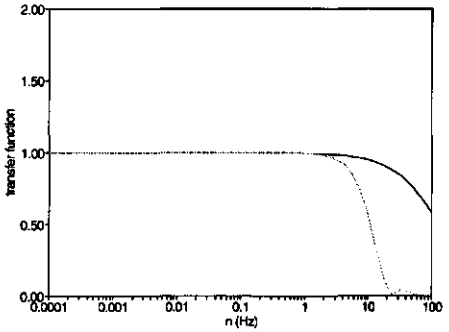

Figure II.6: Example of the transfer function for sensor line averaging for vectors: —— = T_w, ····· = T_u. In both cases p = 0.20 m and u = 5 m/s

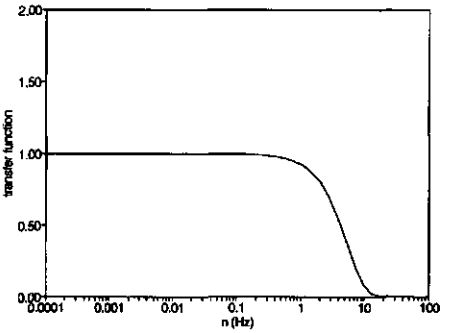

Figure II.7: Example for the sensor separation transfer function T_s for s = 0.20 m and u = 5 m/s

Sensor separation

Ideally, eddy correlation covariances are computed from measurements taken at exactly the same point. In practice, usually a separation between different sensors is necessary. The loss of covariance due to sensor separation is a function of the distance between the sensors and the angle of the wind direction relative to the separation path. For practical purposes Moore (1986) developed a scheme which can be used to correct for both longitudinal and lateral separation, provided that the sensor separation s is small and open to the atmosphere:

$$T_s(f) = \exp\left(-9.9 f^{1.5}\right) \tag{II.20}$$

where f is the normalized frequency, given by $n\,s/u$ (see Figure II.7).

Net transfer functions

The net transfer functions for the several covariances can be found by multiplying the relevant gain functions given above. A net transfer function for the data acquisition system, T_n, can be specified, which applies to all sensors. It is defined by

$$T_n = T_a T_d T_v \tag{II.21}$$

The net transfer functions for the separate variances and covariances depend further on sensor time constant τ_x, averaging path p_x, diffusion coefficient D_x and separation from the w-sensor s_{wx}. The subscript x refers to vertical wind when $x = w$, horizontal wind in both directions for $x = u$, thermocouple temperature for $x = T$, sonic temperature for $x = s$, humidity measured by Lyman-α and Krypton for $x = q$, and humidity and CO_2-concentration measured by the closed path LICOR6262 device for $x = h$ and c, respectively. Then the net transfer functions for the separate variances are given by:

$$\begin{aligned}
T_{uu} &= T_n\, T_{u,v}(p_u)\, T_r^2(\tau_u) \\
T_{ww} &= T_n\, T_w(p_w) \\
T_{TT} &= T_n\, T_r^2(\tau_T) \\
T_{ss} &= T_n\, T_w(p_w) \\
T_{qq} &= T_n\, T_p(p_q) \\
T_{hh} &= T_n\, T_p(p_h)\, T_r^2(\tau_h)\, T_t(D_h) \\
T_{cc} &= T_n\, T_p(p_c)\, T_r^2(\tau_c)\, T_t(D_c)
\end{aligned} \tag{II.22}$$

while the covariance transfer functions read:

$$
\begin{aligned}
T_{uw} &= T_n\ T_r(\tau_u)\ \sqrt{T_w(p_w)\ T_{u,v}(p_u)} \\
T_{wT} &= T_n\ T_s(s_{wT})\ T_r(\tau_T)\ \sqrt{T_w(p_w)} \\
T_{ws} &= T_n\ T_w(p_w) \\
T_{wq} &= T_n\ T_s(s_{wq})\ \sqrt{T_p(p_q)\ T_w(p_w)} \\
T_{wh} &= T_n\ T_s(s_{wh})\ T_r(\tau_h)\ \sqrt{(T_p(p_h)\ T_w(p_w)\ T_t(D_h)} \\
T_{wc} &= T_n\ T_s(s_{wc})\ T_r(\tau_c)\ \sqrt{T_p(p_c)\ T_w(p_w)\ T_t(D_c)}
\end{aligned}
\qquad \text{(II.23)}
$$

Model spectra

For the description of the atmospheric spectra and cospectra the formulations of Kaimal *et al.* (1972) have been used. The formulations provide a description of spectral energy S_{xy} as function of (normalized) frequency $f = n\ z/u$ and stability z/L_v, z being the measuring height. The spectra are derived for the variance of the three wind components and temperature, plus their mutual covariances. Moore (1986) concluded that spectra of the other scalars (humidity and CO_2) resembled the temperature spectra very well, and thus

$$
\begin{aligned}
S_{qq} &= S_{hh} = S_{cc} = S_{TT} \\
S_{wq} &= S_{wh} = S_{wc} = S_{wT}
\end{aligned}
\qquad \text{(II.24)}
$$

Furthermore, the spectra for both horizontal wind components are considered equal as well.

The general function of S_{xx} under *stable conditions* ($z/L_v > 0$) can be represented by

$$
nS_{xx}(n) = \frac{f}{A_x + B_x f^{5/3}} \qquad \text{(II.25)}
$$

where A_x and B_x are functions of the atmospheric stability. Also the cospectra are well reproduced under stable conditions using a general equation:

$$
nS_{wx}(n) = \frac{f}{A_{wx} + B_{wx} f^{2.1}} \qquad \text{(II.26)}
$$

Table II.1 gives the formulations of A_x, B_x, A_{wx} and B_{wx}.

Table II.1: Formulations of A_x, B_x, A_{wx} and B_{wx} for stable (co)variance spectra

Variance spectra	A_x	B_x
$x = w$	$A_w = 0.838 + 1.172\ (z/L_v)$	
$x = u$	$A_u = 0.2\ A_w$	$B_x = 3.124\ A_x^{-2/3}$
$x = T$	$A_T = 0.0961 + 0.644\ (z/L_v)^{0.6}$	
Covariance spectra	A_{wx}	B_{wx}
$x = u$	$0.124\ (1 + 7.9\ z/L_v)^{0.75}$	$2.34\ A_{wx}$
$x = T$	$0.284\ (1 + 6.4\ z/L_v)^{0.75}$	

Unfortunately, the *unstable spectra* are not easily defined, due to a dependence on the boundary layer height z_i. Højstrup (1981) developed suitable expressions for the horizontal and vertical wind velocity:

$$
nS_{ww}(n) = \left(\frac{f}{1 + 5.3 f^{5/3}} + \frac{16 f \xi}{(1 + 17 f)^{5/3}} \right) C_w^{-1} \qquad \text{(II.27)}
$$

and

$$nS_{uu}(n) = \left(\frac{210f}{(1+33f)^{5/3}} + \frac{f\xi}{\zeta + 2.2f^{5/3}} \right) C_u^{-1} \qquad \text{(II.28)}$$

where

$$C_w = 0.7285 + 1.4115\,\xi \qquad C_u = 9.546 + 1.235\xi\zeta^{-2/5}$$

$$\zeta = \left(\frac{z}{z_i} \right)^{5/3} \qquad \xi = \left(\frac{z}{-L_v} \right)^{2/3}$$

Since z_i was not known for most time intervals, a fixed value of 1000 m was chosen, as to represent a typical condition.

No suitable models for atmospheric temperature spectra for unstable conditions are cited in literature. However, Moore (1986) argued that for most conditions the spectra given by Kaimal *et al.* (1972) could be used. For the temperature variance is given

$$nS_{TT}(n) = \begin{cases} \dfrac{14.94f}{(1+24f)^{5/3}} & f < 0.15 \\ \dfrac{6.827f}{(1+12.5f)^{5/3}} & f \geq 0.15 \end{cases} \qquad \text{(II.29)}$$

while the temperature cospectra read

$$nS_{wT}(n) = \begin{cases} \dfrac{12.92f}{(1+26.7f)^{1.375}} & f < 0.54 \\ \dfrac{4.378f}{(1+3.8f)^{2.4}} & f \geq 0.54 \end{cases} \qquad \text{(II.30)}$$

The spectrum of momentum transfer is described by

$$nS_{uw}(n) = \begin{cases} \dfrac{20.78f}{(1+31f)^{1.575}} & f < 0.24 \\ \dfrac{12.66f}{(1+9.6f)^{2.4}} & f \geq 0.24 \end{cases} \qquad \text{(II.31)}$$

During daytime the correction as computed by eq. II.10 was limited to a few percent for all the fast response eddy-correlation sensors. For wind speed measured with cup anemometers the corrections could be as large as 10%, as indicated by McBean (1972). The corrections were considerably larger under stable conditions, as the contribution of high frequencies to the turbulent exchange becomes more significant. However, since the fluxes are then generally small, the absolute significance of the assumptions specified above is not too large.

Based on these theoretical spectra and the transfer functions described above, Figure II.8 gives an example of the net frequency response corrections applied to σ_u^2 and to $\overline{w'T'}$, for a specified height and wind speed.

■ **Various aspects related to fast response measurements**

Apart from the rotation and frequency response corrections some other aspects play a role for the interpretation of the measurements by fast response sensors. We discuss here the quantity actually measured by a cup anemometer, sonic thermometry, and open- and closed path humidity sensors.

Vector averaging of cup anemometers

Since a cup anemometer cannot discern between various wind directions it measures the average vector wind speed $\overline{U}$, rather than the total wind speed in the direction of the average wind,

$\overline{u}$. Bernstein (1967) elaborated a relationship between $\overline{u}$ and $\overline{U}$, which is a function of the standard deviation of the horizontal angle α:

$$\overline{u} = \overline{U} \exp\left(-0.5\,\sigma_\alpha^2\right) \tag{II.32}$$

Van den Hurk and de Bruin (1995) derived expressions for the relationship beteen σ_u and σ_U:

$$\sigma_u \approx \sigma_v \approx \frac{1}{\sqrt{2}} \sqrt{\sigma_U^2 - \overline{U}^2 \left[\exp\left(-0.5\,\sigma_\alpha^2\right) - 1\right]} \tag{II.33}$$

In theory, α must be measured at the same height as the cup anemometer. In practice, however, it is only determined at a single level and assumed to be constant with height over the entire wind profile. Here, σ_α is measured by the sonic anemometer at 4.35 m height during EFEDA-I, and by the wind vane at 10.2 m during EFEDA-II.

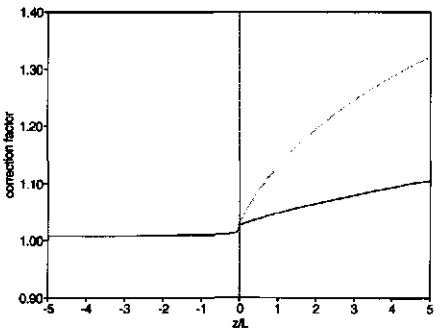

Figure II.8: Example of frequency response corrections as function of z/L_v: —— ΔF_{uw}; ····· ΔF_{wT} Configuration parameters are as follows: z = 10 m, u = 5 m/s, $p_u = p_w$ = 0.20 m, s_{wT} = 0.25 m, τ_c = 0.5 s (thermocouple) and n_s = 10 Hz

Sonic temperature

The temperature obtained by the sonic anemometer (eq. 2.4) needs to be converted to a physical air temperature using the specific humidity. Schotanus *et al.* (1983) have demonstrated that the variance of the sonic temperature and the vertical flux density can be written as

$$\sigma_T^2 = \sigma_{T_{son}}^2 - 1.02\,\overline{T}\,\overline{T'q'} - 0.51^2\,\overline{T}\,\sigma_q^2 - \frac{4\overline{T}^2\overline{u}^2\sigma_u^2}{V_c^4} + \frac{4\,\overline{T}\,\overline{u}\,\overline{u'T'}}{V_c^2} + 2.04\,\frac{\overline{T}^2\overline{u}\,\overline{u'q'}}{V_c^2} \tag{II.34}$$

and

$$\overline{w'T'} = \overline{w'T'_{son}} - 0.51\,\overline{T}\,\overline{w'q'} + 2\,\frac{\overline{T}\,\overline{u}\,\overline{u'w'}}{V_c^2} \tag{II.35}$$

respectively.

During EFEDA-I and EFEDA-II measurements of the open path hygrometer (Lyman-α and Krypton) mounted near the sonic anemometer were used to obtain q. In particular for the systems 1, 3 and 4 in use during EFEDA-I this value is doubtfull and likely too low. During EFEDA-II, comparisons between psychrometer and Krypton results showed that the Krypton gave very reliable values of q. Furthermore, the correction to the variance of the sonic temperature was limited to the first three terms on the right-hand side of eq. II.34.

Webb-correction

As pointed out by Webb *et al.* (1980), the average vertical velocity $\overline{w}$ is unequal to zero when there is a sensible heat flux between the surface and the atmosphere. The vertical flux density of dry air can be written as

$$\overline{w\rho_a} = \overline{w}\,\overline{\rho_a} + \overline{w'\rho_a'} = 0 \tag{II.36}$$

Since according to the Boussinesq approximation

$$\frac{\rho_a'}{\overline{\rho_a}} \approx -\frac{T'}{\overline{T}} \tag{II.37}$$

the average vertical velocity can be obtained from eq. II.36 and is given by $\overline{w'T'} / \overline{T}$.

This mean vertical wind affects the turbulent flux density F_c of any scalar density ρ_c, given by

$$F_c = \overline{w}\,\overline{\rho_c} + \overline{w'\rho_c'} = \frac{\overline{\rho_c}}{\overline{T}}\overline{w'T'} + \overline{w'\rho_c'} \tag{II.38}$$

This so-called Webb-correction applies to any scalar whose density rather than its mixing ratio $r = \rho_c/\rho_a$ is measured. It can be shown that $\overline{\rho_a}\,\overline{w'r'}$ is approximately equal to F_c, in which case the Webb-correction disappears.

The situation is a little more complicated for air mixtures, as moist air. Considering the air as a mixture of dry air and water vapour with density ρ_v, the mean vertical wind velocity is given by

$$\overline{w} = \frac{m_a}{m_v}\frac{\overline{w'\rho_v'}}{\overline{\rho_a}} + \left(1 + \frac{\overline{\rho_v}}{\overline{\rho_a}}\frac{m_a}{m_v}\right)\frac{\overline{w'T'}}{\overline{T}} \tag{II.39}$$

which implies for F_c

$$F_c = \overline{w}\,\overline{\rho_c} + \overline{w'\rho_c'} = \frac{m_a}{m_v}\frac{\overline{w'\rho_v'}}{\overline{\rho_a}}\overline{\rho_c} + \left(1 + \frac{\overline{\rho_v}}{\overline{\rho_a}}\frac{m_a}{m_v}\right)\frac{\overline{w'T'}}{\overline{T}}\overline{\rho_c} + \overline{w'\rho_c'} \tag{II.40}$$

For water vapour $\rho_c = \rho_v$, and eq. II.40 can be rewritten as

$$F_v = \left(1 + \frac{m_a}{m_v}\frac{\overline{\rho_v}}{\overline{\rho_a}}\right)\left(\overline{w'\rho_v'} + \frac{\overline{\rho_v}}{\overline{T}}\overline{w'T'}\right) \tag{II.41}$$

The Webb-correction applicable to open path sensors can be as large as several tens of percents, depending on the sensible heat flux density. Leuning and Moncreiff (1990) show that the Webb-correction for a closed- path system as the LICOR6262 is limited to a few percent by bringing the sampled air to a common temperature. By this procedure a major part of the correction associated with the sensible heat flux density (equal to $(1 / \overline{T})\,\overline{\rho_c}\,\overline{w'T'}$) vanishes. This gives

$$F_c = \frac{m_a}{m_v}\frac{\overline{w'\rho_v'}}{\overline{\rho_a}}\overline{\rho_c} + \left(\frac{\overline{\rho_v}}{\overline{\rho_a}}\frac{m_a}{m_v}\right)\frac{\overline{w'T'}}{\overline{T}}\overline{\rho_c} + \overline{w'\rho_c'} \tag{II.42}$$

and

$$F_v = \left(1 + \frac{m_a}{m_v}\frac{\overline{\rho_v}}{\overline{\rho_a}}\right)\overline{w'\rho_v'} \tag{II.43}$$

for the LICOR6262 CO_2 and water vapour flux, respectively. However, an extra correction accounting for the different temperature and air pressure in the chamber compared to outside conditions has to be introduced. This correction is automatically carried out by the LICOR device.

LICOR signal delay

The closed path LICOR6262 sensor detects gas concentrations in air, after a transport through a

sampling tube. This transport takes some time (in the order of 2 s for 4 m tube). For the EFEDA-II data the delayed signals of ρ_v and ρ_c measured by the LICOR626 device were shifted in time. The time interval was defined as the time delay for which the covariances $\overline{\rho_v' T_{son}'}$ and $\overline{\rho_c' T_{son}'}$ were maximal (McMillen, 1988).

Oxygen absorption by Lyman-α and Krypton

The instrument response of the Lyman-α and Krypton humidiometers, given by eq. 2.5, is based on the assumption that water vapour is the only gas absorbing light at the monochromatic wavelength being detected. However, in practice some other gases (in particular oxygen and ozone) are not entirely transparent at the Lyman-α and Krypton wavelengths. Particularly the contribution of oxygen is of interest, as it is present in much higher concentrations than water vapour. For the present analysis we ignore other gases than oxygen.

A more general formulation of eq. 2.5 includes the contribution of other gases to light absorption:

$$I = I_0 \exp\left(-d_s \sum \frac{k_i \rho_i}{\rho_{i0}}\right) \tag{II.44}$$

where k_i is an absorption coefficient of gas i at standard pressure, and the received light is assumed to be monochromatic. The humidity fluctuations ρ_v' measured by a Lyman-α or Krypton can be expressed as function of the signal fluctuations linearized around the mean signal (see section 2.2.4). Then it can be shown that

$$\rho_v' = -\frac{I'}{d\, k_v \overline{I}} - \frac{k_o}{k_v} \rho_o' \tag{II.45}$$

where the subscript o refers to the oxygen concentration and absorption coefficient. Referring to eq. II.37, the oxygen concentration fluctuations can be approximated by

$$\rho_o' \approx -\frac{C_o m_o p}{R \overline{T}^2} T' \tag{II.46}$$

where C_o is the relative concentration of oxygen (21%) and m_o its molecular weight. This yields for the latent heat flux density an expression where the oxygen contamination is represented by a sensible heat flux density:

$$\overline{w' \rho_v'} = -\frac{\overline{w' I'}}{d\, k_v \overline{I}} + \frac{C_o m_o p}{R \overline{T}^2} \frac{k_o}{k_v} \overline{w' T'} \tag{II.47}$$

For a Krypton KH20 hygrometer $k_v = 0.143$ and $k_o = 0.0085$. The absorption coefficients at Lyman-α are a little more favourable for the detection of water vapour: $k_v = 0.481$ and $k_o = 0.00049$. All these coefficients are slightly temperature dependent. Only the value of k_o for the Krypton wavelength gives rise to carry out a correction according to eq. II.47.

3 Surface temperature and radiometer corrections

- **Surface temperature**

The radiometric surface temperature is obtained from the measurement of longwave radiation in the range 8 - 14 μm emitted by a surface. The relationship between body temperature and measured radiation depends on the radiation frequency range and surface emissivity. The total radiation emitted by a black body of temperature T is given by σT^4, where $\sigma = 5.67\ 10^{-8}$ is the Stefan-Bolzman constant. However, the radiation emitted in a limited frequency range deviates from this law, and can be approximated by aT^b. Around $\lambda = 12$ μm $b \approx 4$, but for the range 8 - 14 μm $a = 1.25\ 10^{-9}$ and $b = 4.5$.

In the longwave frequency range many surfaces don't behave as a black body. This implies that the total amount of emitted radiation is less than σT^4, and this is usually expressed using an effective emissivity ε, defined as

$$\varepsilon = \frac{\int_0^\infty \varepsilon(\lambda) M_\lambda \, d\lambda}{\sigma T^4} \qquad \text{(II.48)}$$

where M_λ is the emittance of the body at wave length λ. Most radiative temperature sensors include a correction for an emissivity < 1. However, downward radiation reaching a surface is partially reflected when $\varepsilon \neq 1$, and observed by the radiation sensor. An expression for the correct surface temperature T_s as function of the measured value $T_{s,m}$ and the surface emissivity assumed by the sensor ε_T is given by

$$T_s = \left(\frac{\varepsilon_T a T_{s,m}^b - (1 - \varepsilon) L_{8-14}^{\downarrow}}{\varepsilon a} \right)^{1/b} \qquad \text{(II.49)}$$

where $L_{8-14}^{\downarrow}$ is the downward radiation in the wave length length range 8 - 14 μm. For EFEDA-I we assumed $\varepsilon = 0.993$ for the plants, 0.973 for the bare soil and 0.98 for the surface seen by the high sensor (Bolle and Streckenbach, 1992). The sensor emissivity was kept at unity for all sensors. $L_{8-14}^{\downarrow}$ is usually not measured directly. Here, we used the semi-empirical expression developed by Idso (1981), reading

$$L_{8-14}^{\downarrow} = \left[0.24 + 2.98\,10^{-8} e_a^2 \exp\left(\frac{3000}{T_a} \right) \right] \sigma T_a^4 + 60\,C \qquad \text{(II.50)}$$

where e_a is the vapour pressure at reference height, specified in mb, T_a the air temperature, and C the cloud cover. In practice, $L_{8-14}^{\downarrow}$ as given by eq. II.50 is about 40% of the total incoming longwave radiation.

- **Obtaining temperature of separate surface components from cable temperature**

The temperature measured by the sensors running over the two horizontal cables were corrected for emissivity and reflection as indicated above. Moreover, some strategy was developed to derive the bare soil temperature, the plant temperature and a weighted average of these from their results.

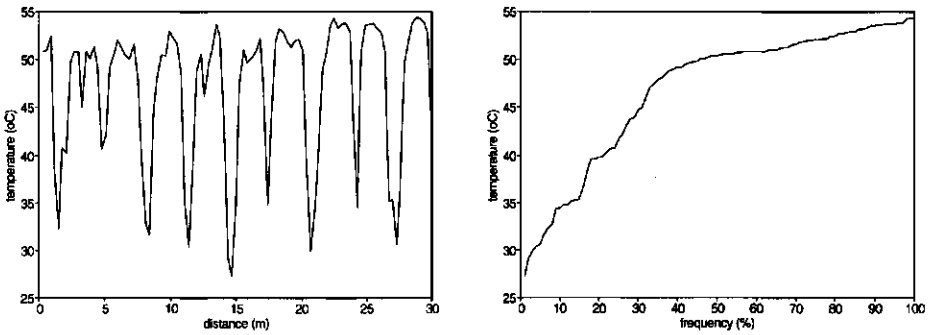

Figure II.9: Time series of surface temperature measurement from the low cable, DOY 163, 14:10 GMT. Shown left is the observed temperature series, and right the cumulative frequency distribution.

A common temperature signal measured by the low cable during daytime is shown in Figure II.9. The difference between the cool plants and warm soil is clearly seen. The cumulative frequency distribution is shown as well. For each time slot the average bare soil temperature was defined as the 95% percentile value of this cumulative distribution. A percentile value < 100% was chosen, in order to ignore incidental high extremes. The exact choice of the percentile value is rather insignificant for the bare soil temperature, as can be seen from Figure II.9. The cool end of the distribution shows a much steeper slope, caused by the partial transparency of the plants. A quite arbitrary 5% percentile

value was chosen as to define the plant temperature of the sample.

A weighted average of the surface temperature was found by relating each temperature reading from Figure II.9 to an effective area. From a set of figures equivalent to Figure II.9 an estimation was made of the position and radius of the plants underneath the cable. These dimensions were found around day 20, and plant growth was not taken into account. The effective area a_i of each measurement position within the radius of a plant was considered to be equal to half an arc with width equal to the distance between two measurements (see Figure II.10). Temperatures outside the radius of the plant were regarded to be representative for the bare soil area between the plants and equally weighted. The average surface temperature T_{sur} was thus defined by

$$T_{sur} = \frac{\sum T_{s,i} a_i}{\sum a_i} \qquad \text{(II.51)}$$

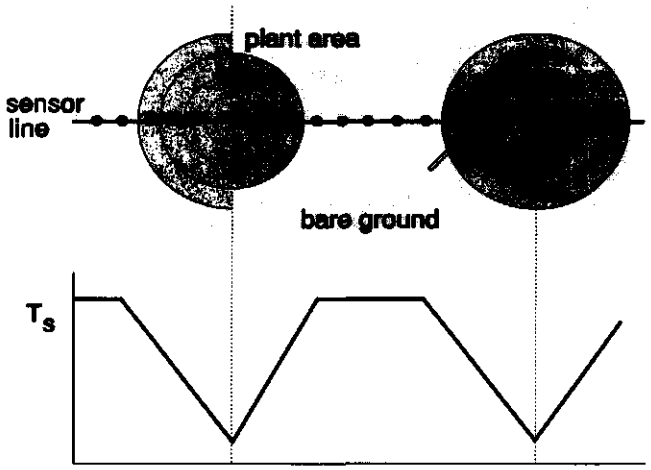

Figure II.10: Schematic representation of representative area per surface temperature sample, indicated by the heavy dots on the sensor line. The shaded plant area represents the area a_i representative for the measurement point indicated by the arrow. The lowest panel shows a schematic record of the measured surface temperature

- **Shading of incoming shortwave and diffuse radiometer**

The incoming radiation sensor applied in EFEDA-II was shaded by the mast early in the morning. Data in the time slots where this occured were replaced by linear interpolations of the neighbouring time slots. Due to the virtual absence of clouds at all days this procedure could be applied safely, and was estimated to give an error of less than 5%, valid for low values of $K^{\downarrow}$. The sensor detecting reflected shortwave radiation in this experiment received a considerable amount of radiation reflected by the mast at about 15 GMT each day. This was corrected for by reducing $K^{\uparrow}$ at this time by a fixed percentage, which was also obtained from the interpolation of neighbouring time slots, measured at several cloud-free days spread over the whole period.

The diffuse radiation was increased by 12% to account for the hemispherical radiation blocked by the shadow ring, following the instructions in the shadowring manual.

- **Difference between longwave and shortwave sensitivity of net radiometers**

The longwave radiation measured by the allwave Schülze-Däke sensor applied in EFEDA-II can be corrected for the difference of sensor sensitivity to short- and longwave radiation. When the incident shortwave radiation is known (measured separately) the corrected longwave radiation is given by

$$L^{\downarrow} = x_l V - \frac{x_l}{x_s} K^{\downarrow} + \varepsilon_b \sigma T_b^4 \qquad \text{(II.52)}$$

where V is the voltage measured, x_l and x_s the gains for longwave and shortwave radiation respectively, and ε_b the body emissivity, which is assumed to be unity here.

4 Soil heat flux density corrections

The soil heat flux density measured using soil heat flux plates is subject to three major sources of error: a non-ideal heat transfer to and through the plate, heat storage in the soil layer above the plate, and ignoring energy transported across the heat flux plate as latent heat.

Non-ideal heat transfer is associated with a poor contact between the soil plate and the surrounding medium, and a difference between the heat conductivity of the plate and that of the soil. A correction factor c_λ for the conductivity difference is given by (Philip, 1961)

$$c_\lambda = 1 - \alpha_p \frac{d_p}{\sqrt{A_p}} \left(1 - \frac{\lambda_T}{\lambda_p} \right) \qquad \text{(II.53)}$$

where α_p is a factor depending on the shape of the heat flux plate (equal to $0.5\pi(8/3\pi)^{-0.5} = 1.70$ for circular plates), d_p the thickness of the plate (≈ 4 mm) and A_p the areal surface (177 cm^2). The soil heat conductivity λ_T was estimated as discussed in section 2.2.5. The conductivity of the plates λ_p was given by the manufacturer. No correction was carried out to account for the poor contact between the sensor and the soil.

The heat storage above the plates was computed similar to the determination of the soil heat flux density by the caloric method (eq. 2.18), where obviously only the change of heat content in the layer between the surface and the installation depth of the sensors is considered. This correction can modify the measured fluxes by more than 100 W/m^2.

For the soil heat flux density computed from the caloric method the temperature rise at the deepest level gives rise to uncertainties in the calculated fluxes. The temperature at 50 cm showed a significant rise during the measurement campaign, and the zero-flux condition at the lower boundary is thus not met. Since no direct measurement of the soil heat flux density at a depth of 50 cm were carried out, no correction could be applied for this.

For each layer and each measuring day $\rho' C_h$ was computed using eq. 2.21. For practical purposes the value of $\rho' C_h$ linearly increased with depth from 10 cm onwards. Also, a linear regression was carried out to account for the temporal change at all levels (see section 2.4.4 for details).

Upward latent heat transfer across the plate may lead to an overestimation of G. This transfer may take place when evaporation occurs below the heat flux plate (Mayocchi and Bristow, 1995). This effect was ignored in the present study.

Appendix III: The bulk leaf boundary-layer resistance

The leaf boundary-layer resistance r_b is the resistance encountered by a scalar when it is transported from the leaf to the ambient air, or the other way round. The resistance describes the transport through a thin laminar sublayer immediately surrounding the leaf. This layer is an internal boundary layer, caused by the wind blowing over the leaf. The thickness of this layer therefore depends on the drag forces exerted on the leaf (wind speed) and on the typical size of the leaf. For small leaves, the laminar boundary layer has no chance to develop when the leaf is exposed to wind, and the leaf boundary resistance will therefore be smaller. In general the leaf boundary resistance is given by the semi-empirical expression

$$r_b = a\sqrt{\frac{l_w}{u(z)}} \qquad \text{(III.1)}$$

The coefficient a is not dimensionless, and holds for l_w expressed in m and u in m/s.

The coefficient is obtained by analysis of dimensionless quantities governing the flow through the laminar sublayer surrounding the leaf. It is valid under the following assumptions:

- the flow in a small layer just over the leaf is laminar. Then the Nusselt number Nu, which defines the ratio of the thickness of the laminar sublayer δ to the characteristic size of the leaf l_w, is a function of the square root of the Reynolds number Re, defined by $u\,l_w/\nu$, with ν the kinematic molecular viscosity
- the temperature is uniformly distributed over the leaf. In this case, Nu can be expressed according to

$$Nu = \frac{l_w}{\delta} = 0.66\,Pr^{0.33}\,Re^{0.5} \qquad \text{(III.2)}$$

  where Pr is the Prandtl number, defined by the ratio of the viscosity and thermal diffusivity of dry air (equal to ± 0.71)
- the exchange of heat occurs at two sides of a leaf
- an excess conductance is caused by buoyancy effects and extra generation of turbulence at the curled edge of the leaf, causing an increase of the coefficient in eq. III.2 to ± 1.08.
- no additional corrections are applied to account for mutual sheltering by leaves (see section 3.2.3)

Under these assumptions eq. III.1 can be obtained by solving the equation

$$\frac{H}{\Delta T} = \frac{\rho c_p}{r_b} = \frac{\lambda_a}{l_w}\left(\frac{l_w}{\delta}\right) \qquad \text{(III.3)}$$

where λ_a is the thermal conductivity of air.

The total resistance of a layer of leaves is inversely proportional to the total leaf area in that layer dL, expressed by

$$r_b(\mathrm{d}L) = \frac{r_b}{\mathrm{d}L} \qquad \text{(III.4)}$$

The leaf boundary resistance will generally be a function of height, due to the dependence on dL and

$u(z)$. Therefore, in cases where a vertical canopy has to be condensed to a virtual source at a single level, a proper vertical average value for r_b must be obtained. This averaging procedure is quite straightforward for cases where profiles of $u(z)$ and dL are known. In that case the total boundary resistance valid for a canopy is obtained by an inversed addition of all resistances in each layer, when these resistances may be thought to be connected in parallel. For infinitly thin layers, the bulk leaf boundary-layer layer resistance r_a^c is given by

$$\frac{1}{r_a^c} = \frac{1}{\overline{r_b}} = \frac{\int_0^h \frac{LAD(z)}{r_b(z)} dz}{LAI} \qquad \text{(III.5)}$$

where $LAD(z)$ is the leaf area density at height z. The integral is taken over height z rather than over total leaf area LAI, to express the functional dependence of r_b on $u(z)$.

For larger scale approximations the detailed information about $LAD(z)$ and $u(z)$ is generally not available. Therefore, some approximation to eq. III.5 is required. Here, the integrated resistance is computed for a large range of canopy structures and wind profiles. The computed resistances are then expressed in terms of the parameters which are assumed available, i.e. the friction velocity u_*, the characteristic leaf size l_w, and the total leaf area LAI.

The within canopy *wind profile* is assumed to obey an exponential decay:

$$u(z) = u(h) \exp\left(1 - \alpha_u \frac{z}{h}\right) \qquad \text{(III.6)}$$

where $u(h)$ is the wind speed at canopy height h, and α_u is an extinction coefficient, depending on the canopy structure, plant spacing etc. A value of 2.5 - 3 is often taken for agricultural crops. The wind speed at $z = h$ is evaluated using the adiabatic logarithmic wind profile:

$$u(h) = \frac{u*}{\kappa} \ln\left(\frac{h - d}{z_{0m}}\right) \qquad \text{(III.7)}$$

In order to give a general expression for eq. III.5, d and z_{0m} are assumed to be a fixed portion of the canopy height, i.e., $d/h = 0.63$, and $z_{0m}/h = 0.13$.

The *distribution of leaves* with height was simulated using a Beta-distribution, given by

$$\beta(x) = \frac{(p + q - 1)!\, x^{p-1} (1 - x)^{q-1}}{(p - 1)!\, (q - 1)!} \qquad \text{(III.8)}$$

in which two integer parameters p and q determine the shape and the value of x where $\beta(x)$ is maximum. The Beta-distribution resembles the Poisson distribution, but its integrated value in the range [0 - 1] is always unity.

Eq. III.5 was evaluated with a great range of parameters. The friction velocity u_* varied from 0.05 to 0.8 m/s, LAI from 0.1 to 3.5, l_w from 0.01 to 0.2 m, and α_u from 1.5 to 3.5. The Beta-distribution was varied using $p = 2$, 4 and 6, and keeping q constant at 2. $p = 2$ corresponds to an almost hemispherical distribution with the maximum leaf area at $z/h = 0.5$, whereas $p = 6$ shows a maximum LAI at $z/h = 0.83$. A total of 432 cases was surveyed.

The best fit of this sample on eq. III.1 was obtained by adopting

$$\overline{r_b} = 97 \frac{\sqrt{\frac{l_w}{u*}}}{LAI} \qquad \text{(III.9)}$$

For the set of variables used here the correlation coefficient was 0.95.

The formulation corresponds best with $p = 4$ and $\alpha_u = 2.5$. For $p = 2$ eq. III.9 underestimates the analytical integration by ± 12%, whereas for $p = 6$ it is overestimated by this amount. For the latter case the integrated resistance is reduced by the convolution of high leaf area densities and high wind speeds near the top of the canopy. When the different leaf area distributions are distinguished, and the factor preceding eq. III.9 is changed accordingly, the correlation coefficient is as large as 0.999 for all cases.

Appendix IV: The photosynthesis model at the leaf scale and calculation of ambient conditions

Using eq. 3.33 the leaf stomatal conductance for water vapour transfer, g_s, can be defined as the ratio of net assimilation rate A_n and concentration difference $C_s - C_i$:

$$g_s = 1.6 \frac{A_n}{C_s - C_i} \tag{IV.1}$$

provided that the cuticular conductance can be ignored, as was assumed here. Additional models for A_n and C_i/C_s are necessary to complete eq. IV.1.

At low radiation levels the net assimilation rate A_n can be regarded as a linear function of the light intensity:

$$A_n = \varepsilon_i I_a - R_d \tag{IV.2}$$

where I_a is the intensity of the intercepted PAR, R_d the dark respiration and ε_i the initial quantum use efficiency. At high light intensities A_n approaches an asymptotic value, A_m. In these conditions, the CO_2-concentration is the limiting factor for photosynthesis. An empirical asymptotic exponential function, as proposed by Goudriaan *et al.* (1985), is used to describe A_n at both low and high light intensities, thereby including the limiting effect of both light and CO_2:

$$A_n = (A_m + R_d)\left\{1 - \exp\left(\frac{-\varepsilon_i I_a}{A_m + R_d}\right)\right\} - R_d \tag{IV.3}$$

The initial quantum use efficiency ε_i is affected by photorespiration, and may be calculated as (Goudriaan *et al.*, 1985)

$$\varepsilon_i = \varepsilon_0 \frac{C_s - \Gamma}{C_s + 2\Gamma} \tag{IV.4}$$

where ε_0 is a maximum efficiency (= 0.017 mg/J PAR for C3 plants), and Γ is the CO_2 compensation concentration, being the equilibrium CO_2-concentration which is achieved when an illuminated leaf is placed in a closed chamber. The gross assimilation is then balanced by the respiration processes, and net photosynthetic rate A_n will be zero. Γ is mainly affected by the photorespiration and approaches 0 for C4 plants. For C3 plants under the current O_2-concentration it depends mainly on leaf temperature T_l. This dependence can be described using a Q_{10}-response function, according to

$$\Gamma = \Gamma(25)\, Q_{10}^{\left(\frac{T_l - 25}{10}\right)} \qquad \text{(IV.5)}$$

where $\Gamma(25)$ is the value of Γ at $T_l = 25°C$, equal to 45 μmol/mol for C3 plants. Q_{10} is taken 1.5 for Γ.

At low values of C_i, A_m is linearly related to the CO_2-concentration according to

$$A_m = (C_i - \Gamma)\, g_m \qquad \text{(IV.6)}$$

where g_m is the mesophyll conductance. At higher values of C_i, A_m is asymptotically bounded by a maximum rate, $A_{m,max}$, related to the ability of plants to allocate the products of the photosynthesis process. A_m is taken as

$$A_m = A_{m,\max}\left\{1 - \exp\left(\frac{-g_m(C_i - \Gamma)}{A_{m,\max}}\right)\right\} \qquad \text{(IV.7)}$$

An expression for $A_{m,max}$ as function of leaf temperature applicable to *Vitis Vinifera* was expressed following Collatz *et al.* (1992), reading

$$A_{m,\max} = \frac{A_{m,\max}(25)\, Q_{10}^{\left(\frac{T_l - 25}{10}\right)}}{\left\{1 + \exp\left(0.3\,(T_1 - T_l)\right)\right\}\left\{1 + \exp\left(0.3(T_l - T_2)\right)\right\}} \qquad \text{(IV.8)}$$

where $A_{m,max}(25) = 2.2$ mg/m^{2}s, $Q_{10} = 2$, and T_1 and T_2 are reference temperatures, taken in this study as 15 and 42°C, respectively (Jacobs, 1994). R_d is estimated as $A_m/9$ (Van Heemst, 1986).

The mesophyll conductance g_m can be derived from the light saturated rate of photosynthesis. g_m can be expressed using a function equivalent to eq. IV.8, with $g_m(25) = 2$ mm/s, $Q_{10} = 2$, $T_1 = 0°C$ and $T_2 = 42°C$, respectively (Jacobs, 1994).

Goudriaan *et al.* (1985) observed a fairly conservative ratio of C_i/C_s. A slightly modified ratio, f, is used to compute $C_s - C_i$:

$$\frac{C_i - \Gamma}{C_s - \Gamma} = f \qquad \text{(IV.9)}$$

Note that using eq. IV.9 $C_i/C_s \rightarrow 1$ as $A_n \rightarrow 0$. f may be fairly conservative, with a value of 0.7 for C3 plants (Goudriaan *et al.*, 1985).

Jacobs (1994) incorporated an effect of air humidity on g_s by assuming that f is a linear function of the ambient humidity deficit, D_s:

$$f = f_0\left(1 - \frac{D_s}{D_{\max}}\right) \qquad \text{(IV.10)}$$

where a minimum assimilation rate, corresponding to a situation where stomata are fully closed but CO_2 is supplied through cuticular conductance, is ignored. For the present species, Jacobs (1994) found $D_{max} = 58.2$ g/kg and $f_0 = 0.916$. In this study the value of f was not allowed to exceed a maximum value of 0.85, taking the average of the range 0.8 - 0.9 reported by Morison and Gifford (1983). The modification caused a typical maximum value of g_s^0 (full sunshine, leaf temperature below 35°C) to be about 20 mm/s rather than 30 mm/s without constraint. This latter value is rather high compared to values reported by for instance Choudhury and Monteith (1986), which justifies this modification. The values of the calibration coefficients in eqs. 3.36 and 3.37 partially depend on the maximum value for f.

According to eqs. IV.9 and IV.10, C_i will never exceed C_s. This implies that application of eq. IV.10 together with eq. IV.1 can yield negative conductance values, because A_n becomes negative as

$I_a \rightarrow 0$ due to dark respiration (see eq. IV.3). In practice the correlation between A_n and g_s is difficult to establish under conditions of low assimilation rates, since the CO_2 concentration gradient will likely be very small. In this study g_s was simply assumed to be zero when $A_n < 0$.

The value of the specific humidity deficit at the leaf scale, D_s, was obtained by extrapolating the deficit profile to a hypothetical source level at $z_{0m} + d$. A specific humidity at leaf level, q_c, is obtained according to

$$q_c = q_a + \frac{E}{\rho}\left(r_a + r_a^c\right) \qquad \textbf{(IV.11)}$$

where E is the measured evaporation rate above the canopy, r_a given by u_a/u_*^2, and r_a^c parameterized according to eq. III.9. A humidity deficit was calculated separately for shaded and sunlit leaves, by taking the measured average leaf temperature in each light category to specify q_{sat}.

The amount of absorbed PAR, I_a, was calculated according to eqs. 3.39 and 3.40 for shaded and sunlit leaves, respectively.

Appendix V: Numerical aspects of the SVAT-models

The computer program in which the coupled SVAT-PBL models were coded consisted of two modules: the PBL- and the SVAT-module. The coupling was carried out at the level z_R, which united the lowest PBL-gridpoint and the reference height of the SVAT's. During each time step first the SVAT-module computed the surface fluxes, followed by a calculation of the PBL-profiles and -height by the PBL-module, generating a new reference temperature, specific humidity and wind speed at z_R.

The SVAT-module contains various parameterizations, as outlined in section 4.1. This appendix describes the program flow of the SVAT-module, for each of the cases described in chapter 6.

- **The reference model**

The sequence of steps to solve the surface energy balance in the reference model closely follows the suggestions made by Deardorff (1978), and is as follows:

1 specify the crop resistance, using environmental variables at canopy height of the previous timestep
2 compute aerodynamic resistance above canopy ($r_a{}^a$) and u_* iteratively from u_a and $\theta_a - \theta_0$, with θ_0 from the previous time- or iteration step. Calculate the aerodynamic resistance to the soil surface ($r_a{}^s$) and to the canopy surface ($r_a{}^c$)
3 calculate q_s
4 compute new value of θ_0 and q_0
5 calculate leaf temperature θ_c, specific humidity q_c, and canopy evaporation fraction ξ from radiative input and θ_0 and q_0
6 update q_0 and repeat step 5 until convergence of θ_c
7 calculate canopy and soil fluxes, and repeat from step 2 onwards until convergence of $r_a{}^a$
8 compute a new value of w_{dew}
9 calculate surface and deep soil temperature from G using the force-restore scheme
10 calculate surface and deep soil moisture content from λE_s and λE_c using the force-restore scheme

- **The case 'big leaf'**

For the case 'big leaf' the program flow is slightly different than the reference model:

1 as in the reference model
2 calculate $r_a{}^a$ as in the reference model, but with θ_0 equal to the temperature extrapolated to z_{0m}
3 open Newton-Raphson iteration for T_{sur} according to

$$T_{sur} = T_{sur}^p - \frac{Q_* - G - \rho\lambda\dfrac{(q_{sur} - q_a)}{r_a + r_s^c} + \rho c_p \dfrac{(\theta_{sur} - \theta_a)}{r_a}}{-4\varepsilon\sigma T_{sur}^3 - 2C\sqrt{\pi}\left(\dfrac{1}{\Delta t} + \dfrac{2\pi}{\tau_1}\right) - \rho\lambda\dfrac{s}{r_a + r_s^c} + \rho c_p \dfrac{(p/p_0)^{0.286}}{r_a}} \qquad \text{(V.1)}$$

where $T_{sur}^p = T_{sur}$ from the previous timestep, and $C = \rho' C_h d_1$. r_a, Q_*, G and C are given by eqs. 4.4, 4.7, 4.8 and 4.48, respectively. Use is made of the linearization of $T_{sur}{}^4$ to $4(T_{sur}^p)^3 (T_{sur} - T_{sur}^p)$, estimating $q_{sat}(T_{sur})$ by $q_{sat}(T_{sur}^p) + s(T_{sur} - T_{sur}^p)$, and discretizing $\partial T_{sur}/\partial t$ as $(T_{sur} - T_{sur}^p)/\Delta t$.

4 repeat steps 2 and 3 until convergence of r_a^a
5 compute surface fluxes from final values of T_{sur} and r_a^a
6 calculate surface and deep soil temperature from G using the force-restore scheme
7 calculate surface and deep soil moisture content from λE using the force-restore scheme, taking $\lambda E_s = 0$

■ **The case 'isotherm'**

The numerical scheme in the case 'isotherm' resembles the 'big leaf' case, in that they both solve the energy balance equation for the surface temperature. The numerical scheme reads:

1 as in the reference model
2 specify the fraction of surface covered by the skin reservoir, C_l
3 calculate r_a^a as in the case 'big leaf'
4 solve for T_{sk} by rewriting a modified version of eq. 4.15 in terms of T_{sk}, and linearizing T_{sk}^4, $\partial T_{sk}/\partial t$ and s using T_{sk} from the previous time- or iteration step. The modification consists of replacing the expression for the soil heat flux (eq. 4.14) by the force-restore expressions, as applied in the case 'big leaf' (eq. 4.8).
5 repeat steps 3 and 4 until convergence of H
6 compute surface fluxes from final value of T_{sk} and r_a^a, using the explicit values of C_l and σ_f
7 calculate surface and deep soil temperature from G using the force-restore scheme
8 calculate surface and deep soil moisture content from λE_s and λE_c, using the force-restore scheme

■ **The case '3 fracs'**

The case '3 fracs' is similar to the previous case, except that the skin temperature is established for each surface fraction separately. The final scheme is given by:

1-2 as in the case 'isotherm'
3-6 as in the case 'isotherm' by taking $C_l = 0$ and $\sigma_f = 0$ (soil only)
7 as 3-6 by taking $C_l = 0$ and $\sigma_f = 1$ (vegetation only)
8 as 3-6 by taking $C_l = 1$ (skin reservoir only)
9 compute the average surface fluxes Q_*, H, λE and G by weighing the fluxes from steps 3-8 as in eq. 4.18
10 calculate an average skin temperature and friction velocity according to the same procedure
11 calculate surface and deep soil temperature from G using the force-restore scheme
12 calculate surface and deep soil moisture content from λE_s and λE_c, using the force-restore scheme

■ **The case 'aero D78'**

The case 'aero D78' is almost equal to the reference case. The only difference is the formulation of r_a^s and r_a^c in step 2.

■ **The case 'aero MH95'**

The numerical scheme in 'aero MH95' also resembles the reference model:

1 as in the reference model
2 compute u_* from u_a and a dimensionless far-field resistor, $\Re_a^a$. Since $\Re_a^a$ corresponds to a reference height of $2h$, it is not equal to the total resistance between z_{0m} and z_R. An extra resistance including a stability correction Ψ_h is applied for the range between $2h$ and z_R:

$$u_* = \frac{u_a}{\Re_a^a + \frac{1}{\kappa}\left[\ln\left(\frac{z_R}{2h}\right) - \Psi_h\left(\frac{z_R}{L_v}\right) + \Psi_h\left(\frac{2h}{L_v}\right)\right]} \qquad \text{(V.2)}$$

with L_v from the previous time step. This implies a stability correction between $2h$ and z_R, but not below $2h$. Calculate the aerodynamic resistances r_a^a, r_a^c, r_a^s and r_n from u_* and the dimensionless resistance coefficients. The resistances are equal for heat and moisture transfer, and r_a^a and r_a^s are computed using the flux partitioning of sensible heat. r_n is incorporated by adding its value to r_a^c
3-10 as in the reference model

- **The cases 'r_c CO_2', 'r_c VB95' and 'r_c fix'**

The numerical sequence of the cases 'r_c CO_2', 'r_c VB95' and 'r_c fix' are equal to the reference model. The ambient conditions used to parameterize the crop resistances are taken from the previous timestep.

- **The case 'r_c big CO_2'**

The case 'r_c big CO_2' is similar to the case 'big leaf'. The humidity deficit is evaluated using the specific humidity at z_{0m} and the average surface temperature.

- **The case 'soil VB95'**

The case 'soil VB95' utilizes a similar numerical scheme as the reference model, except that the steps 9 and 10 are replaced by a solution of the diffusion equations for temperature and soil moisture:

1-8 as in the reference model

9 calculate a new soil temperature profile using a locally implicit scheme (Viterbo and Beljaars, 1995). The diffusion equation (eq. 4.9) is discretized as

$$\rho' C_h \frac{T_i^{n+1} - T_i^n}{\Delta t} = -\frac{G_{i,b} - G_{i,t}}{z_i} \tag{V.3}$$

in which i indicates the spatial coordinate and n the time level. $G_{i,t}$ and $G_{i,b}$ are the heat fluxes at the top and bottom of soil layer i, respectively, discretized as

$$G_{i,b} = -\lambda_{T,i+1/2} \frac{T_{i+1}^n - T_i^{n+1}}{0.5\,(z_i + z_{i+1})} \tag{V.4}$$

$$G_{i,t} = -\lambda_{T,i-1/2} \frac{T_i^{n+1} - T_{i-1}^n}{0.5\,(z_{i-1} + z_i)} \tag{V.5}$$

For λ_T the 'upstream' values are used (see section 4.1.2)

10 calculate C_l

11 specify the root extraction and surface infiltration rate

12 calculate the new soil moisture profile from eq. 4.11 using a global semi-implicit scheme (Viterbo and Beljaars, 1995):

$$\rho_w \frac{\omega_i^{n+1} - \omega_i^n}{\Delta t} = -\frac{F_{i+1/2}^* - F_{i-1/2}^*}{z_i} + \rho_w S_{\omega,i} \tag{V.6}$$

where the moisture fluxes F^* are given by

$$F_{i+1/2}^* = -\rho_w \left[\lambda_{H,i+1/2} \frac{\omega_{i+1}^* - \omega_i^*}{0.5\,(z_i + z_{i+1})} - \gamma_{H,i+1/2} \right] \tag{V.7}$$

and the moisture content is made implicit by

$$\omega_i^* = 1.5\,\omega_i^{n+1} + (1 - 1.5)\,\omega_i^n \tag{V.8}$$

- **The case 'soil r_s^s'**

The program flow in the case 'soil r_s^s' is similar to the reference model. The relative humidity at the soil surface is specified by eq. 4.83, and the specification of q_0 (equivalent to eq. 4.56) is carried out be replacing r_a^s by $r_a^s + r_s^s$.

■ **The case 'soil CM88'**

In the case 'soil CM88' the entire surface flux partitioning is calculated using the scheme of Choudhury and Monteith (1988). No iterations are included:

1 as in the reference case
2 calculate the soil evaporation resistance r_s^s according to eq. 4.82
3 calculate r_a^a and u_* according to Louis (1979), and r_a^s and r_a^c as in the reference model
4 specify $Q_{*,s}$ and $Q_{*,c}$ using the exponential decay (eq. 4.65)
5 solve the temperature and humidity at the soil surface, canopy surface and canopy air layer with the forcings at reference height, and the specified resistance and net radiation values
6 calculate surface energy balance components and update w_{dew}
7 calculate new deep soil temperature
8 compute soil moisture content in top layer and bottom layer using force-restore
9 calculate new depth of upper soil layer

Appendix VI: Values of surface and boundary layer parameters, calculated with the reference SVAT coupled to the PBL-model

This appendix includes the absolute values of the quantities calculated by the reference runs that were analysed in chapter 6, and listed in Table 6.6. For the seven surface types listed in Table 6.2, the daytime surface and entrainment fluxes, and the PBL-height, temperature and specific humidity at specific times are listed in Table VI.1 for the MLS initialization, and in Table VI.2 for DRY.

Table VI.3 lists the reference values in case of the simulation of EFEDA-observations, for which the measured surface fluxes were taken as reference. Also shown are the values calculated using the reference SVAT coupled to the PBL-model.

Table VI.1: Values of analyzed parameters calculated using the reference SVAT coupled to the PBL-model for the MLS initialization

quantity	units	vineyard	vineyard $\sigma_f = 0.4$	vineyard $\sigma_f = 0.7$	vineyard $\sigma_f = 1.0$	vineyard on clay	tigerbush	forest
Q_*^D (day 174)	W/m^2	319	349	366	370	315	355	338
H^D (day 174)	W/m^2	185	166	158	151	196	200	187
λE^D (day 174)	W/m^2	37	104	148	178	55	81	64
G^D (day 174)	W/m^2	97	78	60	42	64	73	87
H_i^D (day 174)	W/m^2	-4	-4	-3	-5	-4	-4	-3
λE_i^D (day 174)	W/m^2	154	166	182	193	173	183	166
z_i^{12} (day 174)	m	1268	1262	1268	1278	1365	1369	1255
z_i^{18} (day 174)	m	1796	1712	1691	1672	1873	1874	1781
z_i^6 (day 175)	m	50	50	50	50	52	52	50
$\Delta\omega^{18}$ (day 174)	mm	-0.66	-1.86	-2.58	-3.12	-0.96	-1.44	-1.14
θ_v^{18} (day 174)	°C	29.9	19.6	29.5	29.4	30.1	30.2	29.9
θ_v^{min} (day 175)	°C	18.6	17.7	17.2	17.2	16.5	17.0	16.5
q^{18} (day 174)	g/kg	9.5	10.2	10.7	10.9	9.5	9.7	9.7
q^{min} (day 175)	g/kg	10.3	10.7	10.7	10.8	9.5	10.4	10.2

Table VI.2: As Table VI.1, for the DRY initialization

quantity	units	vineyard	vineyard $\sigma_f = 0.4$	vineyard $\sigma_f = 0.7$	vineyard $\sigma_f = 1.0$	vineyard on clay	tigerbush	forest
Q_*^D (day 174)	W/m^2	291	325	346	352	302	326	310
H^D (day 174)	W/m^2	129	99	84	74	112	123	117
λE^D (day 174)	W/m^2	57	139	194	230	128	118	97
G^D (day 174)	W/m^2	105	87	68	49	62	85	96
H_t^D (day 174)	W/m^2	-4	-5	-6	-7	-3	-5	-4
λE_t^D (day 174)	W/m^2	43	82	108	128	59	79	63
z_i^{12} (day 174)	m	1195	1122	1107	1095	1215	1218	1125
z_i^{18} (day 174)	m	1651	1495	1434	1380	1572	1639	1559
z_i^6 (day 175)	m	50	50	50	50	50	50	50
$\Delta\omega^{18}$ (day 174)	mm	-1.02	-2.46	-3.42	-4.08	-2.28	-2.10	-1.74
θ_v^{18} (day 174)	°C	32.5	31.9	31.6	31.5	32.2	32.4	32.2
θ_v^{min} (day 175)	°C	17.5	17.2	17.2	17.3	15.3	15.8	15.3
q^{18} (day 174)	g/kg	4.7	5.6	6.2	6.7	5.4	5.2	5.1
q^{min} (day 175)	g/kg	6.6	8.8	9.6	10.1	6.8	8.4	8.1

Table VI.3: Values of analyzed parameters from the observations and calculated using the reference SVAT for the data simulation run

quantity	units	from observations	from reference SVAT
Q_*^D (day 174)	W/m^2	325	347
H^D (day 174)	W/m^2	170	186
λE^D (day 174)	W/m^2	75	58
G^D (day 174)	W/m^2	86	104
H_t^D (day 174)	W/m^2	-16	-11
λE_t^D (day 174)	W/m^2	126	139
z_i^{12} (day 174)	m	2782	2498
z_i^{18} (day 174)	m	3185	3187
z_i^6 (day 175)	m	72	55
$\Delta\omega^{18}$ (day 174)	mm	-	-1.02
θ_v^{18} (day 174)	°C	37.4	37.4
θ_v^{min} (day 175)	°C	21.9	20.7
q^{18} (day 174)	g/kg	5.1	5.0
q^{min} (day 175)	g/kg	3.3	7.4

Samenvatting

Modellen voor niet-gesloten vegetaties voor meteorologische toepassingen

■ **Probleemstelling en afbakening**

Voor de voorspelling van het weer in de nabije toekomst, en het aardse klimaat in de verdere toekomst, zijn grootschalige meteorologische modellen ontwikkeld. Deze beschrijven voor de hele atmosfeer de huishouding van warmte, vocht, straling en andere grootheden. Verschillende studies met weer- en klimaatmodellen hebben aangetoond dat de resultaten gevoelig zijn voor de beschrijving van de uitwisseling van warmte, waterdamp en impuls tussen de atmosfeer en het landoppervlak. Een verandering van bijvoorbeeld de albedo, het bodemvochtgehalte, de aerodynamische ruwheid of de aanwezige vegetatie levert grote veranderingen op in klimaatvoorspellingen. De toepassing van verschillende landoppervlak-modellen is één van de redenen dat klimaatvoorspellingen onderling sterk van elkaar kunnen verschillen. Het is duidelijk dat een realistische beschrijving van landoppervlak-processen van belang is.

Minder duidelijk is hoe realistisch landoppervlak-modellen moeten zijn, en welke mate van detail ze moeten bevatten. Erg gedetailleerde modellen geven wellicht nauwkeuriger voorspellingen, maar zijn in de praktijk moeilijk toepasbaar vanwege de grote hoeveelheid benodigde rekentijd en invoerinformatie. Er moet een keuze worden gemaakt die een optimum biedt tussen complexiteit en nauwkeurigheid enerzijds, en eenvoud en onnauwkeurigheid anderzijds.

Er zijn een groot aantal landoppervlak-modellen in omloop, ontwikkeld voor diverse toepassingen, en met verschillende onderliggende fysische uitgangspunten. Voor gebruik van een landoppervlak-model in grootschalige meteorologische toepassingen moet het een groot aantal verschillende typen oppervlak kunnen beschrijven. Aanvankelijke waren alleen modellen beschikbaar voor een relatief eenvoudig, homogeen oppervlak, maar in de loop der jaren zijn verschillende modellen ontwikkeld die ook complexere typen oppervlak aan kunnen. Tot zo'n type oppervlak behoort een vegetatie die de grond slechts gedeeltelijk bedekt, een zogenaamd *niet-gesloten gewas*. Dit type vegetatie komt met name voor in semi-aride, droge streken, waar water een beperkende factor is voor plantengroei. Modellen voor niet-gesloten gewassen maken onderscheid tussen de planten en de onderliggende kale grond. Voor elk van deze componenten wordt apart uitgerekend hoeveel warmte of waterdamp wordt uitgewisseld met de atmosfeer.

Landoppervlak-modellen – en zeker die voor niet-gesloten vegetaties – beschrijven een groot aantal processen. Ze beschouwen de hoeveelheid energie die het oppervlak ontvangt in de vorm van straling, en berekenen de opwarming van de bodem en de lucht, verdamping door planten en door de bodem, en de verandering van de vochttoestand van de bodem. Al deze processen hangen met elkaar samen, en veranderingen aan een enkel onderdeel van een model kunnen gevolgen hebben voor andere componenten. Doordat de

verschillende modellen gebaseerd zijn op verschillende uitgangspunten zijn de voorspellingen verre van eenduidig. De vraag doet zich voor welke processen en grootheden het warmte- en watertransport boven land het sterkst bepalen, en dus de meeste invloed hebben op de toestand van de atmosfeer.

Bepalend voor deze keuze is de mate waarin de atmosfeer reageert op de beschrijving van het landoppervlak. De onderste, turbulente laag van de atmosfeer (de planetaire of atmosferische grenslaag, met een totale dikte van 0.5 à 3 km) heeft de eigenschap om snel te reageren op veranderingen van het oppervlak. Tegelijkertijd worden de transport-processen aan het oppervlak mede bepaald door de toestand van de atmosfeer. Hierdoor ontstaat een terugkoppeling, die veranderingen kan versterken (positieve terugkoppeling) of verzwakken (negatieve terugkoppeling). Hoe de atmosfeer reageert op het landoppervlak wordt dus mede bepaald door deze terugkoppeling.

In dit proefschrift wordt een studie uitgevoerd waarin verschillende landoppervlakmodellen met elkaar worden vergeleken, en gekeken wordt naar de veranderingen die de atmosferische grenslaag ondervindt als gevolg van een verandering van de beschrijving van het landoppervlak. Hierbij zijn een aantal accenten gelegd:

(1) Een eerste nadruk ligt op een beschouwing van uitwisselingsprocessen boven een *niet-gesloten vegetatie*. Zo'n oppervlak heeft relatief uitgesproken eigenschappen op het gebied van stralingshuishouding, aerodynamica en transport van warmte en waterdamp. Op het moment dat deze studie begon was met name over de modellering van niet-gesloten gewassen relatief weinig bekend. Dit type oppervlak komt echter op grote schaal voor op aarde, en dit vormde een extra aanleiding om ons met dit type oppervlak bezig te houden.

(2) De tweede nadruk ligt op de *fysische benadering* van uitwisselingsprocessen door de diverse modellen. Er wordt gekeken naar de mate waarin de grenslaag reageert op verschillende modellen die één enkel type oppervlak beschrijven, en niet op verschillende oppervlakken die met één enkel model worden gesimuleerd.

(3) Nadruk nummer drie is de *validatie van modellen door waarnemingen*, die bij een niet-gesloten gewas zijn verricht. Deze waarnemingen worden verder ook gebruikt om modellen te ijken, en om als begintoestand en randvoorwaarde te dienen bij de modelsimulaties.

(4) Tenslotte beschouwt deze studie alleen *vertikale uitwisselingsprocessen*. Simulaties worden uitgevoerd met behulp van één-dimensionale modellen.

■ **De metingen**

In twee zomers in 1991 en 1994 zijn metingen uitgevoerd bij een niet-gesloten wijngaard in La Mancha, Spanje. De metingen vonden plaats in het kader van een groot internationaal, deels door de EG gefinancierd project, genaamd EFEDA.

In Juni 1991 verrichtte de vakgroep Meteorologie van de Landbouwuniversiteit Wageningen micrometeorologische waarnemingen in een uitgestrekte wijngaard nabij Tomelloso, circa 100 km ten zuid-oosten van Madrid. Dit betrof metingen van straling, luchttemperatuur en -vochtigheid, windsnelheid, en het transport van warmte en waterdamp, zowel in de grond als in de lucht. Tegelijkertijd werd de aanwezige vegetatie gedetailleerd in kaart gebracht: afmetingen, hoeveelheid bladoppervlak en met vegetatie

bedekte grond, en het verdampingsgedrag van de planten zijn uitvoerig vastgelegd. Tijdens de meetperiode werd het weer gekenmerkt door een vrijwel continue afwezigheid van regen. De temperatuur van de (droge) lucht liep gemiddeld op tot circa 35 °C. Verder groeide de vegetatie sterk. Hierdoor werd het terrein ruwer, en nam de verdamping enigszins toe. De planten wortelden diep genoeg om water uit diepe grondlagen te onttrekken. De bodem droogde langzaam maar zeker uit. Op het verdampingsgedrag van de planten, en op de stralingseigenschappen van het oppervlak wordt later teruggekomen.

Gedurende deze campagne werden door collega's van het Franse Centre National de Réchèrche Météorologique (CNRM) uit Toulouse metingen gedaan aan de toestand van de atmosferische grenslaag, door middel van een temperatuur- en vochtsensor die aan een stijgende ballon waren bevestigd. De gegevens van deze ballon-oplatingen zijn in dit proefschrift gebruikt.

Tijdens de tweede meetcampagne werden metingen verricht over een langere periode, Juni en Juli 1994. Deze meetcampagne was het resultaat van een intensieve samenwerking met het Staring Centrum in Wageningen, en de Universiteit van Kopenhagen. De vegetatiemetingen werden sterk geïntensiveerd, en ook is het transport van CO_2 gemeten. De waarnemingen werden op een soortgelijk veld gedaan als in 1991, maar de planten waren wat jonger en hadden een kleinere hoeveelheid bladoppervlak. Het was nog wat warmer en droger dan in 1991, en behalve de afwezigheid van regen werden er ook nauwelijks wolken gesignaleerd gedurende de meeste dagen. Vooral de vegetatiemetingen die in 1994 zijn verricht zijn voor deze studie gebruikt.

- **Nadere beschouwing van een aantal uitwisselingsprocessen voor niet-gesloten vegetaties**

Een aantal aspecten van de uitwisseling van warmte en waterdamp bij een niet-gesloten gewas zijn nader bekeken, aan de hand van zowel theoretische analyse als van metingen: aerodynamische uitwisseling, reflectie van kortgolvige straling, en de zogenaamde gewasweerstand.

In eenvoudige meteorologische modellen wordt transport doorgaans beschreven aan de hand van *transportweerstanden*. Deze zijn een maat voor de efficientie waarmee een grootheid (bijvoorbeeld warmte) wordt getransporteerd over een gradient van die grootheid (temperatuur). Meestal wordt verondersteld dat de fluxdichtheid (hoeveelheid getransporteerde grootheid per eenheid oppervlak per eenheid tijd) recht evenredig is met de lokale gradient en een uitwisselingscoefficient. Deze theorie wordt aangeduid als *K*-theorie. In sommige gevallen (zoals binnen gewassen) geldt de *K*-theorie niet, en moeten meer geavanceerde modellen worden gebruikt om de fluxdichtheid te beschrijven, zoals bijvoorbeeld zogenaamde *Lagrangiaanse* modellen. Deze modellen berekenen het transport van een grootheid door de trajectoriën van een groot aantal deeltjes te volgen, en nemen derhalve veel rekentijd in beslag. In deze studie is een vereenvoudiging van een Lagrangiaans model ontwikkeld voor toepassing in een twee-component landoppervlak-model, waaronder een model voor niet-gesloten gewassen. Een extra weerstand, een zogenaamde *near-field weerstand*, is geïntroduceerd. Een gevoeligheidsanalyse toont aan, dat onder de meeste omstandigheden het gebruik van *K*-theorie nauwelijks afwijkende resultaten geeft ten opzichte van deze (vereenvoudigde) Lagrangiaanse theorie.

Verder is de Lagrangiaanse theorie gebruikt om nieuwe transportweerstanden in een twee-componenten-model te definieren, zonder – in tegenstelling tot de huidige praktijk – aannames te doen over een effectieve bronhoogte. Met name voor niet-gesloten gewassen is de aanname, dat de bron voor warmte en waterdamp zich op één enkele effectieve hoogte bevindt, dubieus: waterdamp wordt vooral geëmitteerd door de aanwezige planten, terwijl de bron voor warmte zich bevindt aan het oppervlak van de kale grond. In deze studie wordt een wegingsprocedure voorgesteld die de transportweerstanden definieert als functie van de vertikale verdeling van de bronnen. Opnieuw zijn gevoeligheidsstudies gedaan, en zijn de nieuw verkregen weerstanden vergeleken met de waardes van traditionele modellen, verkregen met *K*-theorie. De voornaamste conclusies die hieruit voortkwamen zijn, dat de 'Lagrangiaanse' weerstanden over het algemeen kleiner zijn dan de traditionele weerstanden, en dat de verschillen met de *K*-theorie modellen aanzienlijk zijn. Dit laatste wordt met name veroorzaakt door gebrek aan kennis over turbulentie vlak bij de grond.

De stralingswaarnemingen uit 1991 zijn gebruikt om de *reflectie-eigenschappen van een niet-gesloten gewas* te beschrijven. Via een literatuur-onderzoek zijn de voornaamste aspecten die de reflectie van kortgolvige straling (kortweg: albedo) bepalen op een rij gezet. Voor kale grond wordt de albedo bepaald door de hoeveelheid bodemvocht in de bovenste laag, de ruwheid van het oppervlak, het gehalte aan organisch materiaal en ijzer, en de stand van de zon. Voor gesloten gewassen spelen met name de bladhoekverdeling, de hoeveelheid bladoppervlak per eenheid grond-oppervlak (de Leaf Aera Index of *LAI*), de zonshoogte en de reflectie-eigenschappen van de bladeren en de onderliggende grond een rol. Voor niet-gesloten gewassen wordt de albedo door beide componenten bepaald, maar spelen ook afstand tussen en afmetingen van de planten, en beschaduwing van de grond mee. Met behulp van een aantal empirische vergelijkingen zijn de waarnemingen gefit. De dagelijkse gang van de albedo vertoonde voornamelijk veranderingen bij lage zonshoogten. De veranderingen over de hele maand werden veroorzaakt door twee tegenwerkende aspecten: een verhoging van de albedo door uitdrogende grond, en een verlaging door toenemende vegetatie. Hierdoor bleef voor een bepaalde positie de albedo redelijk gelijkmatig. Bovendien zijn multi-spectrale satelliet-gegevens gebruikt om de horizontale spreiding van de albedo in kaart te brengen. Het bleek dat deze horizontale spreiding veel groter was dan de verandering in de tijd, zowel op een tijdschaal van een dag als die van de hele maand.

Een ander aspect dat in detail is bekeken is de zogenaamde *gewasweerstand*, een maat voor de openingstoestand van de huidmondjes van planten. Een hoge weerstand correspondeert met gesloten huidmondjes, en een lage evapotranspiratie. Met behulp van gegevens uit 1991 heeft Jacobs (1994) een model voor de huidmondjesweerstand ontwikkeld dat gebaseerd is op de modellering van de fotosynthese van planten. De fotosynthese veroorzaakt een transport van CO_2 via diezelfde huidmondjes. Door dit transport te beschrijven met een fotosynthese-model kan de huidmondjesweerstand afgeleid worden. In dit proefschrift is dit model opgeschaald naar gewasniveau, en getest met behulp van 1994-data. Het bleek dat de waarnemingen, opgeschaald naar gewasniveau, redelijk goed werden beschreven met het door Jacobs (1994) ontwikkelde model, en ook dat de ijking die in 1991 was uitgevoerd goed bruikbaar was voor het nieuwe gewas. De prestaties van het model lijken zelfs beter dan die van een veel toegepast model, dat gebaseerd is op een statistische correlatie van de gewasweerstand met omgevingsfactoren. Vergelijking met soortgelijke

waarnemingen uit de literatuur lieten zien dat de Spaanse wijnplanten een sterke gevoeligheid voor de atmosferisch vochtigheid vertoonden, die waarschijnlijk gunstig is onder droge omstandigheden.

■ **Modelsimulaties**

De rest van dit proefschrift is gewijd aan modelsimulaties. Allereerst wordt een beschrijving gegeven van de bestaande landoppervlak-modellen die in de vergelijkingen zijn opgenomen. De eerste is het zogenaamde 'big leaf' model (Monteith, 1965), dat het landoppervlak beschouwt als één enkel groot blad met een uniforme temperatuur en gewasweerstand. Het tweede model is een variatie daarop, en beschouwt het landoppervlak als een isotherme laag met daarin verschillende componenten: een fractie gevormd door kale grond, een fractie vegetatie, en een fractie open water voor de beschrijving van dauw en neerslag-interceptie (Viterbo en Beljaars, 1995; afgekort als VB95). Het derde model is een nieuw ontwikkelde variant op het model van VB95. Het verschil met de oorspronkelijke versie is dat voor elke fractie een aparte energiebalans wordt opgelost, waardoor de fracties verschillende oppervlakte-temperaturen kunnen hebben. Deze variant is afzonderlijk getest voor twee niet-gesloten gewassen waarin de temperaturen van het gewas en de kale grond aanzienlijk kunnen verschillen. In de oude situatie werd de verdamping van de in werkelijkheid koelste component sterk overschat door een te hoge temperatuur. In de nieuwe situatie trad deze overschatting niet meer op. Het vierde model is het twee-component model van Deardorff (1978; hierna D78), waarin straling, aerodynamisch transport en temperatuur van de kale grond en de vegetatie apart wordt beschouwd. Het vijfde model is een variant op D78, maar heeft een meer geavanceerde beschrijving van de aerodynamische uitwisseling binnen het gewas (Choudhury and Monteith, 1988; CM88).

Het gebruikte grenslaagmodel is dat van Troen en Mahrt (1986), waarin vertikaal transport wordt beschreven met behulp van een numeriek diffusieschema. Voor convectieve gevallen (overdag) zijn de diffusie-coefficienten ontleend aan Holtslag en Moeng (1991). Het model geeft een redelijke beschrijving van de groei en opwarming van de grenslaag overdag, het warmte- en vochttransport aan de top van de grenslaag, en de ontwikkeling van een nachtelijke stabiele grenslaag.

■ **Modelsimulaties zonder grenslaageffecten**

Een eerste serie modelvergelijkingen werd uitgevoerd om het effect van de verschillende fysische uitgangspunten in de diverse modellen op de gesimuleerde fluxdichtheden van warmte en waterdamp te testen, en aan te geven welk model de observaties van 1991 het beste beschreef. Hierbij werden alleen de twee component-modellen (VB95, D78 en CM88) betrokken, en grenslaageffecten werden nog niet meegenomen. Waarnemingen op kleine hoogte (3 m) werden gebruikt als randvoorwaarde. Berekende fluxdichtheden van de drie modellen werden vergeleken met waarnemingen. Uit deze vergelijking konden een aantal duidelijke conclusies worden getrokken.

Ten eerste blijkt de simulatie van de bodemwarmtestroom niet goed te worden uitgevoerd met een model dat de opslag van warmte in de bovenste bodemlaag negeert (CM88). Een model dat de bodemwarmtestroom simuleert door de oplossing van een diffusievergelijking (VB95) is vrij gevoelig voor de thermische eigenschappen die worden

opgelegd. Een derde 'force-restore' variant, een vereenvoudiging van het diffusie-model (in D78), bleek de beste resultaten op te leveren.

Een tweede belangrijke conclusie is dat de kwaliteit van de voorspellingen sterk samenhangt met de beschrijving van de aerodynamische weerstand tussen waarnemingshoogte en de kale grond-component van het oppervlak. Deze weerstand heeft een grote invloed op de temperatuur van de kale grond, en die is weer maatgevend voor processen als bodemverdamping, bodemwarmtestroom, opwarming van de lucht, en de temperatuur ter hoogte van het gewas. De weerstanden zoals gemodelleerd in CM88 gaven de beste resultaten, terwijl die in D78 veel te laag waren.

Vervolgens bleken de verschillende beschrijvingen van de gewasweerstand tot grote verschillen in gesimuleerde verdamping te leiden. In zowel D78 als VB95 is die weerstand sterk afhankelijk van de hoeveelheid bodemvocht, en deze afhankelijkheid leidde tot té grote weerstanden en té lage verdampingen.

Opgemerkt moet worden dat het vaak moeilijk is om een 'eerlijke' vergelijking uit te voeren. De modellen verschillen niet alleen in onderliggende theorie, maar ook in benodigde invoer. Deze invoer moet uit veldwaarnemingen worden gehaald.

Uit deze vergelijking is een landoppervlakmodel geconstrueerd dat voor de huidige dataset vermoedelijk de beste resultaten geeft. Het is een combinatie van de force-restore methode ter beschrijving van de bodemwarmtestroom, en de aerodynamische weerstanden en de gewasweerstand van CM88. Dit model dient als referentiemodel in de modelstudies hieronder.

- **Modelsimulaties met grenslaageffecten**

Het laatste hoofdstuk van dit proefschrift beschrijft de modelsimulaties met behulp van een groot aantal variaties van een landoppervlak-model, gekoppeld aan een model voor de grenslaag. Het doel van deze simulaties was om na te gaan hoe de berekende toestand van de grenslaag verandert ten gevolge van een wijziging van de modellering van de landoppervlak-processen. Steeds werd voor een bepaalde simulatie eerst een modelrun gedaan met behulp van het hierboven beschreven referentiemodel, de controlerun. Vervolgens werden *componenten* van dit model vervangen door alternatieve componenten, de simulatie opnieuw verricht, en werden de resultaten uitgedrukt in een relatieve verandering ten opzichte van de controlerun. Dit uitwisselen van componenten werd gedaan om de invloed van elke component apart te kunnen bekijken. Het vervangen van complete modellen heeft als resultaat dat meerdere onderdelen in die modellen verschillende (en mogelijk tegenstrijdige) gevolgen zouden kunnen hebben, en daardoor interpretatie van de berekeningen zou bemoeilijken. De componenten die werden uitgewisseld zijn ondergebracht in vier verschillende groepen:

(1) *oppervlakte-representatie*: hierin werd het twee-component model vergeleken met een 'big leaf' aanpak, en met een al dan niet isotherme enkelvoudige oppervlaktelaag

(2) *bodemwarmtestroom en bodemverdamping*: hierin werd de force-restore methode vergeleken met een diffusieschema, een weerstandsmodel, en een alternatieve beschrijving van de bodemverdamping

(3) *aerodynamische uitwisseling*: hierin werden de weerstanden van CM88 vergeleken met die in D78, en de weerstanden uit de Lagrangiaanse analyse

(4) *gewasweerstand*: hierin werden verschillende modellen, waaronder het fotosynthese-model, vergeleken.

De simulaties zijn uitgevoerd voor drie verschillende initialisaties: twee kunstmatige profielen, en één situatie die in 1991 is gemeten. De kunstmatige profielen benaderen zomerse omstandigheden in respectievelijk gematigde en Mediterrane streken. In alle simulaties diende de Spaanse EFEDA-wijngaard als referentie-oppervlak. In een aantal gevallen werden hierop (kleine) variaties aangebracht.

De computersimulaties zijn geëvalueerd aan de hand van daggemiddelde fluxdichtheden van warmte, waterdamp en bodemwarmtestroom, fluxdichtheden van warmte en waterdamp aan de top van de grenslaag, en de hoogte, temperatuur en vochtgehalte van de grenslaag aan het eind van de middag en aan het eind van de daarop volgende nacht.

De volgende conclusies konden uit deze berekeningen worden getrokken:

(1) Voor de beschrijving van het warmte- en waterdamptransport boven een niet-gesloten vegetatie is een twee-componenten model beter geschikt dan een 'big leaf' model, die met name een forse overschatting van de verdamping veroorzaakt. Ook het onderscheiden van verschillende fracties in een éénlagig model levert aanzienlijk betere resultaten op.

(2) De beschrijving van de bodemwarmtestroom met een weerstandsschema zoals dat in CM88 levert een forse onderschatting van deze grootheid, en daarmee een sterke overschatting van het warmtetransport naar de atmosfeer. De force-restore methode en het diffusiemodel leverden onderlinge verschillen van 30-40% in de bodemwarmtestroom, en circa 20% in atmosferische warmte-fluxdichtheid. Deze verschillen werden voornamelijk veroorzaakt door het verschil in thermische geleiding, veroorzaakt door een verschil in berekend bodemvochtgehalte.

(3) De verschillende methoden om bodemverdamping te berekenen leidden tot aanzienlijke verschillen in de totale verdamping. Deze verschillen waren sterk afhankelijk van het bodemtype. De kwaliteit van alle gebruikte modellen berust sterk op empirische grootheden, en is moeilijk objectief vast te stellen. Voor de droge bodem waarvoor de simulaties zijn uitgevoerd lopen de modellen verder uiteen dan in vergelijkbare studies onder minder extreme omstandigheden in de literatuur. Aan de andere kant is onder droge omstandigheden de totale verdamping van geringe invloed op de ontwikkeling van de grenslaag.

(4) De aerodynamische weerstanden zoals gesimuleerd in CM88 geven de beste beschrijving van de oppervlaktetemperatuur en warmtefluxdichtheid.

(5) De in deze studie gesimuleerde warmtefluxdichtheid aan de top van de grenslaag (de zogenaamde entrainment) is aanzienlijk lager dan uit diverse studies in de literatuur bleek. Het feit dat de entrainment niet direkt is waargenomen maar uit de computersimulaties is gehaald kan een reden voor dit verschil zijn. Vooral het feit dat het effect van windschering op de entrainment in het gebruikte model niet is meegenomen kan van belang zijn. Anderzijds kan de systematische aanwezigheid van een duidelijke residulaag met een inversie op 3 km hoogte, de grenslaaggroei en daarmee de entrainment in de huidige situatie hebben beperkt.

Summary

Sparse canopy parameterizations for meteorological models

■ **Definition of the problem**

For short-range weather prediction, and for predictions of the future global climate, large-scale meteorological models have been developed. These models describe the budgets of heat, moisture, radiation and other quantities for the entire atmosphere. Various studies with weather- and climate models have shown that their results are sensitive to the description of the exchange of heat, moisture and momentum between the land surface and the atmosphere. Changes of for instance the surface albedo, the soil moisture content, the aerodynamic roughness or the present vegetation can lead to major changes in climate predictions. The application of different land surface models is one of the reasons for the discrepancy between various climate predictions. It is clear that a realistic description of land surface processes is of importance.

It is less obvious how realistic land surface models need to be, and what degree of detail they must contain. Very detailed models may provide more accurate predictions, but are hardly applicable in practice owing to the large demand of input information and computer time. A choice must be made between complexity and accuracy on one hand, and simplicity and inaccuracy on the other.

A large number of land surface models, developed for various applications and containing different physical approaches, exists. For application in large scale meteorological applications a large number of surface types must be described by the land surface scheme. Early versions of these land surface models treated the surface as a relatively simple, horizontally homogeneous surface, but in the past decades various models have been developed that can also describe more complex surface types. Such a surface type is a vegation only partially covering the ground, a so-called *sparse canopy*. This surface type is typical for semi-arid, dry areas, where water is a limiting factor for vegetation growth. Sparse canopy models distinguish between plants and the underlying bare ground. For each of these components the exchange of heat and moisture with the atmosphere is calculated separately.

Land surface models – and certainly those for sparse canopies – describe a large number of processes. They consider the amount of energy received by the surface as radiation, and compute the heating of the soil and the air near the surface, evaporation by plants and soil, and the change of the soil moisture content. These processes are strongly interrelated, and changes to a particular part of a model can result in major changes of other components. Because of the different underlying physical concepts of the different models, their results are far from uniform. The question arises, which processes and quantities most strongly affect the transport of heat and moisture above the surface and the state of the atmosphere.

The response of the atmosphere to the description of the land surface is crucial for this choice. The lowest, turbulent atmospheric layer (the planetary or atmospheric boundary layer, 0.5 to 3 km deep), shows a quick response to changes of the land surface. Simultaneously, transport processes near the surface are partially determined by the state of the atmosphere. A feedback loop is formed, which can either increase (positive feedback) or reduce (negative feedback) the effect of a land surface change. This feedback partially determines the response of the atmosphere to the land surface description.

In this thesis a study is carried out in which various land surface schemes are compared. The change of the atmospheric boundary layer as a result of a change of the description of land surface processes is considered. Emphasis is put on the following issues:

(1) A first emphasis is that exchange processes *for a sparse canopy vegetation type* are considered. This surface type has relatively extreme radiative and aerodynamic properties, and the transport of heat and moisture takes place from various sources. At the time this study was started, knowledge about sparse canopy models was rather limited, in spite of the fact that sparse canopies are a very common global surface type. This provided an additional reason to consider this surface type.

(2) The second emphasis is the *physical approach* of exchange processes in different land surface models. The response of the planetary boundary layer to various models describing a single surface type is investigated, rather than simulating different surface types with a single model.

(3) Third, a *model validation using observations taken at a sparsely vegetated site* is carried out. These observations were also used to calibrate models, and to serve as initial or boundary conditions for the conducted model simulations.

(4) Finally, the study only considers *vertical exchange processes*. Simulations are carried out with one-dimensional models.

■ The measurements

In two summers in 1991 and 1994, measurements were carried out at a sparse canopy vineyard site in La Mancha, Spain. The measurement campaigns took place in the context of a large international project, partially sponsored by the EC, entitled EFEDA.

In June 1991 the Department of Meteorology of the Wageningen Agricultural University carried out micrometeorological observations in a large vineyard near Tomelloso, approximately 100 km south-east of Madrid. Measurements of radiation, air temperature and -humidity, wind speed and transport of heat and moisture in both the ground and the air were taken. Simultaneously the characteristic dimensions, leaf area and the surface coverage of the present vegetation was monitored at various times during the period. Also the vegetation evaporation properties were analysed. During the measurement campaign the weather was characterized by an almost continuous absence of rain. The temperature of the (dry) air typically reached values of 35 °C. Moreover, the vegetation showed a significant growth. This caused an increase of the terrain roughness, and a small increase of the evaporation. The plants had a sufficiently large rooting depth to extract water from deep soil layers. The soil moisture content gradually decreased. In the following more attention is paid to the radiation properties of the surface and the evaporation properties of the plants.

During the 1991 campaign colleagues of the Centre National de Réchèrche

Météorologique (CNRM) in Toulouse carried out radiosonde measurements, to monitor the temperature, humidity and wind speed of the planetary boundary layer. The data from this radiosoundings are used in the current study.

During the second field campaign in 1994, measurements were carried out over a longer time span, June and July 1994. This measuring campaign was the result of an intensive collaboration with the Wageningen Staring Centre and the university of Copenhagen. The vegetation measurements were intensified, and also the vertical transport of CO_2 was measured. The observations were taken at a similar site as investigated in 1991, but the plants were somewhat younger and had a smaller leaf area. The weather was warmer than in 1991, and except for the absence of rain hardly any clouds were detected during most days. Particularly the vegetation measurements were used for this study.

- **A number of considered exchange processes**

A number of aspects of the exchange of heat and moisture for a sparse canopy are considered in more detail, using both theoretical analysis and measurements: aerodynamic exchange, reflection of shortwave radiation, and the so-called crop resistance.

In applied meteorological models transport is usually described using *exchange resistances*. These resistances are a measure of the efficieny of the transport of the quantity (say, heat) over a gradient of a constituent (temperature). In most cases it is assumed that the flux density (the amount of transported quantity per unit area per unit time) is proportional to the local gradient and an exchange coefficient. This theory is called *K*-theory. In some cases (for instance, within canopies), *K*-theory is invalid, and sophisticated models must be used to describe the flux density. One of this sophisticated theories is *Lagrangian theory*, which describes the transport of a quantity by considering the trajectories of a large number of released particles. This type of modelling is computationally very expensive. In this study a simplification of a Lagrangian model has been developed for application in a two-component land surface model, including a model for sparse canopies. A new resistance, labeled a *near-field resistance*, is introduced. A sensitivity analysis shows that under most circumstances the use of *K*-theory gives hardly different results compared to this (simplified) Lagrangian theory.

This Lagrangian theory is also used to define new exchange resistances in a two-component model, without – contrary to current practice – adopting assumptions about an effective source height. Particularly for sparse canopies the assumption that sources of heat and water vapour are situated at a similar effective height is doubtful: water vapour is mainly released by the plants, while the heat source is mainly situated at the bare ground surface. In the present study a weighing procedure, defining the exchange resistances as function of the vertical distribution of sources, is proposed. Again sensitivity analyses are carried out, and the newly obtained resistances are compared to the values of traditional models obtained by *K*-theory. The main conclusions are that the 'Lagrangian' resistances are smaller than the traditional resistances, and that the differences with *K*-theory are considerable. This feature is mainly caused by a lack of knowledge about the turbulence close to the ground.

The 1991 radiation observations have been used to describe the *reflection properties of a sparse canopy*. The most important aspects determining the reflection of shortwave

radiation (albedo) were summarized from a literature survey. For bare soil the albedo is determined by the soil moisture content in the very top soil layer, the surface roughness, the content of organic material and iron, and the position of the sun. For closed canopies the leaf angle distribution, the Leaf Area Index, the solar geometry and the reflection properties of the individual leaves and underlying soil play a role. For sparse canopies the albedo is determined by both components, but also by the distance between and dimensions of the individual plants, and by shading of the soil. The observations were fitted using a set of empirical relationships. The diurnal course of the albedo showed mainly changes at rather low solar elevation. Changes over the entire month were caused by two counteracting effects: an increase of the albedo by the drying of the soil, and a reduction by an increase of the vegetation coverage. For a particular position the albedo was fairly constant. Also multispectral satellite observations were used to detect the horizontal variability of the surface albedo, which appeared to be much stronger than the changes in time, both on a diurnal and a monthly time scale.

Another aspect that was considered in more detail is the so-called *crop resistance*, a measure of the aperture of the leaf stomata. A high resistance corresponds to closed stomata and low evaporation rates. Using the 1991 dataset, Jacobs (1994) developed a model for the stomatal resistance based on leaf photosynthesis modelling. Photosynthesis results in a CO_2-transport through the same stomata. By describing this transport using a photosynthesis model the stomatal resistance can be deduced. In the current thesis this model is scaled up to the canopy level, and tested using the 1994 data. It appeared that the 1994 observations, scaled up to the canopy level, were described fairly well by the model of Jacobs (1994), and also that the calibration conducted in 1991 was still usable for the current dataset. The skill of the model even seems to be better than the results of an often applied model, that is based on a statistical correlation between the canopy conductance with environmental factors. Comparisons with similar observations published in literature showed a strong sensitivity of the Spanish vineplants to atmospheric humidity deficit. An enhanced humidity deficit is likely to be favourable under very dry conditions.

- **Model simulations**

The remainder of the thesis is dedicated to model simulations. First a description is given of the existing land surface models that are used in the intercomparison studies. The first is a so-called 'big leaf' model (Monteith, 1965), that treats the surface as a single big leaf with uniform temperature and canopy resistance. The second model is a variation upon this scheme, and considers the land surface as a single isothermal layer with different components: a fraction bare soil, a fraction vegetation, and a fraction open water representing the dew and interception of precipitation (Viterbo and Beljaars, 1995; abbreviated as VB95). The third model is a new variation on VB95, and solves the energy balance for each surface fraction separately. This allows the different fractions to have different surface temperatures. This variation is tested independently for two sparse canopy surface types, in which the temperatures of the canopy and the underlying bare soil can be very different. In the old situation the evaporation of the coolest component was significantly overestimated by a too high surface temperature. In the new situation this overestimation did not occur. The fourth model is the two-component scheme of Deardorff

(1978; hereafter referred to as D78), in which radiation, aerodynamic transfer and temperature of the bare soil and the canopy elements are considered separately. The fifth model is a variation of D78, but contains a more advanced description of the aerodynamic exchange within the canopy layer (Choudhury and Monteith, 1988; CM88).

The model for the planetary boundary layer that was used is published by Troen and Mahrt (1986). In that model the vertical transport is described using a numerical diffusion scheme. For (daytime) convective cases the diffusion coefficients are taken from Holtslag and Moeng (1991). The model gives a fair description of the growth and heating of the planetary boundary layer during daytime, the heat and moisture transport near the top, and the development of a nocturnal stable boundary layer.

- **Model simulations without boundary layer effects**

A first series of model comparisons was executed to test the effect of the different physical approaches adopted in the various models upon the simulated flux densities of heat and water vapour. It was also meant to indicate which model gave an optimal description of the 1991 data. Only the two-component models (VB95, D78 and CM88) were involved in this comparison, and boundary layer effects were not yet included. Observations at a reference height of 3 m were used as boundary condition. Calculated flux densities were compared to observations. A number of clear conclusions could be drawn from this comparison study.

First, the simulation of the soil heat flux density was not carried out accurately with a model ignoring the storage of heat in the upper soil layer (CM88). A model simulating the soil heat flux density by solving a diffusion equation (VB95) appears to be rather sensitive for the adopted soil thermal properties. A third 'force restore' variation, a simplification of the diffusion model (in D78), yielded the best results.

A second conclusion is that the prediction quality is associated with the formulation of the aerodynamic resistance between the reference height and the bare soil surface. This resistance affects the the bare soil temperature, which has an impact on processes as soil evaporation, soil heat flux density, sensible heat flux and the temperature within the canopy air layer. The resistances as modelled in CM88 yielded optimal results, while those in D78 were too low.

The different descriptions of the canopy resistance lead to large relative differences in predicted evaporation rate. In both D78 and VB95 this resistance is strongly determined by the soil moisture content, and this dependence gave rise to too high resistances and too low evaporation rates.

It must be noticed that it is often very difficult to perform an 'honest' model comparison. The models differ in the underlying theory, and in required input data. This input must be extracted from field observations.

The intercomparison was used to construct a land surface scheme that apparently gives optimal predictions for the present dataset. It is a combination of the force-restore method to describe the soil heat flux density, and the aerodynamic and canopy resistance formulation in CM88. This model was used as a reference model for the model studies described below.

■ **Model simulations including boundary layer effects**

The last chapter of this thesis describes model simulations using a large number of variations to a land surface model, coupled to a model for the atmospheric boundary layer. The purpose of these simulations is to investigate the sensitivity of the boundary layer to the parameterization of land surface processes. For each case, first a model run was conducted using the reference model described above, the control run. Then, *components* of this reference model were changed by alternative components, and the simulations were executed again. The results were expressed as relative differences compared to the control run. Changing components rather than complete models was employed to be able to describe the influence of each component separately. Changing complete land surface schemes gives results which are difficult to interpret, since observed changes may have been the result of multiple (and possibly counteracting) effects. The components that have been exchanged are divided into four categories:

(1) *surface representation*: in this category the reference two-component model is compared to a 'big leaf' approach, and to the isothermal and differentiated single layer surface representations

(2) *soil heat flux and soil evaporation*: here the force-restore method is compared to a diffusion scheme, a resistance model, and an alternative description of soil evaporation

(3) *aerodynamic exchange*: in this group the CM88 resistances were compared to the resistance in D78, and to the resistances from the Lagrangian analysis

(4) *canopy resistance*: here different canopy resistance models, including the photosynthesis approach, were compared.

The simulations have been executed for three different initializations: two artificial profiles, and one situation measured in 1991. The artificial profiles resemble typical summertime conditions in temperate and Mediterranean areas, respectively. In all simulations the Spanish EFEDA vineyard served as reference surface. In a number of cases small variations upon this surface were carried out.

The computer simulations have been evaluated by means of daily averaged flux densities of sensible heat, water vapour and soil heat, sensible and latent heat flux densities at the top of the boundary layer, and the boundary layer height, temperature and moisture content near sunset and sunrise.

The following conclusions could be drawn from these calculations:

(1) For the description of the heat and moisture transport for a sparse canopy surface a two component model is more suitable than a 'big leaf' approach, which particularly computes a large overestimation of the surface evaporation. The differentiation between various fractions of the single layer surface yields significantly better results.

(2) The description of the soil heat flux density with a resistance scheme as in CM88 gives rise to a pronounced underestimation of this quantity, associated with a strong overestimation of the sensible heat transport into the atmosphere. The force restore method and the diffusion scheme gave mutual differences of approximately 30 - 40% in soil heat flux density, and 20% in sensible heat flux. These differences were mainly

caused by differences in thermal conductivity, resulting from differences in calculated soil moisture content.

(3) The different methods to compute soil evaporation yielded considerable differences in predicted total surface evaporation. These differences were strongly dependent on the soil type. The quality of the models used relies on empirical quantities, and is difficult to assess objectively. For the dry soil for which the simulations were carried out, the models differed more than in comparable studies under less extreme conditions reported in literature. On the other hand, the contribution of surface evaporation to the atmospheric state is rather limited under the dry conditions explored here.

(4) The aerodynamic resistance as simulated in CM88 resulted in an optimal description of the surface temperature and sensible heat flux density.

(5) The sensible heat flux density at the top of the boundary layer simulated in this study (the so-called heat entrainment) is very low compared to various experimental studies in literature. In this study, entrainment was not observed but calculated, which is one reason for this difference. Particularly the lack of simulating the contribution of wind shear to entrainment may be of importance. Alternatively, the systematic presence of a strong residual layer with an inversion at 3 km height has confined the boundary layer growth, and thus the entrainment.

Literature

Anonymous (1994): *EFEDA CD-ROM Database: Vol. 1, Version 1, June 1994*; European Communities, Directorate General XII for Science, Research and Development.

Baldocchi, D.D. (1992): A Lagrangian random-walk model for simulating water vapour, CO_2 and sensible heat flux densities and scalar profiles over and within a soybean canopy; *Boundary-Layer Meteorol.* **61**, 113-144.

Baldocchi, D.D., B.B. Hicks and P. Camara (1987): A canopy stomatal conductance model for gaseous deposition to vegetated surfaces; *Atmos.Environ.* **21**, 91-101.

Ball, J.T. (1987): Calculations related to stomatal gas exchange; In: E. Zeiger, G.D. Farquhar and I.R. Cowan (Eds.), *Stomatal Function*; Stanford Univ. Press, Stanford, pp. 445-476.

Bastiaanssen, W.G.M. (1995): *Regionalization of surface flux densities and moisture indicators in composite terrain: a remote sensing approach under clear skies in Mediterranean climates*; PhD. thesis, Wageningen Agricultural University, 273 pp.

Bastiaanssen, W.G.M., D.H. Hoekman and R.A. Roebeling (1993): *A methodology for the assessment of surface resistance and soil water storage variability at mesoscale based on remote sensing measurements (A case study with HAPEX-EFEDA data)*; Dept. of Hydrology, Wageningen Agricultural University, 71 pp.

Begg, J.E., J.F. Bierhuizen, E.R. Lemon, D.K. Misra, R.O. Slatyer and W.R. Stern (1964): Diurnal energy and water exchanges in bulrush millet in an area of high solar radiation; *Agric. Meteorol.* **1**, 294-312.

Beljaars, A.C.M. (1992): Numerical schemes for parameterizations; ECMWF seminar proceedings, Sept. 1991; *Numerical methods in atmospheric models*, pp. 1-42.

Beljaars, A.C.M., P. Viterbo, M.J. Miller and A.K. Betts (1995): The anomalous rainfall over the USA during July 1993: sensitivity to land-surface parameterization and soil moisture anomalies; (accepted for publication by *Monthly Weather Rev.*).

Beljaars, A.C.M. and A.K. Betts (1992): Validation of the boundary layer scheme in the ECMWF model; ECMWF Seminar proceedings 7-11 September 1992; *Validation of models over Europe*, Vol. II, 159-195.

Beljaars, A.C.M. and A.A.M. Holtslag (1991): Flux parameterizations over land surface for atmospheric models; *J.Appl.Meteorol.* **30**, 327-341.

Bernstein, A.B. (1967): A note on the use of cup anemometers in wind profile experiments; *J.Appl.Meteorol.* **6**, 280-286.

Betts, A.K. and J.H. Ball (1992): *FIFE-1987 mean surface time series, Data diskette*; Atmospheric Research, Pittsford, VT 05763.

Betts, A.K. and J.H. Ball (1994): Budget analysis of FIFE 1987 sonde data; *J.Geophys.Res.* **99D**, 3655-3666.

Bhumralkar, C.M. (1975): Numerical experiments on the computation of ground surface temperature in an atmospheric general circulation model; *J.Appl.Meteorol.* **14**, 1246-1258.

Black, T.A., C.B. Tanner and W.R. Gardner (1970): Evaporation from a snap bean crop; *Agronomy J.* **62**, 66-69.

Blondin, C. (1991): Parameterization of land-surface processes in numerical weather prediction; In: T.J. Schmugge and J.C. André (Eds.), *Land surface evaporation: measurements and parameterization*; Springer, 31-54.

Blyth, E.M. (1995): Using a simple SVAT-scheme to describe the effect of scale on aggregation; *Boundary-Layer Meteorol.* **72**, 267-285.

Blyth, E.M. and A.J. Dolman (1995): The roughness length for heat of sparse vegetation; *J.Appl. Meteorol.* **34**, 583-585.

Blyth, E.M., A.J. Dolman and N. Wood (1993): Effective resistance to sensible- and latent-heat flux in heterogeneous terrain; *Q.J.R.Meteorol.Soc.* **119**, 423-442.

Bolle, H.J. and B. Streckenbach (1992): *EFEDA - First annual report*; Free University of Berlin, Germany, 259 pp. plus appendices.

Bolle, H.J. and B. Streckenbach (1993): *The Echival Field Experiment in a Desertification Threatened Area - Final Report*; Free Univ. of Berlin, Germany, 461 pp.

Bolle, H.J., J.C. André, J.L. Arrue, H.K. Barth, P. Bessemoulin, A. Brasa, H.A.R. de Bruin, J. Cruces, G. Dugdale, E.T. Engman, D.L. Evans, R. Fantechi, F. Fiedler, A. van de Griend, A.C. Imeson, A. Jochum, P. Kabat, T. Kratzsch, J.-P. Lagouarde, I. Langer, R. Llamas, E. Lopez-Baeza, J. Melia Miralles, L.S. Muniosguren, F. Nerry, J. Noilhan, H.R. Oliver, R. Roth, S.S. Saatchi, J. Sanchez Diaz, M. de Santa Olalla, W.J. Shuttleworth, H. Sogaard, H. Stricker, J. Thornes, M. Vauclin and D. Wickland (1993): EFEDA: European field experiment in a desertification threatened area; *Ann.Geophysicae* **11**, 173-189.

Bosilovich, M.G. and W.-Y. Sun (1995): Formulation and verification of a land surface parameterization for atmospheric models; *Boundary-Layer Meteorol.* **73**, 321-341.

Braud, I., J. Noilhan, P. Bessemoulin, and P. Mascart (1993): Bare ground surface heat and water exchanges under dry conditions: observations and parameterization; *Boundary-Layer Meteorol.* **66**, 173-200.

Braud, I., A.C. Dantas-Antonino, M. Vauclin, J.L. Thony and P. Ruelle (1995): A simple soil-plant-atmosphere transfer model (SISPAT) development and field verification; *J.Hydrol.* **166**, 213-250.

Brown, K.W. and W. Covey (1966): The energy budget evaluation of the micro-meteorological transfer processes within a corn field; *Agric.Meteorol.* **3**, 73-96.

Brutsaert, W. (1982): *Evaporation into the atmosphere*; D. Reidel Publ.Comp., Dordrecht, The Netherlands.

Brutsaert, W. (1986): Catchment-scale evaporation and the atmospheric boundary layer; *Water Resources Res.* **22**, 39S-45S.

Buck, A.L. (1976): The variable path Lyman-alpha hygrometer and its operating characteristics; *Bull.Am.Meteorol.Soc.* **57**, 1113-1118.

Camillo, P.J. and R.J. Gurney (1986): A resistance parameter for bare soil evaporation models; *Soil Sci.* **141**, 95-105.

Campbell, G.S. (1977): *An introduction to environmental biophysics*; Springer-Verlag, New York, 159 pp.

Charney, J.G., W.J. Quirk, S.H. Chow and J. Kornfield (1977): A comparative study of the effects of albedo change on drought in semi-arid regions; *J.Atmos.Sci.* **34**, 1366-1385.

Choudhury, B.J. and J.L. Monteith (1986): Implications of stomatal response to saturation deficit for the heat balance of vegetation; *Agric.For.Meteorol.* **36**, 215-225.

Choudhury, B.J. and J.L. Monteith (1988): A four-layer model for the heat budget of homogeneous land surfaces; *Q.J.R.Meteorol.Soc.* **114**, 373-398.

Choudhury, B.J., R.J. Reginato and S.B. Idso (1986): An analysis of infrared temperature observations over wheat and calculation of latent heat flux; *Agric.For.Meteorol.* **37**, 75-88.

Clapp, R.B. and G.M. Hornberger (1978): Empirical equations for some hydraulic properties; *Water Resources Res.* **14**, 601-604.

Cionco, R.M. (1972): A wind profile index for canopy flow; *Boundary-Layer Meteorol.* **3**, 255-263.

Cionco, R.M. (1978): Analysis for canopy index values for various canopy densities; *Boundary-Layer Meteorol.* **15**, 81-93.

Collatz, G.J., M. Ribas-Carbo, and J.A. Ball (1992): Coupled photosynthesis-stomatal conductance model for leaves of C4 plants; *Aust.J.Plant Physiol.* **19**, 519-538.

Corrsin, S. (1974): Limitations of gradient transport models in random-walks and in turbulence; *Adv. Geophys.* **18a**, 25-60.

Coulson, K.L. and D.W. Reynolds (1971): The spectral reflectance of natural surfaces; *J.Appl. Meteorol.* **10**, 1285-1295.

Covey, W. (1963): A method for the computation of the wind profile parameters and their standard errors; *Prod.Res.Rep.* **72**, Agric.Res.Serv., U.S.Agric.Dep., pp. 28-33.

Cowan, I.R. (1968): Mass, heat and momentum exchange between stands of plants and their atmospheric environment; *Q.J.R.Meteorol.Soc.* **94**, 523-544.

Cowan, I.R. (1982): Regulation of water use in relation to carbon gain in higher plants; In: O.L. Lange, P.S. Nobel, C.B. Osmond and H. Ziegler (Eds.), *Encyclopedia of Plant Physiology, New Series, Vol. 12B*; Physiological Plant Ecology II, Springer Verlag, Berlin, pp 589-615.

Culf, A.D. (1992): An application of simple models to Sahelian convective boundary-layer growth; *Boundary-Layer Meteorol.* **58**, 1-18.

Daughtry, C.S.T. (1990): Direct measurements of canopy structure; *Rem.Sens.Rev.* **5**, 45-60.

Deardorff, J.W. (1972): Theoretical expression for the countergradient vertical flux; *J.Geophys.Res.* **77**, 5900-5904.

Deardorff, J.W. (1978): Efficient prediction of ground surface temperature and moisture, with inclusion of a layer of vegetation; *J.Geophys.Res.* **83**, 1889-1903.

De Bruin, H.A.R. (1982): *The energy balance of the Earth's surface: a practical approach*; PhD-thesis, KNMI, De Bilt, The Netherlands.

De Bruin, H.A.R. (1983): A model for the Priestley-Taylor parameter α; *J.Climate Appl. Meteorol.* **22**, 572-578.

De Bruin, H.A.R. (1987): Physical aspects of the planetary boundary layer with special reference to regional evapotranspiration; In: T.A. Black *et al.* (Eds.), *Estimation of areal evapotranspiration.* Proceedings of an international workshop held during the XIXth General Assembly of the Int. Union of Geodesy and Geophysics at Vancouver, Canada, 9-22 Aug. 1987; IAHS Publ. no 177, IAHS Press, Wallingford, UK.

De Bruin, H.A.R., W. Kohsiek and B.J.J.M. van den Hurk (1993): A verification of some methods to determine the fluxes of momentum, sensible heat and water vapour using standard deviation and structure parameter of scalar meteorological quantities; *Boundary-Layer Meteorol.* **63**, 231-257.

De Bruin, H.A.R., B.J.J.M. van den Hurk and W. Kohsiek (1995): The scintillation method tested over a dry vineyard area; (in press by *Boundary-Layer Meteorol.*)

Denmead, O.T. and E.F. Bradley (1985): Flux-gradient relationships in a forest canopy; In: B.A. Hutchison and B.B. Hicks (Eds.), *The forest-atmosphere interaction*; D. Reidel Publ., Dordrecht, pp. 421-441.

Dickinson, R.E. (1983): Land surface processes and climate - surface albedos and energy balance. *Adv.Geoph.* **25**, 305-353.

Dickinson, R.E. (1988): The force-restore model for surface temperatures and its generalizations; *J.Climate* **1**, 1086-1097.

Dickinson, R.E., A. Henderson-Sellers, P.J. Kennedy and M.F. Wilson (1986): *Biosphere-Atmosphere Transfer Scheme (BATS) for the NCAR Community Climate Model*; NCAR Technical Note NCAR/TN-275+STR, 69 pp.

Dickinson, R.E. and A. Henderson-Sellers (1988): Modelling tropical deforestation: A study of GCM land surface parameterizations; *Q.J.R.Meteorol.Soc.* **114**, 439-462.

Dickinson, R.E., A. Henderson-Sellers, C. Rosenzweig and P.J. Sellers (1991): Evapotranspiration models with canopy resistance for use in climate models: a review; *Agric.For.Meteorol.* **54**, 373-388.

Dickinson, R.E., A. Henderson-Sellers and P.J. Kennedy (1993): *Biosphere-Atmosphere Transfer Scheme (BATS) Version 1e as coupled to the NCAR Community Climate Model*; NCAR Technical Note NCAR/TN-387+STR, 80 pp.

Dolman, A.J. (1993): A multiple source land surface energy balance model for use in GCMs; *Agric.For.Meteorol.* **65**, 21-45.

Dolman, A.J. and J.B. Stewart (1987): Modelling forest transpiration from climatological data; In: Swanson, Bernier and Woodard (Eds.), *Forest Hydrology and Watershed Management*; IAHS-publ. 167, pp. 319-327.

Dolman, A.J. and J.S. Wallace (1991): Lagrangian and K-theory approaches in modelling evaporation from sparse canopies; *Q.J.R.Meteorol.Soc.* **117**, 1325-1340.

Dolman, A.J., C.R. Lloyd and A.D. Culf (1992): Aerodynamic roughness of an area of natural open forest in the Sahel; *Ann.Geophys.* **10**, 930-934.

Driedonks, A.G.M. (1981): *Dynamics of the well-mixed atmospheric boundary layer*; KNMI-report WR 81-2, KNMI, De Bilt, The Netherlands, 189 pp.

Driedonks, A.G.M. (1982a): Models and observations of the atmospheric boundary layer; *Boundary-Layer Meteorol.* **23**, 283-306.

Driedonks, A.G.M. (1982b): Sensitivity analysis for the equations for a convective mixed-layer; *Boundary-Layer Meteorol.* **22**, 475-480.

Droogers, P., G.D. van Abeele, J. Cobbaert, C.P. Kim, R. Rössleröva, M. Soet and J.N.M. Stricker (1993): *Basic data sets description and preliminary results of EFEDA-Spain*; Dept. of Water Resources, Wageningen Agricultural University, 103 pp.

Droppo, J.G. and H.L. Hamilton (1973): Experimental variability in the determination of the energy balance in a deciduous forest; *J.Appl.Meteorol.* **12**, 781-791.

Dyer, A.J. and B.B. Hicks (1970): Flux-gradient relationships in the constant flux layer; *Q.J.R.Meteorol.Soc.* **96**, 715-721.

El-Kilani, R.M.M., A.F.G. Jacobs and J.H. van Boxel (1994): *Intermittent canopy turbulent transport, correlations time domain maps and the resulting inherent inadequacy of using large time averaged second order closure to describe canopy turbulent transport processes*; Proc. 21st Conf. on Agricultural and Forest Meteorology and 11th Conf. on Biometeorology and Aerobiology, March 7-11, 1994, San Diego Calif., pp. 80-83.

Ellingson, R.G., J. Ellis and S. Fels (1991): The intercomparsion of radiation codes used in climate models: longwave results; *J.Geoph.Res.* **96**, 8929-8953.
Feddes, R.A. (1971): *Water, heat and crop growth*; Mededelingen Landbouwhogeschool 71-12, Wageningen, The Netherlands, 184 pp.
Friborg, Th. (1995): *The use of carbon dioxide fluxes in climatology*; PhD-thesis Copenhagen Unniversity, 67 pp.
Garratt, J.R. (1978): Transfer characteristics for a heterogeneous surface of large aerodynamic roughness; *Q.J.R.Meteorol.Soc.* **104**, 491-502.
Garrat, J.R. (1992): *The atmospheric boundary layer*; University Press, Cambridge, UK, 316 pp.
Garrat, J.R. (1993): Sensitivity of climate simulations to land-surface and atmospheric boundary-layer treatments - a review; *J.Climate* **6**, 419-449
Garratt, J.R. and B.B. Hicks (1973): Momentum, heat and water vapour transfer to and from natural and artificial surfaces; *Q.J.R.Meteorol.Soc.* **99**, 680-687.
Gates, D.M. (1980): *Biophysical Ecology*; Springer Verlag, New York, 611 pp.
Goudriaan, J. (1977): *Crop micrometeorology: a simulation study*; Wageningen Center for Agricultural Publishing and Documentation, Wageningen, 249 pp.
Goudriaan, J. (1988): The bare bones of leaf angle distribution in radiation models for canopy photosynthesis and energy exchange; *Agric.For.Meteorol.* **43**, 155-170.
Goudriaan, J. and H.H. van Laar (1978): Relations between leaf resistance, CO_2-concentration and CO_2-assimilation in maize, beans, lalang grass and sunflower; *Photosynthetica* **12**, 241-249.
Goudriaan, J., H.H. van Laar, H. van Keulen and W. Louwerse (1985): Photosynthesis, CO_2 and plant production; In: W. Day and R.K. Atkin (Eds.), *Wheat growth and modelling*; NATO ASI series, Series A, Vol. 86, Plenum Press, New York, 107-122.
Goutorbe, J.P., T. Lebel, A. Tinga, P. Bessemoulin, J. Brouwer, A.J. Dolman, J.H.C. Gash, M. Hoepffner, P. Kabat, Y.H. Kerr, B. Monteny, S. Prince, F. Said, P. Sellers and J. Wallace (1994): HAPEX-Sahel: a large scale study of land atmospheric interactions in the semi-arid tropics; *Ann.Geophysicae* **12**, 53-64.
Graser, E.A. and C.H.M. van Bavel (1982): The effect of soil moisture upon soil albedo; *Agric.Meteorol.* **27**, 17-26.
Halldin, S. and A. Lindroth (1992): Errors in net radiometry. Comparison and evaluation of six radiometer designs; *J.Atmos.Ocean.Techn.* **9**, 762-783.
Henderson-Sellers, A. and V. Gornitz (1984): Possible climatic impacts of land cover transformations, with particular emphasis on tropical deforestation; *Clim.Change* **6**, 231-258.
Henderson-Sellers, A. and V.B. Brown (1992): Project for Intercomparison of Land-surface Parameterization Schemes (PILPS); *PILPS workshop report and first science plan*; IGPO publication series No. 5, Science and Technology Corporation, Hampton, Virginia, USA, 32 pp. plus annexes.
Henderson-Sellers, A., Z.-L. Yang and R.E. Dickinson (1993): The project for intercomparison of land-surface parameterization schemes; *Bull.Am.Meteorol.Soc.* **74**, 1335-1349.
Henderson-Sellers, A., A.J. Pitman, P.K. Love, P. Irannejad and T.H. Chen (1995): The project for intercomparison of land-surface parameterization schemes (PILPS): phases 2 and 3; *Bull.Am.Meteorol.Soc.* **76**, 489-503.
Hicks, B.B. (1973): Eddy fluxes over a vineyard; *Agric.Meteorol.* **12**, 203-215.
Hill, R.J., G.R. Ochs and J.J. Wilson (1992): Measuring surface-layer fluxes of heat and momentum using optical scintillation; *Boundary-Layer Meteorol.* **58**, 391-48.
Højstrup, J. (1981): A simple model for the adjustment of velocity spectra in unstable conditions downstream of an abrubt change in roughness and heat flux; *Boundary-Layer Meteorol.* **21**, 341-356.
Holtslag, A.A.M. and A.P. van Ulden (1983): A simple scheme for daytime estimates of the surface fluxes from routine weather data; *J.Clim. and Appl.Meteorol* **22**, 517-529.
Holtslag, A.A.M. and C.-H. Moeng (1991): Eddy diffusivity and countergradient transport in the convective atmospheric boundary layer; *J.Atmos.Sci.* **48**, 1690-1698.
Holtslag, A.A.M. and F.T.M. Nieuwstadt (1986): Scaling the atmospheric boundary layer; *Boundary-Layer Meteorol.* **36**, 201-209.
Holtslag, A.A.M., E.I.F. de Bruijn and H.-L. Pan (1990): A high resolution air mass transformation model for short-range weather forecasting; *Month.Wea.Rev.* **118**, 1261-1575.
Holtslag, A.A.M., E. van Meygaard and W.C. de Rooy (1995): A comparison of boundary layer diffusion schemes in unstable conditions over land; (in press by *Boundary-Layer Meteorol.*).
Horton, R., P.J. Wierenga and D.R. Nielsen (1983): Evaluation of methods for determining the apparent thermal diffusivity of soil near the surface; *Soil.Sci.Soc.Am.* **47**, 25-32.

Huband, N.D.S. and J.L. Monteith (1986): Radiative surface temperature and energy balance of a wheat canopy. I: comparison of radiative and aerodynamic canopy temperature; *Boundary-Layer Meteorol.* **36**, 1-17.

Huntingford, C., S.J. Allen and R.J. Harding (1995): An intercomparison of single and dual-source vegetation-atmosphere transfer models applied to transpiration from Sahelian savannah; *Boundary-Layer Meteorol.* **74**, 397-418.

Idso, S.B. (1981): A set of equations for full spectrum and 8- to 14-μm and 10.5- to 12.5-μm thermal radiation from cloudless skies; *Water Resources Res.* **17**, 295-304.

Idso, S.B., R.D. Jackson, R.J. Reginato, B.A. Kimball, and F.S. Nakayama (1975): The dependence of bare soil albedo on soil water content; *J.Appl.Meteorol.* **14**, 109-113.

Inclán, M.G. and R. Forkel (1995): Comparison of energy fluxes calculated with the Penman-Monteith equation and the vegetation models SIB and Cupid; *J.Hydrol.* **166**, 193-212.

Jacobs, A.F.G. and J.H. van Boxel (1988): Changes of the displacement height and roughness length of maize during a growing season; *Agric.For.Meteorol.* **42**, 53-62.

Jacobs, A.F.G. and W.A.J. van Pul (1990): Seasonal changes in the albedo of a maize crop during two seasons; *Agric.For.Meteorol.* **49**, 351-360.

Jacobs, C.A. and P.S. Brown (1973): An investigation of the numerical properties of the surface heat-balance equation; *J.Appl.Meteorol.* **12**, 1069-1072.

Jacobs, C.M.J. (1994): *Direct impact of atmospheric CO_2 enrichment on regional transpiration*; PhD-thesis, Wageningen Agric. Univ., The Netherlands, 179 pp.

Jacobs, C.M.J. and H.A.R. de Bruin (1992): The sensitivity of regional transpiration to land-surface characteristics: significance of feedback; *J.Climate* **5**, 683-698.

Jacobs, C.M.J., B.J.J.M. van den Hurk and H.A.R. de Bruin (1995): Stomatal behavior and photosynthetic rate of unstressed grapevines in semi-arid conditions; (in press by *Agric.For. Meteorol.*)

Jarvis, P.G. (1976): The interpretation of the variations in leaf water potential and stomatal conductance found in canopies in the field; *Phil.Trans.R.Soc.London*, Ser. B, **293**, 593-610.

Jarvis, P.G., G.B. James and J.J. Landsberg (1976): Coniferous forest; In: J.L. Monteith (Ed.), *Vegetation and the atmosphere*, Vol. 2, Academic Press, 171-240.

Kaimal, J.C., J.C. Wyngaard and D.A. Haugen (1968): Deriving power spectra from a three-component sonic anemometer; *J.Appl.Meteorol.* **7**, 827-834.

Kaimal, J.C., J.C. Wyngaard, Y. Izumi and O.R. Cote (1972): Spectral characteristics of surface layer turbulence; *Q.J.R.Meteorol.Soc.* **98**, 563-589.

Kawatani, T. and R.N. Meroney (1970): Turbulence and wind speed characteristic within a model canopy flow field; *Agric.Meteorol.* **7**, 143-158.

Kelliher, F.M., R. Leuning, M.R. Raupach and E.-D. Schulze (1995): Maximum conductances for evaporation from global vegetation types; *Agric.For.Meteorol.* **73**, 1-16.

Keijman, J.Q. (1974): The estimation of the energy balance of a lake from simple weather data; *Boundary-Layer Meteorol.* **7**, 399-407.

Kim, J. and S.B. Verma (1991a): Modeling canopy photosynthesis: scaling up from a leaf to canopy in a temperate grassland ecosystem; *Agric.For.Meteorol.* **57**, 187-208.

Kim, J. and S.B. Verma (1991b): Modelling canopy stomatal conductance in a temperate grassland ecosystem; *Agric.For.Meteorol.* **55**, 149-166.

KNMI (1981): Codevorm en codes voor de SYNOP en de KLIM; KNMI, The Netherlands, 168 pp. (in Dutch)

Kohsiek, W. (1982): Measuring C_T^2, C_Q^2 and C_{TQ} in the unstable surface layer, and relations to the vertical fluxes of heat and moisture; *Boundary-Layer Meteorol.* **24**, 89-107.

Kohsiek, W., H.A.R. de Bruin, H. The and B. van den Hurk (1993): Estimation of the sensible heat flux of a semi-arid area using surface radiative temperature measurements; *Boundary-Layer Meteorol.* **63**, 213-230. (See also: Kohsiek *et al.*, 1994)

Kohsiek, W., H.A.R. de Bruin, H. The and B. van den Hurk (1994): Corrigendum to 'Estimation of the sensible heat flux of a semi-arid area using surface radiative temperature measurements'; *Boundary-Layer Meteorol.* **69**, 215-217.

Kondo, J., N. Saigusa and T. Sato (1990): A parameterization of evaporation from bare soil surfaces; *J.Appl.Meteorol.* **29**, 385-389.

Kondo, J., N. Saigusa and T. Sato (1992): A model and experimental study of evaporation from bare-soil surfaces; *J.Appl.Meteorol.* **31**, 304-312

Koracin, D. and R. Berkowicz (1988): Nocturnal boundary-layer height: observations by acoustic sounders and predictions in terms of surface-layer parameters; *Boundary-Layer Meteorol.* **43**, 65-83.

Koster, R. and M. Suarez (1992): Modelling the land surface boundary in climate models as a composite of independent vegetation stands; *J.Geophys.Res.* **97**, 2697-2715.
Krikke, R.H. (1994a): *Quicksel Manual*; Dept. of Meteorology, Wageningen Agricultural University, 19 pp.
Krikke, R.K. (1994b): *Comparison of detrended variance calculation methods*; Dept. Of Meteorology, Agricultural University, Wageningen.
Kustas, W.P., B.J. Choudhury, M.S. Moran, R.J. Reginato, R.D. Jackson, L.W. Gay and H.L. Weaver (1989): Determination of sensible heat flux over sparse canopy using thermal infrared data; *Agric.For.Meteorol.* **44**, 197-216.
Legg, B.J. and M.R. Raupach (1982): Markov-chain simulation of particle dispersion in inhomogeneous flows: the mean drift velocity induced by a gradient in Eulerian velocity variance; *Boundary-Layer Meteorol.* **24**, 3-13.
Lenschow, D.H., J.C. Wyngaard and W.T. Pendell (1980): Mean-field and second-moment budgets in a baroclinic, convective boundary layer; *J.Atmos.Sci.* **37**, 1313-1326.
Leuning, R. and J.B. Moncreiff (1990): Eddy-covariance CO_2 flux measurements using open- and closed-path CO_2 analysers: corrections for analyser water vapour sensitivity and damping of fluctuations in air sampling tubes; *Boundary-Layer Meteorol.* **53**, 63-76.
Leuning, R. and K.M. King (1992): Comparison of eddy-covariance measurements of CO_2 fluxes by open- and closed-path CO_2 analysers; *Boundary-Layer Meteorol.* **59**, 297-311.
Lloyd, C.R., J.H.C. Gash and M.V.K. Sivakumar (1992): Derivation of the aerodynamic roughness parameters for a Sahelian savannah site using the eddy correlation technique; *Boundary-Layer Meteorol.* **58**, 261-271.
Louis, J.-F. (1979): A parametric model of vertical eddy fluxes in the atmosphere; *Boundary-Layer Meteorol.* **17**, 187-202.
Mahfouf, J.F. and J. Noilhan (1991): Comparative study of various formulations of evaporation from bare soil using in situ data; *J.Appl.Meteorol.* **30**, 1354-1365.
Mahrt, L. and H.-L. Pan (1984): A two-layer model for soil hydrology; *Boundary-Layer Meteorol.* **29**, 1-20.
Malhi, Y.S. and B.J.J.M. van den Hurk (1992): Net radiometer comparison experiments during the EFEDA-campaign; In: H.J. Bolle and B. Streckenbach (Eds.), *EFEDA - first annual report*; Univ. of Berlin, 241-254.
Manabe, S. (1969): The atmospheric circulation and hydrology of the Earth's surface; *Mon.Weather Rev.* **97**, 739-774.
Mayocchi, C.L. and K.L. Bristow (1995): Soil surface heat flux: some general questions and comments on measurements; *Agric.For.Meteorol.* **75**, 43-50.
McArthur, A.J. (1990): An accurate solution to the Penman equation; *Agric.For.Meteorol.* **51**, 87-92.
McBean, G.A. (1972): Instrument requirements for eddy correlation measurements; *J.Appl.Meteorol.* **11**, 1078-1084.
McClatchey, R.A., R.W. Fenn, J.E.A. Selby, F.E. Volz and J.S. Garing (1971): Optical properties of the atmosphere; *Rep. Air Force Cambridge Res.Lab.-71-0279*, Bedford, Massachussets, 85 pp.
McIntosh, D.H. and A.S. Thom (1983): *Essentials of meteorology*; Taylor & Francis Ltd, London, 238 pp.
McMillen, R.T. (1988): An eddy-correlation technique with extended applicability to non-simple terrain; *Boundary-Layer Meteorol.* **43**, 231-245.
McNaughton, K.G. and P.G. Jarvis (1983): Predicting effects of vegetation changes on transpiration and evaporation. In: T.T. Kozlowski (Ed.), *Water deficits and plant growth, Vol. 7*, Academic Press, New York, pp. 1-47.
McNaughton, K.G. and T.W. Spriggs (1986): A mixed layer model for regional evaporation; *Boundary-Layer Meteorol.* **34**, 243-262.
McNaughton, K.G. and B.J.J.M. van den Hurk (1995): A 'Lagrangian' revision of the resistors in the two-layer model for calculating the energy budget of a plant canopy; *Boundary-Layer Meteorol.* **74**, 261-288.
Menenti, M., W.G.M. Bastiaanssen and D. van Eick (1989): Determination of surface hemispherical reflectance with Thematic Mapper data; *Remote Sensing Environ.* **28**, 327-337.
Meyers, T.P. and K.T. Paw U (1986): Testing of a higher-order closure model for modelling airflow within and above plant-canopies; *Boundary-Layer Meteorol.* **37**, 297-311.
Meyers, T.P. and K.T. Paw U (1987): Modelling the plant canopy micrometeorology with higher-order closure principles. *Agric.For.Meteorol.* **41**, 143-163.
Michels, B.I. and A.F. Moene (1991): *The contribution of the Department of Meteorology, WAU, to the EFEDA pilot study: project performance and results on crop development and roughness parameters*; Dept. of Meteorology, Wageningen Agricultural University, 78 pp.

Michels, B.I. and A.M. Jochum (1995): Heat and moisture flux profiles in a region with inhomogeneous surface evaporation; *J.Hydrol.* **166**, 383-408.
Milly, P.C.D. and K.A. Dunne (1994): Sensitivity of the global water cycle to the water-holding capacity of land; *J.Climate* **7**, 506-526.
Mintz, Y. (1984): The sensitivity of numerically simulated climates to land surface boundary conditions. In: J.T. Houghton (Ed.), *The Global Climate*, Cambridge University Press, pp. 79-105.
Moene, A.F., H.A.R. De Bruin and A.A.M. Holtslag (1995): Validation of the surface parametrization of HIRLAM using surface-based measurements and remote sensing data; KNMI Scientific report WR 95-07, 45 pp.
Moene, A.F. (1992): Intercomparison of energy fluxes measured during EFEDA; Dept. of Meteorology, Wageningen Agricultural University, Wageningen, The Netherlands, 33 pp.
Moeng, C.-H. and J.C. Wyngaard (1984): Statistics of conservative scalars in the convective boundary layer; *J.Atmos.Sci* **41**, 3161-3169.
Moeng, C.-H. and J.C. Wyngaard (1989): Evaluation of turbulent transport and dissipation closures in second-order modeling; *J.Atmos.Sci.* **46**, 2311-2330.
Moncreiff, J.B., J.M. Massheder, H.A.R. De Bruin, J. Elbers, T. Friborg, B.G. Heusinkveld, P. Kabat, S. Scott, H. Sogaard and A. Verhoef (1995): A system to measure surface fluxes of momentum, sensible heat flux, water vapour and carbon dioxide; (Accepted for publication by *J.Hydrol.*)
Monna, W.A.A., W. Kohsiek, G.J. Prangsma, J.N. Roozekrans and J.G. van der Vliet (1994): EFEDA-91 Documentation of measurements obtained by KNMI; Techn.Rep. TR-171, KNMI, De Bilt, The Netherlands, 13 pp.
Monteith, J.L. (1965): Evaporation and the environment; *Symp.Soc.Exp.Biol.* **19**, 205-234.
Monteith, J.L. (1973): *Principles of environmental physics*; Edward Arnold Press, London.
Monteith, J.L. (1981): Evaporation and surface temperature; *Q.J.R.Meteorol.Soc.* **107**, 1-27.
Monteith, J.L. (1993): The exchange of water and carbon by crops in a mediterranean climate. *Irrig. Sci.* **14**, 85-91.
Monteith, J.L. (1995a): Accomodation between transpiring vegetation and the convective boundary layer; *J.Hydrol.* **166**, 251-264.
Monteith, J.L. (1995b): A reinterpretation of stomatal responses to humidity; *Plant, Cell and Environment* **18**, 357-364.
Monteith, J.L., G.S. Campbell and E.A. Potter (1988): Theory and performance of a dynamic diffusion porometer; *Agric.For.Meteorol.* **44**, 27-38.
Moore, C.J. (1986): Frequency response corrections for eddy correlation systems; *Boundary-Layer Meteorol.* **37**, 17-35.
Morison, J.I.L. and R.M. Gifford (1983): Stomatal sensitivity to carbon dioxide and humidity: a comparison of two C3 and two C4 grass species; *Plant Physiology* **71**, 789-796.
Mott, K.A. and D.F. Parkhurst (1991): Stomatal response to humidity in air and helox. *Plant, Cell and Environment* **14**, 509-515.
Myers, V.I. and W.A. Allen (1968): Electro-optical remote sensing methods as nondestructive testing and measuring techniques in agriculture; *Applied optics* **7**, 1819-1838.
Noilhan, J. and S. Planton (1989): A simple parameterization of land surface processes for meteorological models; *Mon.Weather Rev.* **117**, 536-549.
Norman, J.M. (1982): Simulation of microclimates; In: J.L. Hatfield and I.J. Thompson (Eds.), *Biometeorology in integrated pest management*; Academic Press, New York, pp. 205-234.
Norman, J.M. and J.M. Welles (1983): Radiative transfer in an array of canopies; *Agronomy J.* **75**, 481-488.
Oke, T.R (1978): *Boundary layer climates*; Methuen & Co Ltd, London, UK, 372 pp.
Panofsky, H.A., H. Tennekes, D.H. Lenschow and J.C. Wyngaard (1977): The characteristics of turbulent velocity components in the surface layer under convective conditions; *Boundary-Layer Meteorol.* **11**, 355-361.
Panofsky, H.A. and J.A. Dutton (1984): *Atmospheric turbulence; models and methods for engineering applications*; Wiley and Sons, New York
Paulson, C.A. (1970): The mathematical representation of wind speed and temperature profiles in the unstable atmospheric surface layer; *J.Appl.Meteorol.* **9**, 857-861.
Pereira, A.R. and R.H. Shaw (1980): A numerical experiment on the mean wind structure inside canopies of vegetation; *Agric.For.Meteorol.* **22**, 303-318.
Philip, J.R. (1957): Evaporation, and moisture and heat fields in the soil; *J.Meteorol.* **14**, 354-366.
Philip, J.R. (1961): The theory of heat flux meters; *J.Geophys.Res.* **66**, 571-579.
Philip, J.R. (1963): The damping of a fluctuating concentration by continuous sampling through a tube; *Aust.J.Phys.* **16**, 454-463.

Press, W.H., B.P Flannery, S.A. Teukolsky and W.T. Vetterling (1986): *Numerical Recipes*; Cambridge University Press, Cambridge, 818 pp.
Priestley, C.H.B. and R.J. Taylor (1972): On the assessment of surface heat flux and evaporation using large-scale parameters; *Mon.Weather Rev.* **100**, 81-92.
Raupach, M.R. (1988): Canopy Transport Processes; In: W.L. Steffen and O.T. Denmead (Eds.), *Flow and Transport in the Natural Environment: Advances and Applications*; Springer-Verlag, Berlin, pp. 95-127.
Raupach, M.R. (1989a): A practical Lagrangian method for relating scalar concentrations to source distributions in vegetation canopies; *Q.J.R.Meteorol.Soc.* **115**, 609-632.
Raupach, M.R. (1989b): Applying Lagrangian fluid mechanics to infer scalar source distributions from concentration profiles in plant canopies; *Agric.For.Meteorol.* **47**, 85-108.
Raupach, M.R. (1991): Vegetation-atmosphere interaction in homogeneous and heterogeneous terrain: some implications of mixed-layer dynamics; *Vegetatio* **91**, 105-120.
Raupach, M.R. (1992): Drag and drag partition on rough surfaces; *Boundary-Layer Meteorol.* **60**, 375-395.
Raupach, M.R. and J.J. Finnigan (1988): 'Single layer models of evaporation from plant canopies are incorrect but useful, whereas multilayer models are correct but useless': discuss; *Aust.J.Plant.Physiol.* **15**, 705-716.
Raupach, M.R. and A.S. Thom (1981): Turbulence in and above plant canopies; *Ann.Rev.Fluid.Mech.* **13**, 97-129.
Robinson, S.M. (1962): Computing wind profile parameters; *J.Atmos.Sci.* **19**, 189-190.
Rowntree, P.R. (1991): Atmospheric parameterization schemes for evaporation over land: basic concepts and climate modeling aspects; In: Schmugge and André (Eds.), *Land Surface Evaporation; Measurement and Parameterization*; Springer-Verlag, New York, pp. 5-30.
Rowntree, P.R. and A.B. Sangster (1986): Remote Sensing needs identified in climate model experiments with hydrological and albedo changes in the Sahel; Proc. ISLSCP Conference, Rome, ESA SP-248, pp. 175-183.
Sato, N., P.J. Sellers, D.A. Randall, E.K. Schneider, J. Shukla, J.L. Kinter III, Y-T. Hou and E. Albertazzi (1989): Effects of implementing the Simple Biosphere model in a General Circulation Model; *J.Atmos.Sci.* **18**, 2757-2782.
Sawford, B.L. (1986): Generalized random forcing in random-walk turbulent dispersion models; *Phys.Fluids* **29**, 3582-3585.
Schmugge, T.J. and J.C. André (Eds.) (1991): *Measurement and parameterization of land surface evaporation fluxes*; Springer Verlag, New York.
Schotanus, P., F.T.M. Nieuwstadt and H.A.R. de Bruin (1983): Temperature measurement with a sonic anemometer and its applications to heat and moisture fluxes; *Boundary-Layer Meteorol.* **26**, 81-93.
Sellers, P.J. (1985): Canopy reflectance, photosynthesis and transpiration; *Int.J.Remote Sensing* **6**, 1335-1372.
Sellers, P.J., Y. Mintz, Y.C. Sud and A. Dalcher (1986): A simple biosphere model (SiB) for use within general circulation models; *J.Atmos.Sci.* **43**, 505-531.
Sellers, P.J., F.G. Hall, G. Asrar, D.E. Strebel and R.E. Murphy (1988): The first ISLSCP field experiment (FIFE); *Bull.Am.Meteorol.Soc.* **69**, 22-27.
Sene, K.J. (1994): Parameterisations for energy transfers from a sparse vine crop; *Agric.For.Meteorol.* **71**, 1-18.
Shao, Y., R.D. Anne, A. Henderson-Sellers, P. Irannejad, P. Thornton, X. Liang, T.H. Chen, C. Ciret, C. Desboroough, O. Balachova, A. Haxeltine and A. Ducharne (1994): *Soil moisture simulation: a report of the RICE and PILPS workshop*; Clim.Impacts Centre, IGPO Publ. Seri. No. 14, 179 pp.
Shaw, R.H. and A.R. Pereira (1982): Aerodynamic roughness of a plant canopy: a numerical experiment; *Agric.Meteorol.* **26**, 51-65.
Shiozawa, S. and G.S. Campbell (1990): Soil thermal conductivity; *Rem.Sens.Rev.* **5**, 301-310.
Shukla, J. and Y. Mintz (1982): Influence of land surface evapotranspiration on the Earth's climate; *Science* **215**, 1498-1501.
Shuttleworth, W.J (1988): Macrohydrology - the new challenge for process hydrology; *J.Hydrol.* **100**, 31-56.
Shuttleworth, W.J. and J.S. Wallace (1985): Evaporation from sparse crops - an energy combination theory; *Q.J.R.Meteorol.Soc.* **111**, 839-855.
Shuttleworth, W.J. and R.J. Gurney (1990): The theoretical relationship between foliage temperature and canopy resistance in sparse crops; *Q.J.R.Meteorol.Soc.* **116**, 497-519.

Shuttleworth, W.J., J.H.C. Gash, C.R. Lloyd, D.D. McNeil, C.J. Moore and J.S. Wallace (1988): An integrated micrometeorological system for evaporation measurement; *Agric.For.Meteorol.* **43**, 295-317.

Sinclair, T.R., L.H. Allen and E.R. Lemon (1975): An analysis of errors in the calculation of energy flux densities above vegetation by a Bowen-ratio profile method; *Boundary-Layer Meteorol.* **8**, 129-139.

Slater, P.N. (1980): *Remote-sensing optics and optical systems*; Addison-Wesley Publ.Comp., Reading, UK, 575 pp.

Stewart, J.B. (1988): Modelling surface conductance of pine forest; *Agric.For.Meteorol.* **43**, 19-35.

Stull, R.B. (1988): *An introduction to Boundary Layer Meteorology*; Kluwer Academic Publ., Dordrecht, The Netherlands, 666 pp.

Sud, Y.C., P.J. Sellers, Y. Mintz, M.D. Chou, G.K. Walker and W.E. Smith (1990): Influence of the biosphere on the global circulation and hydrological cycle - a GCM simulation experiment; *Agric.For.Meteorol.* **52**, 133-180.

Taylor, G.I. (1959): The present position in the theory of turbulent diffusion; *Adv.Geophys.* **6**, 101-112.

Ten Berge, H.F.M. (1990): *Heat and water transfer in bare topsoil and the lower atmosphere*; PUDOC, Wageningen, The Netherlands, 207 pp.

Tennekes, H. (1973): A model for the dynamics of the inversion above a convective boundary layer; *J.Atmos.Sci.* **30**, 558-567.

Tennekes, H. and J.L. Lumley (1972): *A first course in turbulence*; MIT Press, Massachusetts, 300 pp.

Thom, A.S. (1972): Momentum, mass and heat exchange of vegetation; *Q.J.R.Meteorol.Soc.* **98**, 124-134.

Thom, A.S. (1975): Momentum, mass and heat exchange of plant communities. In: J.L. Monteith (Ed.), *Vegetation and the Atmosphere, Vol. 1: Principles*; Academic Press, Orlando, USA, pp. 57-109.

Tillman, J.E. (1991): In situ water vapor measurements in the Lyman-alpha and infrared spectrum: theory and components; In: Schmugge and André (Eds.), *Land Surface Evaporation; Measurement and Parameterization*; Springer-Verlag, New York, pp. 313-335.

Troen, I. and L. Mahrt (1986): A simple model of the atmospheric boundary layer; sensitivity to surface evaporation; *Boundary-Layer Meteorol.* **37**, 129-148.

Turner, N.C. (1991): Measurement and influence of environmental and plant factors on stomatal conductance in the field; *Agric.For.Meteorol.* **54**, 137-154.

Van Asselt, C.J., A.F.G. Jacobs, J.H. van Boxel and A.E. Jansen (1991): A rigid fast-response thermometer for atmospheric research; *Meas.Sci.Technol.* **2**, 26-31.

Van de Griend, A.A. and M. Owe (1994): Bare soil surface resistance to evaporation by vapor diffusion under semi-arid conditions; *Water Resources Res.* **30**, 181-188.

Van de Griend, A.A., M. Owe, H. Vugts and S.D. Prince (1989): Water and surface energy balance modeling in Botswana; *Bull.Am.Meteorol.Soc.* **70**, 1404-1411.

Van den Hurk, B.J.J.M. (1995): *The influence of the detrending algorithm on computed eddy-correlation covariance*; Dept. of Meteorology, Agricultural University, Wageningen.

Van den Hurk, B.J.J.M. and D.D. Baldocchi (1990): Random-walk models for simulating water vapor exchange within and above a soybean canopy; NOAA Technical Memorandum ERL ARL-185, NOAA, Air Resources Laboratory, Silver Springs, Maryland, 46 pp.

Van den Hurk, B.J.J.M. and A.C.M. Beljaars (1995): Impact of some simplifying assumptions of the new ECMWF surface scheme; (submitted for publication to *J.Appl.Meteorol.*)

Van den Hurk, B.J.J.M. and H.A.R. de Bruin (1993): Surface fluxes measured during EFEDA; In: Bolle, H.J. and B. Streckenbach (Eds.), *The ECHIVAL Field Experiment in a Desertification-threatened Area (EFEDA) - Final report*, Univ. of Berlin, pp. 141-227.

Van den Hurk, B.J.J.M. and H.A.R. de Bruin (1995): Fluctuations of the horizontal wind under unstable conditions; *Boundary-Layer Meteorol.* **74**, 341-352.

Van den Hurk, B.J.J.M. and K.G. McNaughton (1995): Implementation of near-field dispersion in a simple two-layer surface resistance model; *J.Hydrol.* **166**, 293-311.

Van den Hurk, B.J.J.M., A. Verhoef, A.R. van den Berg and H.A.R. de Bruin (1995): An intercomparison of three vegetation/soil models for a sparse vineyard canopy; (In press by *Q.J.R. Meteorol.Soc.*)

Van Haneghem, I.A. (1981): *Een niet-stationaire naaldmethode (warmtegeleiding, warmtecapaciteit, contactweerstand)*; PhD-thesis, Dept. of Physics, Wageningen Agricultural University, The Netherlands, 187 pp.

Van Heemst (1986): Potential crop production. In: H. van Keulen & J. Wolf (Eds.), *Modelling of agricultural production: weather, soil and crops*. Simulation Monographs, Pudoc, Wageningen.

Van Wijk, W.R. (1963): *Physics of plant environment*; North Holland Publishers, Amsterdam, 382 pp.

Verhoef, A. (1995): *Surface energy balance of shrub vegetation in the Sahel*; PhD-thesis, Dept. of Meteorology, Wageningen Agricultural University, 247 pp.

Verhoef, A., B.J.J.M. van den Hurk, A.F.G. Jacobs and B.G. Heusinkveld (1995): Thermal soil properties for a vineyard (EFEDA-I) and a savanna (HAPEX-Sahel) site; (in press by *Agric.For. Meteorol.*).

Viterbo, P. and A.C.M. Beljaars (1995): *An improved land surface parameterization scheme in the ECMWF-model and its validation*; Technical Report TR 75, ECMWF, Reading, 52 pp. (also accepted for publication by *J. Climate*)

Waggoner, P.E. and W.E. Reifsnyder (1968): Simulation of the temperature, humidity and evaporation profiles in a leaf canopy. *J.Appl.Meteorol.* **7**, 400-409.

Wallace, J.S., J.M. Roberts and M.V.K. Sivakumar (1990): The estimation of transpiration from sparse dryland millet using stomatal conductance and vegetatian area indices; *Agric.For. Meteorol.* **51**, 35-49.

Warrilow, D.A., A.B. Sangster and A. Slingo (1986): *Modelling of land surface processes and their influence on European climate*; UK Met.Office, Bracknell, England, 92 pp.

Webb, E.K., G.I. Pearman and R. Leuning (1980): Correction of flux measurements for density effects due to heat and water vapour transfer; *Q.J.R.Meteorol.Soc.* **106**, 85-100.

Wieringa, J. (1993): Representative roughness parameters for homogeneous terrain; *Boundary-Layer Meteorol.* **63**, 323-363.

Wilson, N.R. and R.H. Shaw (1977): A higher-order closure model for canopy flow; *J.Appl.Meteorol.* **16**, 1198-1205.

Wilson, J.D., B.J. Legg and D.J. Thomson (1983): Correct calculation of particle trajectories in the presence of a gradient in turbulent velocity variance; *Boundary-Layer Meteorol.* **27**, 163-169.

Winkel, T. and S. Rambal (1990): Stomatal conductance of some grapevines growing in the field under a Mediterranean environment; *Agric.For.Meteorol.* **51**, 107-121.

Wiscombe, W.J. and S.G. Warren (1980): A model for the spectral albedo of snow. 1: Pure snow; *J.Atmos.Sci.* **37**, 2712-2733.

Wong, S.C., I.R. Cowan and G.D. Farquhar (1979): Stomatal conductance correlates with photosynthetic capacity; *Nature* **282**, 424-426.

Wyngaard, J.C. (1988): Flow distortion effects on scalar flux measurements in the surface layer: implications for sensor design; *Boundary-Layer Meteorol.* **42**, 19-26.

Wyngaard, J.C., Y. Izumi and S.A. Collins Jr. (1971): Behaviour of the refractive-index-structure parameter near the ground; *J.Opt.Soc.Am.* **61**, 1646-1650.

Xue, Y., P.J. Sellers, J.L. Kinter and J. Shukla (1991): A simplified biosphere model for global climate studies; *J.Climate* **4**, 345-364.

Curriculum

Bartholomeus Johannes Josephus Martinus van den Hurk (geboren op 19 november 1963 te Heeze, Noord-Brabant) legde de eerste twee jaar van de middelbare school af op het Strabrecht College in Geldrop. In 1982 behaalde hij het VWO examen aan het vd Putt-lyceum in Eindhoven, en begon aan een studie Milieuhygiëne, oriëntatie Luchthygiëne en -verontreiniging, aan de Landbouwuniversiteit Wageningen. Gedurende zijn studietijd zat hij een jaar in het bestuur van studentenvereniging SSR, en richtte in 1987 samen met zijn broer Stone De Stichting Lens op, een amateur muziektheater-gezelschap. In 1989 studeerde hij af, na een tweetal afstudeervakken Meteorologie, twee afstudeervakken Luchthygiëne, en een stage bij Dennis Baldocchi aan het Atmospheric Turbulence and Diffusion Division van NOAA in Oak Ridge, TN USA.

Hierna heeft hij gedurende anderhalf jaar zijn vervangende dienstplicht vervuld aan de Vakgroep Meteorologie van de Wageningse Landbouwuniversiteit. In die periode werkte hij aan diverse kleine projekten, onder begeleiding van Henk de Bruin. Aansluitend aan die periode werd hij aan dezelfde vakgroep aangesteld als wetenschappelijk assistent bij het in dit proefschrift beschreven EFEDA-projekt. Opnieuw onder supervisie van Henk de Bruin coördineerde hij de bijdrage van de vakgroep Meteorologie aan het veldexperiment in Spanje in 1991, en heeft zich daarna ruim een jaar beziggehouden met dataverwerking, contacten onderhouden met andere participanten aan het EFEDA-projekt, en met modelstudies. In de loop van deze periode kwam een gedeeltelijke NWO-promotieplaats vrij. Nadat de oorspronkelijke promotie-opdracht enigszins werd aangepast aan de ervaring die hij binnen de EFEDA-werkzaamheden had opgedaan, werd in het kader van de resterende, door NWO gesubsidieerde, aanstelling naar de in dit proefschrift beschreven promotie toegewerkt. Vanaf september 1995 werkt hij via een tijdelijke aanstelling bij het KNMI aan de toepassing van satellietgegevens voor bodemvochtinitialisatie in weermodellen.

Bart van den Hurk is getrouwd met Christien Alferink, en heeft (nog) geen kinderen.